14th European Coating Symposium

ECS Book of Abstracts

September 6-9, 2021, Brussels, Belgium

Pre-Symposium Course "Dynamics of Liquid Film Coatings
Theory and Applications" on 6 September 2021

ECS Symposium from 7 to 9 September 2021

Editors:
Jean-Marie Buchlin
Miguel Mendez
Benoît Scheid

ULB UNIVERSITÉ LIBRE DE BRUXELLES

von KARMAN INSTITUTE FOR FLUID DYNAMICS

FOREWORD

Welcome to the 14th European Coating Symposium.

On behalf of the organizing committee, it is our great pleasure to warmly welcome you to the 14th European Coating Symposium (ECS) in Brussels. The 14th symposium, organized by the von Karman Institute and the Université Libre de Bruxelles, follows the footsteps of the previous editions and continues to gather researchers from academia and industry to share and discuss advancements in coating science.

The scientific program committee has helped us to put together an outstanding symposium with close to 70 oral and poster presentations. Despite the challenging historical moment, this edition continues to keep the tradition, started in 1995, of being a truly international meeting with a strong European dimension.

We wish to express our gratitude to everybody who has helped organizing the event, and in particular to the researchers presenting their work. Ultimately, it is you who will create a successful ECS meeting. Special thanks to our sponsors and exhibitors, who have ensured the economic viability of the symposium. Finally, we also wish to thank the International Coating Science and Technology (ISCST) to fostering continuous co-operation between the European and American coating research communities

We hope you will have the chance to experience and enjoy Brussels and its surroundings, and we wish you a rewarding and enjoyable ECS 2021

Once again, welcome to Brussels and to the ECS2021!

Prof. Benoît Scheid
Université Libre de
Bruxelles

Prof. Miguel Mendez
von Karman Institute for
Fluid Dynamics

Prof. Jean-Marie Buchlin
von Karman Institute for
Fluid Dynamics

SPONSORS

We warmly thank the following sponsors:

ORGANIZING COMMITTEE

ECS2021 Symposium Chairs

Prof. Miguel A. Mendez

Environmental and Applied Fluid Dynamics Department von Karman Institute for Fluid Dynamics (VKI)

Prof. Benoît Scheid

Unité de recherche en Physique des fluides Ecole polytechnique de Bruxelles, Université Libre de Bruxelles (ULB)

Local Organizing Committee

Contact: ecs2021@vki.ac.be

Jean-Marie Buchlin, von Karman Institute
Christelle Debeer, von Karman Institute
Dominique Landuyt, von Karman Institute
Simone Kratochvil, von Karman Institute
Karine Triqueneaux, Université Libre de Bruxelles

SCIENTIFIC COMMITTEE

ECS Presidents

President: Peter Schweizer (Switzerland/Industry)
Vice President: Wilhelm Schabel (Germany/Academia)

ECS Board

Philip Scharfer, Chairman ECS 2019
Gilbert Gugler, Chairman ECS 2017
Ike de Vries and Anton A. Darhuber, Chairmen ECS 2015
Jocl De Coninck, Chairman ECS 2013
Martti Toivakka, Chairman ECS 2011
Wilhelm Schabel, Chairman ECS 2009
Laurent Limat, Chairman ECS 2007
Hadj Benkreira, Chairman ECS 2005
Peter Schweizer, Chairman ECS 2003
Jean-Marie Buchlin, Chairman ECS 2001

ECS Scientific Committee

I=Industry; A=Academic

Peter Schweizer (I)
Schweizer Coating, Fribourg, Switzerland

Hadj Benkreira (A)
University of Bradford, UK

Jean-Marie Buchlin (A)
von Karman Institute, Bruxelles, Belgium

Laurent Limat (A)
University of Paris, France

Wilhelm Schabel (A)
KIT, Karlsruhe Institute of Technology, Germany

Philip Scharfer (A)
KIT, Karlsruhe Institute of Technology, Germany

Alex Routh (A)
Cambridge University, UK

Martti Toivakka (A)
Abo Akademi University, Finland

Gilbert Gugler (A)
Iprint Institute, Fribourg, Switzerland

Max Mueller (I)
Roche Diabetes Care, Mannnheim, Germany

Anton Darhuber (A)
TU/e, Eindhoven University of Technology, Netherlands

Ta-Jo Liu (A)
National Tsing Hua University, Taiwan

Masato Yamamura (A)
Kyushu Inst. of Technology, Japan

Satish Kumar (A)
University Minnesota, US

Frank Kleine Jäger (I)
BASF SE, Ludwigshafen, Germany

Kyung Hyun Ahn (A)
Seoul National University, South Korea

Phil Gaskell (A)
Durham University, UK

Ike de Vries (A)
Holst Center,TNO, Eindhoven, Netherlands

Harald Döll (I)
TSE Troller, Switzerland

Robert Beer (I)
WiFag Polytype, Switzerland

Miguel Mendez (A)
von Karman Institute, Belgium

Ludovic Pauchard (A)
CNRS, Paris, France

Fritz Bircher (A)
Iprint Institute, Fribourg, Switzerland

David Seveno (A)
Univ. of Leuven, Belgium

Benoit Scheid (A)
Univ. Libre de Bruxelles, Belgium

Anne Gosset (A)
University of Coruna, Spain

Daniel Eggerath (I)
FMP Technology GmbH, Germany

Jaekwook Nam (A)
Seoul National University (SNU), Korea

Wolfgang Haselrieder (A)
TU Braunschweig, IPAT , Germany

Tequila Harris (A)
Georgia Institute of Technology, USA

TABLE OF CONTENTS

Session: Interface Dynamics

INTERFACE DYNAMICS

Proceedings ECS 2021
Brussels, Belgium, September 7-9, 2021

Abstract T-70

TO DRIP OR NOT TO DRIP: PATTERN FORMATION OF A THIN FILM FLOWING UNDER AN INCLINED PLANE

***P. G. Ledda*[1], *G. Lerisson*[1], *G. Balestra*[2] and *F. Gallaire*[1]**

[1]Laboratory of Fluid Mechanics and Instabilities, EPFL, Lausanne, Switzerland
[2] iPrint Institute, HEIA-FR, HES-SO University of Applied Sciences and Arts Western Switzerland, Fribourg, Switzerland

Email: pier.ledda@epfl.ch

Abstract
We discuss the pattern formation of a thin film flowing under an inclined plane, with theoretical, experimental and numerical analyses, in the context of the Rayleigh-Taylor instability and in the absence of inertia.

Keywords: *coating, instability, rivulets, dripping*

A very viscous Newtonian fluid is injected under an inclined glass plate, with a constant flow rate (Fig. 1(a)). We study the dynamics of the flat film to spanwise perturbations at the inlet. Spanwise-periodic and streamwise-aligned structures, called rivulets, invade the domain (Fig. 1(b)).

The emergence of rivulet structures is numerically and experimentally rationalized via the weakly non-linear impulse response of a flat film. The fully non-linear evolution leads to a steady pattern characterized by rivulets. The rivulet profile is described by a two-dimensional static pendant drop with imposed flow rate.

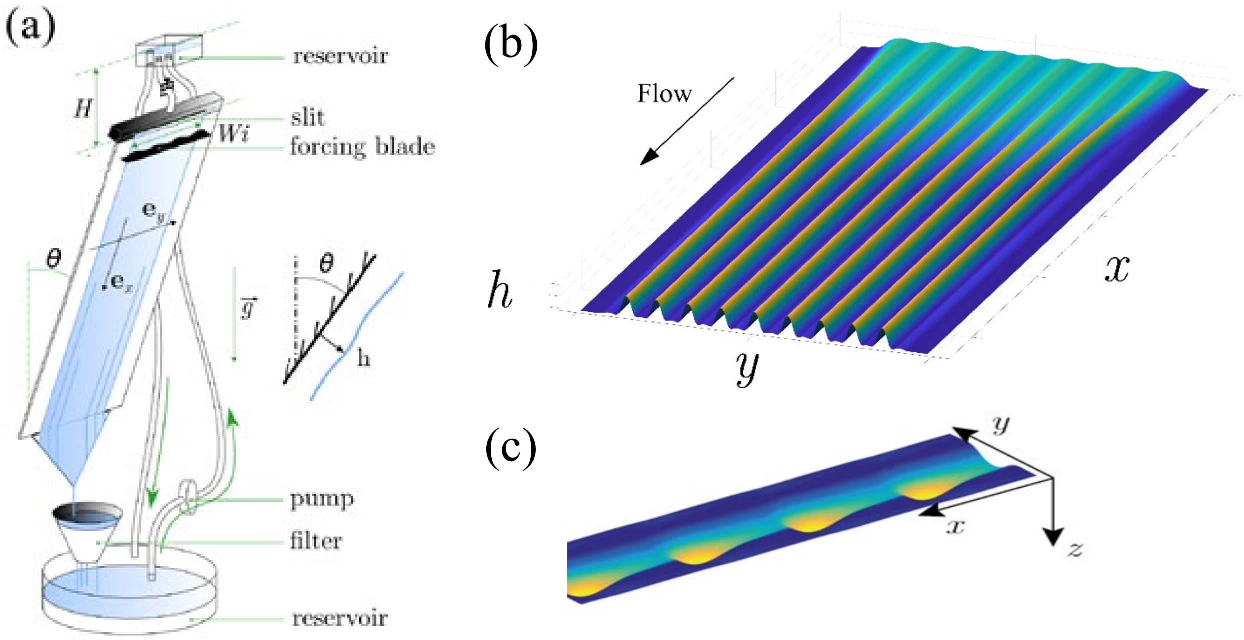

Figure 1. (a) Flow configuration and experimental set-up. (b) Experimental measurement of the film thickness in which rivulets invade the domain. (c) Sketch of a rivulet with lenses.

A secondary stability analysis on the rivulet profile reveals that as the flow rate or the inclination angle are decreased the rivulets are progressively stabilized until quenching of the instability.

As a result of the instability, lenses traveling on the rivulets are observed (Fig. 1(c)), which are numerically studied in the context of imposed temporal harmonic forcing at the inlet.

In a last step, these lenses may eventually drip from the inclined ceiling.

Proceedings ECS 2021
Brussels, Belgium, September 7-9, 2021

Abstract T-15

SPANWISE STRUCTURING AND RIVULET FORMATION IN SUSPENDED FALLING LIQUID FILMS

***M. Rietz*[1], *B. Scheid*[2], *R. Kneer*[1], *W. Rohlfs*[3]**

[1]WSA, RWTH Aachen University, Augustinerbach 6, 52056 Aachen, Germany
[2]TIPs, Université libre de Bruxelles, Avenue F.D. Roosevelt 50, 1050 Bruxelles, Belgium
[3]Department of Thermal and Fluid Engineering, University of Twente, Drienerlolaan 5, 7522 NB Enschede, The Netherlands

Email: rietz@wsa.rwth-aachen.de

***Keywords**: Falling films, instability, rivulet formation*

A cascade of primary and secondary fluid dynamical instabilities leads to complex patterns of waves on the surface of falling liquid films. In suspended falling films, i.e. films on the underside of a bounding wall with arbitrary inclination, the surface film topology evolves towards a distinct spanwise structuring into rivulets, which is potentially accompanied by dripping events. The separation of evolving rivulets was shown to be predicted by the Rayleigh-Taylor (RT) mechanism with satisfying accuracy for falling films characterized by low Reynolds number and low Kapitza number (Rietz, 2017). However, experimental data of Charogiannis et al. (Charogiannis, 2018) point to the frequency selection mechanism being more intricate if a film flow of larger Reynolds and Kapitza numbers is considered.

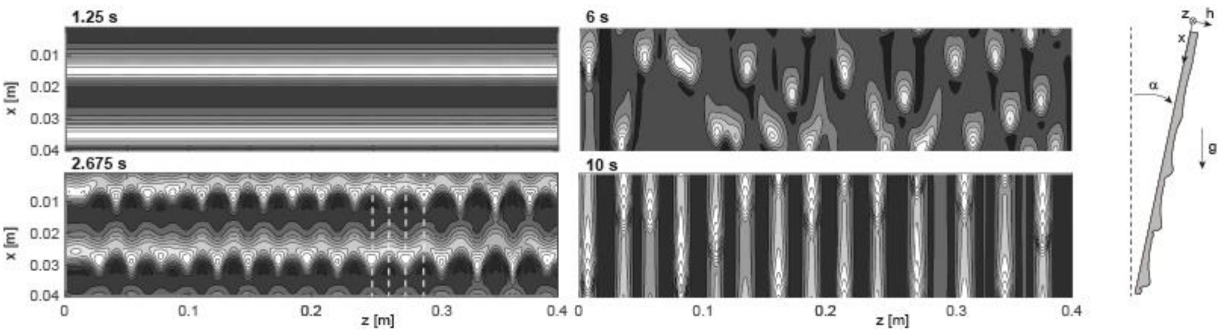

Figure 1. Exemplary simulation result for the temporal evolution of a suspended liquid film displaying an asynchronous destabilization of consecutive wave fronts and reorganization into rivulets. Lighter colors depict larger film heights. Parameters: α = 15°, Re = 1, Ka = 13.1.

The present study elucidates the evolution of a suspended falling film from varying imposed initial conditions to the emergence of spanwise modulations and rivulet formation. The study is carried out by means of numerical simulations employing a weighted residual integral boundary layer (WRIBL) formulation for falling liquid films (Kalliadasis, 2012). Varying imposed initial conditions, Reynolds number, Kapitza number as well as wall inclination several possible causes for a deviation of observed spanwise wavelengths from the one predicted by the RT mechanism are identified. This includes asynchronous destabilization of consecutive wavefronts (see Fig. 1), secondary instabilities of developing wavefronts, competing short wave capillary instabilities as well as rivulet interaction. We show that stability analysis of initially developing 2D traveling waves allows to predict the long-term spanwise structuring of the film over a wide parameter range despite the presence of intermediate regimes of wave-to-wave interaction and flow reorganization.

In this context, the long-term evolution of the film is followed for up to 100 seconds using the simulation tool WaveMaker (Rohlfs, 2018). To visualize the process of spanwise structuring of the film surface.

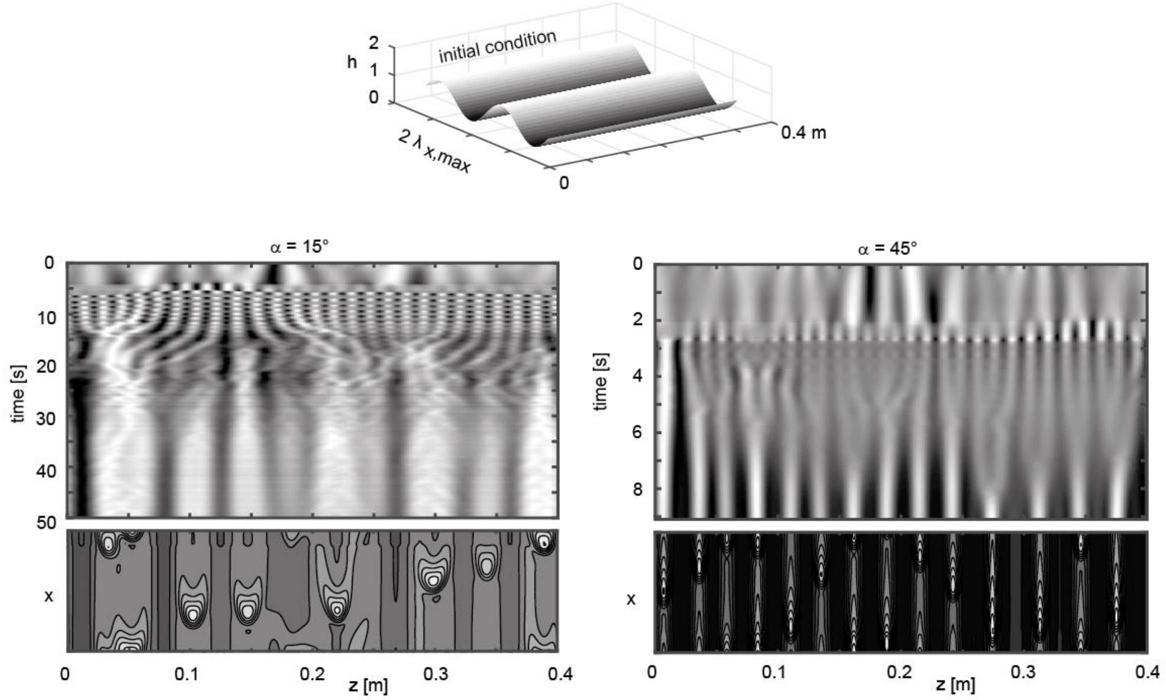

Figure 2. Temporal plots of the normalized average spanwise film height profile $\bar{h}_{z,norm}(t, z)$ and spatial plots of the last simulated time step for two different wall inclinations and employing the shown initial condition. Dark to light colors span the value range [0,1] of the normalized mean spanwise film height profile. Spatial plots of the last time step are normalized by the minimum and maximum film height. Parameters: Re = 1, Ka = 13.1.

From the beginning, where very small spanwise variations are present, to the late stages of film evolution, where large amplitude quasi-stationary rivulets are formed, the mean spanwise film topology is normalized based on the minimum and maximum values at each respective timestep as defined in equation (1).

$$\bar{h}_{z,\mathrm{norm}}(t,z) = \frac{\bar{h}_z(t,z) - \bar{h}_{z,\mathrm{min}}(t)}{\bar{h}_{z,\mathrm{max}}(t) - \bar{h}_{z,\mathrm{min}}(t)} \quad with\ \bar{h}_{z,\mathrm{norm}}(t,z) \in [0,1] \tag{1}$$

Exemplary results are shown in Fig. 2 for two different inclinations and employing the illustrated initial condition for the film topology. The given representation of the film evolution clearly shows the process of spanwise structuring, beginning with the primary growth of spanwise film height modulations and followed by regimes of wave-to-wave interaction and flow reorganization into well separated quasi steady rivulets. Our results should be useful in predicting wave patterns in suspended falling films arising in thin film evaporators or in coating processes.

References

Charogiannis, A., Denner, F., van Wachem, B. G. M., Kalliadasis, S., Scheid, B. and Markides, C. N. (2018). Experimental investigations of liquid falling films flowing under an inclined planar substrate. *Physical Review Fluids*, 3, 114002.
Kalliadasis, S., Ruyer-Quil, C., Scheid, B. and Velarde, M.. (2012). Falling Liquid Films, *Spinger-Verlag*. Rietz, M., Scheid, B., Gallaire, F., Kofman, N., Kneer, R and Rohlfs, W. (2017). Dynamics of falling films on the outside of a vertical rotating cylinder: Waves, rivulets and dripping transitions. *Journal of Fluid Mechanics*, 832, 189-211.
Rohlfs, W., Rietz, M. and Scheid, B. (2018). Wavemaker: The three-dimensional wave simulation tool for falling liquid films. *SoftwareX*, 7, 211-216.

Proceedings ECS 2021
Brussels, Belgium, September 7-9, 2021

Abstract T-21

EXPERIMENTAL INVESTIGATION OF FALLING LIQUID FILMS ON VERTICAL AND INCLINED FIBERS

***A. Pour Karimi*[1], *M. Rietz*[1], *B. Scheid*[2], *R. Kneer*[1], *W. Rohlfs*[3]**

[1]WSA, RWTH Aachen University
Augustinerbach 6, 52056 Aachen, Germany

[2]TIPs, Université libre de Bruxelles
Avenue F.D. Roosevelt 50, 1050 Bruxelles, Belgium

[3]Department of Thermal and Fluid Engineering, University of Twente
Drienerlolaan 5, 7522 NB Enschede, The Netherlands

Email: pour@wsa.rwth-aachen.de

***Keywords**: Falling film, thin film, fiber*

An improved understanding of the flow characteristics of falling liquid films in different flow regimes plays a substantial role in optimizing relevant industrial processes such as fiber coating technology and structured packings for distillation processes. Break up of a homogeneous liquid film into droplets on cylindrical fibers is an undesirable effect if it is encountered for instance in coating of wires and optical fibers. In other applications such as cooling systems, bead formation might be a desired effect as the surface area of the film increases, potentially amplifying achievable heat or mass transfer rates. This work presents an experimental study on liquid films on vertical and inclined fibers in the Plateau–Rayleigh regime and provides a complementary understanding of the reported regimes in literature for films on vertical fibers (Kliakhandler, 2001, Duprat, 2007, Sadeghpour, 2017) while extending the investigations to stability and dripping analysis for an inclined configuration.

We present a wide range of empirical data using fluids of different viscosity and address possible effects that varying nozzle geometries may add to the dynamics of the film flow. Film thickness profile, bead size, bead spacing, as well as bead traveling speed are determined using optical measurement methods and image analysis.

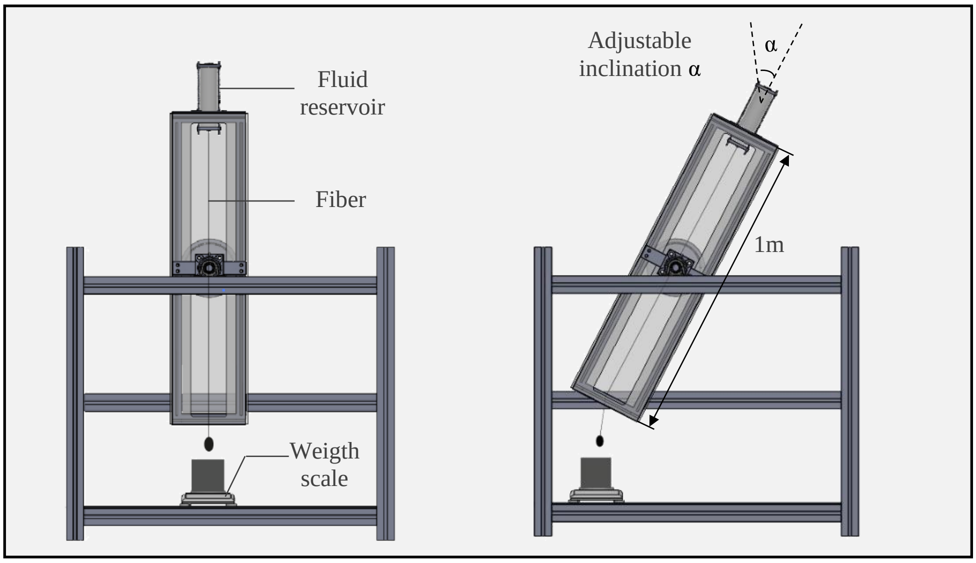

Figure 1. Experimental setup. Left: Vertical configuration. Right: Inclined configuration.

The experimental setup allows to vary the inclination in the range from zero to ninety degrees, enabling us to investigate the effect of fiber inclination on the film dynamics. This particularly includes the onset of dripping, dripping mass flow rates in dependence of fiber thickness, nozzle geometry and volume flow rate at the nozzle outlet.

Exemplary experimental procedure and results

In given experimental results, the setup is arranged as follows. A silicon oil v50 (density = 948 kg/m , kinematic viscosity = 50 mm^2/s, surface tension = 0.021 N/m) flows out of the fluid container through a casting nozzle with an inner diameter of D_{Ni} = 1.5 mm and a wall thickness of δ = 0.3 mm down a vertical plastic fiber of diameter D_f= 0.45 mm. The fiber is mounted to the container ceiling using a magnet with free movement in X-Y coordinates. This enables aligning the string in the center of the nozzle and therefore guaranties an axisymmetric flow at the nozzle outlet for both vertical and inclined alignment. A computer programmed weight scale with the precision of 1 gr is used to monitor the current mass flow rate by measuring the liquid mass in the collector tank, which is located under the fiber and its attached weight. During each measurement, due to the trivial variation of the liquid height in the fluid container (<1%), the mass flow rate is considered as constant.

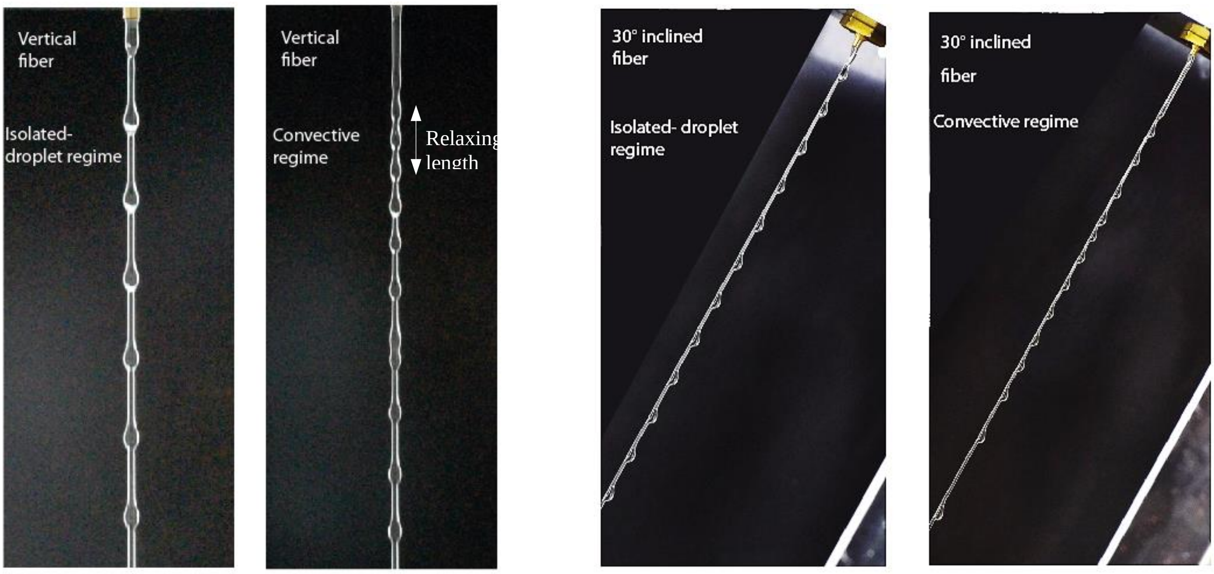

Figure 2. Experimental results for fiber radius R = 0.45; Nozzle diameter D_N = 1.5 mm for vertical and inclined fibers. Left: Falling film on vertical fiber. Right: Falling film on inclined fiber.

Snapshots of the developed film flow for the given setup are illustrated in Fig. 2 for the vertical and an inclined configuration. Depending on the imposed mass flow rate different flow regimes are detected. The isolated droplet regime is established when the mass flow rate is low, for the given setup in the range of 0.01 - 0.03 g/s. In this regime, uniformly sized droplets form directly at the nozzle outlet and move along the entire length of the fiber with constant spacing and frequency. The beads neither grow nor are damped in time and remain in a consistent shape along the entire length of the domain. The transition to the convective regime is observed with an increasing mass flow rate. In the convective regime, the size of the beads, their spacing, and their frequency vary along the length of the fiber. Variations in bead size and therefore bead velocity lead to coalescence events, which are not observed in the isolated droplet regime. One of the characteristics of the convective regime is the presence of a uniform film without any visible perturbations at the outlet, which is referred to as relaxing length. Notice that the described regimes and the transition between regimes are affected strongly by the nozzle geometry (Sadeghpour, 2017). Depending on the geometry of the nozzle different type of regimes can be detected for smaller or larger mass flow rates. For the case of an inclined fiber with low to moderate inclinations, having a mass flow rate comparable to the case of vertical fiber we were able to observe similar types of regimes.

The only difference is that the film is not axisymmetric, but rather the beads flow down suspended on the underside of the fiber. It is observed that the regime change has a significant influence on the film stability and the occurrence of dripping in case of the inclined configuration. Through the convective nature of the flow with growing bead size for instance as a result of coalescence events, a critical bead size may be reached and dripping occurs.

References

Sadeghpour, A., Zeng, Z., Ju, S.Y. (2017). Effects of nozzle geometry on the fluid dynamics of thin liquid films flowing down vertical strings in the Rayleigh−Plateau regime. *Langmuir*, 33, 6292−6299

Kliakhandler, I.L., Davis, S.H., and Bankoff, S.G. (2001). Viscous beads on vertical fiber. *Journal of Fluid Mechanics*, 429, 381-390

Duprat, C., Ruyer-Quil, C., Kalliadasis, S. and Giorgiutti-Dauphiné, F. (2007). Absolute and convective instabilities of a viscous film flowing down a vertical fiber. *Physical Review Letters*, 98, 244502-4

Proceedings ECS 2021
Brussels, Belgium, September 7-9, 2021

Abstract T-22

DIP-COATING FLOW IN THE PRESENCE OF TWO IMMISCIBLE LIQUIDS

***L. Champougny*[1], *B. Scheid*[2], *A. A. Korobkin*[3], *and J. Rodríguez-Rodríguez*[1]**

[1]Fluid Mechanics Group, Department of Thermal and Fluid Engineering, Universidad Carlos III de Madrid, Avenida de la Universidad 30, 28911 Leganés (Madrid), Spain

[2]Transfers, Interfaces and Processes (TIPs), Université Libre de Bruxelles, C.P. 165/67, Avenue F.D. Roosevelt 50, 1050 Brussels, Belgium

[3]School of Mathematics, University of East Anglia, Norwich Research Park, Norwich NR4 7TJ, United Kingdom

Email: lchampou@ing.uc3m.es

Abstract

Dip-coating is a common technique used to cover a solid surface with a thin liquid film. This process consists in withdrawing the object to be coated at controlled speed from a liquid bath in which it is initially immersed. The thickness of the entrained thin film was successfully predicted by the theory developed by Landau & Levich (Levich & Landau, 1942) and Derjaguin (Derjaguin, 1943) in the 1940's, in the case of a smooth plate dragged out of a single pure Newtonian liquid. Since then, several generalizations of this theory have been proposed to describe effects arising, for example, from interfacial or bulk liquid rheological properties, or substrate roughness (Rio & Boulogne, 2017).

In this work, we present an extension of the dip coating theory of Landau-Levich-Derjaguin (LLD) to the case where the bath contains two immiscible liquids, layered atop one another. This configuration, sometimes referred to as gas/liquid/liquid compound interface in the literature, finds important applications in the context of environmental science (Liss & Duce, 2005) (sea surface microlayer, oil spills) or semiconductor electronics (Jinkins, et al., 2017).

In our study, we model the situation in which both liquid phases are dragged, giving birth to a superposition of two liquid films on the substrate (see Fig. 1).

We report how the thicknesses of the coated films depend on the ratios of the properties of the two liquids (viscosity, density, surface tension), as well as on the dimensionless thickness of the top liquid layer H. For all the parameters tested, the thickness of the upper film, h , is always much smaller than the one of the lower film, $h1$, .

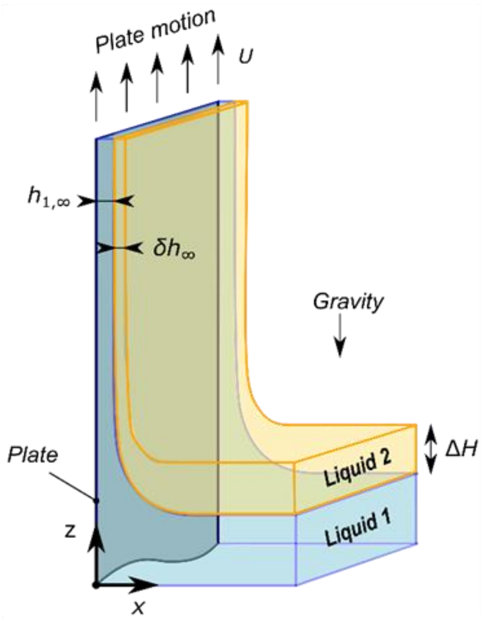

Figure 1. Sketch of the dip-coating configuration under investigation and corresponding notations.

Abstract T-22

Importantly, we find that a double film solution only exists in finite regions of the parameter space, which we dub "existence islands". Finally, we also show that the liquid/ liquid and liquid/gas interfaces evolve independently from each other as if only one liquid was coated, except for a very small region where their separation falls quickly to its asymptotic value and the shear stresses at the two interfaces peak. Interestingly, we find that the final coated thicknesses are determined by the values of these maximum shear stresses (Champougny, Scheid, Korobkin, & Rodríguez-Rodríguez, 2021).

Keywords: *liquid coating, liquid/liquid/air interfaces, lubrication approximation*

References

Champougny, L., Scheid, B., Korobkin, A. A., & Rodríguez-Rodríguez, J. (2021). Dip-coating flow in the presence of two immiscible liquids. *arXiv preprint arXiv:2011.07356*.
Derjaguin, B. V. (1943). On the thickness of the liquid film adhering to the walls of a vessel after emptying. *Acta Physicochim. URSS*, 20, 349-352.
Jinkins, K. R., Chan, J., Brady, G. J., Gronski, K. K., Gopalan, P., Evensen, H. T., . . . Arnold, M. S. (2017). Nanotube alignment mechanism in floating evaporative self-assembly. *Langmuir*, 33(46), 13407-13414.
Levich, B., & Landau, L. (1942). Dragging of a liquid by a moving plate. *Acta Physicochim. URSS*, 17, 42.
Liss, P. S., & Duce, R. A. (2005). *The sea surface and global change.* Cambridge University Press.
Rio, E., & Boulogne, F. (2017). Withdrawing a solid from a bath: How much liquid is coated? *Advances in colloid and interface science, 247, 100-114.*

This project has received funding from the European Union's Horizon 2020 research and innovation programme under the Marie Sklodowska-Curie grant agreement No 882429

FILM COATING DURING WATER EXIT OF A CIRCULAR CYLINDER

***L. Vincent*[1], *J. Rivero*[1,2], *I. Ashraf*[3], *S. Dorbolo*[3], *R. Falla*[4], *V. Terrapon*[4], *B. Scheid*[1]**

[1] Transfers, Interfaces and Processes (TIPs), Université Libre de Bruxelles (ULB)
C.P. 165/67 Avenue F.D. Roosevelt, 50, 1050 Brussels, Belgium

[2] Departamento de mecánica y fabricación industrial, Universidad de Mondragon
Loramendi, 4. Apartado 23 - 20500 Arrasate, Mondragon, Spain

[3]GRASP, Institute of Physics, Université de Liège Building B5a, 4000 Liège, Belgium
[4]Aerospace and Mechanical Engineering, Université de Liège, Liège, BE
Building B52/3, Allée de la Découverte, 94000 Liège, Belgium

Corresponding author: lionel.vincent@ulb.be

Abstract
We study the inertial coating of a cylinder as it is lifted out of a liquid bath, from the formation of a bulge ahead of the object to the drainage of the liquid film. We use a combined numerical, experimental and theoretical approach to study the overall dynamics, and we develop a reduced-order model to predict characteristics of the liquid film. We show that the film height is affected by many parameters, including the tank width, the starting depth, and the object's wake.

Keywords: *coating, thin film, interfacial dynamics, wake*

1. Introduction

When an object is lifted out a liquid bath, it lifts and entrains a certain quantity of liquid as it crosses the interface. Part of this volume is eventually deposited on the object's surface as a film. To predict the film characteristics, it is necessary to characterize the various phases governing its formation and dynamics. Each phase may depend on a large number of factors, including the shape and the motion of the object, the flow regime, or even the boundary conditions. The entire process is complex and the dynamics as a whole is not amenable to theoretical predictions, which calls for experimental and numerical approaches to gain insight. Here, we propose a combined theoretical, numerical and experimental study of the fluid flow induced by the lifting of a horizontal circular cylinder out of a liquid bath. We examine in detail the two main phases of the exit: the initial rise, characterized by a bulge at the free surface ahead of the cylinder, and the film dynamics as the object crosses the interface. We choose to focus on the inertial regime; however, we also characterize the effect of the object's wake, a viscous manifestation that affects the exit dynamics early on.

2. Theoretical background – non-dimensional parameters

For an object crossing the interface in the inertial regime, the water exit dynamics has been shown to be governed primarily by an inertia-to-gravity balance, expressed by the Froude number $Fr = U^2/ga$, where U is the cylinder's speed, (its radius, and ' the acceleration of gravity (Liju et al., 2001; Telste, 1987). A second important parameter is the starting depth d. When d is large, it is expected that transient effects will not impact the exit dynamics, whereas when d is small, gravitational waves are triggered at the interface and may alter the film thickness (Tyvand & Miloh, 1995). Finally, the wake development is expected to be controlled by the Reynolds number, defined as $RE=pU(2a)/\mu$, where p, is the liquid density and μ its dynamic viscosity (Koumoutsakos & Leonard, 1995).

3. Experimental and numerical procedure

The experimental setup consists of a water tank $(W, L_1, D) = (785 \text{ x } 275 \text{ x } 725 \text{ mm})$ in which a cylinder is initially immersed horizontally at $d = 12a$ or $24a$. The cylinder radius is either a=25 mm, with length L between 25 and 250 mm, or $a = 12.5$ mm and $L = 250$ m (aspect ratio $AR = L/a$ between 1 and 12). A stepper motor and rack-and-pinion system moves the cylinder with a constant velocity between 0.1 and 1 m/s ($Fr = 0.08 - 8.1$, $Re = 2500 - 50\,000$) after a short acceleration period. A high-speed camera is used to acquire side and front view images at 2500 fps, and images were post-processed with an in-house MATLAB code.

In complement, we set up two-dimensional Navier-Stokes simulations using COMSOL. We use an Arbitrary Lagrangian-Eulerian (ALE) formulation using an adaptative mesh locally refined in the vicinity of curved boundaries, and featuring a specific treatment at the boundary (BALE) (Rivero-Rodríguez et al., 2021). Linear Lagrangian interpolants are used for the pressure, and quadratic interpolants are used for the velocity and geometry. The time stepping is done via the Backward Differentiation Formula (BDF) at the 2nd order with a fixed time step $dt = 3.10^{-3}$. A first set of simulations mirrors the experimental conditions. A second set explores a wider range of parameters and investigates the effect of boundary conditions on the cylinder's surface: no-slip and stress-free.

4. Results and discussion

Characteristic bulge height – wake-induced surge excess

The characteristic bulge height h^* is the thickness of the layer above the cylinder when the cylinder's top reaches the undisturbed water level. Figure 1 shows the increase of h^* as Fr is increased, in experiments (circles) and simulations (squares). The cylinder aspect ratio AR plays an important role: h^* increases sharply with AR for short cylinders. However, experiments and 2D simulations agree for $AR = 12$ and all Fr, suggesting 3D effects are small enough for this AR.

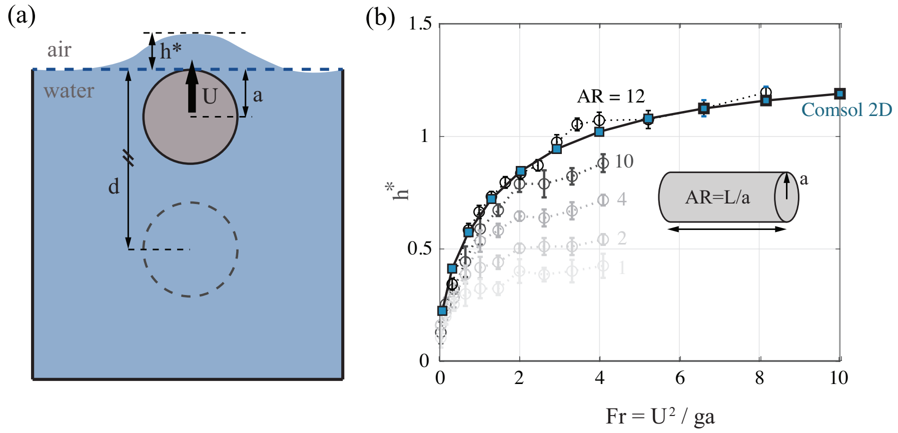

Figure 1. Characteristic bulge height h^* for various Froude numbers and aspect ratios: experiments (circles) and 2D Navier-Stokes simulation (blue squares). No-slip conditions, $d = 12a$.

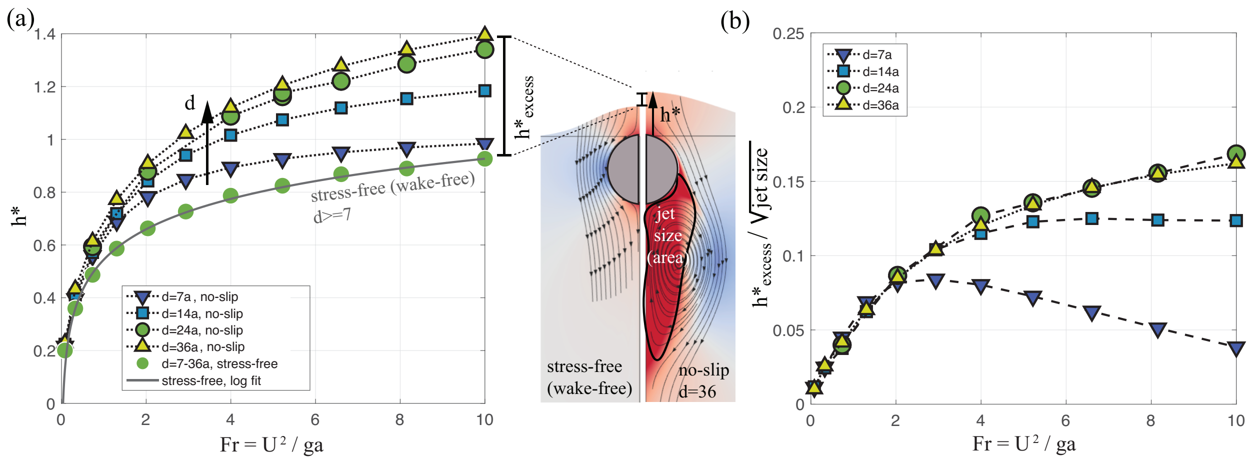

Figure 2. (a) h^* for various Fr and d, stress-free and no-slip; (b) Surge excess normalized by $\sqrt{jetsize}$.

Figure 2 shows the change of h^* as the starting depths d is varied ($Re = 10\,000$). When d increases, h^* increases as well for all Froude numbers. This rise is not seen when no wake is present (lower green circles), suggesting that the wake plays a part in the bulge growth. We identified a relationship between wake size (jet size), and the observed excess of h^* (surge excess). Normalizing the latter by $\sqrt{jetsize}$, we obtain an excellent collapse of the data for Froude numbers such that $Fr < d/3$.

Film thinning and deposited volume

As the crossing proceeds, the bulge thins and spreads around the cylinder, and turns into a quasi-uniform layer of liquid while continuing to drain (see figure 3). The thinning is roughly exponential in fashion and its rate can be estimated by considering the gravity-driven drainage of a uniform annular layer. However, observed thinning rates are substantially faster than predicted for larger-than-unity Froude numbers, suggesting a missing physical ingredient; we identified this ingredient as an additional pressure gradient along the cylinder caused by the pre-existing fluid motion.

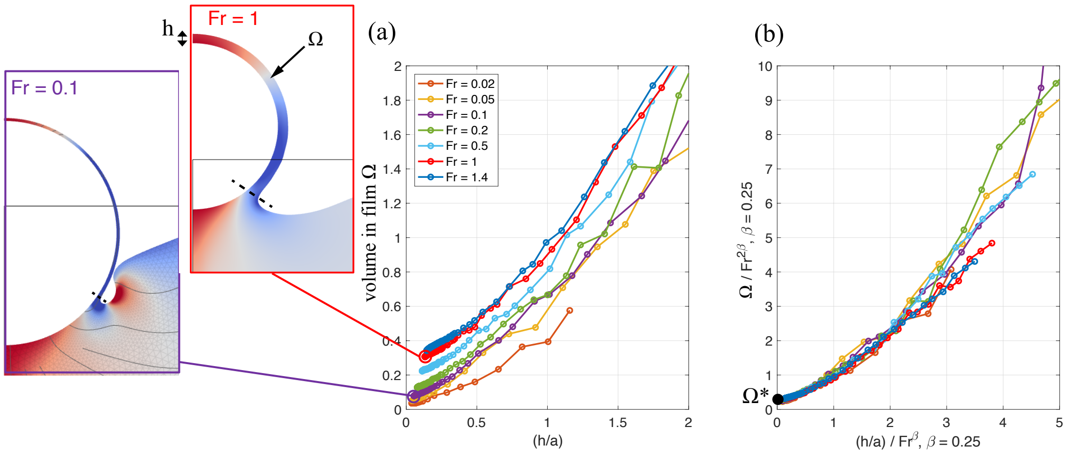

Figure 3. (a) raw and (b) renormalized non-dimensional volume in film during drainage phase (wake-free).

Figure 3 shows the evolution of the non-dimensional volume of the liquid film $\Omega = V/a^2$ as it spreads and drains during interface crossing, as a function of film thickness. Renormalizing the film thickness and the film volume by $Fr^{1/4}$ and $Fr^{1/2}$ respectively, we uncover a universal behaviour allowing us to predict the final volume deposited as a film on the cylinder: $\Omega^* \approx 0.22\, Fr^{1/2}$.

5. Conclusions

We propose a combined theoretical, numerical and experimental study of the water exit of a horizontal circular cylinder in the inertial regime, characteristic of large exit velocities. We demonstrate that the bulge height is primarily a logarithmic-style function of the Froude number (exit velocity), and three-dimensional effects. Surprisingly, it is also an increasing function of starting depth even for deep starts. We show that this effect is due to the wake's presence and uncover a novel correlation between bulge height and wake size. Finally, we adapt existing drainage models to account for observed thinning rates and we propose a renormalization allowing the prediction of the deposited volume.

References

Koumoutsakos, P., & Leonard, A. (1995). High-resolution simulations of the flow around an impulsively started cylinder using vortex methods. *Journal of Fluid Mechanics*, *296*, 1–38. https://doi.org/10.1017/S0022112095002059

Liju, P.-Y., Machane, R., & Cartellier, A. (2001). Surge effect during the water exit of an axisymmetric body traveling normal to a plane interface: Experiments and BEM simulation. *Experiments in Fluids*, *31*(3), 241–248. https://doi.org/10.1007/s003480100277

Rivero-Rodríguez, J., Pérez-Saborid, M., & Scheid, B. (2021). An alternative choice of the boundary condition for the arbitrary Lagrangian-Eulerian method. Journal of Computational Physics, 443, 110494. https://doi.org/10.1016 j.jcp.2021.110494

Telste, J. H. (1987). Inviscid flow about a cylinder rising to a free surface. Journal of Fluid Mechanics, 182, 149–168. Tyvand, P. A., & Miloh, T. (1995). Free-surface flow due to impulsive motion of a submerged circular cylinder. Journal of Fluid Mechanics, 286, 67–101.

Proceedings ECS 2021
Brussels, Belgium, September 7-9, 2021

Abstract T-59

ANALYSIS OF THE FILM DRAINAGE AND WAKE SEPARATION OF A CYLINDER RISING ACROSS A FREE SURFACE, USING THE PARTICLE FINITE ELEMENT METHOD (PFEM)

R. Falla[1], R. Boman[1], L. Vincent[2], B. Scheid[2], J-P. Ponthot[1], V.E. Terrapon[1]

[1]Aerospace & Mechanical Engineering Department, University of Liège (ULiège), Liège, BE

[2]Transfers, Interfaces and Processes (TIPs) laboratory, Université Libre de Bruxelles (ULB), Brussels, BE

Email: romain.falla@uliege.be

Abstract

The rise of a two-dimensional cylinder lifted out of a liquid is simulated during the different stages of the process, including initial free surface deformation, fluid entrainment and film thinning on the body surface, until the liquid column breakup in the wake. Simulations rely on the Particle Finite Element Method (PFEM) with a boundary recognition algorithm based on the α-shape method and a new mesh adaptation technique. The evolution of the film on the body surface and in the wake is investigated for several Reynolds and Froude numbers.

Keywords: *thin film - free surface - interface crossing - Particle Finite Element Method (PFEM)*

1. Introduction

The problem of a body rising towards and crossing a free surface has many practical applications, such as in coating for example, and has thus been the subject of numerous studies. The case of a cylinder has for instance been investigated numerically by Telste (1987), Moshari et al. (2014), Greenhow & Moyo (1997). Experimental work on the water exit of a sphere includes among others Wu et al. (2017) for a sphere pulled at constant velocity, Truscott et al. (2016) for buoyant spheres. Lijy et al. (2001) have investigated both numerically and experimentally the water exit of a more general axisymmetric body.

We consider here the same problem as that of Telste (1987), but we take into account both viscous effects and wake dynamics. The simulations rely on the Particle Finite Element Method (PFEM) (Oñate & Idelsohn, 2004; Cremonesi et al., 2020). The PFEM is a Lagrangian method where the fluid elements are described by finite elements that are moving in time. It is therefore well adapted to treat free-surface flows. Because the nodes move with the flow, the domain must be continuously re-meshed using a fast Delaunay triangulation. The boundary recognition is performed using the α-shape technique (Edelsbrunner & Mücke, 1994), which enables to track the deformation of the free surface and to represent fluid separation processes. Using two-dimensional simulations, we analyze the time evolution of the thin film around the cylinder and the wake behind the cylinder.

2. Theory

The 2D incompressible Navier-Stokes equations are discretized using a finite element approach with an implicit backward-Euler time integration scheme. Both pressure and velocity fields are approximated using linear shape functions. A monolithic pressure stabilizing Petrov-Galerkin (PSPG) scheme (Hughes et al., 1986; Cerquaglia, 2019) is used to circumvent the spurious pressure oscillations that would otherwise result from the violation of the Ladyzhenskaya–Babuška–Brezzi (LBB) when using this type of shape functions (Sani et al., 1981).

Remeshing using the Delaunay triangulation keeps all the mesh elements that belong to the convex hull of the entire set of nodes. Therefore, in the regions where the surface is locally concave, the α-shape technique is needed to differentiate between mesh elements that truly represent the fluid and those that should be discarded (Bernadini & Bajaj, 1997). Because of the small scales arising in the film and the wake, mesh adaptation is essential for computational efficiency. To overcome the limitation of the traditional α-shape criterion, which requires a mesh with elements of approximately uniform size, we introduce a local parameter α that is proportional to the target mesh size. This local target mesh size is computed as the minimum value of several criteria that are based on the time-evolving geometry of the problem (e.g., distance from a solid surface) and/or the current solution (e.g., velocity gradient magnitude, free-surface curvature). Finally, other criteria based on boundary nodes are added to ensure a sharper selection of the fluid elements compared to the classical α-shape criterion. This leads to a significant reduction of mass creation and destruction from one iteration to another.

3. Methodology

We consider different simulations of a two-dimensional cylinder rising at constant velocity through a liquid pool and crossing the free surface, as illustrated in Figure 1. Several Reynolds and Froude numbers and different values of the release depth are investigated. In each simulation, we systematically capture the evolution of the film thickness above the apex of the cylinder. Moreover, at low Reynolds number, as the wake is symmetric, we also follow the evolution of the thickness of the liquid column below the cylinder after it has crossed the free surface. At higher Reynolds number, we focus on the wake dynamics and its interaction with the free surface during the interface crossing.

4. Results and discussion

In the limit of a very thin film, initial results show that the film thickness above the apex of the cylinder transitions from an inertial regime with an exponential decrease rate to a viscous regime with a power-law decrease rate. For larger film thickness, it is shown that the exponential decrease rate is preceded by another regime where the thickness can be expressed using a Lambert *W* function applied to an exponential. Both Lambert *W* and exponential regimes can be obtained mathematically with a few assumptions through a simple model that only takes into account the mass conservation equations and neglects viscous effects. The comparison between numerical results and the fitted analytical approximation is shown in Figure 2. A relatively good match is observed between simulation results and the fitted analytical model, except towards the end, where viscous effects become important. Similar analyses are performed for the wake.

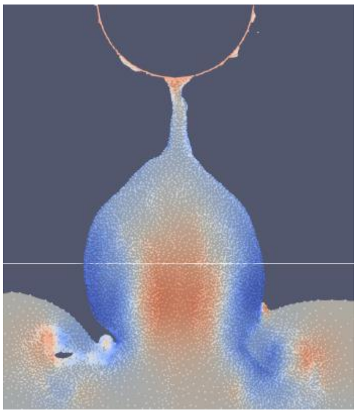

Figure 1. Liquid column below the rising cylinder at time t^*= 9.4 after a release at a depth y_0^* = -6 with respect to the position of the free surface (indicated by the horizontal white line). The color contours represent the vertical velocity component; Froude number Fr_a = 1.02 and Reynolds number Re_D = 25000. All quantities are made non-dimensional with the radius and vertical velocity of the cylinder, except the Reynolds number that is based on the cylinder diameter.

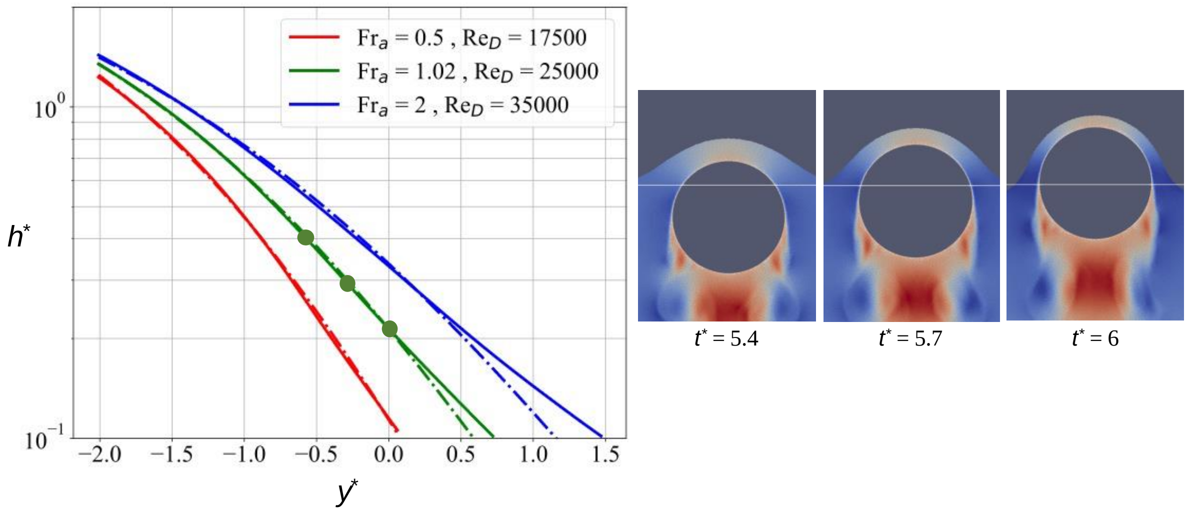

Figure 2. (Left) Film thickness h^* at the cylinder apex as a function of the position y^* of the cylinder center with respect to the initial free surface for different cases and a release depth y_0^* = -6. Numerical results (continuous line) are compared with the fitted analytical model (dash-dot line). The three green dots correspond to the three snapshots shown on the right. (Right) Contour of the vertical velocity at three time instants during the interface crossing as indicated by the green dots on the left plot. The white line corresponds to the initial free-surface position. All quantities are made non-dimensional with the radius and vertical velocity of the cylinder, except the Reynolds number that is based on the cylinder diameter.

5. Conclusions

The use of the PFEM with mesh adaptation has allowed us to simulate the initial rise and subsequent interface crossing of a two-dimensional cylinder pulled out of a liquid bath until the wake breakup. Numerical results and a simplified physical model based on some assumptions suggest a scaling for the time evolution of the film thickness at the cylinder apex. Future work will focus on further improving the spatial resolution of the simulations and on validating the numerical results with ongoing experimental measurements. Additionally, the dependence of the film and wake dynamics on the Froude and Reynolds number will be further investigated.

Acknowledgment: We thank the F.R.S.-FNRS for financial support through the PDR-WOLFLOW (31226867-T.0021.18) project.

6. References

Bernadini, F., Bajaj, C.L. (1997). Sampling and reconstructing manifolds using alpha-shapes. Purdue University. Department of computer science technical reports. Paper 1350. Report No. 97-013.

Cerquaglia, M.L. (2019). Development of a fully-partitioned PFEM-FEM approach for fluid-structure interaction problems characterized by free surfaces, large solid deformations, and strong added-mass effects. Ph.D. thesis, university of Liege. http://hdl.handle.net/2268/233166.

Cremonesi, M., Franci, A., Idelsohn, S. (2020). A state-of-the-art review of the particle finite element method (PFEM). Archives of Computational Methods in Engineering. 27: 1709–1735.

Edelsbrunner, H., Mücke, E.P. (1994). Three-dimensional alpha shapes. ACM Transactions on Graphics. 13(1): 43-72.

Greenhow, M., & Moyo, S. (1997). Water entry and exit of horizontal circular cylinders. Phil. Trans. R. Soc. Lond. A, 355, 551–563.

Hughes, T.J.R., Franca, L.P., Balestra, M. (1986). A new finite element formulation for computational fluid dynamics: V. circumventing the babuška-brezzi condition: a stable Petrov-Galerkin formulation of the stokes problem accommodating equal-order interpolations. Computer Methods in Applied Mechanics. 59(1), 85-99.

Liju, P.-Y., Machane, R., & Cartellier, A. (2001). Surge effect during the water exit of an axisymmetric body traveling normal to a plane interface: Experiments and BEM simulation. Experiments in Fluids, 31(3), 241–248.

Moshari, S., Nikseresht, A. H., & Mehryar, R. (2014). Numerical analysis of two- and three-dimensional buoyancy driven water-exit of a circular cylinder. Int. J. Nav. Archit. Ocean Eng., 6, 219–235.

Oñate E & Idelsohn, S.R. (2004). The particle finite element method — an overview. International Journal of Computational Methods. Vol. 1 No. 2: 267–307.

Sani, R.L., Gresho, P.M., Lee, R.L., Griffiths, D.F. (1981). The cause and cure (?) of the spurious pressures generated by certain FEM solutions of the incompressible Navier-Stokes equations: Part 1&2. International Journal for Numerical Methods in Fluids. Part 1: Vol 1: 17-43, Part 2: Vol 1: 171-204.

Telste, J. Taylor, D. (1987). Inviscid flow about a cylinder rising to a free surface. Journal of fluid mechanics. 182: 149-168

Truscott, T. T., Epps, B. P., & Munns, R. H. (2016). Water exit dynamics of buoyant spheres. Physical Review Fluids, 1(7): 074501.

Wu, Q. G., Ni, B. Y., Bai, X. L., Cui, B., & Sun, S. L. (2017). Experimental study on large deformation of free surface during water exit of a sphere. Ocean Engineering, 140, 369–376.

Proceedings ECS
2021
Brussels, Belgium, September 7-9, 2021

Abstract T-50

FILM FORMATION OF VISCOPLASTIC LIQUIDS IN SLOT COATING PROCESS

***Ivan R. Siqueira*[1], *Paulo R. Souza Mendes*[2] and *Marcio S. Carvalho*[2]**

[1]Department of Chemical & Biomolecular Engineering, Rice University
Houston, USA

[2]Department of Mechanical Engineering, Pontifical Catholic University of Rio de Janeiro.
Rio de Janeiro, Brazil

Email: msc@puc-rio.br

Abstract

The fundamentals of free surface coating flows of Newtonian liquids are well established. However, many coating liquids show strong non-linear behavior, with a viscosity that varies with shear rate. Some particle suspension presents a yield stress, below which the material behaves like a solid. The effect of viscoplas-ticity in coating flows is not well understood and it may play an important role in the flow behavior and consequently in the operability limits of coating processes. In this work, we present a computational study of the effect of viscoplasticity in the film formation region of a slot coating flow. The viscoplastic nature of the coating material is modeled with a new regularized vis-cosity function, and the equations of motion are coupled with the elliptic mesh generation method to capture the position of the free surface. The resulting model is solved numerically with a fully-implicit finite ele-ment method. The results show that the viscoplastic nature of the coating material changes the dynamics in the downstream section of a slot coater dramatically in comparison to a Newtonian liquid at the same oper-ating conditions. The position of the unyielded regions where the material displays a solid-like behavior and the shape of the downstream meniscus are strong functions of the film thickness-to-coating gap ratio, capil-lary number, and plastic number, a dimensionless parameter used to measure the intensity of the material viscoplasticity. The low-flow limit of viscoplastic slot coating flows is also examined, and the predictions suggest that the coating window corresponding to a uniform and stable operation enlarges as the coating material grows more viscoplastic.

***Keywords**: slot coating, rheology, suspension, viscoplastic liquids*

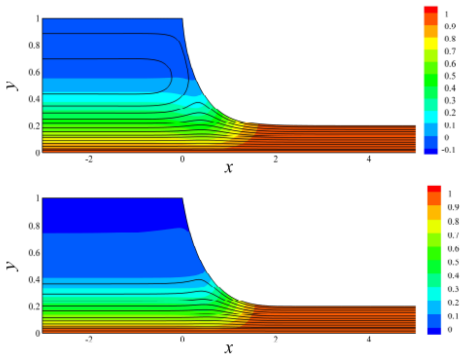

Figure 1. Horizontal velocity field and flow streamlines in slot coating for a Newtonian fluid (left) and a viscoplastic material at Pl = 0:6 (right).

References

Weinstein, S. J. and Ruschak, K. J. (2004). Coating Flows, Annual Review of Fluid Mechanics, 36, 29-53.

Carvalho, M. S. and Kheshgi, H. S. (2000). Low-Flow limit in slot coating: Theory and experiments, AIChE Journal, 46 (10), 1907-1917.

Lee, J. and Nam, J. (2016), A simple model for viscoplastic thin film formation for coating flows, Journal of Non-Newtonian Fluid Mechanics, 229,16-26.

Souza Mendes, P. R. and Thompson, R. L. (2012). A critical overview of elasto-viscoplastic thixotropic modeling, Journal of Non-Newtonian Fluid Mechanics, 187, 8-15.

NEW SCALING LAWS AND SIMILARITY SOLUTIONS FOR BOTH STEADY AND UNSTEADY GRAVITY-DRIVEN THIN FILM FLOW OVER CURVED SUBSTRATE

***M. Scholle*[1], *P. H. Gaskell*[2]**

[1]Institute for Flow in Additively Manufactured Porous Media, Heilbronn University, Heilbronn, Germany
[2]Department of Engineering, Durham University, Durham, UK

Email: markus.scholle@hs-heilbronn.de

Abstract
The present contribution is directed at the less well researched topic of film flow on curved substrate. To this end an exhaustive investigation has been performed for a variety of curved surfaces - cylinders cones and spheres - orientated in different planes. Although rich in behaviour, the results presented are restricted to the case of full coverage for both continuously fed and fix-volume deposition scenarios. Modelling is centred on the advantageous use of a first integral formulation of the governing Navier-Stokes equations. Associated scaling laws and similarity solutions are reported together with the discovery and proof that all such surfaces can be conveniently grouped together as related families.

Keywords: *coating, modelling, thin films, scaling laws*

1. Introduction

Within the coating community investigations involving the deposition of thin functional films on planar substrate and the development of models capable of predicting their behaviour have played a key role in the advancement of understanding, which in turn has been translated into numerous direct industrial applications. Examples include their stability (Yih, 1963), maximising throughput and coating quality (Kistler & Schweizer, 1997) and the effects of nonuniform substrate on the related free surface behaviour (Schörner & Aksel, 2018).

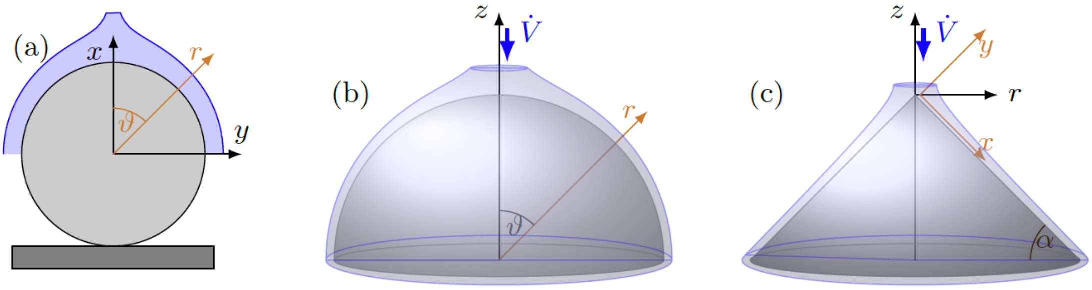

Figure 1. Continuously fed film flow over (a) a horizontally aligned cylinder, (b) a hemisphere and (c) a cone

2. Theory

In an analogous fashion to Maxwell's use of potential fields in developing his classical electro-magnetic theory and governing equations, a potential-based first integral of the Navier-Stokes (NS) equation in terms of a stream function vector $\vec{\Psi}$ constituting the velocity via $\vec{u} = \nabla \times \vec{\Psi}$, a traceless symmetric tensor potential (a_{ij}) and a scalar potential Φ has been developed by (Scholle et aL., 2018). For steady flows a variational principle is available, which in turn significantly facilitates the formulation of the theory in terms of curvilinear coordinates q_1, q_2 and q_3, for instance cylindrical or spherical coordinates. Assuming a neutral direction, i.e., the flow does not depend on q_3, and utilising the special form

$$\vec{\Psi} = \psi \nabla q_3 \,, \qquad \overline{a}_{ij} = \sum_{\mu,\nu=1}^{2} a_{\mu\nu}\, \partial_i q_\mu \partial_j q_\nu \,,$$

for the stream function vector and the traceless tensor potential, variation of the action integral w.r.t. the two fields a and a deliver the field equations

$$\begin{aligned} \varrho\frac{u_1^2-u_2^2}{2} &= \frac{|\nabla q_1|}{|\nabla q_2|}\partial_1(|\nabla q_2|[\eta u_1-|\nabla q_1|\partial_1\Phi])-\frac{|\nabla q_2|}{|\nabla q_1|}\partial_2(|\nabla q_1|[\eta u_2-|\nabla q_2|\partial_2\Phi]) \\ \varrho u_1u_2 &= \frac{|\nabla q_2|}{|\nabla q_1|}\partial_2(|\nabla q_1|[\eta u_1-|\nabla q_1|\partial_1\Phi])+\frac{|\nabla q_1|}{|\nabla q_2|}\partial_1(|\nabla q_2|[\eta u_2-|\nabla q_2|\partial_2\Phi]) \end{aligned} \tag{1}$$

Likewise, the dynamic boundary condition related to stress equilibrium at a free surface can also be recasted in a first integral form for the tensor potential as a condition for the scalar potential (with tangential and normal vector $\vec{t},\vec{n}$):

$$\nabla\Phi+\frac{\sigma}{2}\vec{n}-\frac{1}{2}\int U\,\vec{t}\,\mathrm{d}s=0 \tag{2}$$

with surface tension σ and potential energy density U for an external conservative force, the gravity in the present case. The mathematical formulation is completed by the kinematic boundary condition at a free surface and the no-slip/no-penetration condition at solid walls.

3. Solution method

For steady flow with continuous feed from above the relevant field equations (1) become integrable by (i) neglecting inertia and (ii) applying an asymptotic analysis, underpinned by the long-wave approximation, as already demonstrated by (Scholle et al., 2019) for 2D film flows. Following the same steps, a single equation for the local film thickness results. Analytic solutions are available. Corresponding analytic solutions for unsteady flows with a constant volume instead of a constant flux can also be obtained within the framework of the lubrication approximation by replacing the kinematic boundary condition for steady flow by its unsteady analogue:

$$0=\mathrm{D}_tF(q_1,q_2,t)=\frac{\partial F}{\partial t}+\vec{u}\cdot\nabla q_1\frac{\partial F}{\partial q_1}+\vec{u}\cdot\nabla q_2\frac{\partial F}{\partial q_2}, \tag{3}$$

where $F(q_1,q_2,t)=0$ is the implicit representation of the unknown free surface, while for the velocity field $\vec{u}$ the already known lubrication solution is assumed. Solutions methods for the above PDE depend on the geometry: due to a missing characteristic geometric length a similarity solution is available in case of the flow over a cone, while in case of the horizontally aligned cylinder and the hemisphere separation solutions can be found. Both different types of solutions, however, reveal the laws of scale mentioned at the outset. Integration constants occurring in the analytic solutions are determined by the constraint of a constant total volume.

4. Results for steady flow

Regarding the steady flow over a cone, the resulting the local thickness $h=h(x)$ and the velocity profile $u=u(x,y)$ read:

$$\begin{aligned} \frac{x}{L} &= \left[1+2\cos\left(\frac{1}{3}\arccos\left(1-\frac{27h^8}{2L^8}\right)\right)\right]\frac{L^3}{3h^3}-\frac{5h}{8L}\tan\alpha\,, \\ u &= \frac{\varrho g\sin\alpha}{2\eta}\frac{2h(x)y-y^2}{1-h(x)^2\left(x+\frac{5}{8}h(x)\tan\alpha\right)^{-2}}\,, \end{aligned}$$

in terms of a characteristic length obtained via $L^4=6\eta\,\dot{V}\,/\varrho g\sin(2\alpha)$ from the flow rate. Resulting thickness profiles for different cone angles α are shown in Fig. 2, revealing a slight dependence on the inclination angle in the region near the tip. Far away from the tip, the profiles can be well approximated by the simple expression $h\approx L\sqrt[3]{L/x}$.

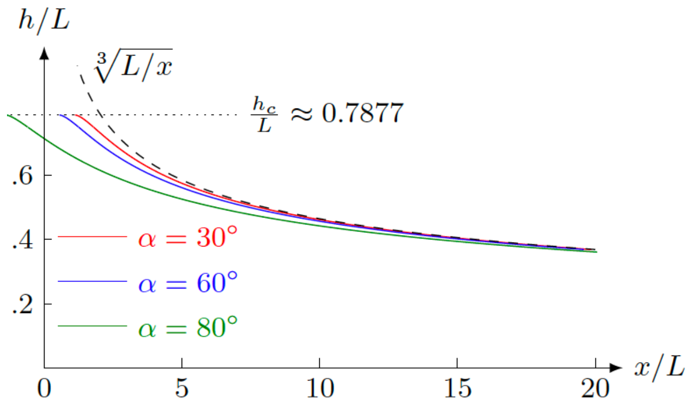

Figure 2. Film thickness predictions for film flow over a cone.

For the steady flow over half-cylinder and hemispheres, corresponding results for the local thickness $h = h(\vartheta)$ and the velocity profile $u = u(r, \vartheta)$ read:

$$\vartheta = \begin{cases} \arcsin\left(\dfrac{1+h_e}{1+h}\dfrac{2(1+h_e)^2[h_e - \ln(1+h_e)] - h_e^2}{2(1+h)^2[h-\ln(1+h)] - h^2}\right), & \text{half} - \text{cylinder}, h_e = h\left(\dfrac{\pi}{2}\right) \\ \arcsin\left(\sqrt{\dfrac{1+h_e}{1+h}\dfrac{4+3h_e}{4+3h}\dfrac{h_e^3}{h^3}}\right), & \text{hemisphere,} \end{cases}$$

$$u_\vartheta = \frac{\varrho g r_0^2}{2\eta}\frac{1+h(\vartheta)}{1+z}(2h(\vartheta) + h(\vartheta)^2 - z)z\sin\vartheta, \qquad z = \frac{r - r_0}{r_0},$$

The thickness profile contains the equatorial film thickness as the only parameter. In Fig. 3 some representative thickness profiles are presented for the flow over a horizontally aligned cylinder and over a hemisphere. For the latter it is demonstrated in the diagram at the right that after scaling with the equatorial thickness look rather similar and very close to the simple expression .

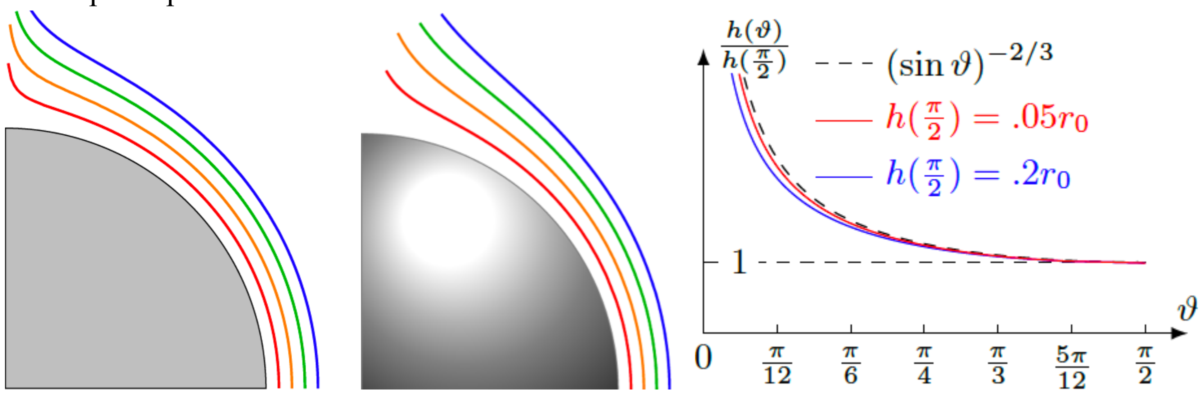

Figure 3. Free surface profile predictions for film flow over a half-cylinder (left) and a hemisphere (right).

5. Results for unsteady flow

Since in case of a fluid volume spreading over a cone there is no characteristic length in the entire problem, similarity solutions are available both for the flow over a plane and a cone, making use of the following substitutions:

$$\xi = axt^\gamma$$
$$h(x,t) = bt^\delta H(\xi)$$

with the similarity variable ξ and the thickness profile function $H(\xi)$ depending on the latter. By inserting above substitution into the kinematic boundary condition (3), the two powers result in $\gamma = -1/5$ and $\delta = -2/5$, implying that the film thickness is decreasing according to the power law $\sim t^{-2/5}$. Considering conservation of total volume, the propagation of the moving front can be estimated according to $x_f(t) \sim t^{1/5}$. These results are in accordance with (Acheson & Acheson, 1990).

In case of flow over a horizontally aligned cylinder and over a hemisphere no similarity solution is available since the Radius r_0 enters the problem as a characteristic length. Nevertheless, separation solutions of the form

$$h(\vartheta, t) = h_0 F(\vartheta) G(t)$$

can be found with:

$$G(t) = \frac{1}{\sqrt{1 + Ct}}.$$

indicating the time evolution of the film thickness leading to the long-time approximation $h \sim t^{-1/2}$. Again, conservation of total volume implies the time evolution of the propagating front $\vartheta_f = \vartheta_f(t)$ as

$$\frac{3\eta(1+n)^{-1}h_0^{-2} + 2\varrho g r_0 t}{3\eta(1+n)^{-1}h_0^{-2} + 2\varrho g r_0 t_1} = \left[1 - \frac{2\Gamma\left(\frac{2n+5}{6}\right)}{\sqrt{\pi}\Gamma\left(\frac{n+1}{3}\right)}\, {}_2F_1\left(\frac{1}{2}, \frac{2-n}{3}; \frac{3}{2}; \cos^2\vartheta_f\right)\cos\vartheta_f\right]^3$$

with $n = 0$ for the half-cylinder and $n = 1$ for the hemisphere, which in good approximation recovers the result reported by (Takagi & Huppert, 2009):

$$\vartheta_f(t) \approx \frac{\pi}{2} t^{\frac{1}{2n+2}}.$$

6.Conclusions

In combination with long-wave lubrication approximation, the potential-based first integral approach proves to be beneficial for finding analytical solutions for film flows over curved substrates, especially such with a certain symmetry. Corresponding analytic solutions for unsteady flows with a constant volume instead of a constant flux obtained by replacing the kinematic boundary condition for steady flow by its unsteady analogue,delivering analytical solutions which in turn reveal the laws of scale, which asymptotically result in the scaling laws formerly suggested by (Acheson & Acheson, 1990) and (Takagi & Huppert, 2009).These findings may form the basis for corresponding stability analyses to study the onset of unsteady phenomena such as solitary waves and, in the case of incomplete wetting, rivulet formation.

References

Acheson, D. J., Acheson, F. D. J. (1990). Elementary Fluid Dynamics. Clarendon Press.

Schörner M., Aksel, N. (2018). Films over topography: from creeping flow to linear stability, theory, and experiments, a review. *Acta Mechanica*, 229, 1453-1482.

Scholle, M., Gaskell, P. H., Marner, F. (2018). Exact integration of the unsteady incompressible Navier-Stokes equations, gauge criteria, and applications. *Journal of Mathematical Physics*, 59(4) Art. No. 043101.

Scholle, M., Gaskell, P. H., Marner, F. (2019). A Potential Field Description for Gravity-Driven Film Flow over Piece-Wise Planar Topography. *Fluids*, 4(2) Art. No. 4020082.

Kistler, S. F., Schweizer, P. M. (1997). Liquid Film Coating, Chapman and Hall.

Takagi, D., Huppert, H. E. (2009). Flow and instability of thin films on a sphere. *Journal of Fluid Mechanics*, 647, 221–238.

Yih, C. (1963). Stability of Liquid Flow down an Inclined Plane. *Physics of Fluids*, 6(3), 321-334.

Proceedings ECS 2021
Brussels, Belgium, September 7-9, 2021

Abstract T-58

GRAVITY-DRIVEN FILM FLOW OVER CORRUGATED, UNIFORMLY HEATED AND INCLINED SUBSTRATE

George R Daly, Philip H. Gaskell and Sergi Veremieiev

Department of Engineering, Durham University, Durham, UK
Corresponding author: p.h.gaskell@durham.ac.uk

Keywords: *modelling, stability, analysis, finite elements*

Over the past three decades or so, interest in film flow over substrates exhibiting surface topography – whether localised [1,2] or periodically varying [3] – has burgeoned, the latter half of this interval having seen increased interest in such films that are heated and, in particular matters, affecting their stability [4].

The problem of interest concerns gravity-driven flow down a smoothly corrugated substrate heated uniformly from below, with the fluid assumed to be both incompressible and Newtonian while allowing its surface tension to be vary with temperature. The mathematical framework adopted is that of the Weighted-Integral-BoundaryLayer (WIBL) approach popularised by [5], with reduction of the governing Navier-Stokes and energy equations leading to a thermal analogy of the forth-order model for isothermal flow reported in [6], including both vertical fluid inertia and viscous terms which become significant when the amplitude of the substrate corrugations are large. Findings from the analysis are compared with corresponding numerical solutions of the full governing equation set using a purpose written finite element analogue, enabling comparisons to be made between predictions of free-surface disturbance and temperature; explored also is the flow through the film in the form of steamline and isothermal contour plots - neither of which have not been considered before. It is found that this model predicts extremely well the free surface temperature at moderate Prandtl number.

Next, the stability characteristics of the problem are explored using Floquet-Fourier theory, with the interaction between substrate topography and the thermo-capillary instability modes investigated as a set of neutral stability curves. Although there is no relevant experimental data currently available for the heated film problem with which to compare, recent existing finite element based predictions of the behaviour, in the form of such curves, for the isothermal flow case [7] are taken as a reference point from which to explore the effect of both heating and cooling. Finally, to further underpin the efficacy of the model, the degenerate case of the classical problem of film flow down a completely planar uniformly heated substrate is solved, the result of which shows excellent agreement when compared with the corresponding Orr-Sommerfeld solution and those of more complete and regularised models.

References

1. M.M.J. Decre and J.C. Baret,´ *J Fluid Mechanics* 487, 147–166 (2003).
2. P.H. Gaskell, P.K. Jimack, M. Sellier, H.M. Thompson and M.C.T. Wilson, *J Fluid Mechanics* 509, 885–891 (2004).
3. C. Pozrikidis, *J Fluid Mechanics* 188, 275–300 (1988).
4. S.J.D. D'Alessio, J.P. Pascal, H.A. Jasmine and K.A. Ogden, *J Fluid Mechanics* 665, 418–456 (2010).
5. C. Ruyer-Quil and P. Manneville, *European Physics J B* 15, 357–369 (2000).
6. S. Veremieiev and D.H. Wacks, Physics of Fluids 32(2), Art. No. 022101 (2019).
7. Y. Trifonov, Physics of Fluids 26, Art. No. 114101 (2014).

Abstract T-65

EVOLUTION OF THREE-DIMENSIONAL WAVES IN LIQUID FILMS ON MOVING SUBSTRATES

T. Ivanova[1], ***F. Pino***[1], ***B. Scheid***[2], ***M. Mendez***[1]

[1]EA Department, von Karman Institute for Fluid Dynamics, Sint-Genesius-Rode, Belgium
[2]TIPs laboratory, Université Libre de Bruxelles, Belgium
Corresponding author: ivanova@vki.ac.be

Abstract
We analyze the stability of liquid films on vertical and moving substrates. This configuration is interesting for vertical coating processes such as hot-dip galvanizing or vertical slot-die coating. We extend a classic 3D integral model for falling liquid films to account for the substrate motion and numerically investigate the response of the flow to various 2D and 3D disturbances. The results highlight the stabilizing effects of the substrate motion and provide insights into the physics of interface instabilities in these flows.

1. Introduction

The evolution of waves in liquid films plays a fundamental role in many coating processes. Their occurrence delimits the range of operating conditions and influences the quality of final products. In liquid films falling along a vertical wall, waves naturally develop and evolve through various patterns due to a fascinating interaction between inertial, viscous, gravitational, and capillary forces (Kalliadasis et al). The dynamics and stability of these waves have been extensively studied through various models of reduced dimensionality (Demekhin et al, 2007, Ruyer Quil et al, 2014), based on the integral formulation of the boundary layer equations. These models enable analytical insights on these flows' stability ranges and allow for computationally inexpensive simulations of their nonlinear dynamics. Recently, integral models have been extended (Mendez et al, 2020) to the case of a liquid filmevolving on a moving substrate in the presence of pressure gradient and shear stress at the interface. This allowed for studying the stability of the jet wiping process in hot-dip galvanizing by analysing the response of the liquid film to different perturbations in the impinging jet. Although the analysis was limited to 2D models, the simulations suggests that thin films are remarkably more stable on a moving substrate than on a fixed one. This work aims at investigating the reasons for this difference and to study how the different kinematic condition influences the stability of the liquid interface. First, we extend integral models in (Mendez et al, 2020) to a three-dimensional setting. Then, we numerically investigate the nonlinear response of the flow to 2D and 3D disturbances for various substrate speeds and film thicknesses.

2. A 3D Integral Model for Liquid Films on Moving substrates

The flow configuration of interest is illustrated in Figure 1. The liquid is assumed to be incompressible with kinematic viscosity ν, density ρ, dynamic viscosity μ and surface tension σ. The substrate moves at velocity U_p in the opposite direction of gravity, along axis x, while z is the span-wise direction. The liquid thickness is thus a function $h(x,z)$. The figure recalls the main reference quantities, indicated with square brackets, used to nondimensionalise the problem. Dimensionless quantities are denoted with hats, hence for example $\hat{h}=h/[h]$. The figure also recalls the main dimensionless numbers of the problem, which are the Reynolds number *Re* and the Capillary number *Ca*. For more details on the choice of the scaling variables, the reader is referred to (Mendez et al, 2020).

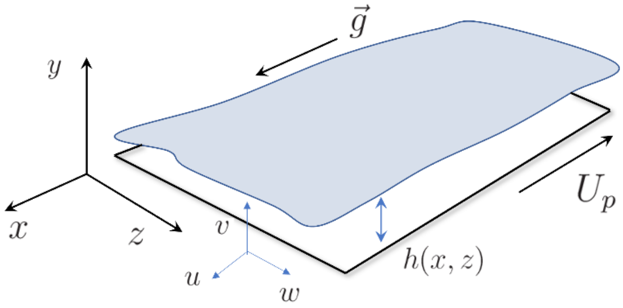

Reference Scales

$[h] = \sqrt{\nu U_p/g}$

$[x] = Ca^{-1/3}\sqrt{\nu U_p/g}$

$[u] = U_p$

$[v] = Ca^{1/3}U_p$

$[q] = U_p[h]$

$[t] = Ca^{-1/3}\sqrt{\nu/U_p g}$

Dimensionless Numbers

$Re = \sqrt{U_p^3/g\nu_l}$

$Ca = \mu U_p/\sigma$

$\delta = Ca^{1/3}Re$

Figure 1: Sketch of the flow domain and list of reference quantities used to scale variables (indicated in square brackets) together with the relevant dimensionless numbers.

The analysis of this problem using the Navier-Stokes equations and the related dynamic and kinematic conditions involve five variables, namely the velocity components $u=(u,v,w)$, the pressure p and the liquid thickness h. Instead, the analysis via integral models only requires three variables, namely the volumetric flux $q=(q_x,q_z)$, defined as $q_x=\int_0^h u\,dy$ and $q_z=\int_0^h w\,dy$, and the film thickness h. The integral model derived in this work is an extension of the work in (Demekhin et al, 2007) to the problem of a moving substrate. Keeping the self-similarity assumption, this model yields a system of hyperbolic PDEs, which in conservative form reads:

$$\begin{aligned}
\partial_{\hat{t}}\hat{h} + \partial_{\hat{x}}\hat{q}_x + \partial_{\hat{z}}\hat{q}_z &= 0,\\
\partial_{\hat{t}}\hat{q}_x + \partial_{\hat{x}}\left(\frac{6}{5}\frac{\hat{q}_x^2}{\hat{h}} + \frac{2}{5}\hat{q}_x + \frac{1}{5}\hat{h}\right) + \partial_{\hat{z}}\left(\frac{6}{5}\frac{\hat{q}_x\hat{q}_z}{\hat{h}} + \frac{1}{5}\hat{q}_z\right) &= \frac{1}{\delta}\left(\hat{h} - \frac{3}{\hat{h}} - \frac{3\hat{q}_x}{\hat{h}^2}\right),\\
\partial_{\hat{t}}\hat{q}_z + \partial_{\hat{x}}\left(\frac{6}{5}\frac{\hat{q}_x\hat{q}_z}{\hat{h}} + \frac{1}{5}\hat{q}_z\right) + \partial_{\hat{z}}\left(\frac{6}{5}\frac{\hat{q}_z^2}{\hat{h}}\right) &= \frac{1}{\delta}\left(-\frac{3\hat{q}_z}{\hat{h}^2}\right).
\end{aligned}$$

The reduced Reynolds number is denoted by δ, and extensional viscous stress and surface tension have been neglected. The full derivation of the model will be presented in the extended version of this work.

3. Numerical methods and Test Cases

An in-house finite volume solver was developed by extending the 1D solver by (Mendez et al, 2020). This combined the two-step versions of Lax-Wendroff and Lax-Friedrichs schemes through flux limiters. The simulation analysed the evolution of thickness disturbances on a baseline thickness $\hat{h}_0$. Three thicknesses and two Reynolds numbers were analysed. For each of these, fourteen simulations with varying dimensionless frequency $\hat{f}=f[t]$, in the range $\hat{f}=[0.005, 0.2]$, were carried out for two kinds of disturbances. These are two-dimensional planar waves traveling along $\hat{x}$ and three-dimensional waves produced by modulating the previous with a Gaussian function along $\hat{z}$.

Waves propagate in the direction of the substrate, hence the disturbances were located on one side of the domain. Both the size of the domain and the mesh size vary from test case to test case. Specifically, considering that waves propagate at about $\hat{u}\approx 1$ and their wavelength is of the order of $\hat{\lambda}\approx 1/\hat{f}$, the domain length in the stream-wise direction is taken as $L=8\lambda$ while the width is taken as $W\approx L/10$. The grid spacing is taken as $\Delta x=\lambda/363$ and $\Delta z=1/100$ while the time step is taken such that the CFL number is 0.3. This yields a numerical diffusion $\mu_n=\Delta x^2/\Delta t$ which is $\mu_n \propto \Delta x$.

4. Results and discussion

A snapshot of liquid film interface in response to a 2D disturbance is shown in Figure 2 for two different operating conditions. The first one on the top considers a thin film of water with $\rho = 1000\,\mathrm{kg/m^3}, \nu = 1\,\mathrm{mm^2/s}$, while the one on the bottom considers a thin film of liquid zinc with $\rho = 6500\,\mathrm{kg/m^3}, \nu = 0.46\,\mathrm{mm^2/s}$. In both, the dimensionless thickness is set to $\hat{h}_0 = 0.2$, and the dimensionless perturbation frequency is $\hat{f} = 0.2$.

The sinusoidal flow disturbances are located at $\hat{x} = -40$, i.e., on the left. The relevant dimensionless operating conditions are recalled in the Figure's caption. Despite the relative high Reynolds number and the rather low dimensionless frequency, these waves tend to dissipate even if surface tension is neglected. The figure shows the envelope of wave maxima and minima, for which an exponential law can be identified, yielding the decay rate ω_i. An increase in the perturbation frequency yields a faster decay rate. The full version of the article presents the decay rates of the disturbances for various operating conditions. The increasing of the Reynolds number results in a more pronounced distortion of the wave form, but despite that the flow remains stable.

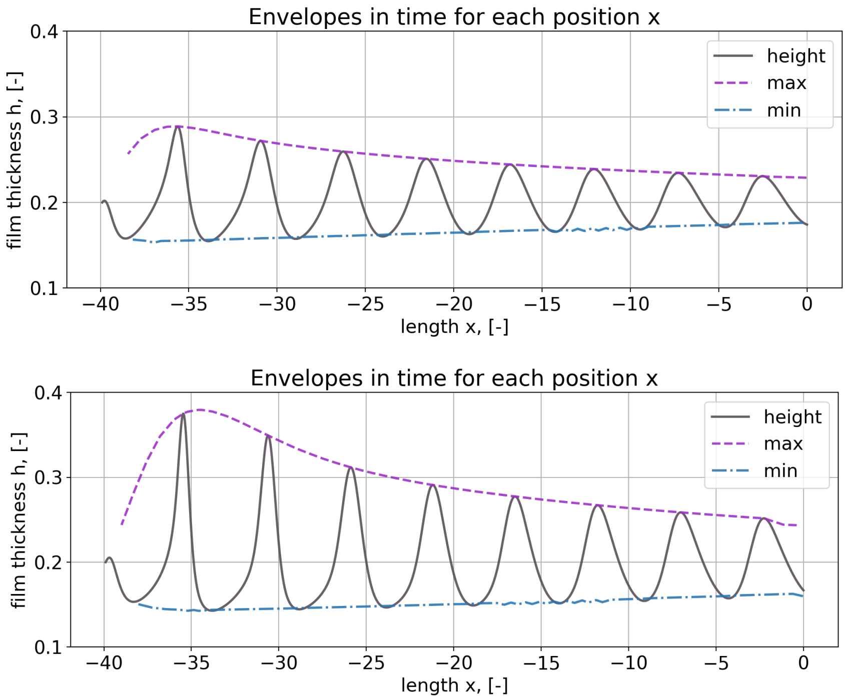

Figure 2: 2D waves evolving on a liquid film on a moving substrate with $\hat{h}_0 = 0.2$. *The substrate motion is from left to right; gravity is from right to left. The figure on the top represents a water film with Re = 319 and Ca =0.62, i.e.* $\delta = 76$. *The figure on the bottom considers a liquid zinc film with Re=956 and Ca=0.54, i.e.* $\delta = 148$.

Figure 3 shows the spatio-temporal map of 2D waves on the left and their spectrogram on the right. The propagation speed for both 2D and 3D waves is approximately constant despite the nonlinear behaviour results in appreciable distortion of the wave front. This is an important difference with respect to the case of liquid films falling along a fixed wall, in which region with larger film thickness tends to move faster. For the case of a film on a moving substrate, it can be shown that for the steady state flows, the velocity of the flow near the interface decreases as the thickness increases, unless $\hat{h}_0 > 1$. For sufficiently thin films ($\hat{h}_0 \ll 1$), it can be shown that the velocity of kinematic waves decreases with the film thickness and hence the primary mechanism for the interface instability is missing.

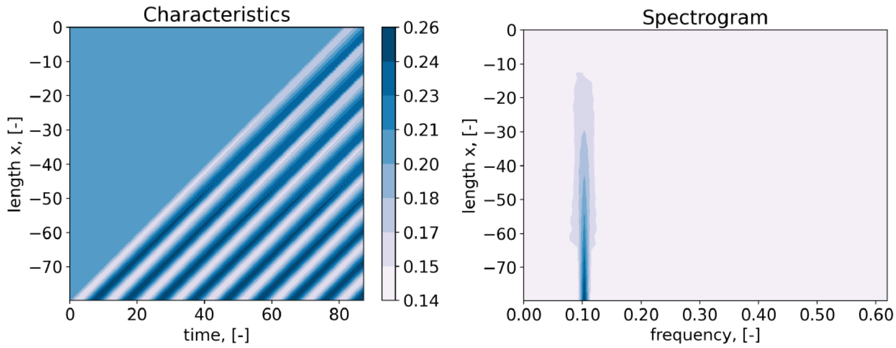

Figure 3: Left: spatio-temporal maps of the evolution of 2D waves in a liquid film over a moving substrate, showing that the wave speed is approximately constant despite the evolution of the wavefront. Right: spectrogram of the wave propagation: neither wave merging, nor frequency crosstalk is observed. The operating conditions in these plots are the same as in Figure 2 (top).

Finally, Figure 4 shows a snapshot of the liquid interface subject to a 3D perturbation. As in the 2D case, waves decay as they evolve and their region of influence of the perturbation remains overall limited in the $\hat{z}$ direction. Contrary to what happens in, e.g., shallow water flows, the wave propagation is not isotropic but strongly biased in the direction of the substrate.

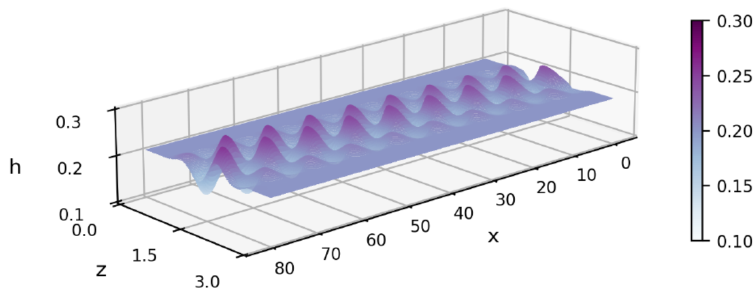

Figure 4: Evolution of a 3D wave on a liquid film along a moving substrate. The substrate moves towards $\hat{x}\rightarrow\infty$ while gravity is in the opposite direction (cf. Figure 1). Three-dimensional disturbances are introduced at $\hat{x}=93$.

5. Conclusions

We used an integral modelling approach to describe the evolution of three-dimensional waves in liquid films evolving on a moving substrate. We developed an efficient finite volume solver for its numerical investigation and analysed the liquid response to various disturbances. The main differences over the case of falling films are analysed and discussed in the presentation and in the extended version of this article.

Acknowledgements

This work has been supported by ArcelorMittal. Fabio Pino is supported by a FRIA grant from FNRS.

References

Demekhin, E., & Kalaidin, E. (2007). Three-dimensional localized coherent structures of surface turbulence. I. scenarios of two-dimensional–three-dimensional transition. *Physics of Fluids*, 19 (114103). Kalliadasis, S., Ruyer-Quil, C., Scheid, B., Velard, M.G. (2012), Falling Liquid Films, Springer.

Mendez, M., Gosset, A., Scheid, B., Balabane, M., & Buchlin, J.-M. (2021). Dynamics of the jet wiping process via integral models. *Journal of Fluid Mechanics*, 911.

Ruyer Quil, C., Kofman, N., Mergui, S., (2014), Dynamics of Falling Liquid Films, *The European Journal E37(4):9982.*

Abstract T-69

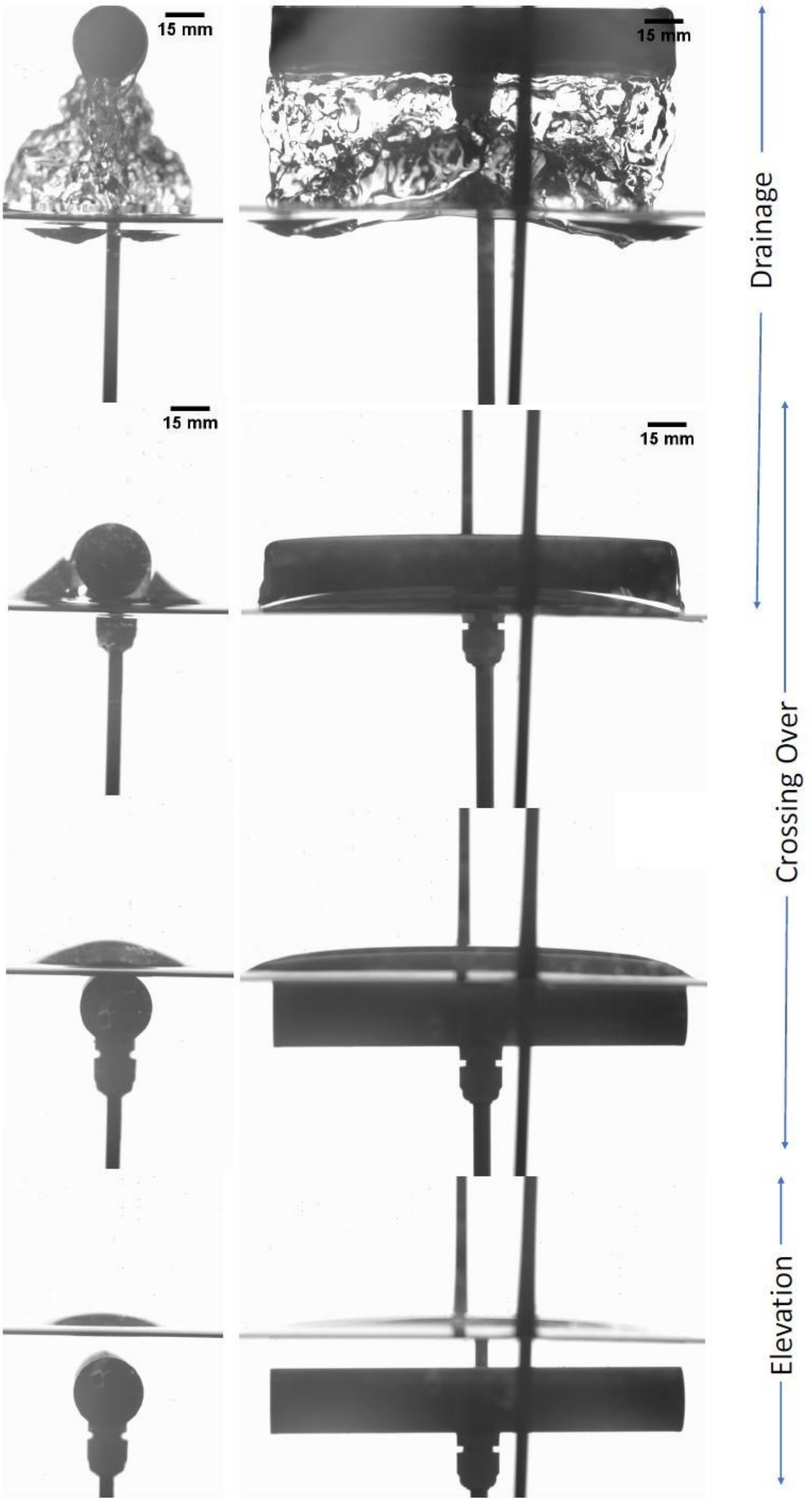

Figure 1: Exit Dynamics of a cylinder moving in the water and exiting thewater surface for AR=12 at Cylinder velocity, U =1.0 m/s and Froude Number Fr=8.2.

ECS21
EUROPEAN COATING SYMPOSIUM BRUSSELS

Proceedings ECS 2021
Brussels, Belgium, September 7-9, 2021

Abstract T-63

MODELLING OF MAGNETIC WIPING VIA INTEGRAL MODEL

***F. Pino*[1], *M.A. Mendez*[1], *B. Scheid*[2]**

[1]*EA Departament, von Karman Institute, Belgium*
[2]*TIPs laboratory, Universite Libre de Bruxelles, Belgium, bscheid@ulb.ac.be*
Corresponding author : fabio.pino@vki.ac.be

***Keywords**: hot-dip galvanizing, magnetic wiping, liquid film, integral modelling.*

In many coating processes, the control of coating thickness involves the continuous removal of liquid from a moving substrate. In hot-dip galvanizing this is performed by impinging gas jets, in a process known as jet wiping. Although being a simple and cost-effective technique, in certain operating conditions this process leads to harmful undulation patterns in the final coating, due to hydrodynamic instabilities [1]. Several alternatives have been proposed [2]. Among these, the use of magnetic wiping has been considered as viable solution to assist or eventually replace the gas jet actuation.

This work analyses the magnetic wiping, as a standalone solution and in conjunction with the jet wiping, via integral models. The wiping actuators are modelled as source terms. In classic jet wiping, these are the pressure gradient and the shear stress distribution generated by the impinging jet, obtained via empirical correlations. In magnetic wiping, the actuation is due to the magnetic field generated by a permanent magnet [3,4], modelled as a Gaussian distribution along stream-wise direction.

Simplified steady state models formulation were used to analyse and to compare efficiency of the two wiping approaches, and to explore new avenues for their combination. Possible technical challenges in their implementation are analysed. For the magnetic wiping, these include the development of high induced currents, and thus the heating of the liquid, as well as the formation of stationary humps in the liquid film portion upstream the wiping region. These features are shown in Figure 1, which shows two examples of steady-states thickness distribution for different intensities of the magnetic field.

After extending the integral modelling to dynamic conditions, a stability analysis of the process is proposed for both cases, using classic normal mode expansion. These integral models were derived assuming the velocity profile's self-similarity [1] and were used to compute the neutral stability curves for various operating conditions.

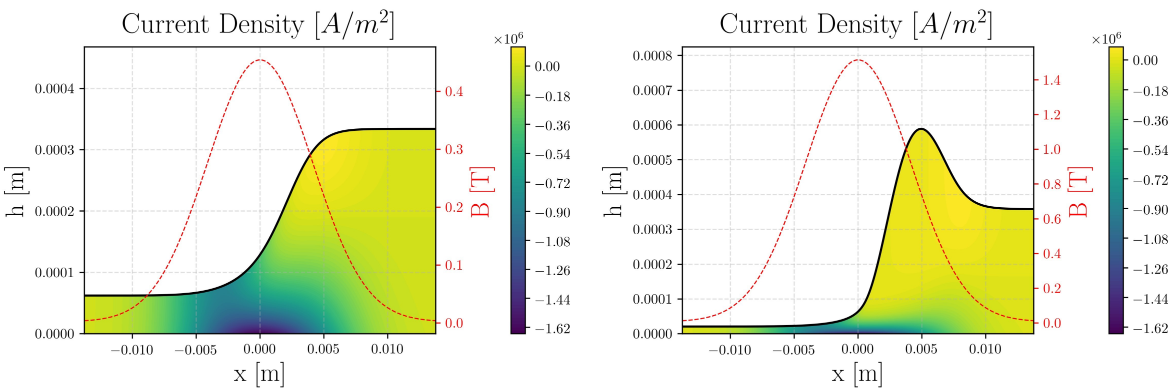

Figure 1: Examples of steady state solution for different intensities of the magnetic fields, scaled in terms of Hartman number Ha =(σ[B]2Up/ρg)1/2, with [B]the maximum intensity of the magnetic field, g the gravity acceleration(from left to right) and σ the electrical conductivity. On the right, the high Ha results in a solitary hump in the run-back flow.

Abstract T-63

References

Mendez, M. A., et al. "Dynamics of the Jet Wiping Process via Integral Models." arXiv preprint arXiv:2004.13400 (2020).
Bregand, O ; Crahay, J ; Gerkens, P . "New wiping techniques to efficiently produce suitable coating layers at highspeed in the hot dip galvanising process." Publications Office of the EU (2010).
Lloyd-Jones, C., H. A. Barker, and V. J. Worner. "Investigation into magnetic wiping techniques as alternative to gaswiping on hot dip galvanising lines." Ironmaking steelmaking 25.2 (1998): 117.
Dughiero, Fabrizio, et al. "New DC electromagnetic wiping system for hot-dip coating." COMPEL-The internationaljournal for computation and mathematics in electrical and electronic engineering (2011).

Proceedings ECS 2021
Brussels, Belgium, September 7-9, 2021

Abstract T-46

COATING FLOW ON A ROTATING HORIZONTAL CIRCULAR CYLINDER SUBJECT TO A RADIAL ELECTRIC FIELD

***R. A. McKinlay*[1], *A. W. Wray*[1], *S. K. Wilson*[1]**

[1]Department of Mathematics and Statistics, University of Strathclyde
Livingstone Tower, 26 Richmond Street, Glasgow, G1 1XH, UK

Email: rebecca.a.mckinlay@strath.ac.uk

Abstract
Coating flow on a rotating horizontal circular cylinder is a well-studied problem in fluid mechanics (Moffatt, 1977) and affords numerous industrial applications, such as rotational moulding and spin coating in microfabrication (Ruschak, 1985). Electrohydrodynamically driven flows are of significant interest, and indeed the modelling of them has recently been the subject of a major review (Papageorgiou, 2019). Industrial applications arise from the ability to use an electric field to control the behaviour of a fluid, for example in suppressing instabilities for coating, or enhancing instabilities to increase interfacial area to aid heat and mass transfer rates. In the present work, the two-dimensional dynamics of a layer of an electrified, perfectly conducting Newtonian fluid flowing on the outer surface of a rotating horizontal circular cylinder are studied (Figure 1). The rotating cylinder is an electrode held at a constant potential and a concentric outer electrode, whose potential is allowed to vary spatially, encloses the system, inducing electrostatic forces at the interface. The long-wave approximation (Wray et al., 2017) is used along with the Method of Weighted Residuals (Ruyer-Quil & Manneville, 2000) to derive a reduced-order model that incorporates the effects of the electric stress, rotation, gravity, viscosity, inertia, and capillarity. This model is investigated both numerically and analytically, and is also validated against known results (Pukhnachev, 1977). Novel models governing the electric potential, asymptotically correct up to second order, are derived and are validated against Direct Numerical Simulations.

Keywords: *electrohydrodynamics, reduced models, thin film, thick film*

Abstract T-46

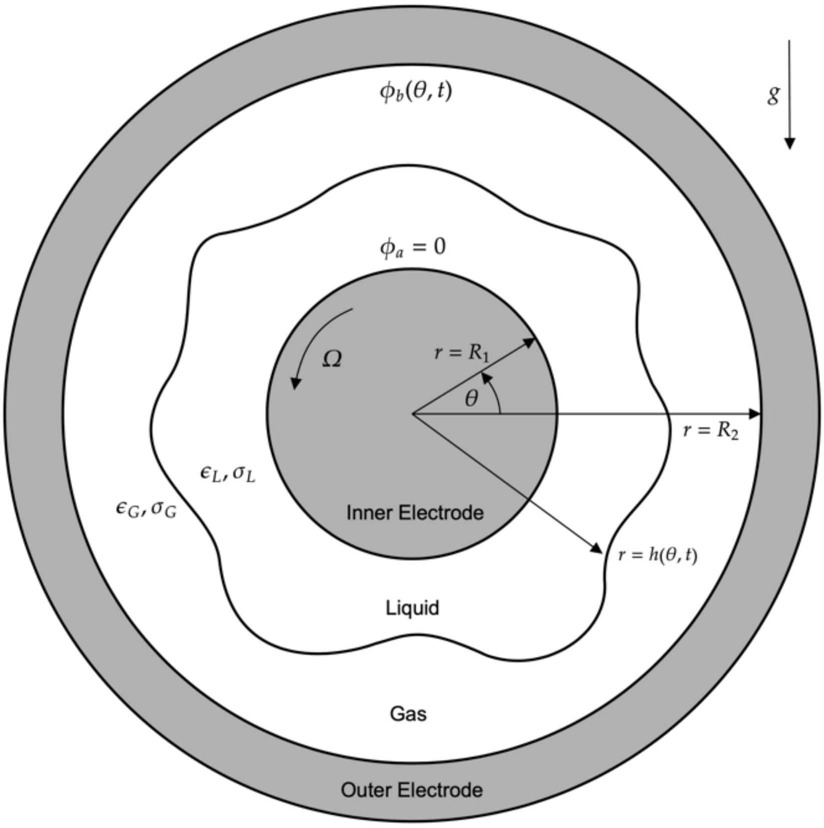

Figure 1. Geometry of the problem considered.

References

Moffatt, H. K. (1977). Behaviour of a viscous film on the outer surface of a rotating cylinder. *Journal de Mécanique*, 16, 651-673.

Papageorgiou, D. T. (2019). Film flows in the presence of electric fields. *Annual Review of Fluid Mechanics*, 51, 155-187.

Pukhnachev, V. V. (1977). Motion of a liquid film on the surface of a rotating cylinder in a gravitational field. *Journal of Applied Mechanics and Technical Physics*, 18 (3), 344–351.

Ruschak, K. J. (1985) Coating flows. *Annual Review of Fluid Mechanics*, 17 (1), 65–89.

Ruyer-Quil, C., Manneville, P. (2000). Improved modeling of flows down inclined planes. *The European Physical Journal B*, 15, 357-369.

Wray, A. W., Papageorgiou, D. T., and Matar, O. K. (2017). Reduced models for thick liquid layers with inertia on highly curved substrates. *SIAM Journal on Applied Mathematics,* 77, 881-904.

Proceedings ECS
2021
Brussels, Belgium, September 7-9, 2021

Abstract T-64

ON THE UNDULATION AND THE TWO-WAY COUPLED INSTABILITY OF THE JET WIPING PROCESS

***D. Barreiro-Villaverde*[12], A. Gosset[3], M.A. Mendez[2]**

[1] CITIC Research, Universidade da Coruña
Campus de Elviña, 15071, A Coruña, Spain
[2]Environmental and Applied Fluid Dynamics, von Karman Institute for Fluid Dynamics
B-1640 Waterloosesteenweg 72, Sint-Genesius-Rode, Belgium
[3]Technological Research Center (CIT), Universidade da Coruña
Campus de Esteiro, 15403 Ferrol, Spain
Email: david.barreiro1@udc.es

Abstract
Jet wiping is a crucial step in the hot-dip galvanization process in which planar gas jets control the thickness of a coating layer withdrawn from a bath with molten zinc. This work uses a numerical methodology developed to capture the relevant features of the gas-liquid interaction in jet wiping; in particular, we are interested in the two-phase mechanism responsible for the long-wavelength defects in the final coating, usually referred to as undulation. The numerical model combines Large Eddy Simulation (LES) and Volume of Fluid (VOF) methods to reproduce three wiping configurations validated with experimental data (Exp. Therm. Fluid Sci., vol. 103, 2019, pp. 48-67). We apply the multiscale Proper Orthogonal Decomposition (mPOD) to classify the wave structures on the film according to their energy and frequency content. An extended version is implemented to correlate the undulations with specific gas jet motion, allowing for a complete description of the mechanism of waveformation.

Keywords*: jet wiping, film flow, two-phase CFD simulation, modal analysis*

1. Introduction

Jet wiping is a metering technique used in the hop-dip galvanization process to control the zinc coating weight on steel substrates. As sketched in Fig.1, a slot gas jet impinges on the liquid film dragged by the solid substrate, reducing the coating thickness and developing a run-back flow. It is the most widely used technique because it is contactless and energy-efficient, although the violent break-up of the run-back flow (splashing) and the formation of undulations in the final coating limit the range of operational windows.

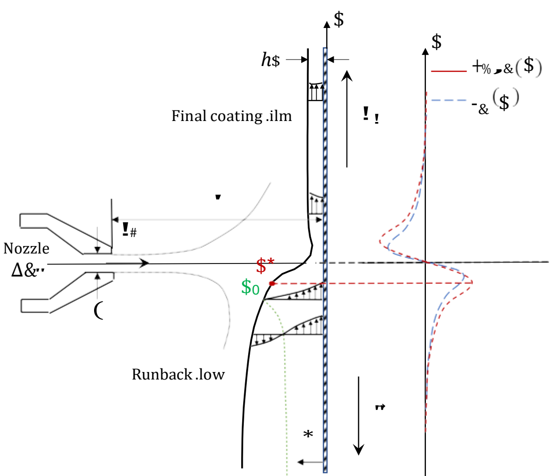

Figure 1. Sketch of the jet wiping process.

The final coating thickness is a function of the stand-off distance Z, the nozzle opening d, the substrate speed U_p, and the gas jet velocity U_j; the latter being determined by the static pressure in the stagnation chamber of the nozzle $11P_N$. The momentum exchange between the gas jet and liquid film is described by the wiping actuators, namely the streamwise pressure gradient $_{x}p_{g}$ and shear stress at the interface $_{g}$. Reduced-order models based on the long-wave approximation have been developed to predict the mean coating thickness in industrial galvanization lines. In these models, however, the gas-liquid interaction is assumed to be one-way (ie., the gas jet perceives the liquid film as a dry flat plate), so these models are unable to predict the undulation dynamics.

Numerical simulations using Large Eddy Simulation (LES) and Volume of Fluid (VOF) have been carried out to characterize the flow in a 2D simulation of jet wiping in industrial conditions (Pfeiler et al., 2017). The same numerical strategy was used for a 3D jet wiping configuration using dipropylenglicol as a working liquid (Myrillas et al., 2013). They reported jet oscillations at temporal scales compatible with the undulations in the film, although they were not attributed to a specific flow instability. The industrial jet wiping with liquid zinc has been studied with a 3D VOF grid-adaptive code (Aniszewski et al., 2020), but the computational cost limited the simulations to the study of film atomization at the initial stages of the wiping. A recent experimental campaign allowed the characterization of the gas and liquid film simultaneously for a wide range of wiping regimes (Mendez et al., 2019a). The spectral matching between the gas and film flows suggested that the mechanism of wave formation results from a two-phase coupling instability. The structures unveiled in the modal decomposition of the gas flow resemble the ones encountered in flow configurations with hydrodynamic feedback.

This work aims at modelling the jet wiping process with 3D VOF LES simulations for a complete description of the undulation mechanism. The numerical model has been validated with experiments in terms of mean final thickness (Barreiro-Villaverde et al., 2019). We apply the multiscale Proper Orthogonal Decomposition (mPOD) to identify the main undulation patterns in the film. An extended mPOD based on correlation analysis is implemented to isolate the associated structures in the gas.

2. Numerical methodology and modal analysis

The CFD simulations combine Large Eddy Simulation (LES) for the turbulent gas flow and Volume of Fluid (VOF) to account for the two-phase nature of the problem. Three simulations were performed with interFoam, an incompressible two-phase flow solver of the OpenFOAM package that implements an algebraic VOF formulation based on the transport of the volume fraction field α. The LES methods involves a low pass filtering of the Navier-Stokes equations, modelling the effect of sub-grid scales with an additional turbulent viscosity given by the Smagorinsky model.

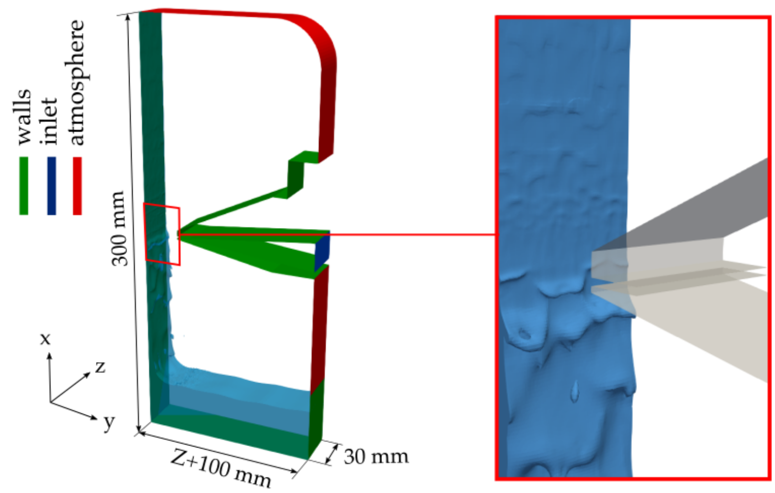

Figure 2. 3D domain with boundary conditions (left) and a snapshot of the film reconstruction (right).

The three configurations reproduce two standoff distances and two nozzle pressures (Case 1: Z=18 mm, ΔP_N=425 Pa | Case 2: Z=18 mm, ΔP_N=875 Pa | Case 3: Z=25 mm, ΔP_N=875 Pa) using air (ρ_g=1.2 kg/m3, μ_g=1.776·10^{-5} Pa·s) and dipropyleneglicol (ρ_l=1023 kg/m3, μ_l=0.075 Pa·s, σ=0.032 N/m). The time step ranges between 1.5·10^{-6} and 7·10^{-7} to ensure that the Courant number is always below 0.95, and the physical simulation time for each case is 2 s after the transient. The entire project consumed 3.5 M CPU hours of priority access in the Spanish Supercomputing Network (RES).

We apply the multiscale Proper Orthogonal Decomposition (mPOD) to isolate the different spatio-temporal scales in the film flow (Mendez et al., 2019b). The decomposition breaks the datasets as a linear combination of elements (r-modes) characterized by a temporal evolution y_r, spatial structure f_r, and amplitude S_r. Multi Resolution Analysis (MRA) filter the temporal correlation matrix $K=D^TD$ in the frequency domain; thus, the spectral content of the modes is constrained to a specific frequency range imposed with a filter bank. We normalize the thickness distributions to attribute comparable energy to both the undulations in the final film and run-back flow; otherwise, the decomposition would be biased towards the big waves in the run-back flow due to the energy optimality essence of the method. First, we compute the modes in the liquid to detect the most dominant undulation patterns. Second, we use the temporal structure of these modes to project the gas flow fields, namely the velocity fields and wiping actuators. This step allows detecting correlated structures between the undulations and the seemingly chaotic gas flow.

3. Results

The numerical methodology was previously validated in terms of mean final thickness (Barreiro-Villaverde et al., 2019). The frequency spectras in figure 3 shows satisfactory agreement between the experimental and numerical datasets for the final film $\mathcal{H}_{ff}$, runback flow $\mathcal{H}_{rb}$, and gas jet $\hat{\mathcal{Y}}$; all computed from the leading modes obtained from the modal decomposition. These results reinforce the two-way coupling hypothesis, since the same frequency peak at ≈ 20 Hz is present in the gas and in the liquid.

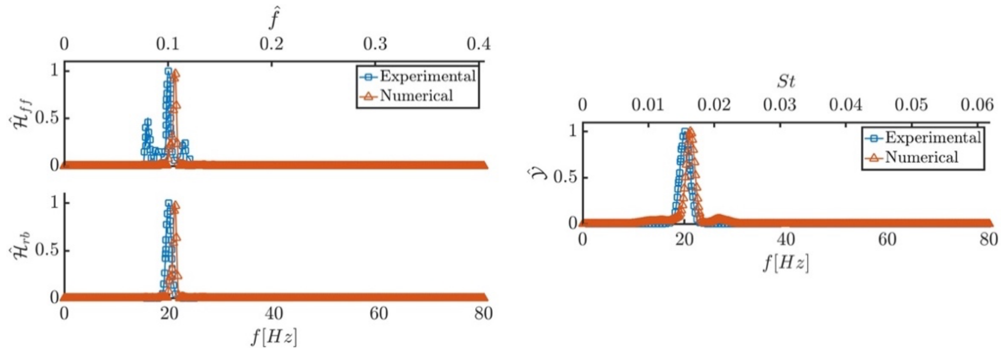

Figure 3. Numerical and experimental frequency spectras in the final film $\hat{\mathcal{H}}_{ff}$, run-back $\hat{\mathcal{H}}_{rb}$ and gas jet $\hat{\mathcal{Y}}$.

It can be shown that a travelling wave pattern must be described by two sinusoidal functions delayed π/2 in time and space. Hence, we only consider the most energetic pairs of modes obtained in the mPOD decomposition that fulfill this criterion. Figure 4 shows that the spatial structure ϕ_2 associated to one of the leading modes preserves most of the flow features observed in the snapshot of the normalized film thickness $\check{h}$. The reconstruction built from these dominant modes portrays two-dimensional wave patterns that originate close to the impingement and propagate in opposite directions along the final film and run-back flow. Moreover, the frequency peaks of these modes match perfectly the one in the gas jet, proving that it must result from a two-phase coupling interaction. The same holds for the rest of the cases, even when the liquid film shows strong three-dimensional patterns. We refer to this pattern as the 2D coupled undulation.

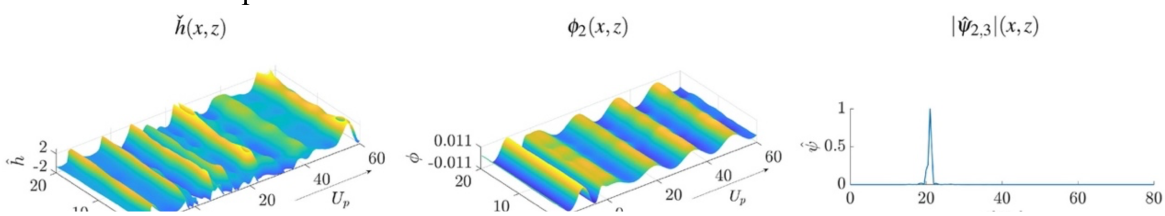

Figure 4. Snapshot of the normalized thickness $\check{h}$ (left), spatial structure of one of the leading modes in the liquid ϕ_2 (middle), and associated frequency spectra $|\hat{\psi}_{2,3}|$ (right).

The extended mPOD allows revealing the structures in the gas jet correlated with the 2D coupled undulation. Figure 5 illustrates the fluctuating velocity field and wiping actuators distributions associated to the undulation and taken at a z constant midplane. The vortical structure below the nozzle axis indicates a periodical deflection of the lower side jet and airflow detachment associated to the formation of the run-back waves; the effect of this mechanism on the wiping actuators is a pulsation of the pressure gradient at this location. An exhaustive analysis of the three investigated cases with the full description of the mechanism is provided in (Barreiro-Villaverde et al., 2021).

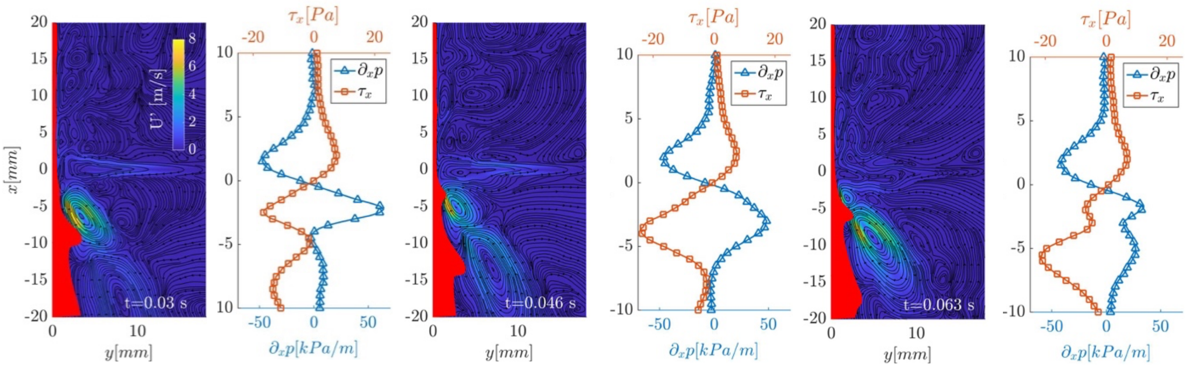

(a) (b) (c) (d) (e) (f)

Figure 5. mPOD filtered fluctuating velocity field (a,c,e) and wiping actuators (b,d,f) for three time steps.

5. Conclusions

The numerical methodology presented in this work allowed for a full description of the hydrodynamics of the jet wiping process. The multiscale modal analysis unveiled a two-dimensional wave pattern present in the entire domain for all the cases: the 2D coupled undulation. These are most likely caused by a gas-liquid interaction in the run-back flow that modulates the wiping efficiency of the gas jet. In a next step, we will apply this methodology to investigate the process in improved similarity conditions with respect to the industrial galvanization lines.

References

Aniszewski, W., Saade, Y., Zaleski, S., & Popinet, S. (2020). Planar jet stripping of liquid coatings: Numerical studies. *International Journal of Multiphase Flow*, 132, 103399.

Barreiro-Villaverde, D., Gosset, A., Mendez, M. A., & Buchlin, J.-M. (2019). Validation of the high-fidelity CFD simulations of the jet wiping process. ECS19 *Proceedings booklet*. Heidelberg, Germany.

Barreiro-Villaverde, D., Gosset, A., & Mendez, M. A. (2021). On the dynamics of jet wiping: Numerical simulations and modal analysis. *Physics of Fluids*, 33(6).

Mendez, M. A., Gosset, A., & Buchlin, J. M. (2019a). Experimental analysis of the stability of the jet wiping process, part II: Multiscale modal analysis of the gas jet-liquid film interaction. *Experimental Thermal and Fluid Science*, 106, 48–67.

Mendez, M. A., Balabane, M., & Buchlin, J. M. (2019b). Multi-scale proper orthogonal decomposition of complex fluid flows. *Journal of Fluid Mechanics*, 870, 988–1036.

Myrillas, K., Rambaud, P., Mataigne, J. M., Gardin, P., Vincent, S., & Buchlin, J. M. (2013). Numerical modeling of gas-jet wiping process. *Chemical Engineering and Processing: Process Intensification*, 68, 26–31.

Pfeiler, C., Eßl, W., Reiss, G., Ecker, W., Riener, C. K., & Angeli, G. (2017). LES-VOF Simulation and POD Analysis of the Gas-Jet Wiping Process in Continuous Galvanizing Lines. *Steel Research International*, 88(9), 1600507.

DRYING AND WETTING

Proceedings ECS 2021
Brussels, Belgium, September 7-9, 2021

Abstract T-25

STRATIFICATION IN THE DRYING OF BI-DISPERSE COLLOIDAL FILM: EVOLUTION OF THE NORMAL STRESS AND MICROSTRUCTURE

***Jae Hwan Jeong*, Young Ki Lee, and Kyung Hyun Ahn**

School of Chemical and Biological Engineering, Seoul National University
Seoul, 08826 Korea

Email: ahnnet@snu.ac.kr

Abstract
Recently, the formation of a stratified layer has been reported in the drying process of bi-disperse colloidal films of different sizes. This stratification has attracted attention due to the uniformity issues within the film or due to the practical applications of the multi-layer coatings. Although several simulation studies have been developed to figure out the stratification, they mainly focused on the drying conditions where the stratification is observed. In this study, we perform Brownian dynamics simulations to understand the stratification mechanism in the drying process of bi-disperse colloidal film. We first confirm that the stratified layer is more pronounced for high Péclet numbers, matched well with previous reports. At high Péclet numbers, the small particles are accumulated at the interface, which induces the localization of the normal stress and an increase of the normal stress at the interface. While at the substrate, the normal stress maintains its initial value and then increases with the accumulation region touching the substrate. We quantitatively analyze this evolution of the normal stress, which accounts for the driving force of the stratification. In addition, we correlate the normal stress development with the local microstructural change during drying, which guides us to demonstrate the mechanism behind the stratification.

Keywords: *Brownian dynamics, drying, stratification, normal stress, microstructure*

1. Introduction
Drying of colloidal film is encountered in many industrial applications, including inkjet printing, fabrication of electronic devices, and manufacturing of secondary batteries. In these systems, the colloidal films have complex formulations, containing colloidal mixtures of different sizes and other additional binders. Recently, Fortini *et al.* reported that a stratified layer consisting of only small particles was formed near the interface during the drying process of bi-disperse colloidal film (Fortini *et al.*, 2016). This small-on-top stratification has received a lot of attention, and many studies have been conducted to find the drying conditions where this phenomenon occurs. Several physical models have provided a useful way to capture the reasons and conditions of the stratification. Nevertheless, they still leave unanswered questions about the stress and microstructural development when the stratification occurs. Therefore, the necessity of simulation studies has been emphasized recently. Here, we carry out a simulation study to understand the stratification mechanism during the drying process of bi-disperse colloidal film.

Abstract T-25

2. Theory

Several physical models have provided a useful way to capture the reasons and conditions of the stratification. Nevertheless, they still leave unanswered questions about the stress and microstructural development when the stratification occurs. Therefore, the necessity of simulation studies has been emphasized recently. Here, we carry out a simulation study to understand the stratification mechanism during the drying process of bi-disperse colloidal film.

3. Experimental procedure

To describe the drying process of colloidal film, we adopt overdamped Langevin dynamics (Brownian dynamics) simulation. Simulations are performed over a wide range of evaporation rates (Péclet number) to observe the change in the stratification dynamics. At the same time, the normal stress and microstructural development are observed and analyzed quantitatively.

4. Results and discussion

At high Péclet numbers, the small particles are accumulated at the interface, which induces the localization of the normal stress and an increase of the normal stress at the interface. While at the substrate, the normal stress maintains its initial value and then increases with the accumulation region touching the substrate. This localized stress plays an important role in resulting in the small-on-top structure.

5. Conclusions

In this study, we studied the normal stress and microstructural development in the drying process of bi-disperse colloidal film by using the Brownian dynamics simulation. We carried out the simulations with colloidal mixtures of two different sizes over a wide range of Péclet numbers. We quantitatively analyzed the evolution of the normal stress, which accounts for the driving force of the stratification. In addition, we correlated the normal stress development with the local microstructural change during drying, which guides us to demonstrate the mechanism behind the stratification.

References

Fortini, A., Martín-Fabiani, I., De La Haye, J. L., Dugas, P.-Y., Lansalot, M., D'agosto, F., . . . Sear, R. P. (2016). Dynamic stratification in drying films of colloidal mixtures. Physical Review Letters, 116(11), 118301.

Proceedings ECS 2021
Brussels, Belgium, September 7-9, 2021

Abstract T-48

SORPTION AND MASS TRANSPORT INVESTIGATIONS IN POROUS THIN FILMS APPLIED TO THE POST-DRYING PROCESS OF LITHIUM-ION BATTERY ELECTRODES

T. Heckmann[1,2]***, J. Eser***[1,2]***, P. Scharfer***[1,2]***, W. Schabel***[1,2]

[1]Thin Film Technology (TFT),
[2]Material Research Center for Energy Systems (MZE)
Karlsruhe Institute of Technology (KIT)
Karlsruhe, Germany

Email: thilo.heckmann@kit.edu

Abstract

For competitive battery cells, an important prerequisite is energy savings in the cell production. An essential cost factor in the manufacturing process of Li-ion batteries poses the post-drying process. In this process, moisture adsorbed from the air is withdrawn from the compounds of the battery by a high energy input. If not removed, the adsorbed moisture reacts with the electrolyte during operation of the battery, which leads to its degeneration. Literature has revealed a connection between electrochemical performance and the remaining moisture content. Therefore, the post-drying step needs to be better understood, to effectively reduce the residual moisture to the lower ppm region which is necessary to ensure high battery performances. A simulation along with precise and comprehensive sorption equilibrium data of water and the kinetics of mass transfer reveals optimization potential to reduce the high drying energy consumption and to optimize the process as well as cell properties.

This work investigates the water transport and sorption equilibria in porous electrodes during post-drying of the electrodes. Complete Li-ion battery anodes and cathodes as well as their single materials have been investigated by means of different methods and set ups. The measurement values are compared for different experimental setups. Moreover, the kinetics of mass transfer is subject of the investigations, focusing on various pressure ranges to utilize different mass-transport mechanisms during post-drying. The results of these investigations compile to a comprehensive process simulation that enables the comparison and evaluation of various process routes.

Acknowledgements:

This work contributes to the research performed at CELEST (Center for Electrochemical Energy Storage Ulm Karlsruhe) and Material Research Center for Energy Systems (MZE). The authors would like to acknowledge financial support of the Federal ministry of Education and Research (BMBF) via the ProZell cluster-projects “Epic” (Grant number: 03XP0295A) and “Sim4Pro” (Grant number: 03XP0242C).

Keywords: *coating, lithium-ion-batteries, simulation*

Proceedings ECS 2021
Brussels, Belgium, September 7-9, 2021

Abstract T-27

INFRARED AND SURFACE-EMITTING LASER BASED DRYING OF BATTERY ELECTRODE COATINGS

A. Altvater[1, 2]***, K. Ly***[1, 2]***, S. Spiegel***[1, 2]***, J. Mohacsi***[1, 2]***, P. Scharfer***[1, 2]***, W. Schabel***[1, 2]

[1]Thin Film Technology (TFT),
[2]Material Research Center for Energy Systems (MZE)
Karlsruhe Institute of Technology (KIT)
Karlsruhe, Germany

Email: andreas.altvater@kit.edu

Abstract

Electricity storage systems will become an increasingly important aspect of the energy industry in the future, especially for electromobility. Due to their properties such as high energy density, high power density and high cycle stability, lithium-ion batteries (LIB) are considered the basis for electrification. Within the production of battery electrodes, particularly the drying process plays a decisive role. With an optimized drying process, the efficiency of electrode production can be increased by minimizing waste, drying time and energy costs, and by improving electrode quality. In this work, the drying of battery electrodes by means of additional energy input via infrared and sur-face-emitting laser radiation was compared with purely convective drying. For this purpose, the radiation energy sources were first characterized with regard to energy input and homogeneity as a function of the operating parameters. Subsequently, an anode slurry was prepared by dispersing the active material graphite, conductive carbon black and a polymeric binder system in water, which is coated on a thin copper substrate and dried in a defined manner. The influence of the drying parameters - heat transfer coefficient, air temperature and the energy input by infrared or surface-emitting lasers on the drying time and the quality of the electrodes was evaluated. Layer temperature and drying rate were modelled and compared with measurements of temperature and mass loss. A mechanical quality parameter for the electrode layers was determined by measuring the adhesion between coating and substrate. Defects and particularly crack formation during drying were observed, as a quality parameter for cohesion of the binder-particle structure and their network within the coating.

This work contributes to the research performed at CELEST (Center for Electrochemical (Center for Electrochemical Energy Stor-age Ulm Karlsruhe) and Material Research Center for Energy Systems (MZE) and is funded by the Federal Ministry of Education and Research (BMBF) under Project ID 03XP0295 (Epic) and 03XP0345 (InMiTro).

Keywords: *drying, lithium-ion-batteries, infrared*

Proceedings ECS 2021
Brussels, Belgium, September 7-9, 2021

Abstract T-18

INKJET PRINTING LINES ONTO THIN, MOVING POROUS MEDIA - EXPERIMENTS

Vignesh Murali, Jos C. H. Zeegers and Anton A. Darhuber

Department of Applied Physics
Eindhoven University of Technology, The Netherlands

a.a.darhuber@tue.nl

***Keywords**: Inkjet printing, infrared thermography, paper, porous media, evaporation, evaporative cooling*

Inkjet printing consists of the ejection and deposition of ink droplets on substrates that are moving underneath the printhead [1]. For printing on paper, water-based inks have been developed that are beneficial from an environmental standpoint. The printing of semi-infinite lines on moving paper substrates lead to a steady-state distribution of moisture and heat, which are a suitable way to study the interplay between heat and masstransfer. Lateral wicking and evaporative mass loss are the dominant mass transfer mechanisms, while evaporative cooling reduces the temperature of paper by up to 6K. Our goals were to develop an experimental setup and procedure to systematically measure the moisture content and temperature of paper as functions of the speed of the motion of the substrate (UIJ) and the frequency of droplet deposition. We use light transmission imaging and infrared thermography to measure the moisture content and temperature distributions, respectively. Fig. 1(a) shows a schematic of our setup. It consists of a sheet of paper, mounted 10 mm above an area light source and fastened onto a motorized translation stage. An inkjet printhead is placed 5 mm above the paper surface. A CCD and an IR camera measure the transmitted intensity and the temperature of paper, respectively. Fig. 2(a) shows the transmission image corresponding for UIJ= 0.1 mm/s and t= 600s after commencement of inkjetting, with Fig. 2(b) showing the corresponding IR image.

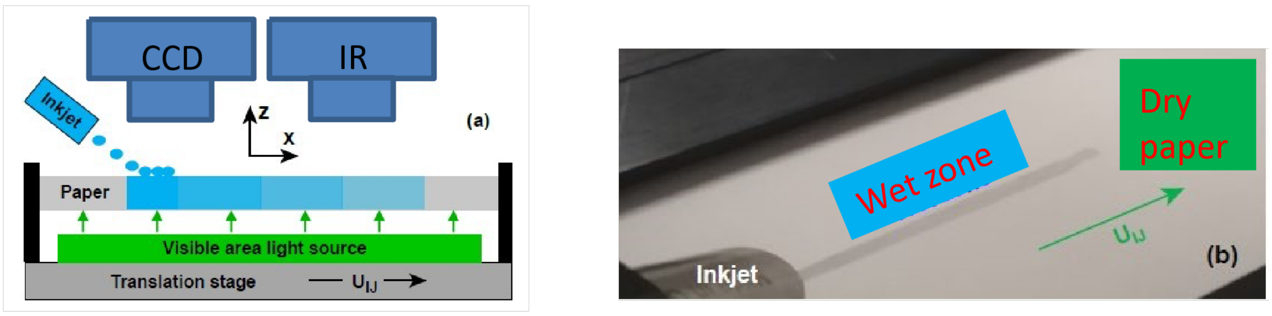

Fig. 1: (a) Schematic of the experimental setup. (b) Top-view photograph of a line being printed.

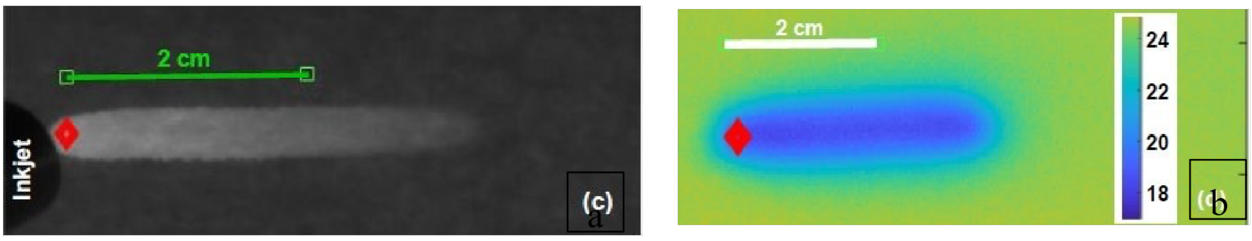

Fig.2: (a) Optical transmission image of a printed line for UIJ= 0.1 mm/s and t=300s after commencement of inkjetting. (b) The corresponding IR image.

Abstract T-18

Besides conducting systematic experiments, we also developed a theoretical model for heat and mass transfer including evaporative cooling. The results of our simulations agree well with the measured data. Details of the model will be introduced in a separate presentation.

References

[1] H. Wijshoff, Physics Reports **491**, 77-177 (2010) .

Proceedings ECS
2021
Brussels, Belgium, September 7-9, 2021

Abstract T-39

SIMULATION OF DRYING FOR POLYMER-PARTICLE-COMPOSITES

***Víctor Gracia*[1,2]*, Philip Scharfer*[1,2] *and Wilhelm Schabel*[1,2]**

[1]Thin Film Technology (TFT)
[2]Material Research Center for Energy Systems (MZE)
Karlsruhe Institute of Technology (KIT), 76131 Karlsruhe, Germany

Email: victor.bravo@kit.edu

Keywords: *drying, polymers, composites, plate-like*

Polymer-particle-composites have been relevant in the last decade for the research of applied materials because particles can functionalize polymer films and better their physical properties. Some examples include electrical conductance, biocompatibility, mechanical stabilization of the polymer matrix and optical properties. Said improvements are dependent on the particle distribution in the dry film, which can be controlled by changing the drying conditions. In previous studies from Cardinal, 2010 and Baesch, 2017 the drying of spherical particles was studied.

A simulation is developed to predict the concentration profiles at different values of the Sedimentation N_S and Péclet Pe_C number. Plotting the results of the simulations with Pe_C as a function of N_S predicts 3 different drying regimes: Sedimentation (S): the particle concentration reaches 90 % of the maximum packing concentration at the bottom of the film, Diffusion (D): the particle concentration does not reach 90 % of the maximum packing concentration at any position in the film, and Evaporation (E): the particle concentration reaches 90 % of the maximum packing concentration at the top of the film. In Figure 1, there is a summary of the mass flux equations for each component used to calculate the concentration profiles by substituting them in equation (1). Also, both boundary conditions at the top of the film (evaporation) and at the bottom (no flux) are summarized.

$$\frac{\partial \phi_i}{\partial \tau} = \frac{\partial}{\partial z} \Gamma_i \qquad (1)$$

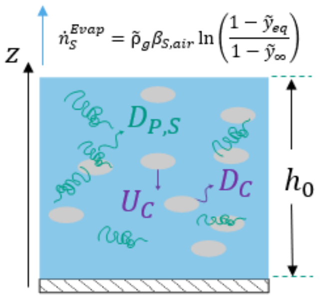

Particles C	Polymer P	Solvent S
$\Gamma_C = \phi_C \tilde{V}_C \dot{n}_S^{Evap}$	$\Gamma_P = \phi_P \tilde{V}_P \dot{n}_S^{Evap}$	$\Gamma_S = -(1-\phi_S)\tilde{V}_S \dot{n}_S^{Evap}$
$\Gamma_C = -D_C(\phi_C)\frac{\partial \phi_C}{\partial z} + U_C(\phi_C)\phi_C$	$\Gamma_P = -\frac{D_{P,S}}{(1-\phi_C)}\frac{\partial \phi_P}{\partial z} - \frac{\phi_P}{(1-\phi_C)^2}\frac{\partial \phi_C}{\partial z} - \phi_P \Gamma_C$	$\Gamma_S = -\frac{D_{P,S}}{(1-\phi_C)}\frac{\partial \phi_S}{\partial z} - \frac{\phi_S}{(1-\phi_C)^2}\frac{\partial \phi_C}{\partial z} - \phi_S \Gamma_C$
$\Gamma_C = 0$	$\Gamma_P = 0$	$\Gamma_S = 0$

Figure 1. Summary of the mass transport equations and the boundary conditions during the drying process (Baesch, 2017)

In this work, the influence of geometry on the regime maps was investigated. To this end, the sedimentation velocity and viscosity at different particle concentrations were measured and fitted to the Batchelor model (Batchelor,1972), to prove if the drying of polymer-plate-like-particle-composites could be simulated in the same manner as spherical particles. Using the fitted parameters, concentration profiles were simulated and new regime maps as a function of the particle shape were produced.

References

1. Cardinal C. M., Jung Y. D., Ahn K.H. and Francis L. F. (2010). Drying regime maps for particulate coatings. *AIChE J*. **11**, 2769-2780.
2. Baesch S., Scharfer P., Schabel W. and Francis L.F. (2017). Influence of the drying conditions on the particle distribution in particle-filled polymer films: Predictive simulation of the particle distribution during drying. *J. Compos. Mater*. **24**, 3391-3403.
3. Batchelor G.K. (1972) Sedimentation in a dilute dispersion of spheres. *J. Fluid Mech.* **52**, 245-268.

Proceedings ECS 2021
Brussels, Belgium, September 7-9, 2021

Abstract T-04

DIFFUSION-REACTION COUPLING IN PHASE SEPARATING PHOTO-CURABLE COATINGS

T. Ogata, Y. Mawatari, Y. Saito, M. Yamamura

Department of Applied Chemistry, Kyushu Institute of Technology
Sensui 1-1, Tobata, Kitakyushu, Fukuoka, Japan

Email: yamamura@che.kyutech.ac.jp presenting/corresponding author

Abstract
We examined the diffusion-reaction coupling in photo-curable, phase-separating liquid film coatings, in which a front of the conversion profile propagates as a travelling wave. The attenuated-total-reflection infrared (ATR-FTIR) spectroscopy measurements revealed that a short time (< 1 s) UV exposure onto the top coating surface promoted a solvent diffusion along the irradiation direction. After the light was turned off, the solvent at the bottom surface diffused back toward the top surface or retained a constant concentration, depending on the phase-separated microstructures.

***Keywords**: frontal photo polymerization, UV curing, phase separation, reaction-diffusion coupling*

1. Introduction

Photo-responsive monomers polymerize upon irradiation of ultra-violet (UV) light with an aid of photo-initiator. Fundamental understanding of the photopolymerization processing is of crucial importance not only in functional coatings but also in 3D printing, photolithography of microcircuits, microfluidic devices, and dental restoratives. In the presence of photo attenuation in a reactive liquid, a monomer-to-polymer conversion profile becomes non-uniform and propagates from the illuminated surface into the unpolymerized area as a travelling wave (Terrones and Pearlstein, 2001, Cabral et al., 2004, Warren et al., 2005), sometimes refferred to as frontal photopolymerization (FPP). For miscible fluids, successful physical models have been presented to describe FPP processes by considering a diffusion-reaction coupling. As the radical polymerization reactions locally consume the reactant in the photo-irradiated area, a concentration gradient forms along the light intensity profile and consequently drives a diffusion of unreacted monomer (Hennessy et al., 2015, 2017). When the system contained monomers with different reactivity, the high-reactive monomer component diffuses toward the exposed area (Sakaguchi et al., 2004, Sanchez et al., 2005), whereas the low-reactive component is extruded from the exposed area (Leewis et al., 2004), leading to a spatial temporal variation in compositions (Kragt et al., 2018).

However, few physical models are currently available for describing FPP of immiscible fluids. When the product of polymerization reaction, i.e., polymer, is incompatible with co-exiting component(s), the systems becomes thermodynamically unstable upon UV irradiation and undergoes a spontaneous photo-induced phase separation (PIPS) via the spinodal decomposition or the nucleation mechanism. Fig. 1 schematically shows a specific case when the system contains non-reactive solvent that is immiscible with the polymer. A directional photo irradiation first creates a traveling front of non-uniform conversion profile (Fig. 1a), followed by the secondary front that separates phase-separating and non-separating layers (Fig. 1b), and eventually results in the development of phase structures across the thickness. This frontal PIPS shows rich physics including (i) evolutions of solvent-rich and polymer-rich demixed phases, (ii) solvent migration from the exposed area to the dark area as would the low-reactive monomer, (iii) monomer migration toward the exposed area, (iv) enhanced or hindered polymerization reactions depending on the local solvent concentration, and (v) solvent diffusion guided by bi-contineous phase structures. Despite the fact that the frontal PIPS combined with a subsequent solvent removal is a promising route to fabricate asymmetric porous polymeric films (Yoshihara and Yamamura, 2019), the diffusion mechanism is still unresolved because of complex diffusion-reaction coupling in a non-equilibrium state.

Abstract T-04

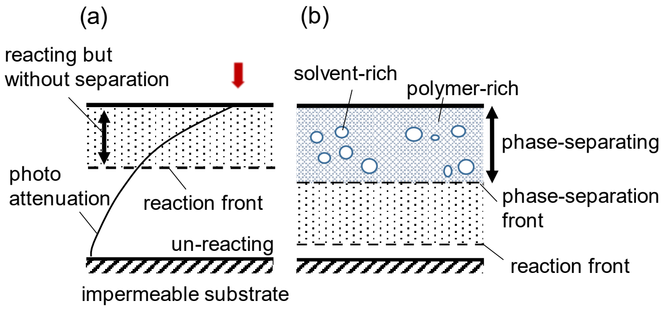

Fig. 1 Frontal photo-induced phase separation. (a) a directional photo irradiation first creates a traveling front of non-uniform conversion profile. (b) A further reaction induces the secondary front that separates phase-separating and non-separating layers.

In this article, we show time-evolutions of the local solvent concentration and the monomer conversion during a frontal photo-induced phase separation processsing of photo-curable liquid film coatings using the attenuated-total-reflection infrared (ATR-FTIR) spectroscopy. The local solvent concentration at the bottom coating surface first increased within 2~3 s after the onset of photo irradiation and then slowly decreased after ceasing the photo irradiation. The maximum concentration of solvent at different compositions and UV intensities obeyed a single master curve with respect to the monomer-to-polymer conversions when interconnected phase structures developed via the spinodal decomposition. In contrast, the solvent concentration retained when the cured solution involved island-see phase structures, indicating different diffusion modes that depend on the phase-separated microstructures inside the coating.

2. Experimental procedure

We used methyl-ethyl-ketone (MEK, Wako Chemical) as a solvent, phenylbis (2,4,6-trimethlybensoyl-) phosphine oxide (Irg819, BASF) as a photo-initiator, and polyester-acrylate (Aronix-M9050, Mw=1000~1500, Toagosei) as a photo-reactive monomer, respectively. MEK was chosen as the solvent, which is immiscible with products of photo-polymerization reactions of Aronix-M9050. Those chemicals were used as purchased without any further purification. The ternary solution was prepared with a constant monomer-to-initiator mass ratio of 9 w/w and coated on a ZnSe prism for attenuated-total-reflection infrared (ATR-FTIR) spectroscopy using IRAffinity-1 (MIRAcle 10, Shimadzu) in order to measure local compositions in the vicinity of liquid-prism interface of 0.7-2 μm in depth. The coated area was specified as 1 cm^2 by attaching a 2 -mm-thick silicone shim on the prism. The pre-determined volume of the solution was ejected from a pipette and coated with a liquid film thickness ranging between 200 and 1000 μm at room temperature. The glass cover was set on the shim surface to minimize solvent evaporation during the measurements. To promote photo-polymerization reactions, an ultraviolet light of 365 ± 5 nm in wavelength was irradiated for 1 s onto the closed solution sample from the LED light source (HSL-50UV365-4UTK, CCS) set on top of the prism surface with a distance of 8.7 cm. The UV intensity at the prism surface was measured using the power meter (C6060-365-03, Hamamatsu) and regulated to be 20 ~ 45 mW/cm^2. The spectra of each fluid were collected with an interval of 2~3 s immediately after the UV irrdiation within the range of 1500 cm^{-1} to 700 cm^{-1} with either single or 20 scans and a resolution of 4 cm^{-1}. To identify the local composition from the IR spectrum, we built calibration curves from the spectra of ternary solutions of known concentrations. We observed three distinct absorption peaks at 808, 981, and 1363 cm^{-1} associated with the out-of-plane bending C-H vibration on C=C double bond in polyester-acrylate, the unreactive C-O bonds in polyester-acrylate, and the symmetric stretching of CH_3 bonds in MEK, respectively. We employed a cubic function of A_{1363}/A_{981} with respect to the solvent mass fraction (x) as $A_{1363}/A_{981} = a_0 + a_1 x + a_2 x^2 + a_3 x^3$, where A_λ denotes the absorbance at the wavelength λ. The constants a_0~ a_3 were assumed to be given by the linear functions with the mass fraction of Irg819. The solvent mass fraction was obtained by solving the cubic function for each absorbance ratio at different times.

The monomer-to-polymer conversion was defined as amounts of polymerized monomers relative to the initial amount of the monomer and calculated by $1-(A_{808}/A_{981})^t/(A_{808}/A_{981})^0$ where the superscripts 0 and t represent the absorbance ratio before and after the photo irradiation. To identify the phase-separation modes, a He-Ne laser (Edmond) of = 532 nm in wavelength and 5 mm in beam diameter was passed through the photo-irradiated wet film with a circular photomask.

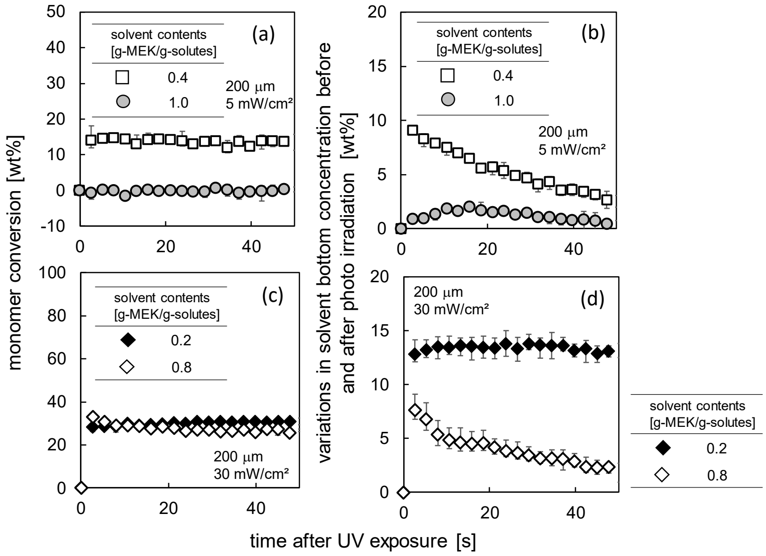

Fig. 2 Time evolutions in (a)(c) monomer-to-polymer conversion and (b)(d) differences in solvent bottom concentration before and after light exposure at different UV intensities of (a)(b) 5 mW/cm² and (c)(d) 30 mW/cm².

The CMOS camera (WAT-01U2, Wantec) was used to capture the static light scattering pattern on a white screen as a digital image. The line profiles of the green values after the RGB image decomposition were obtained for three different lines that crossed at the center of the mask. The line profile exhibited a peak at a critical radial coordinate r_c when the phase separation via the spinodal decomposition (SD) created ordered, bi-continuous structures with a characteristic length scale. We used the scattering angle $\theta = \tan^{-1}(r_c/L)$ to calculate the scattering vector $|q| = 4\lambda/\pi \cdot \sin(\theta/2)$ and the length scale $1/|q|$ where L denotes the distance between the sample and screen surfaces. We distinguished the SD mode from the formation of island-sea structures via the nucleation and growth (NG) mechanism where the line profile became broad and showed no distinct peak at any radial positions.

3. Results and discussion

Fig. 2 showed the time-evolutions of the monomer-to-polymer conversion (a and c) and the differences in solvent bottom concentration before and after light exposure (b and d) at different UV intensities of (a)(b) 5 mW/cm² and (c)(d) 30 mW/cm², respectively. These intensities were chosen because the weak photo exposure resulted in no apparent phase separation, whereas the strong light irradiation lead to the developments of phase-separated bi-continuous structures via the spinodal decomposition mode and island-sea structures via the nucleation mode at the solvent concentrations of 0.8 and 0.2 g-MEK/g-solutes, respectively. In the former case of 5 mW/cm² light exposure, the monomer conversion at the coating bottom was negligible small at a high solvent concentration of 1.0 g-MEK/g-solutes (closed circles in (a) and (b)). The local solvent concentration at the bottom coating surface first increased and then decreased with increasing elapsed time, implying that the travelling reaction front induces forward and backward solvent diffusion with respect to the direction of photo irradiation. The decrease in the bulk solvent concentration resulted in a higher monomer conversion and a faster rise in the solvent content at the bottom surface (open rectangles in (a) and (b)). The light scattering experiments showed that a photo-induced phase separation onset as we increased the UV intensity up to 30 mW/cm². The monomer-to-polymer conversions remained constant and agreed each other at two different solvent concentrations (Figs. 2c and 2d). The photo-cured coating in the presence of bi-continuous phase structure showed a significant decay in the local solvent content (open diamonds in (c) and (d)), whereas the coating bottom kept a high constant concentration of the solvent in the island-sea domain structures.

Abstract T-04

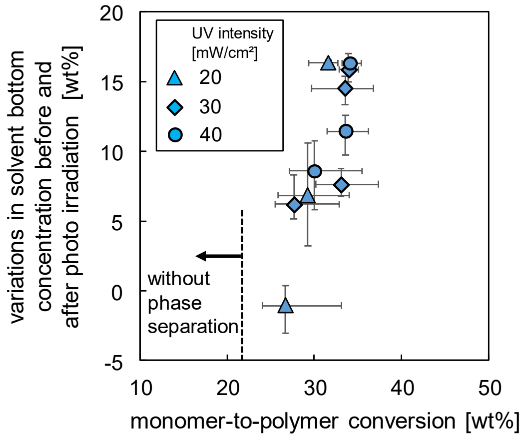

Fig. 3 Effect of monomer-to-polymer conversion on the variations in solvent concentration before and after photo irradiation at the bottom coating surface. The increases in solvent concentration at the bottom surface obey a master curve for different UV light intensities and liquid compositions.

These facts imply that interconnected solvent-rich phases in the bi-continuous structure play as a diffusional path and guide the solvent molecules to transport across the thickness. From a practical viewpoint, such a structure-guided solvent diffusion possibly assists a relaxation of concentration gradients and thus help us to achieve more uniform compositional profiles inside the photo-curing coatings.

We systematically conducted the similar measurements and summarized the variations in solvent concentration before and after photo irradiation at the bottom coating surface with respect to the monomer-to-polymer conversions, particularly focusing on irradiation conditions under which spinodal demoposition took place. As illustrated in Fig. 3, the increases in solvent concentration due to photo irradiation collapse into a single band for different UV light intensities and liquid compositions. This master curve is useful to predict the increament in local solvent concentration under a given UV irradiation condition.

References

Cabral, J.T., Hudson, S.D., Harrison, C., Douglas, J.F. (2004). Frontal photopolymerization for microfluidic applications, *Langmuir*, 20, 10020-10029
Hennessy, M.G., Vitale, A., Matar, O.K., Cabral, J.T. (2015). Controlling frontal photopolymerization with optical attenuation and mass diffusion, *Physical Review E* 91, 062402
Hennessy, M.G., Vitale, A., Matar, O.K., Cabral, J.T. (2017). Monomer diffusion into static and evolving polymer networks during frontal photopolymerisation, *Soft Matter*, 13, 9199
Kragt, A.J. J., Broer, D.J., Schenning, A.P. H. J. (2018) Easily processable and programmable responsive semi-interpenetrating liquid crystalline polymer network coatings with changing reflectivities and surface topographies, *Advanced Functional Materials* 28, 1704756
Leewis, C.M., de Jong, A.M., van IJzendoorn, L.J., Broer, D.J. (2004). Reaction-diffusion model for the preparation of polymer gratings by patterned ultraviolet illumination, *Journal of Applied Physics* 95, 4125-4139
Sakaguchi, Y., Kawahara, K., Yamada, T., Okazaki, Y., Imahashi, S. (2004). Diffusion of unreacted monomers detected by atr ftir spectroscopy in a photosensitive printing plate after the photoreaction, *Journal of Applied Polymer Science* 92, 2903-2907
Sanchez, C., de Gans, B., Kozodaev, D., Alexeev, A., Escuti, M.J., van Heesch, C., Bel, T., Schubert, U.S., Bastiaansen, C.W.M., Broer, D. (2005). Photoembossing of periodic relief structures using polymerization-induced diffusion: a combinatorial study, *Adv. Mater.*, 17, 2567-2571
Terrones, G., Pearlstein, A.J. (2001). Effects of optical attenuation and consumption of a photobleaching initiator on local initiation rates in photopolymerizations, *Macromolecules* 34, 3195-3204
Yoshihara, H., Yamamura, M. (2019). Formation mechanism of asymmetric porous polymer films by photoinduced phase separation in the presence of solvent, *Journal of Applied Polymer Science*, 136, 47867
Warren, J.A., Cabral, J.T., Douglas, J.F. (2005). Solution of a field theory model of frontal photopolymerization, *Physical Review E* 72, 021801

Proceedings ECS 2021
Brussels, Belgium, September 7-9, 2021

Abstract T-82

CONTACT LINE DYNAMICS ON A SOFT COATING, AND DROPS SLIDING DOWN A PLANE COATED WITH A VISCOELASTIC LAYER

Mathieu Oléron, Julien Dervaux, Laurent Limat, Matthieu Roché

Université de Paris, CNRS, Laboratoire MSC, Matière et Systèmes Complexes, France
laurent.limat@univ-paris-diderot.fr, presenting/cooresponding author

Abstract
We have investigated the velocity and shape of drops sliding down an inclined plate, coated with a thin layer of elastomer, and interpreted the observations with a non-linear model of elastowetting, able to treat large interface slopes and finite deformations of the coating. The main particularity of this model is the appearance of a dynamical effective hysteresis, even at low velocity, linked to the viscoelasticity of the substrate, and the existence of an elastic singularity at contact line, traveling with this one and displacing Neumann equilibrium. Compared to more classical drops sliding on a rigid substrate, surprising "guitar" shaped drops are observed, with a marked tendency to avoid corner singularity for very soft substrates. Also, the scenari of drop tail fragmentation into droplets are completely modified.

Keywords: *Wetting, Elastowetting, Wetting dynamics, drops, soft coating, singularities, non-linear elasticity, morphogenesis*

Abstract T-11

DROPLETS WETTING A FROSTED GLASS SURFACE

Stephane Dorbolo[1]

[1]FNRS-University of Liege, Belgium

Abstract
A simple rough surface is considered: the frosted glass: the glass surface is rough. Consequently, regarding the wetting properties of water, the frosted glass is parahydrophilic following the nomenclature by Marmur (Marmur, 2012). The hysteresis of the contact angle is very large. This behaviour contrasts with the silicone oil that wets the frosted glass very well. We compare the trajectory of droplets made of silicone oil and made of water along an incline plane made of frosted glass. In particular, we were able to study the long-range motion (up to 100 times the size of the droplet) because the frosted glass surface state is very robust regarding cleaning and dusty environment. The droplet releases some liquid on the plate during the motion, losing mass. As a consequence, the speed decreases with time along a logarithmic law. A simple model is deduced to obtain the scaling with time. Finally, remarkable properties are reported concerning the possibility to implement open micro-fluidic channels on the frosted glass.

Keywords: *droplet, rough surface, micro-flow*

1. Introduction
Rough and hydrophilic surfaces are called parahydrophilic surfaces and are characterized by a high hysteresis of the contact angle. As far as wetting is concerned, the roughness provides numerous pinning centres and also significantly increases the surface of contact between the liquid and the material. The frosted glass is probably one of the best model-system because it is cheap, largely available and easy to fabricate, in a word *low-tech*. The motion of single droplets made of oil and made of water is studied on an incline plane. The aim is to capture the long range motion since liquid is released on the frosted glass plate.

2. Experimental procedure
The commercial frosted glass (Saint-Gobain) is obtained by attacking a plate of glass with an acid. The result is a random network of pyramids of 2 μm height and separated by 30 μm. The contact angle hysteresis is large up to 90°; the receding angle being 0° because the roughness acts as pining centres for the contact line (see Fig.1a). In the presentation, we will inspect the wetting properties of the silicone oil (20 cSt) and of the water. Two geometrical situations will be considered: the glass plate is horizontal or tilted.

3. Results and discussion
Concerning the silicone oil, the wetting properties were first considered on a horizontal frosted glass plate. Indeed, we can simply observe the spreading of a single droplet taking advantage of the fact that the frosted glass turns to be transparent when some liquid fills the crevices. As the silicone oil does not evaporate, the slow spreading could be observed during three months. The shape of the stain remained circular during the whole experiment. Measuring the radius of the stain as a function of time, different regimes predicted by Cazabat et al (Cazabat, 1986) have been observed. Eventually, the spreading stopped and the average thickness of the oil layer could be deduced.

Abstract T-11

On an incline plane, the droplets start moving when the angle is above a given value predicted by Furmidge's model (Furmidge, 1962). The driving force (the parallel to the plate component of the weight of the droplet) has to exceed the adhesion forces. Therefore, the angle from which the droplet starts sliding depends on the droplet volume and on the nature of both substrate and droplet. The behaviour of the oil droplet and of the water droplet were compared on the tilt frosted glass plate. Once in motion, the main difference resides in the lateral shape of the trace released by the droplet. Indeed, the silicone oil spreads along the lateral direction of the motion while the water droplet does not extend at all along that direction. According to the angle of inclination (and consequently according to the speed of the droplet), the shape of the stain released by the oil droplet looks like a comet or like an oblong shape (Fig.1b left). On the other hand, the water droplet that slides along such a surface releases a well-defined wake that corresponds to the surface touched by the droplet (Fig.1b right).

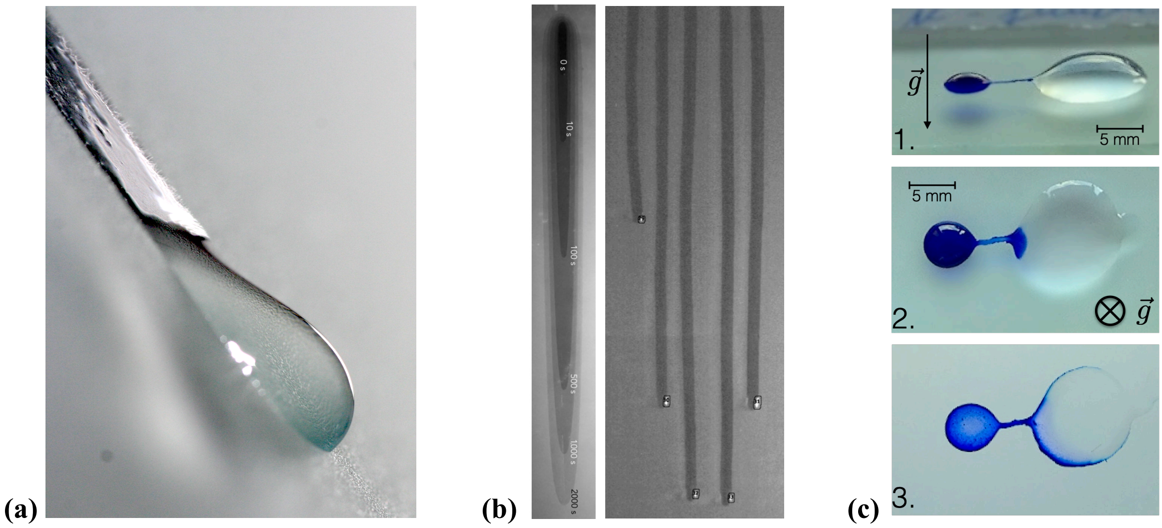

Figure 1. (a) Water droplet sliding along an incline frosted glass plate (angle=75°, droplet length ~ 10 mm). The front presents an advancing angle of about 90° while, at the rear, the receding contact angle is 0°. (b) Comparison of the traces released by an oil droplet and water droplets (left and right respectively) when sliding along a 65° incline frosted glass plate. We can see in the case of oil that the shape changed with time: comet shape after 100 s and oblong shape at 4000 s. (c) Micro-channel drawn using a pen between two sessile droplets. The water coloured in blue flows to the large droplet on the right.

The speeds of sliding of the oil droplet and the water droplet were measured as a function of the angle of inclination and of the volume of the droplet. Compared to the previous literature, the speed measurements could be performed on a large space scale (typically 100 times the size of the droplet). Indeed, the frosted glass properties are not very sensitive to the cleaning process or to the dust environment. Repeatable measurements on a long plate are therefore easily obtained. The position of the tip of the oil stain and the position of the water droplet were used to estimate the speed of the two droplet kinds. The position was found to evolve as a logarithm law of the time. This, in turn, means that the speed decreases exponentially with the position of the droplet. Since the droplets are sliding, they lose weight as a trace is always released on the frosted glass plate. A simple model was deduced to rationalise the observations. The wake of the water droplet on the incline was analysed. By colouring the frosted glass, the flow of liquid in the wake was evidenced. The water was shown to follow the motion of the droplet in the middle of the wake, i.e. the droplet releases a water film that drains back to the droplet. On the other hand, the flow goes upwards on the side.

Finally, the high hysteresis of the contact line allows to write "channel" on the surface of the frosted glass using a simple pen (Fig.1c). This channel may link two sessile droplets distant of several centimetres. When the droplets have different size, the water can flow from one to another droplet because of the difference of Laplace pressure between the droplets.

Abstract T-11

4. Conclusions

The frosted glass is a very common material, cheap and easy to handle. The high hysteresis properties of the contact line allows to use this material as a substrate for drawing fluidic circuit if water in considered. On the other hand, the material is easily wetted by oil. The way the oil invades the micro-crevices is still to uncover to explain that the oil stain remains circular on a long period of time. The speed of droplets along the inclined frosted glass has been shown to rapidly decrease due to the loss of liquid on the frosted glass. The flow in the wake (mainly the drainage) is also to be investigated and explained.

References

Cazabat, A.M. and Cohen Stuart, M.A. (1986). Dynamics of wetting: effects of surface roughness. *J. Phys. Chem.*, 90, 5845–5849.
Furmidge, C.G.L. (1962). The sliding of liquid drops on solid surfaces and a theory for spray retention. *J. Colloid Interface Sci*., 17, 309–324.
Marmur, A. (2012). Hydro- hygro- oleo- omni-phobic? Terminology of wettability classification. *Soft Matter*, 8, 6867.

Proceedings ECS 2021
Brussels, Belgium, September 7-9, 2021

Abstract T-13

FORMULATING STRATIFIED FILMS USING DIFFUSION AND DIFFUSIOPHORESIS

***C. R. Rees-Zimmerman*[1], *A. F. Routh*[1]**

[1]Department of Chemical Engineering and Biotechnology, University of Cambridge
Philippa Fawcett Drive, Cambridge CB3 0AS, UK

Email: crr34@cam.ac.uk

Abstract
This work investigates phenomena controlling stratification in drying films, given that a variety of particle arrangements are observed experimentally. Being able to control this would allow formulation of self-stratifying coatings. A general colloidal hydrodynamics model is derived which allows different phenomena to be included. Scaling arguments and numerical solutions suggest that an excluded volume effect called diffusiophoresis is a key contributor to small-on-top stratification.

Keywords: *fundamentals in film drying, diffusion, diffusiophoresis, paints*

1. Introduction

Stratification in drying films – how a mixture of differently-sized particles arranges itself upon drying – is examined. It is seen experimentally that smaller particles preferentially accumulate at the top surface (Figure 1, bottom right), but it is not fully understood why (Routh, 2013). Understanding this could allow the design of formulations that self-assemble during drying to give a desired structure. Potential applications are across a wide range of industries, from a self-layering paint for cars, to a biocidal coating in which the biocide stratifies to the top surface, where it is required.

2. Theory

On the basis of diffusional arguments alone, it would be expected that larger particles stratify to the top surface (Figure 1, top right). However, other physical processes, including diffusiophoresis (Sear & Warren, 2017), may also be important. By deriving transport equations, the magnitude of different contributions can be compared, and numerical solutions for the film profile are produced.

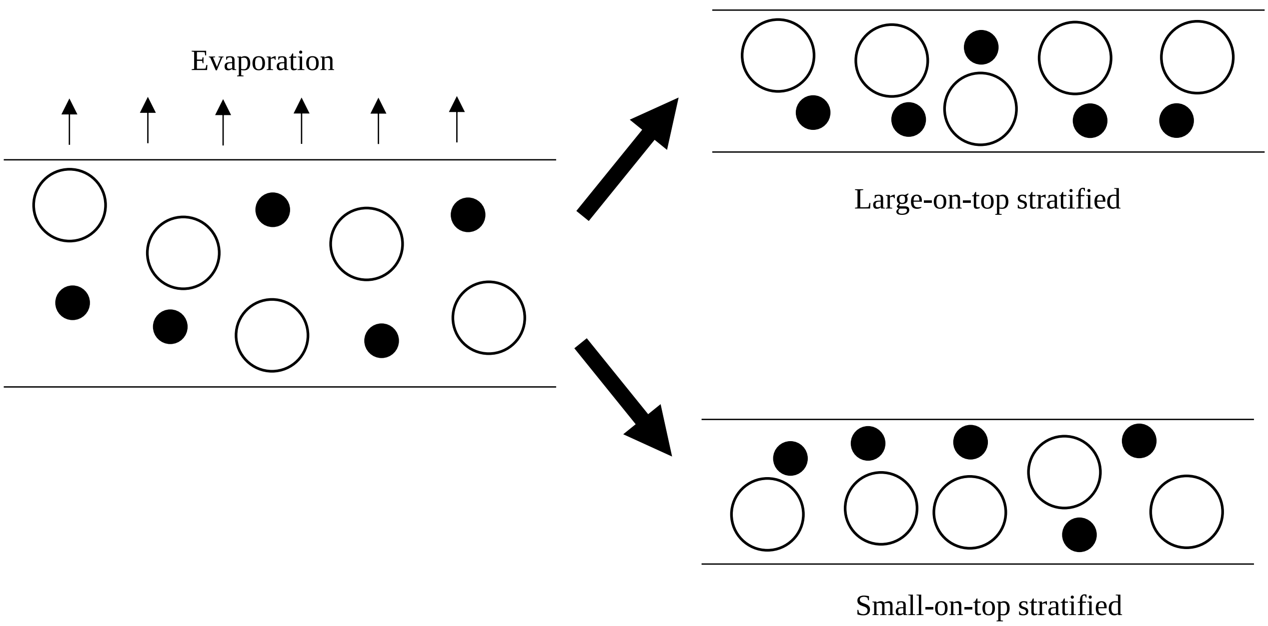

Figure 1. Schematic of the drying of a film containing two sizes of particles, and possible dried film formations.

Diffusiophoresis is the migration of particles along a concentration gradient of a different solute species. A particular diffusiophoresis mechanism that has been hypothesised to cause small-on-top stratification is an excluded volume effect, where small particles (component 1) are excluded from a distance R_{DP} around the edge of each of the large particles (component 2) (Figure 2).

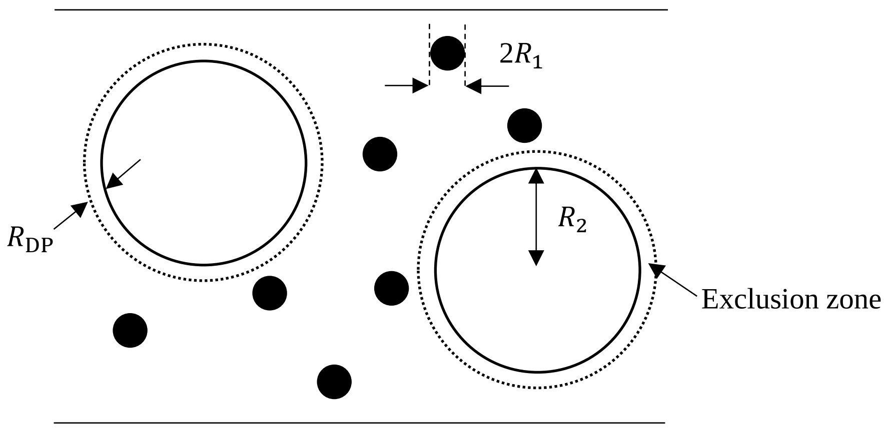

Figure 2. Schematic of the exclusion zones around the larger particles, which give rise to diffusiophoresis.

3. Solution procedure

In order to probe the significance of diffusiophoresis, the model is run with and without diffusiophoresis, for a bidisperse mixture. In addition, the diffusiophoresis term can be varied in strength. Since the top surface is receding due to evaporation, a coordinate transform is carried out to a frame with fixed boundaries. The resulting system of partial differential equations is solved numerically using a finite volume method.

4. Results and discussion

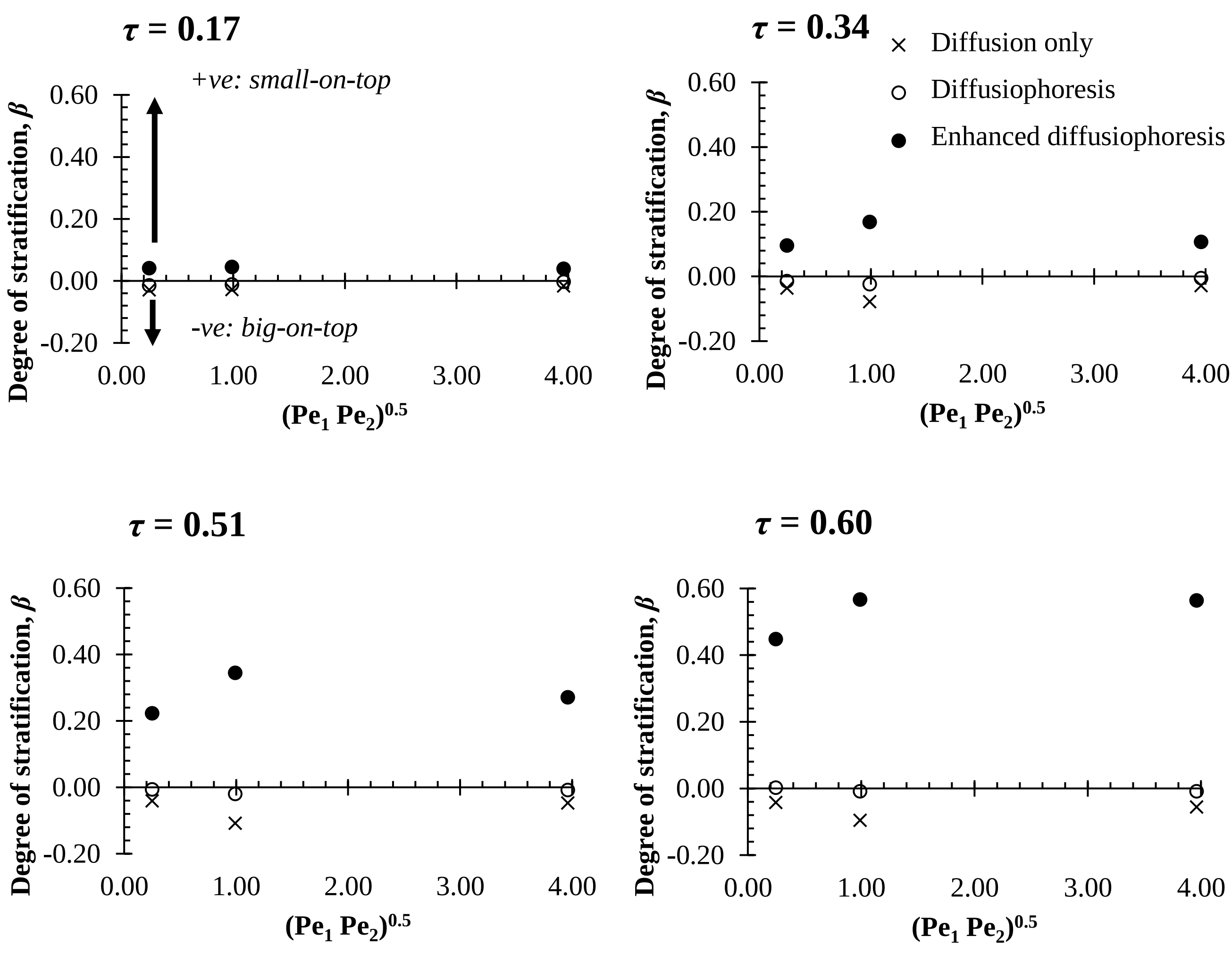

Figure 3. Degree of stratification at scaled times τ = 0.17, 0.34, 0.51 *and* 0.60, *as a function of the geometric average Péclet number, without, with, and with enhanced, diffusiophoresis. These films are bidisperse mixtures, with initial volume fractions of 0.1 of each component, and a particle size ratio of 2.*

To compare the regimes, the numerical model is solved with different values of the dimensionless group the Péclet number, a measure of the ratio of evaporation to diffusion:

$$\mathrm{Pe} = \frac{6\pi\eta R\dot{E}H}{kT}, \tag{1}$$

where η is the solvent viscosity, R is the particle radius, E is the evpoaration rate, H is the initial height of the film, and kT is the thermal energy (Routh & Zimmerman, 2004). A degree of stratification parameter, β, is defined,

$$\beta = 2\left[\frac{\langle\hat{z}_1\rangle - \langle\hat{z}_2\rangle}{\hat{z}(H)}\right], \tag{2}$$

where $\langle\hat{z}_1\rangle$ denotes the average position of particles of component 1 up the scaled height of the film, and $\hat{z}(H)$ denotes the initial scaled height of the film.
Figure 3 presents a summary of the results. It can be seen that the diffusion-only model leads to large-on-top stratification; adding diffusiophoresis promotes β in the direction of small-on-top. In the diffusion-only and enhanced diffusiophoresis cases, the greatest magnitudes of β are reached as the Péclet numbers straddle one, and β increases with time. The non-enhanced diffusiophoresis results remain negligibly stratified throughout.

5. Conclusions

For hard spheres, it is predicted that diffusiophoresis counteracts the effect of diffusion, resulting in approximately uniform films. When the diffusiophoresis strength is increased, the small particles are predicted to stratify to the top surface. This suggests that diffusiophoresis does contribute to experimental observations of small-on-top stratification, but it might not be the only promoting factor. The contribution of diffusiophoresis is being tested in subsequent work using a Hele-Shaw cell experiment.

References

Routh, A.F. (2013). Drying of thin colloidal films. *Rep. Prog. Phys.* 76(4), 046603.
Routh, A.F. & Zimmerman, W.B. (2004). Distribution of particles during solvent evaporation from films. *Chem. Eng. Sci.* 57, 2961–2968.
Sear, R.P. & Warren, P.B. (2017). Diffusiophoresis in non-adsorbing polymer solutions: the Asakura-Oosawa model and stratification in drying films. *Phys. Rev. E.* 96(6), 062602.

Proceedings ECS 2021
Brussels, Belgium, September 7-9, 2021

Abstract T-28

CONTACT-LINE DEPOSITS FROM MULTIPLE EVAPORATING DROPLETS

***Stephen K. Wilson*[1], *Alexander W. Wray*[1], *Patrick S. Wray*[2] and *Brian R. Duffy*[1]**

[1]Department of Mathematics and Statistics, University of Strathclyde,
Livingstone Tower, 26 Richmond Street, Glasgow, G1 1XH, UK
[2]Drug Product Science and Technology, Bristol-Myers Squibb,
Reeds Lane, Moreton, Wirral, CH46 1QW, UK

Email: s.k.wilson@strath.ac.uk presenting/corresponding author

Abstract
Building on the recent theoretical work of Wray et al. (2020) concerning the competitive diffusion-limited evaporation of multiple thin sessile droplets in proximity to each other, we obtain theoretical predictions for the spatially non-uniform densities of the contact-line deposits (often referred to as “coffee stains” or “ring stains”) left on the substrate after droplets containing dispersed solid particles have completely evaporated. Neighbouring droplets interact via their vapour fields, which results in a spatially non-uniform “shielding” effect. We give predictions for the deposits from a pair of identical droplets, which show that the deposit is reduced the most where the droplets are closest together, and demonstrate excellent quantitative agreement with experimental results of Pradhan and Panigrahi (2015). We also give corresponding predictions for a triplet of identical droplets arranged in an equilateral triangle as shown in Fig. 1, which show that the effect of shielding on the deposit is more subtle in this case. Further details are given by Wray et al. (2021).

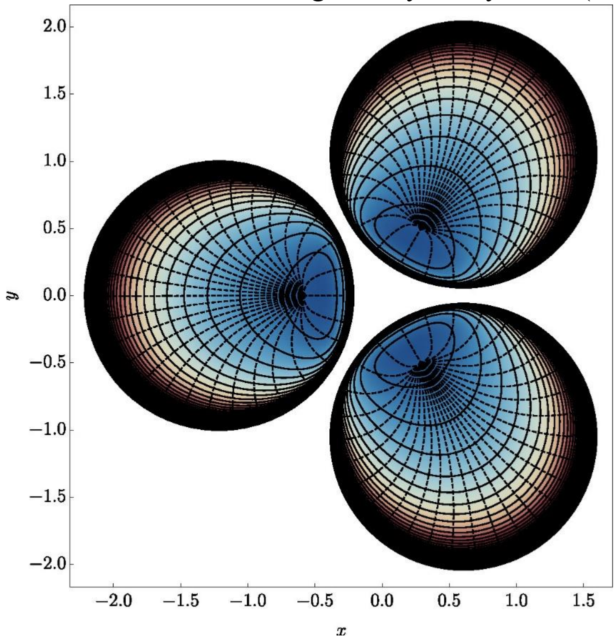

Figure 1. Contours of the local evaporative fluxes and the resulting streamlines of the depth-averaged flows (dashed curves) for a triplet of identical droplets of unit radius.

***Keywords**: Droplets, Evaporation, Particles, Contact-Line Deposits, Coffee Stains, Ring Stains, Shielding Effect*

References
Pradhan, T. K. and Panigrahi, P. K. (2015). Deposition pattern of interacting droplets. *Coll. Surf. A Physicochem. Eng. Asp.*, **482**, 562-567 (2015).
Wray, A. W., Duffy, B. R., and Wilson, S. K. (2020). Competitive evaporation of multiple sessile droplets. *J. Fluid Mech.*, **884**, A45 (2020).
Wray, A. W., Wray, P. S., Duffy, B. R., and Wilson, S. K. (2021). Contact-line deposits from multiple evaporating droplets. To appear in *Phys. Rev. Fluids* (2021).

ADVANCES IN DRYING OF THICK ANODES FOR USE IN HIGH-ENERGY CELLS

J. Kumberg[1,2], K. Ly[1,2], P. Scharfer[1,2], W. Schabel[1,2]

[1]Thin Film Technology (TFT), Karlsruhe Institute of Technology (KIT),
76131 Karlsruhe, Germany

[2]Material Research Center for Energy Systems (MZE), Karlsruhe Institute of Technology (KIT),
76131 Karlsruhe, Germany

Email: kevin.ly@kit.edu

Abstract
Lithium-ion batteries are a substantial part of today's electromobility. Optimized electrode designs and corresponding production processes are currently being investigated in research and development. One approach for optimizing electrode designs of lithium-ion batteries is to increase film thickness. This improves the ratio of active material to inactive components, resulting in a higher energy density. Studies on thick electrodes, though, show transport limitations of lithium-ions, restricted electron transport and therefore an insufficient usage of this electrode design.

It is known that the drying process of battery electrodes has an enormous influence on electrode quality. The formation of the microstructure and the distribution of additives, like binder and carbon black, throughout the film strongly depends on the drying conditions. An inhomogeneous binder distribution leads to reduced adhesion force and cell performance. For understanding the influence of the drying step on thick electrodes, the drying process has to be investigated in detail. This work presents a study of the drying process of electrodes with various electrode thicknesses. Therefore, a mathematical model to calculate solvent loading and film temperature over drying time will be introduced. Furthermore, an experimental setup for the measurement of gravimetric drying curves and the experimental validation will be addressed.

This work contributes to the research performed at CELEST (Center for Electrochemical Energy Storage Ulm Karlsruhe) and Material Research Center for Energy Systems (MZE). The authors would like to acknowledge financial support of the Federal ministry of Education and Research (BMBF) via the ProZell cluster-projects "HighEnergy" (Grant number: 03XP0073B) and "HiStructures" (Grant number: 03XP0243C).

***Keywords**: drying, gravimetric drying curves, lithium-ion battery*

Proceedings ECS 2021
Brussels, Belgium, September 7-9, 2021

Abstract T-19

ELASTOHYDRODYNAMIC DEWETTING OF THIN LIQUID FILMS CONFINED BETWEEN TOPOGRAPHICALLY PATTERNED SURFACES

Maciej Chudak[1], Vaishali Chopra[2], René Hensel[2], and Anton A. Darhuber[1]

[1] Department of Applied Physics, Eindhoven University of Technology, The Netherlands
[2] INM - Leibniz Institute for New Materials, Saarbrücken 66123, Germany

Corresponding author: a.a.darhuber@tue.nl

Keywords: *dewetting, thin liquid films, patterned surfaces*

The dewetting of thin liquid films confined between elastic surfaces is relevant in the contexts of offset printing, coating applications using deformable rollers and underwater adhesion. [1] We have studied the dewetting of a partially wetting liquid when an initially fully wetted micropatterned surface in a Wenzel state is brought into contact with a soft, elastic hemisphere, see Fig. 1. The micropatterned surface consists of a glass substrate covered with a rigid micropillar array with pillar heights of 1 µm

and center-to-center distances d_p varying between 10 and 50 µm. Due to the resulting contact pressure, the liquid rapidly thins in the contact area. Because the liquid is partially wetting, the pattern and elastomer surfaces can come into direct contact through nucleation and growth of one or several dry spots. Although the tops of the pillars are dewetted swiftly, the dewetting of the 'valleys' inbetween the pillars is much slower. We found that depending on the pattern geometry, the dewetting process can exhibit very different characteristics. For large d_p, it is reminiscent of the dewetting of flat, unpatterned surfaces. For intermediate d , a highly anisotropic growth

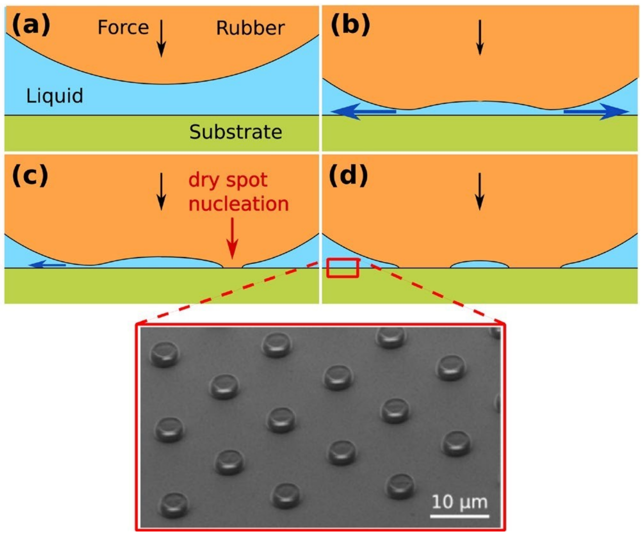

We compared our experimental results with fully-coupled threedimensional numerical simulations based on linear elasticity, the Reynolds equation, and a disjoining pressure formalism [1], which reproduce the key features of the observed phenomena well. An example is shown in

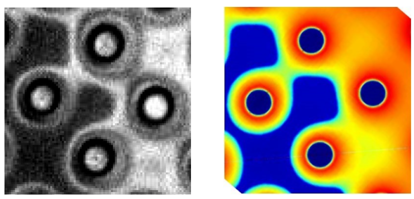

Fig. 2 for d_p = 14 µm. Fig. 2.

Moreover, we have performed contact mechanics simulations to better understand the expansion of a dry spot from one unit cell of the micropillar array to an adjacent one.

Acknowledgments
This project has received funding from the European Union's Horizon 2020 research and innovation programme under the Marie Skłodowska-Curie grant agreement no. 642861.

References
1. M. Chudak, V. Chopra, R. Hensel, A.A. Darhuber. Langmuir **36**, 11929-11937 (2020) .

Proceedings ECS 2021
Brussels, Belgium, September 7-9, 2021

Abstract T-66

TRANSIENT DYNAMICS OF CONTACT ANGLES

D.Fiorini[1,2], ***M.A. Mendez[2], A. Simonini[2], D. Seveno[1] and J. Steelant[3,4]***

[1]Department of Materials Engineering, KU Leuven,
Kasteelpark Arenberg, 3001 Leuven, , Belgium

[2]EA Departament, von Karman Institute,
Chaussée de Waterloo 72, 1640 Rhode-Saint-Genèse, Belgium

[3]Department of Mechanical Engineering, KU Leuven
Celestijnenlaan, 3001 Leuven, Belgium

[4]ESTEC-ESA,
Keplerlaan 1, 2200AG Noordwijk, The Netherlands

Email: domenico.fiorini@vki.ac.be presenting/corresponding author

Abstract
A gas-liquid interface forms a contact angle with a solid surface. The value of the contact angle is a function of the contact line velocity but behaves largely different depending on the presence of inertia in the motion of the gas-liquid interface. In this work, we investigate the transient dynamics of the contact angle by using inverse methods. The dynamic contact angle is reconstructed as a causal factor producing different observations of a gas-liquid interface shape. The results show a strong impact of inertia at the macroscales of the contact line, while at the microscales these effects appear negligible.

1. Introduction
A moving gas-liquid interface forms a dynamic contact angle at the contact line with a solid wall. The dynamic contact angle directly impacts the interface shape and strongly influences the capillary forces involved in its motion. It is thus fundamental to accurately predict the dynamic contact angle in applications such as drop manipulations in microfluidic systems (Willmott et al., 2020) and liquid management in space systems (White & Troian, 2018), to name a few. Several theoretical and empirical correlations have been developed to relate the contact angle to the contact line dynamics. Most of these works focus on a ``quasi-static" condition, usually linking the contact angle to the contact line velocity via the capillary number (Blake, 2006). Several authors (see (Bian et al., 2003; Quéré, 1997; Shardt et al., 2014; Willmott et al., 2020) and references cited therein) have shown that these approaches fail in the presence of inertia, which prompted the idea of correlations able to account for the time history of the contact line dynamics (see (Bian et al., 2003)). This work investigates the behavior of the dynamic contact angle of a space-substitute fluid for an interface motion strongly affected by inertia. The challenges in the accurate measurement of the dynamic contact angle are overcome using indirect methods based on meniscus equations for inertia dominated interface motion.

2. Experimental procedure
The analyzed test case is a quasi-capillary U-tube with 4 mm radius (Figure 1). The U-tube is partially filled with the test liquid which is suddenly released from an un-balanced configuration where the interface position on the two sides is controlled by pressure. The interface dynamic is monitored via high-speed visualization. The images are corrected for optical distortion (Darzi & Park, 2017) and processed via image processing techniques. The liquid tested is HFE7200, which is a synthetic liquid characterized by small equilibrium contact angles. This liquid is often used at ambient conditions to simulate typical properties of cryogenic space fluids.

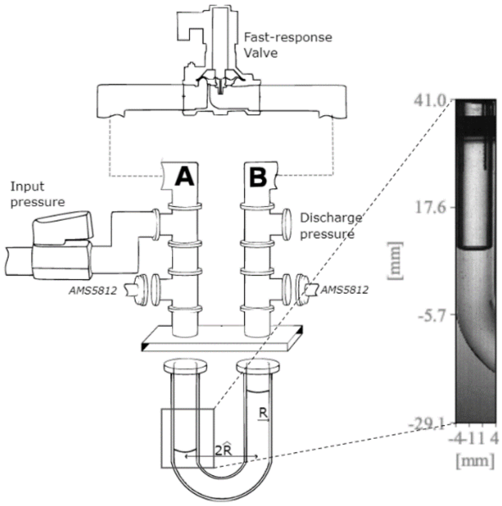

Figure 1. Schematic diagram of experimental setup. The side A is initially pressurized to control the initial interface position, while a fast response valve allows for suddenly release the pressure difference at the beginning of the experiment.

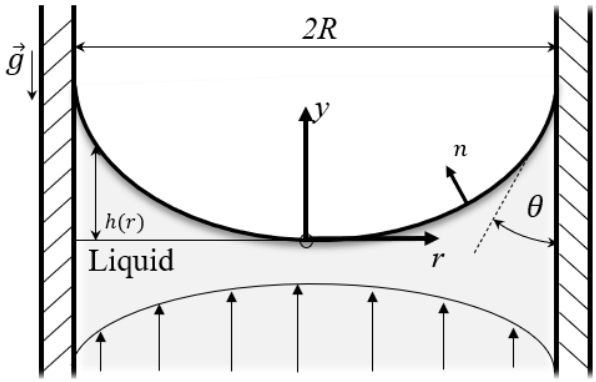

Figure 2. Schematic of the interface model. The origin is located at the interface, in the center of the channel, and moves with it (i.e. h(0,t) = 0 for all times).

3. Theory

The interface shape is modeled by considering a force balance including the Laplace pressure, gravity, the viscous pressure at the contact line and the effects of inertia. Referring to Figure 2 this yields to the following boundary value problem:

$$\begin{cases} \nabla \cdot \boldsymbol{n} + l_c^{-2} h - 3\dfrac{Ca}{R-r} F(\theta) + H_a = 0 \\ \partial_r h(R,t) = ctg(\theta(R,t)) \\ \partial_r h(R,t) = 0 \end{cases} \tag{1}$$

The fluid has density ρ, dynamic viscosity μ and surface tension σ. $l_c = \sqrt{(\sigma/\rho g)}$ is the Capillary length of the liquid, $Ca = \mu U_{cl}/\sigma$ is the Capillary number and U_{cl} is the contact line velocity. $h(r,\, t)$ is the interface height, herein assumed to be axisymmetric, and $\nabla \cdot \boldsymbol{n}$ is the interface curvature. The shorthand notation ∂_r is used to denote partial derivatives with respect to the radial coordinate r. The axes are located at the center of the interface, i.e. such that $h(0,\, t) = 0$ for all times, and R is the tube radius. The first boundary condition involves the (unknown) contact angle, with ctg the cotangent.
$F(\theta)$ is a correction factor (Delon et al., 2008) which for small angles can be approximated as $\sin(\theta)\,/\theta^2$. H_a is a correction factor introduced in this work to account for the impact of the flow inertia on the liquid interface. This term reads:

$$H_a(r,t) = \frac{\rho a_i (R c_t)}{\sigma}\left(1 - e^{-\frac{r-R}{l_i}}\right) \tag{2}$$

a_i is the acceleration of the interface, c_t and l_i are factors to be tuned to correct the interface shape. We use an optimization routine to solve the inverse problems of the curve fitting and contact angle identification. The inverse problems can be written as nonlinear least square problems, where a function $f(x|\boldsymbol{w})$, parametrized by the weight vector $\boldsymbol{w}$, must be fitted to dataset a $(x_i y_i)$ with $i\ in\ [1, n_p]$. The weights are thus computed from the minimization of the l_2 norm of thedifference between data and model prediction:

$$J(\boldsymbol{w}) = \sum_{\boldsymbol{r}=\boldsymbol{0}}^{\boldsymbol{R}} \left(h_{th}^2(r) - h_{ex}^2(r)\right); \quad \boldsymbol{w} \coloneqq c_t, l_i, \theta \tag{3}$$

4. Results and discussion

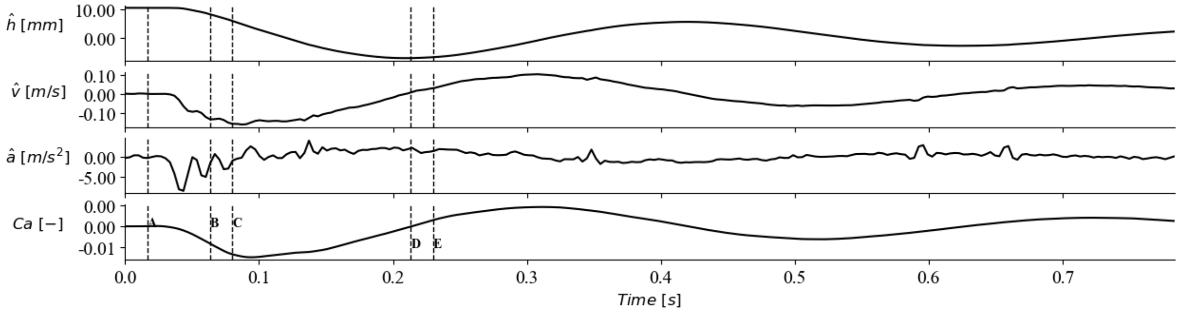

Figure 3.From the top to the bottom: time evolution in the first 0.8 seconds of the experiments for (1) the liquid mean interface $\hat{h}$, themean interface velocity $\hat{v}$ (2) and acceleration $\hat{a}$ (3), both computed via smoothed differentiation, and (4) Capillary number computed with the contact line velocity.

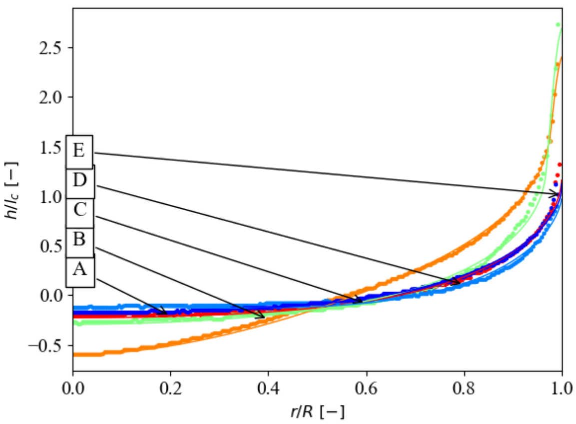

Figure 4. Half meniscus detected interface points (circles) and regression of interface shape (solid line).

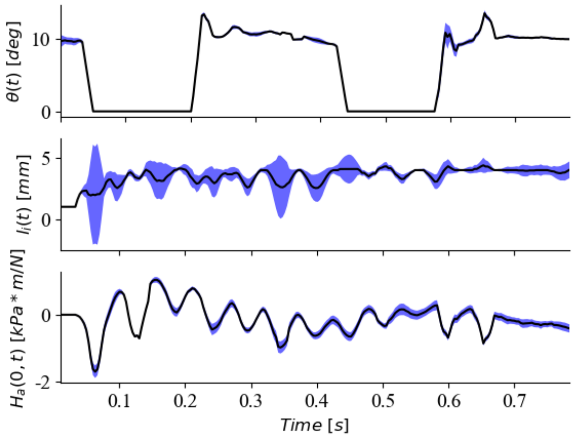

Figure 5. From the top to the bottom the results of the regression of the interface model: (1) Dynamic contact angle, (2) characteristic length l_i and (3) H_a amplitude factor. The uncertainties on the regression of the coefficients are shown.

Figure 3 shows the time evolution of interface position, velocity, acceleration, and Capillary number on the side B of the tube. The mean interface displacement behaves as a second-order system. The acceleration profile of the mean interface level oscillates, at a frequency of approximately 20 Hz, due to the elastic behaviour of the interface once released from its initial position. The Capillary number profile follows the behaviour of the interface profile. According to the literature (Delon et al., 2008; Eggers, 2005) the Capillary number is expected to exceed a critical value below which the contact line vanishes: in these conditions a thin liquid film is produced at the wall and it is not possible to define a (macroscopic) contact angle anymore (Eggers, 2005). Figure 4 shows the interface shape observed experimentally and reconstructed using eq. (1) for 5 configurations (A-B-C-D-E) extracted from Figure 3. Figure 5 shows the behaviour of the regression coefficients for the boundary value problem of the interface shape. The reconstructed contact angle (first plot of Figure 5) remains approximately constant for most of the experiment, except for the regions where the receding Capillary number surpasses the critical value. The formation of a thin film of approximately constant thickness in similar conditions has also been observed experimentally by Maleki et al., 2007, who considered it as the result of a sharp transition of the contact angle to zero.

The second and third plots of Figure 5 show that the correction for the inertia effects plays a fundamental role in the prediction of the interface shape with large acceleration. Inertia tends to increase or decrease the size of the meniscus because of the acceleration produced by the oscillations reported in Figure 3. This is visible in curves B and C of Figure 4. In a simplified quasi-static balance, which does not account for the contribution of inertia, the oscillations of the interface are necessarily explained by oscillations of the contact angle, which is the only parameter for the inverse problem. However, if the contribution of inertia is modelled through the additional term (H_a), the interface oscillations are allowed to be decoupled from the contact angle and the contact line dynamics in general. This model yields better predictions, suggesting that the interface oscillations are linked to the inertia of the channel flow underneath the interface. Accordingly, the inertial model correctly predicts a much smaller oscillation of the dynamic contact angle.

5. Conclusions

This work investigated, experimentally, the dynamics of a moving contact line within a quasi-capillary U-Tube. The focus was given to the shape of the gas-liquid interface and the dynamic of the contact angle as a function of contact line velocity and acceleration.The experimental set up allowed for visualizing the gas-liquid interface during its motion, while image processing techniques allowed for accurate interface detection. We solved the inverse problems of the regression of the measured interface with an analytical expression obtained from a force balance at the interface. This allows to obtain more accurate contact angle quantification respect to traditional tangent line methods, which tend to overestimate the value of the contact angle and are more subjected to the bias of the deformation of the interface due to inertial factors. Future work will explore new correlations to account for the prediction of the transition of the contact angle due to the critical capillary number and provide a more comprehensive description of the correlation derivation's sensitivity and uncertainty.

References

Bian, X., Schultz, W. W., & Perlin, M. (2003). Liquid slug motion and contact lines in an oscillatory capillary tube. *Journal of Fluid Dynamics (under Revision), Http://Wwwpersonal. Umich. Edu/Schultz/Manuscripts/ BianSchultzPerlin. Pdf*, *146*, 151.
Blake, T. D. (2006). The physics of moving wetting lines. *Journal of Colloid and Interface Science*. https://doi.org/10.1016/j.jcis.2006.03.051
Darzi, M., & Park, C. (2017). Optical distortion correction of a liquid-gas interface and contactangle in cylindrical tubes. *Physics of Fluids*, *29*(5). https://doi.org/10.1063/1.4982902
Delon, G., Fermigier, M., Snoeijer, J. H., & Andreotti, B. (2008). Relaxation of a dewetting contact line. Part 2. Experiments. Journal of Fluid Mechanics, 604, 55–75. https://doi.org/10.1017/S0022112008000979
Eggers, J. (2005). Existence of receding and advancing contact lines. Physics of Fluids, 17(8), 1–10. https://doi.org/10.1063/1.2009007
Maleki, M., Reyssat, E., Quéré, D., & Golestanian, R. (2007). On the Landau - Levich transition. Langmuir, 23(20), 10116–10122. https://doi.org/10.1021/la700822y
Quéré, D. (1997). Inertial capillarity. Europhysics Letters, 39(5), 533–538. https://doi.org/10.1209/epl i1997-00389-2 Shardt, O., Waghmare, P. R., Derksen, J. J., & Mitra, S. K. (2014). Inertial rise in short capillary tubes. RSC Advances, 4(28), 14781–14785. https://doi.org/10.1039/c4ra00580e
Ting, C.-L., & Perlin, M. (1995). Boundary conditions in the vicinity of the contact line at a vertically oscillating upright plate: an experimental investigation. Journal of Fluid Mechanics, 295, 263–300. https://doi.org/10.1017/ S0022112095001960
White, N. C., & Troian, S. M. (2018). Why Capillary Flows in Slender Triangular Grooves Are So Stable Against Disturbances. ArXiv, 1–18.
Willmott, G. R., Briole, A., & Szczepaniak, F. (2020). Inertial capillary uptake of drops. Physical Review E, 101(4), 43109.

Proceedings ECS 2021
Brussels, Belgium, September 7-9, 2021

Abstract T-45

TRANSIENT THREE-DIMENSIONAL FLOW FIELD MEASUREMENTS OF SHORT-SCALE MARANGONI INSTABILITIES IN DRYING POLY(VINYL ACETATE)-METHANOL THIN FILMS

M. Tönsmann[1,2], P. Scharfer[1,2], W. Schabel[1,2]

[1]Thin Film Technology (TFT),
[2]Material Research Center for Energy Systems (MZE),
Karlsruhe Institute of Technology (KIT), Karlsruhe, Germany

Email: wilhelm.schabel@kit.edu
***Keywords**: polymer film, drying, micro particle tracking velocimetry, Marangoni convection*

1. Introduction

Thin polymer films are an essential component of membranes, novel organic electronic devices and low-cost sensors. Inhomogeneous drying conditions may result in undesired Marangoni convection and a free-surface deformation deteriorating device performance. Since surface tension of multi-component solutions or suspensions depend on both temperature and composition (Tönsmann et al., 2021), control of local heat and mass transfer by means of tuning the material system or the experimental boundary conditions while drying should lead to a homogenous solute deposition.

2. Experimental procedure

In order to investigate the flow field within drying thin films, a new measurement technique (µPTV) has been developed in preliminary studies. It is based on tracking fluorescent particles in drying polymer solutions with an inverse microscope. A technique called "off-focus imaging" (Speidel et al., 2003) allows the tracking along the line-of-sight direction by tracking of diffraction rings of tracer particles, which are not in the focal plane. This enables us to measure three-dimensional flow fields in films while drying. (Cavadini et al., 2018; Tönsmann et al., 2019) Figure 1 (a) shows a schematic representation of the optical measurement setup and Figure 1 (b) shows exemplarily a camera frame of tracer particles and diffraction rings.

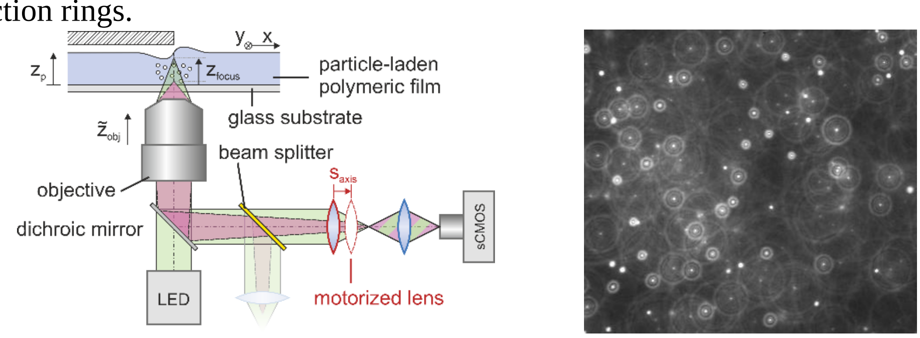

(a) (b)

Fig. 1. Micro Particle Tracking Velocimetry: (a) Schematic drawing of the optical measurement setup with a single camera. (b) Exemplary camera image showing tracer particles and diffraction rings.

Our measurement technique gives unique insights, which will allow us to identify process parameters crucial to the surface homogeneity of thin films and printed structures. The 3D µPTV results are combined with one-dimensional film drying simulations, which give additional access to transient local concentrations and temperatures in the drying films.

3. Results

New flow field results will be presented with a focus on transient stability thresholds in drying poly(vinyl acetate)-methanol films. It will be demonstrated that some films are convectively stable while others exhibit short-scale Marangoni instabilities in form of vertical convection cells. In addition, assessments are being made regarding the applicability of thermal and solutal Marangoni numbers as an indicator of the stability threshold.

Abstract T-45

Future investigations will focus on deliberate lateral drying inhomogeneities and the resulting Marangoni flows as well as complementary material systems.

References

Cavadini, P., Weinhold, H., Tönsmann, M., Chilingaryan, S., Kopmann, A., Lewkowicz, A., Miao, C., Scharfer,
P., & Schabel, W. (2018). Investigation of the flow structure in thin polymer films using 3D µPTV enhanced by GPU. *Experiments in Fluids*, 59(4), 370.
Speidel, M., Jonáš, A., & Florin, E.-L. (2003). Three-dimensional tracking of fluorescent nanoparticles with subnanometer precision by use of off-focus imaging. *Optics Letters*, 28(2), 69.
Tönsmann, M., Kröhl, F., Cavadini, P., Scharfer, P., & Schabel, W. (2019). Calibration Routine for Quantitative
Three-Dimensional Flow Field Measurements in Drying Polymer Solutions Subject to Marangoni Convection. *Colloids and Interfaces*, 3(1), 39.
Tönsmann, M., Scharfer, P., Schabel, W. (2021), *Surfaces and Interfaces*, Manuscript under Review.

Proceedings ECS 2021
Brussels, Belgium, September 7-9, 2021

Abstract T-84

CONTACT LINE DYNAMICS ON A SOLID SUBSTRATE BELOW MELTING TEMPERATURE OF LIQUID DROPLETS

R. Herbaut[1,2], P. Brunet[2], L. Royon[1], L. Limat[2]

1Université de Paris, CNRS, Laboratoire Interdisciplinaire des Énergie de Demain (LIED), UMR 8236, 10 rue Alice Domon et Léonie Duquet, 75013 Paris

[2]Université de Paris, CNRS, Laboratoire Matière et Systèmes Complexes (MSC), UMR 7057, 10 rue Alice Domon et Léonie Duquet, 75013 Paris

Email: laurent.limat@univ-paris-diderot.fr

***Keywords**: wetting dynamics, phase change, sliding drops, morphogenesis, non-linearities, solidification, finite contact angles.*

Contact line dynamics on solids under freezing conditions is of central importance for many applications such as 3D printing or control of freezing on aircraft wings. We have investigated the different dynamics assumed by contact lines for liquid drops maintained static on a moving solid silicium plate at several velocities, below melting temperature of the liquid (see fig. 1). These experiments has shown that solidification can induce liquid pinning near contact-line, which can lead to stick-slip dynamics of spreading[1]. We related the observations to an analytical model of contact line dynamics with solidification, that we have recently developed[2]. This model is able to explain a stick-slip behavior of contact line dynamics at low temperature and low velocities. To complete our first model, we have added a new thermodynamic approach which gives a prediction of solidification velocities who occurs on cold substrate, and shows a transition of dynamics phase change between low and high ΔT (difference between melting temperature and substrate temperature) observed experimentally[4,5]. Our approach puts forward this velocity transition by estimating the two kinds of phase change, nucleation and aggregation. A sketch of the situation modelled at contact line is suggested in Fig. 1. This quadruple contact line implies a solidification front in the mesoscopic region, which was first suggested by the Schiaffino and Sonin[6] model but facing some difficulty to adapt the divergence of heat flux at the corner, that we have approximated analytically.

The flow of the liquid phase in the solid corner is supposed to be viscosity-driven, following the Stokes law, while phase change develops and advances within the solid-liquid corner, following the Stefan law and matching the geometry conditions. The comparison between the angles predicted by model and the experiments [2,3] shows a good agreement. The prediction of critical arrest velocities can match even more quantitatively, when the cut-off length is assumed to depend on temperature, a framework which remains to be rigorously justified. Furthermore, the different experiments available have shown that the pinning of the contact line occurs with two distinct regimes of critical velocities[4,5].

Considering all these features, we have also suggested a thermodynamic approach based on aggregation and nucleation of solid[7,8]. First, we calculate the aggregation velocity for solidification V_{diff}, with liquid molecules close to the solid front that « jump » from one site to another by diffusion to a nearby site of solid molecules and aggregate at the liquid surface. Then, these molecules rearrange within the solid. The Turnbull approximation and the Stokes-Einstein equation provide a diffusive solidification velocity scaling as $\left(V_{diff} \propto \frac{\Delta T k_B T}{6\pi a^2 \mu}\right)$. We note that the linear dependance of velocity upon ΔT agrees with de Ruiter et al3. Next, the probability of a local spontaneous nucleation gives an estimation of nuclei rate that we associate with the most probable size of nuclei from the expression of the Gibbs energy, which allows us to have an estimation of explosive velocity solidification already observed by Koldeweij[5], given by

$$V_{nuclei} \propto A exp\left(\frac{-B}{\Delta T}\right)$$

In our model, we combine the two velocities ($V = V_{diff} + V_{nuclei}$) and compare the resultant one with different critical velocities measured by experiments[4].

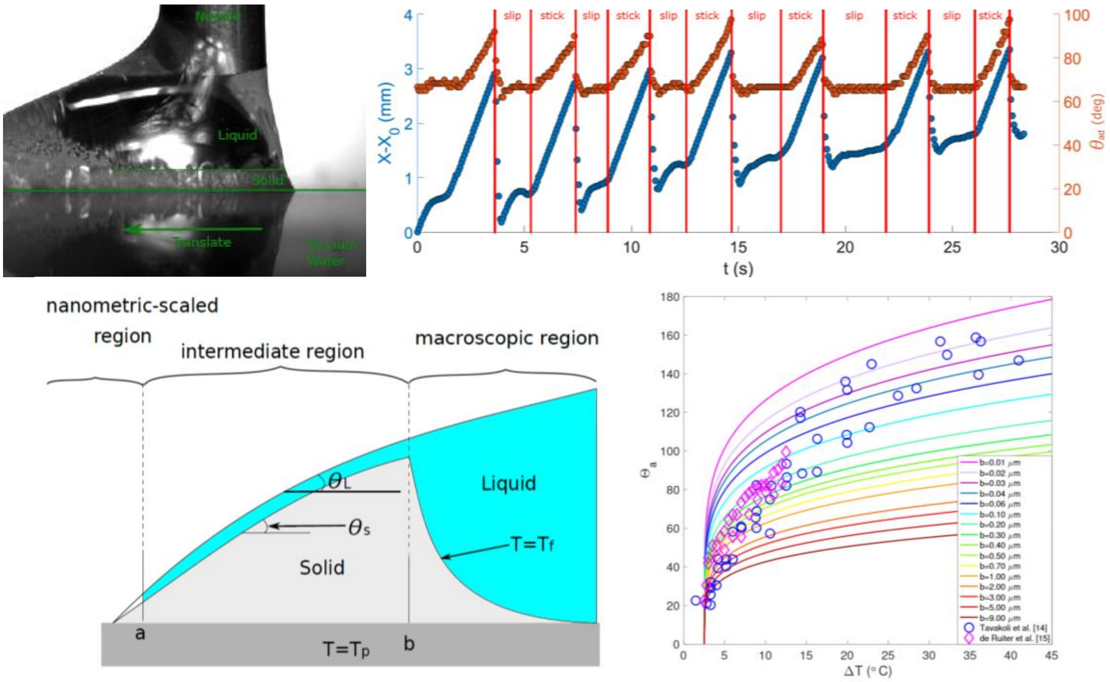

Figure 1. Top-left: in the experiment a moving plate is pushed at constant velocity below a static liquid drop. Top right: A typical record of the contact angle and contact line position evolutions, at low velocity, with stick-slip Bottom: a sketch of a quadruple contact line and a comparison between model an experimental data of arrest contact angle

As expected from our model, we observe a diffusive regime at low ΔT, and the liquid-solid interface progresses by aggregation of liquid molecules in the solid bulk. Conversely, the estimation of nucleation velocity gives good agreement for relatively high ΔT, which becomes dominant over diffusive-driven (aggregation) solidification, this situation corresponding to the second regime with an « explosive » nucleation of solid germs. As a perspective, we will compare the limit of our model with different experimental data from the literature. Furthermore, we will develop some technical approach to determine independently the surface tension between liquid and solid, which in our model remains an adjustable parameter.

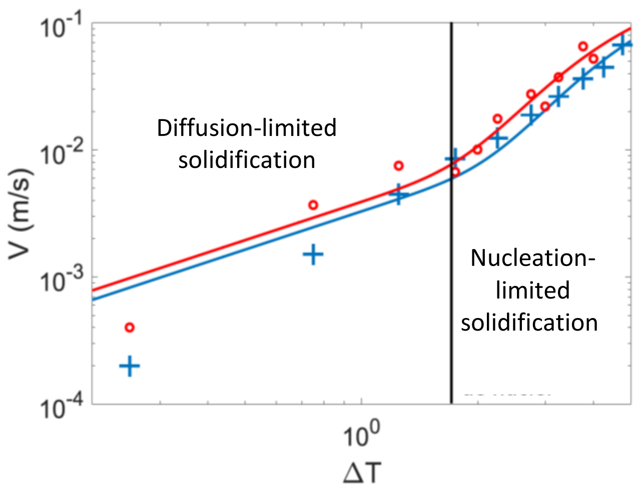

Figure 2. Comparaison between thermodynamical approach and experimental measurements (red : n-hexadecan ; blue : n-pentadecan)

Abstract T-01

References

1. Herbaut, R., Brunet, P., Limat, L., & Royon, L. (2019). *Physical Review Fluids*, *4*(3), 033603.
2. Herbaut, R., Dervaux, J., Brunet, P., Royon, L., & Limat, L. (2020). *The European Physical Journal Special Topics*, *229*(10), 1867-1880. .
3. De Ruiter, R., Colinet, P., Brunet, P., Snoeijer, J. H., & Gelderblom, H. (2017). 043602. .
4. Tavakoli, F., Davis, S. H., & Kavehpour, H. P. (2015). *Journal of Coatings Technology and Research*, *12*(5), 869-875.
5. Koldeweij, R. B., Kant, P., Harth, K., de Ruiter, R., Gelderblom, H., Snoeijer, J. H., ... & van Limbeek, M. A. (2020). I *arXiv preprint arXiv:2005.12189*.
6. Schiaffino, S., & Sonin, A. A. (1997). *Physics of fluids*, *9*(8), 2227-2233.
7. Turnbull, D. (1952). *The Journal of chemical physics*, *20*(3), 411-424.
8. Turnbull, D. *The Journal of Chemical Physics* 18.5 (1950): 768-769.

POSTER SESSION

Proceedings ECS 2021
Brussels, Belgium, September 7-9, 2021

Abstract T-83

HYDRODYNAMICS OF AQUEOUS THIN FILMS OF SURFACTANTS WHILE DRYING

C. Robert,[1,2,3] ***L. Maillaud***[4], ***J. Teisseire***[4], ***F. Mondiot***[1], ***C. Monteux***[2] ***and A. Antkowiak***[3]

[1] Surface du Verre et Interfaces, UMR 125, CNRS/Saint-Gobain, Aubervilliers, France
[2] Sciences et Ingénierie de la Matière Molle, UMR 7615, CNRS/ESPCI, Paris, France
[3] Institut Jean Le Rond d'Alembert, UMR 7190, CNRS/Sorbonne Université, Paris, France [4] Groupe Revêtements Fonctionnels par voie Liquide, SGR Paris, Aubervilliers, France

Email: clement.robert2@saint-gobain.com

Keywords: *wet coating, surfactants, Marangoni flows, dewetting, instability*

Wet film deposition is a key process in glazing industry as it is a quick and efficient way to functionalise large surfaces. Achieving thin and homogeneous waterborne coatings on glazing is a major challenge. Although attractive, the development of such coatings is still limited by the apparition of defects in the liquid film during the drying step. Yet, in extended flat films Marangoni flows, induced by surface tension gradients, can result in defects (Kheshgi, 1991) or film dewetting (Karpitschka, 2017).

In this pitch and poster session, we tackle how the coupling of solvent evaporation and surfactant adsorption at the surface can induce Marangoni flows and hydrodynamic instabilities in drying flat films. The influence of the coating conditions (evaporation rate, initial thickness, viscosity) and the surfactant adsorption dynamics over the film stability are questioned.

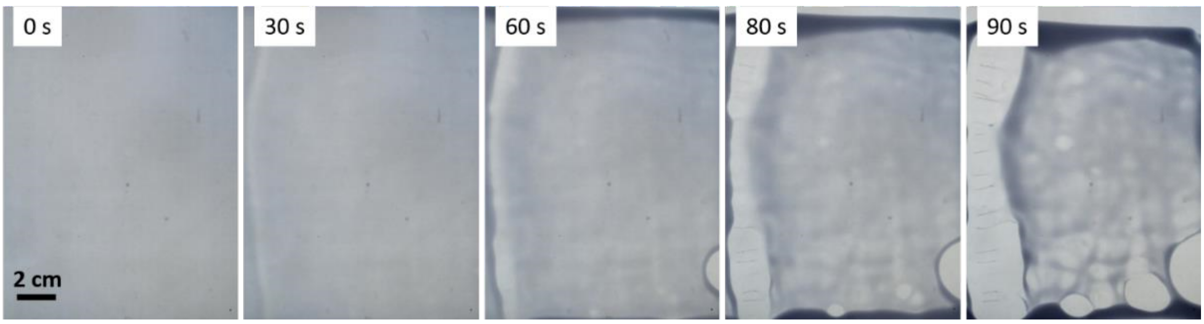

Figure 1. Snapshots of an aqueous film of SDS (82 mM) that is drying under a relative humidity of 30%. A die is added for observation. An instability develops in the centre of film with an emergent wavelength of the order of the centimetre.

Abstract T-83

Aqueous solutions of surfactants are blade coated on a horizontal glass plate under controlled atmosphere into thin films of thickness in the range [10 μm, 100 μm]. As shown in Figure 1, under strong evaporation rate, a thin film of an aqueous solution of SDS is strongly unstable. A consistent mechanism relaying on an evaporation-induced Marangoni instability is suggested.

For a broader comprehension, this phenomenon is rationalised through a lubrication model and with numerical simulations using the Navier-Stokes solver Basilisk (basilisk.fr) with a multilayer description (Popinet, 2020). Toward this goal, surface tension effects (Laplace pressure and Marangoni flows) were implemented for the multilayer solver and are very promising for numerical simulations of liquid films.

References

Karpitschka, S., Liebig, F., & Riegler, H. (2017) . Marangoni contraction of evaporating sessile droplets of binary mixtures. Langmuir, 33(19) , 4682-4687.
Kheshgi, H. S., & Scriven, L. E. (1991) . Dewetting: Nucleation and growth of dry regions. Chemical engineering science, 46(2) , 519-526.
Popinet, S. (2020) . A vertically-Lagrangian, non-hydrostatic, multilayer model for multiscale free-surface flows. Journal of Computational Physics, 418, 109609.

Proceedings ECS 2021
Brussels, Belgium, September 7-9, 2021

Abstract T-38

INVESTIGATION OF DRYING OF HIGHLY-CONCENTRATED PARTICULATE GRANULAR SYSTEMS FOR BATTERY APPLICATIONS

***K. Ly*[1,2], *E. Wiegmann*[3], *A. Kwade*[3], *P. Scharfer*[1,2], *W. Schabel*[1,2]**

[1]Thin Film Technology (TFT), Karlsruhe Institute of Technology (KIT), 76131 Karlsruhe, Germany

[2]Material Research Center for Energy Systems (MZE), Karlsruhe Institute of Technology (KIT), 76131 Karlsruhe, Germany

[3]Institute for Particle Technology (iPAT), TU Braunschweig (TU-BS), 38104 Braunschweig, Germany

Email: kevin.ly@kit.edu

Abstract

Lithium-ion batteries have become an indispensable part of modern life. Due to their high energy and power density, lithium-ion batteries are expected to be used primarily in the field of electromobility in the future. The desire for higher performance, cost efficiency and safety poses various challenges for the automotive industry and battery research. The drying process of battery electrodes has an enormous influence on the electrode quality. It determines electrode characteristics and most importantly cell performance. The major problem during drying is the migration of binder to the electrode surface, resulting in an inhomogeneous binder-distribution throughout the film.

As for state of the art electrodes, drying is one of the most cost-intensive process steps, a new approach for reducing the solvent content in electrode-processing and therefore increasing the cost-efficiency for the battery manufacturing process will be investigated in this work. By reduction of sol-vent content and the usage of granulates in battery-paste manufacturing, the storage stability of the produced electrode pastes is several weeks. This leads to a decoupling of paste and electrode production and a significant increase in production flexibility. In terms of the drying step it is essential to investigate the influence of the highly-concentrated particulate granular system on the drying process. Especially the influence on pore structure, film consolidation and binder migration is crucial for understanding the drying process. For this purpose, a series of fundamental studies will be conducted. This work presents the experimental methods for the investigation of the drying behaviour under defined process conditions. These are mainly gravimetric drying tests and investigations by means of cryo-SEM for the elucidation of the pore emptying mechanism, as well as investigations with a magnetic suspension balance for the disclosure of the sorption behaviour. This work contributes to the research performed at CELEST (Center for Electrochemical Energy Storage Ulm Karlsruhe) and Material Research Center for Energy Systems (MZE). The authors would like to acknowledge financial support of the Federal ministry of Education and Research (BMBF) via the InZePro cluster-project “GranuProd” (Grant number: 03XP0344C). In addition, the authors would like to thank ARLANXEO Deutschland GmbH for providing the binder used in this project.

***Keywords**: drying, granulate system, lithium-ion battery*

Abstract T-43

RECENT ADVANCES IN DRYING CONCEPTS FOR FORMAT AND MATERIAL FLEXIBLE BATTERY ELECTRODES

J. Mohacsi[1,2], A. Altvater[1,2], P. Scharfer[1,2], W. Schabel[1,2]

[1]Thin Film Technology (TFT)
Karlsruher Institut für Technologie, Kaiserstraße 12, 76131 Karlsruhe, Germany
[2]Material Research Center for Energy Systems (MZE)
Karlsruhe Institute of Technology, Strasse am Forum 7, Bldg. 30.48, 76131 Karlsruhe, Germany

Email: jonas.mohacsi@kit.edu

Abstract
The increasing demand for energy storage may position battery cells as one of the main players in the process of the energy transition concerning aspects like e-mobility. Current production systems for battery cells produce standardized high quality cells, but are not specifically adaptable to customer requirements. Therefore, an aim is the flexibility of the manufacturing process in terms of format, material and quantity. A crucial step in the production process of battery cells is the drying of the battery electrodes. In order to achieve the desired properties such as thermal conductivity or ionic conductivity in the complex porous structure of the active material layer, a controlled and homogeneous drying process of the electrodes is essential. Moreover, aspects of energy efficiency play an increasingly important role in battery production and thus also in the drying process.

Consequently, the subject of the research project is the development and optimization of new drying concepts, in particular for format and material flexible battery electrodes. A main aspect is the research of suitable drying nozzle concepts. Applying CFD-simulations and conducting experiments using thermochromic liquid crystals (TLC), nozzles are developed and optimized. Furthermore, measures for additional heat sources in the drying process are examined, e.g. using infrared radiators or surface lasers. These applications allow highly targeted energy input in specific phases during the process, which leads to an increase of energy efficiency and a reduction in process time compared to conventional methods without affecting the electrode properties. The investigations will supply knowledge for the development of an optimized laboratory dryer which reproduces the conditions of industrial battery production and represents a benchmark solution for high-efficiency electrode drying.
This work contributes to the research performed at CELEST (Center for Electrochemical Energy Storage Ulm Karlsruhe) and Material Research Center for Energy Systems (MZE). The authors would like to acknowledge financial support of the Ministry of Science, Research and Arts Baden-Württemberg (MWK-BW) and the Federal Ministry of Education and Research (BMBF) under project ID 03XP0369A (AgiloBat2).

***Keywords**: lithium-ion battery, drying, electrodes, flexible, agile*

Proceedings ECS 2021
Brussels, Belgium, September 7-9, 2021

Abstract T-41

FILM PROCESSING OF BATTERY ELECTRODES FOR SODIUM-ION BATTERIES ALONG THE PROCESS CHAIN IN RELATION TO PARTICLE PROPERTIES

J. Klemens[1,2], P.Scharfer[1,2], W. Schabel[1,2]

[1]Thin Film Technology (TFT), Karlsruhe Institute of Technology (KIT), Karlsruhe
[2]Material Research Center for Energy Systems (MZE), Karlsruhe Institute of Technology (KIT), Karlsruhe

Email: julian.klemens@kit.edu

Abstract
Electrochemical storage is a key technology of the current century. In the future, electricity storage systems will become more important components of energy systems, especially for the upcoming electric mobility and for everyday use. Lithium-ion batteries (LIB) are currently the most important electrochemical energy storage devices. The largely mature technology is characterized by high gravimetric and volumetric energy densities.

Keywords*: coating, drying, microstructure formation*

1. Introduction
Sodium-ion-batteries (SIB, see Fig. 1) have the potential to replace lithium-ion-batteries in some areas and to open up new fields of application.

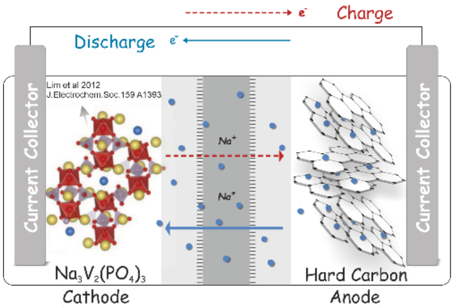

Figure 1. Schematic setup of a sodium-ion battery with sodium-vanadium-phosphate (cathode) and hard carbon (anode) as host materials for sodium ions Na+.

SIB could be one of the sustainable and environmentally friendly but also powerful and reliable storage systems, especially for medium and large energy storage systems. Furthermore, the advantages such as the availability of resources and the cost per watt-hour (Wh) make SIB attractive. The technology is already being investigated on a pilot scale (Klemens, 2020), but is not yet industrially manufactured. As with LIB, energy storage is based on the principle of de- and intercalation of ions in host lattices. Due to the larger ion diameter of sodium ions compared to lithium ions, graphite is not suitable as anode material. Currently, the most promising anode material for SIB is hard carbon. Hard carbon is a carbon-based material that does not transform into graphitic structures even at very high temperatures (above 3000 °C) and can be produced by pyrolysis from organic compounds or from natural and synthetic precursors. In terms of manufactured electrodes, the specific capacity depends on the particle properties, electrode processing and the resulting optimum component distribution. In addition to the influence of particle properties on processing, these correlations will be linked to electrochemical properties at the cell level. In this work, the influence of properties on the coating and drying behavior and the developing microstructure of hard carbon as anode for sodium-ion-batteries is investigated. The focus is on developing a systematic relationship between parameters of the electrode microstructure (such as porosity or pore radius distribution) as a function of different particle morphologies and drying conditions.

References
Klemens, J., Scharfer, P., Schabel, W., Hofmann, J., Wurba, A.K., Bold, B., Maliha, S., Schollenmeyer, P., Fleischer, J. (2020). Congress of the German Academic Association for Production Technology, 171-181

Proceedings ECS 2021
Brussels, Belgium, September 7-9, 2021

Abstract T-76

A WORKFLOW FOR DESIGNING CONTOURED AXISYMMETRIC NOZZLES FOR EFFECTIVE COLD SPRAY COATINGS

***F.L. Zavalan*, A. Rona**

School of Engineering, University of Leicester
University Road, Leicester, LE1 7RH, United Kingdom
Email: flz1@leicester.ac.uk

Abstract
This study aims to improve on the metal particle delivery of current commercial cold spray nozzles by performing a multi-objective optimization of the nozzle inner wall profile. This is done using two aerospace design codes based on the Method of Characteristics. A radiused throat combined to an S-shaped divergent improves the impact pattern and velocity of the particles. This design approach can be built up in complexity to further improve the deposition performance of cold spray nozzles.

Keywords: *cold spraying, nozzle design, process optimization, computational fluid dynamics (CFD)*

1. Introduction

Cold spraying is increasingly attractive as a material coating technique as it retains the original properties of the feedstock and it can produce oxide-free deposits. This technique consists in accelerating powder particles to a high velocity by a high-speed flow and spraying them onto a substrate, where they plastically deform at impact and form a coating (Alkimov et al., 1990; Papyrin et al., 2007; Yin et al., 2016). Whereas many cold spray facilities use conical convergent-divergent nozzles for accelerating the particles, it is of interest to consider a workflow to design contoured axisymmetric nozzles that enhance the radial uniformity of the velocity in the carrier phase. In this study, the performance of a conventional conical cold spray nozzle is compared with that of a new axisymmetric nozzle designed with a smooth throat and contoured for a parallel outflow. The new nozzle profile is obtained by a multi-objective optimization using two aerospace design codes based on the Method of Characteristics (MOC). A three-dimensional Computational Fluid Dynamics (CFD) model is developed to provide a preliminary assessment of the flow and particle behaviour in a lightly laden jet, in which well-dispersed titanium particles are accelerated by a compressible gas.

2. Numerical methodology

In order to improve the acceleration of the particles through the conduit, a bell-shaped nozzle is proposed, to replace the conical convergent-divergent shape of the cold spray nozzles in current use by industry. The design of the new nozzle is obtained by using the code developed by Alcenius and Schneider (1994) in conjunction with the CONTUR code (Sivells, 1978). The new nozzle is designed by varying the nozzle inlet convergent angle, the throat radius of curvature, and the peak slope in the divergent part. A heuristic optimization is performed by varying systematically these three parameters, in a sequence of about 20 numerical experiments. The inlet diameter, throat diameter and overall length are kept the same as those of the nozzle it is based on, so it can replace it on the cold spray commercial system.

The baseline numerical set-up consists of a conical convergent-divergent nozzle, namely, the Out4 nozzle manufactured for the Impact Innovations 5/11 cold spray system from Impact Innovations GmbH. The performance of the baseline nozzle is tested numerically by CFD. The CFD domain has a diameter of 600 mm and a length of 671 mm. The nozzle is supplied with compressed nitrogen at 5 MPa and 1373.15 K. The substrate is placed at an axial distance of 35 mm from the nozzle exit plane. The axial particle feeder has a diameter of 4 mm and it is located at the nozzle inlet. Titanium particles are injected at a constant rate of 3 g/s with an initial particle velocity of 10 m/s and an initial temperature of 298.15 K. Particles are assumed spherical and are injected in the converged flow solution by using a Rosin-Rammler particle size distribution.

This model uses the two-way coupling approach in ANSYS FLUENT® v19.5. The steady gas expansion is computed by a Reynolds-Averaged Navier-Stokes (RANS) Shear Stress Transport k-ω model (Eulerian reference frame), and the particle motion is determined by the Discrete Phase Model (Lagrangian reference frame). More information about the numerical model used in this study can be found in (Zavalan and Rona, 2021). To compare the performance of different engineering design solutions, it is often useful to translate the desirable outcomes into numerical values that can be prioritized by weight-averaging them. In this work, the authors have elected to define the penalty function Φ that the better design minimizes. This penalty function is defined as $\Phi = a(1\text{-}Z1) + aZ2 + 2aZ3$, where $a = 0.25$ is an adjustable coefficient that reflects the design intent. The first parameter, $Z1$, represents the ratio of the mass-weighted particle speed evaluated just off the substrate to the maximum gas velocity. The second one, $Z2$, is the mass-weighted standard deviation of the particle speed normalized by the mass-weighted mean particle speed, and the third parameter, $Z3$, represents the coefficient of variation (COV), which is a point-to-point measure of the uniformity in the spread of the particles over the substrate face (Gunzburger and Burkardt, 2004).

3. Results and discussion

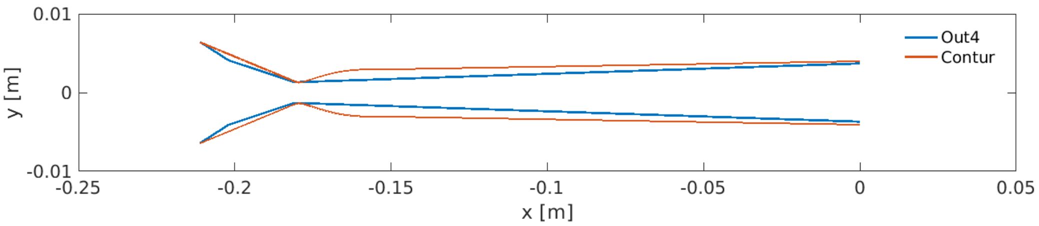

Figure 1. Nozzle geometries.

The lowest value of the function Φ is obtained for a nozzle with a divergent part 1.6 mm shorter than the baseline nozzle and an exit diameter of 8 mm. A nozzle inlet convergent angle of 12°, a throat curvature radius to throat radius ratio of 6 and an inflection angle of 7° characterize the redesigned nozzle. The efficiency of the best performing cold spray nozzle shape within the parameter space investigated is compared with that of the commercial conical convergent-divergent nozzle. In Figure 1, the profiles of the internal wall of the conical convergent-divergent nozzle, by the blue line, and of the redesigned nozzle, by the red line, can be observed. The baseline geometry is hereafter referred to as the Out4 nozzle and the redesign output as the Contur nozzle.

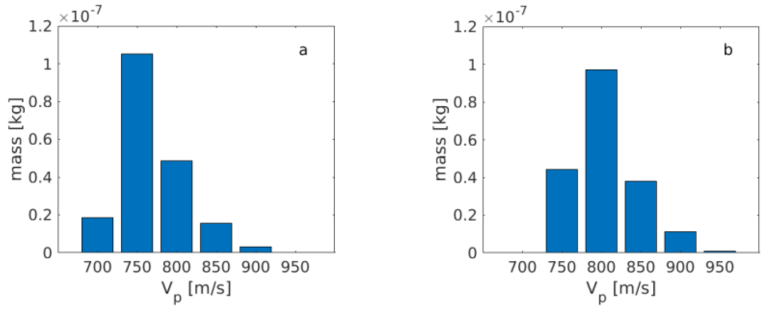

Figure 2. Mass-weighted velocity distribution of titanium particles on impact with the substrate located at 35 mm from the nozzle exit (a) Out4 nozzle and (b) Contur nozzle.

Figure 2 presents the mass-weighted velocity distribution of titanium particles at 35 mm from the nozzle exit plane. It can be observed that, by redesigning the nozzle, the particle speed distribution has changed, the titanium particles reaching a higher speed under the same conditions. The mean predicted particle speed is 743.36 m/s with the Out4 nozzle, while it is 36.49 m/s higher with the Contur nozzle. This indicates a two-fold advantage delivered by the redesign. On one hand, since the peak particle velocity is directly related to the particle kinetic energy, there is potential for a more energetic plastic deformation upon impact, which may improve the metal deposition characteristics. Additionally, the removal of lower velocity particles may reduce waste of powder feed, since lower velocity particles either rebound or poorly attach to the substrate.

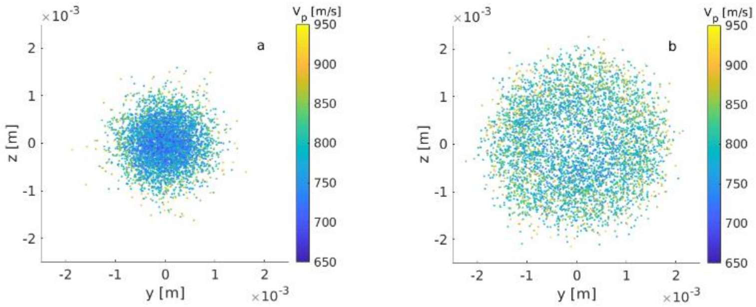

Figure 3. Radial spread of the titanium particles on impact with the substrate located at 35 mm from the nozzle exit. (a) Out4 nozzle and (b) Contur nozzle.

In Figure 3, it can be seen that the radial distribution of the particles is also affected by the redesign, by which the particles are visibly spread out more by the Contur nozzle. The baseline Out4 nozzle is predicted to direct most of the particles radially close to the nozzle axis. This is likely to cluster the particles so that some of them will strike the substrate in the same place. Over time, this particle overlap will increase the angle of the deposited material, thereby creating deposits with a conical profile, rather than an even layer, the latter being more desirable in a metal spray deposition process. Therefore, the redesigned nozzle produces a more spread out and even particle impact pattern.

The performance of the Out4 and of the Contur nozzles based on the penalty function parameters is also analyzed. On all three counts, the Contur nozzle outperforms the baseline nozzle. The Z_1 is 7.21% higher than that of the Out4 nozzle and the Z_2 is 5.51% lower. The most significant difference between the two nozzles is in terms of Z_3, this being 24.34% lower than that of the Out4 nozzle. Therefore, by redesigning the nozzle, its performance is improved by 19.96%, based on the change in Φ.

4. Conclusions

The new nozzle shape delivers a 4.91% higher mean particle velocity at the same operating conditions used by the industry standard nozzle. A 24.34% more radially uniform particle deposition profile is obtained, based on the coefficient of variation Z_3. These improvements are conducive to forming a more homogeneous metal coating. This nozzle design approach has excellent exploitation potential in cold
spray coating technology as well as in additive manufacturing, to form better bonded deposits.

Acknowledgements: The PhD research of Florentina-Luiza Zavalan is funded by EPSRC (EPSRC CDT Grant number EP/L016206/1) in Innovative Metal Processing. This research used the ALICE High Performance Computing Facility at the University of Leicester.

References

Alcenius, T.J. and Schneider, S.P. (1994). Status Report for NASA Langley Grant NAG-1-1133: Development of a Code for Wall Contour Design in the Transonic Region of Axisymmetric and Square Nozzles, *NASA-CR-194857*. Alkimov, A.P. et al. (1990). A Method of Cold Gas-Dynamic Deposition. *Sov. Phys. Dokl.*, 35(12), 1047-1049. Gunzburger, M. and Burkardt, J. (2004). Uniformity measures for point samples in hypercubes.
Papyrin, A. et al. (2007). *Cold Spray Technology*. Elsevier Science.
Sivells, J.C. (1978). A computer program for the aerodynamic design of axisymmetric and planar nozzles for supersonic and hypersonic wind tunnels. *ARO Inc.*, ADEC-TR-78-63.
Yin, S. et al. (2016). Gas Flow, Particle Acceleration, and Heat Transfer in Cold Spray: A review. *J. Therm. Spray Technol.*, 25, 874-896.
Zavalan, F.L. and Rona, A. (2021). Parametric Redesign of a Convergent-Divergent Cold Spray Nozzle. *Thermal Spray 2021: Proceedings from the International Thermal Spray Conference*, 221-228.

Proceedings ECS
2021
Brussels, Belgium, September 7-9, 2021

Abstract P-79

DYNAMICS OF A QUASI-CAPILLARY CHANNEL FLOW IN ACCELERATING CONDITIONS

***M. Ratz*[1], *D. Fiorini*[2], *A. Simonini*[2], *C. Cierpka*[1], *M.A. Mendez*[2]**

[1]Institute of Thermodynamics and Fluid Mechanics, Technische Universität Ilmenau, Germany
[2]EA Department, von Karman Institute for Fluid Dynamics, Sint-Genesius-Rode, Belgium

Abstract
We investigate the behaviour of accelerating contact lines inside a quasi-capillary channel. Both advancing and receding contact lines are investigated. The meniscus is observed using Level Detection and Recording (LeDaR) and Time-Resolved Particle Image Velocimetry (TR-PIV) to quantify the shape of the meniscus and the flow field beneath it. The experimental data is used to investigate whether the classic models of capillary flows are sufficient in describing a dynamic meniscus and especially the dynamic contact angle in the presence of strong acceleration. The experimental results show important phenomena inside the channel such as two large counter-rotating vortices and properties of a pulsatile flow which are not considered in the usual derivations of capillary flows.

Keywords: *Dynamic contact angle, Time-Resolved PIV, Capillary*

1. Introduction

The dynamics of a gas-liquid interface moving along a wall play an important role in many wetting and dewetting processes such as inkjet printing or slot die coating. The modelling of these processes heavily depends on the balance of forces which act on the interface. Among these, the capillary force depends on the curvature of the interface which is linked to the angle of the interface with the wall, called the contact angle.

When modelling these flows, there is a fundamental problem when calculating the contact angle. It cannot be calculated by means of the Navier-Stokes equation; it is needed as a boundary condition during its solution. Thus, the contact angle is usually predicted through a model (Hoffmann, 1975) which is often based on the capillary number Ca. However, these correlations are only valid in quasi-static conditions, meaning an acceleration close to zero. These correlations are verified using a model of a capillary flow. Many of such models exist (Washburn, 1921; Levine et al., 1976), however, they often use simplified approaches such as a circular interface shape or a parabolic velocity profile.

This work aims to investigate dynamic contact lines in the presence of strong acceleration. This is done by means of an experimental setup consisting of a quasi-capillary channel. The interface is observed using Level Detection and Recording (LeDaR) and Time-Resolved PIV (TR-PIV) to investigate the dynamic meniscus as well as the flow field beneath it. The experimental data is used to examine whether the classic models of capillary flows are also valid in dynamic conditions.

2. Experimental Setup

A sketch of the experimental setup is shown on the left in Figure 1. This consists of a rectangular channel with a width δ of 5 mm and a depth L of 250 mm. The channel has a height h of 150 mm and is open to the surrounding air. Water is used as the operating fluid. An advancing contact line is achieved by inducing a pressure step inside the facility by means of an external tank which releases pressurized air into the reservoir. After the initial rise, the interface oscillates for 3 seconds and then comes to rest. A receding configuration is achieved by opening the release valve to the surrounding air. The right side of Figure 1 shows the experimental setup for TR-PIV measurements.

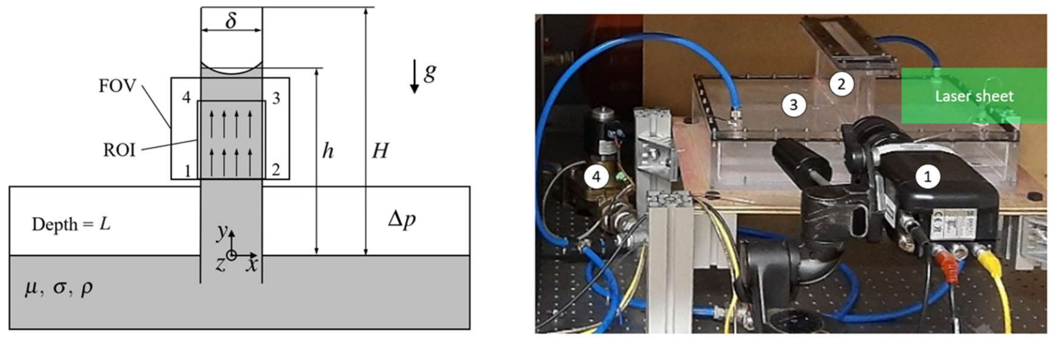

Figure 1: Left: Sketch of the 2D-Channel with the associated variables. Right: Experimental setup for the TR-PIV measurements with the camera (1), the channel (2), the reservoir (3) and the release valve (4).

Initial tank pressures Δp in the range from 1000 to 1500 Pa are used for the advancing configuration. The receding contact line is observed with different release speeds of the pressure. This allows to investigate the effect of different dynamic conditions on the shape of the flow field and the meniscus. The interface shape is observed by means of the LeDaR technique. Images are recorded at a frequency of 500 Hz. The TR-PIV measurements are carried out with an acquisition frequency of 1200 Hz. The achieved scaling factors are 51 px/mm for the LeDaR measurements and 60 px/mm for the TR-PIV measurements.

3. Data Processing

The LeDaR images are processed with a gradient-based filter to detect the position of the meniscus in each image. Two methods are used to interpolate the interface shape at the wall. The first one is the fitting of a hyperbolic cosine and the second one a Gaussian Process Regression. The obtained shapes are used to calculate dynamic parameters such as the contact angle or the mean and contact line velocity.

The PIV images are processed with a standard adaptive multigrid interrogation scheme. An adaptive Region of Interest (ROI) is used to capture the flow field beneath the meniscus at each time step. The resulting flow field is smoothed and interpolated with a regression based on Proper Orthogonal Decomposition and Radial Basis Functions (Raben et al., 2012). This approach allows an analytical calculation of velocity gradients. Vortices in the flow are estimated by means of the Q-field (Hunt et al. 1988).

4. Results and Discussion

A snapshot of the gas-liquid interface is shown on the left side in Figure 2. It shows the detected interface points in green, the Gaussian Process Regression in red and the fit of the hyperbolic cosine in yellow. The snapshot is taken during the first descent of the interface after the initial rise. The initial pressure is $\Delta p = 1500$ Pa. In this case, the two methods to calculate the interface show a good agreement, the yellow and red curve are almost identical.

The right side of Figure 2 shows the contact angle over the capillary number; the reference velocity is the one from the contact line. These are calculated from Gaussian Process Regression. The resulting orbit is very complex and yields different contact angles for one capillary number and vice-versa. This clearly shows that the contact angle cannot be interpreted as a function of just the capillary number as it is usually done in quasi-static conditions. In the presence of strong acceleration, the contact angle must depend on more dynamic properties. The full version of this article presents a more detailed analysis of the two different methods for the interface fit during the entire oscillation. A contact angle correlation based on an additional acceleration term is proposed.

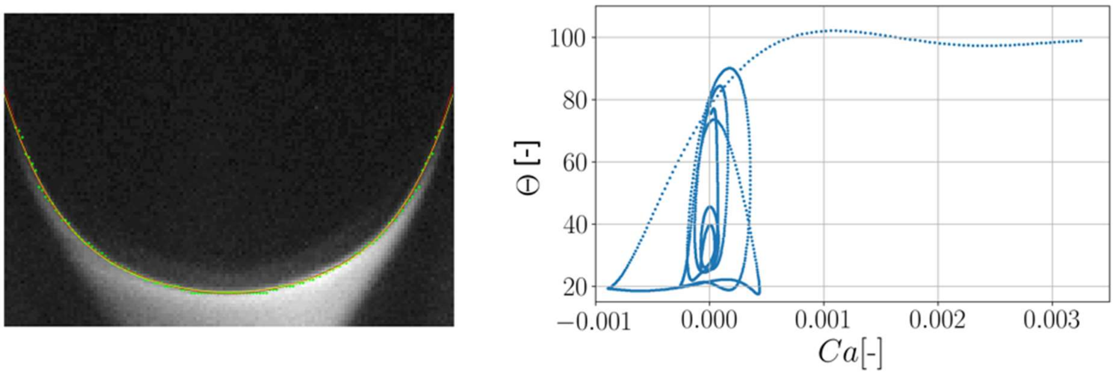

Figure 2: Left: Raw LeDaR Image during the oscillation. Green points are the detected interface, Red curve the Gaussian Process Regression and the yellow curve the hyperbolic cosine fit. Right: Contact angle over the Capillary number during an experiment with an oscillating interface. The capillary number is calculated with the contact line velocity.

Figure 3 shows the velocity field on top of the Q-field beneath the meniscus, on the left for an advancing contact line and on the right for a receding one. The velocity field is high pass filtered with a Gaussian Blur of $\sigma = 15$ and a truncation after 2.5 standard deviations. Both cases have similar dynamic parameters, the acceleration is $|a| \approx 1000$ mm/s and the mean velocity $|v| \approx 280$ mm/s, 120 mm/s for the advancing and receding case respectively. Both cases show two counter-rotating vortices which are very asimilar. These have different properties, such as their extend in the channel, the strength of the vortex and their position inside the channel. This suggests a strong dependence of the velocity field on the shape of the meniscus as the large difference in the flow field cannot be explained with just the different mean velocities.

These large differences are further investigated in the full version of this article. Snapshots of the velocity fields are compared for different dynamic properties and the behaviour of the vortices during the oscillation of the meniscus analysed. Furthermore, the results of the TR-PIV measurement are linked back to the underlying model which does not consider these differences. Further problems are highlighted by looking at the horizontal velocity profile far from the interface which shows properties of a pulsatile flow.

5. Conclusion

We conducted experimental campaigns inside a narrow channel in which advancing and receding contact lines were investigated. The results show a big difference in the shape of the flow field for the two different configurations. These differences are present close to the meniscus as well as far from it. Furthermore, the classic models for capillary flows are shown to be insufficient in describing the dynamics of the interface when subjected to strong acceleration.

Abstract P-79

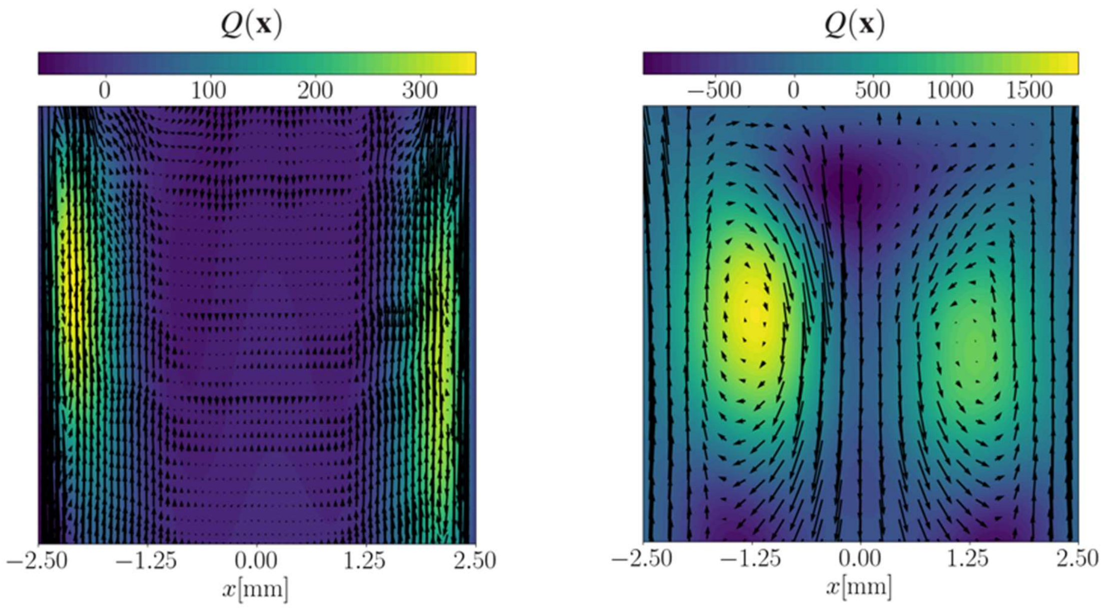

Figure 3: Left: High pass filtered velocity field on top of the Q-field for an advancing contact line. The mean velocity is |v| ≈ 280 mm/s and the acceleration |a| ≈ 1000 mm/s. Right: High pass filtered velocity field on top of the Q-field for a receding contact line. The mean velocity is |v| ≈ 120 mm/s and the acceleration |a| ≈ 1000 mm/s.

References

Hoffman RL (1975), A study of the advancing interface. i. interface shape in liquid—gas systems. *Journal of Colloid and Interface Science* 50:228 – 241

Hunt J, Wray A, and Moin P (1988), Eddies, streams, and convergence zones in turbulent flows. in Studying Turbulence Using Numerical Simulation Databases, *2. Proceedings of the 1988 Summer Program, Stanford, California, USA, June 27 - July 22*

Levine S, Reed P, Watson E, and Neale G (1976), A theory of the rate of rise of a liquid in a capillary. *Journal of Colloid and Interface Science*. pages 403–419. Academic Press

Raben SG, Charonko JJ, and Vlachos PP (2012), Adaptive gappy proper orthogonal decomposition for particle image velocimetry data reconstruction. Measurement Science and Technology 23:025303

Washburn EW (1921) The dynamics of capillary flow. *Physical Review* 17:273–283

Proceedings ECS 2021
Brussels, Belgium, September 7-9, 2021

Abstract T-60

MULTILAYER APPLICATION TO MINIMIZE GAS AND WATER PERMEATION FOR POLYMER ELECTROLYTE MEMBRANE WATER ELECTROLYSIS (PEM-WE)

Nadine Zimmerer[1,2]***, Philipp Quarz***[1,2]***, Angela Kruth***[3]***, Bernd Oberschachtsiek***[4]***, Philip Scharfer,***[1,2]***, Wilhelm Schabel***[1,2]

[1]Thin Film Technology (TFT), Karlsruhe Institute of Technology (KIT), 76131 Karlsruhe, Germany
[2]Material Research Center of Energy Systems (MZE), Karlsruhe Institute of Technology (KIT), 76131 Karlsruhe, Germany

[3]Leibnitz Institute of Plasma Science and Technology (INP), 17489 Greifswald, Germany
[4]The hydrogen and fuel cell center ZBT GmbH, 47057 Duisburg, Germany

Email: nadine.zimmerer@kit.edu

Abstract
In view of the desired energy transition and the increasing demand for energy storage systems with regard to renewable energies, electrolysers offer the possibility to store energy chemically in form of hydrogen. Hydrogen is an environmentally friendly energy carrier which can be stored and used with-out greenhouse gas or any harmful emissions and plays therefore an outstanding role for the industrial as well as for the mobility sector. Pressure electrolysers offer considerable efficiency advantages over atmospherically operated systems. A current challenge in the pressure electrolysis of water is the undesirable crossover of oxygen and hydrogen. The cross-over leads to a considerable loss of efficiency and poses safety risks. To minimize cross-over effects, a graphene barrier layer should be applied to the proton conducting membrane. Graphene qualifies as an ideal membrane component in PEM-water electrolysis (PEM-WE) due to its excellent proton conductivity and barrier properties towards ions and molecules. The out-standing mechanical stability of the ultra-thin barrier material increases moreover the possible work pressure and long-term stability of the proton conducting membrane. Based on these advantages of the graphene barrier layer, the development of a strategy for coating and drying of a multilayer, consisting of a graphene layer and a catalyst layer, onto the proton conducting membrane will play a crucial role for a cost-efficient production of PEM-WE. Therefore, different approaches will be investigated. First the multilayer is coated on a decal-film and laminated to the PEM membrane using a calendaring step, as it is the currently established process for proton conducting membrane-electrode assemblies (MEA). In order to increase the efficiency of the technology, the decal process is to be replaced by direct membrane coating. A key challenge of direct membrane coating is the interaction of the substrate with the solvent of the ink. In addition to the challenges of direct coating.

Keywords: *graphene barrier, PEM-electrolysis, fuel cells, multilayer coating*

Abstract T-74

OLIGOMERS OF BISPHENOL A DIGLYCIDYL ETHER IN EPOXY CAN COATINGS

***A. Lestido Cardama*[1], *R. Sendón*[1], *J. Bustos*[2], *M. I. Santillana*[2], *P. Paseiro Losada*[1], *A. Rodríguez Bernaldo de Quirós*[1]**

[1]Department of Analytical Chemistry, Nutrition and Food Science, Faculty of Pharmacy, University of Santiago de Compostela (Spain)

[2]National Food Center, Spanish Agency for Food Safety and Nutrition, Majadahonda, Madrid (Spain)
Email: antia.lestido@usc.es

Abstract
A variety of different materials are used for the coatings of food and beverage cans, but epoxy polymers are the types of coatings most widely used. Besides epoxy monomers, migrants from epoxy coatings may also contain BADGE adducts with chain stoppers or reaction products of either solvents or phenolic monomers, which can be formed during the curing process. These substances could be released and migrate into foods. The objective of this study is the identification of these potential unreacted substances/ oligomers that could migrate from epoxy coatings by liquid chromatography coupled to tandem mass spectrometer (LC-MS/MS). For this, the can was extracted with acetonitrile at room temperature for 24 hours. The mass spectrometer was operated in positive and negative atmospheric pressure chemical ionisation (APCI) mode. MS data were acquired in full scan mode up to 1000 m/z. Several chromatographic peaks with different m/z values were detected. These masses were compared with the available literature based on the possible starting substances. BADGE derivatives were identified: BADGE.H2O.BPA, cyclo-di-BADGE, BADGE(n=1)H2O.BPA, BADGE.BPA.BuOH or BADGE(n=1)BPA, among others. This research was funded by the Ministerio de Ciencia, Innovación y Universidades, Fondo Europeo de Desarrollo Regional (FEDER), and Agencia Estatal de Investigación Ref. No. PGC2018-094518-B-I00 “MIGRACOATING” (MINECO/FEDER, UE).

Keywords: *BADGE oligomers, can coating, LC-MS/MS*

CHARACTERIZATION OF POLYESTER COATINGS BY FTIR-ATR, CONFOCAL RAMAN MICROSCOPY AND MALDI-TOF MS

***A. Lestido Cardama*[1], *P. Vázquez Loureiro*[1], *R. Sendón*[1], *J. Bustos*[2], *P. Paseiro Losada*[1], *A. Rodríguez Bernaldo de Quirós*[1]**

[1]Department of Analytical Chemistry, Nutrition and Food Science, Faculty of Pharmacy, University of Santiago de Compostela (Spain)

[2]National Food Center, Spanish Agency for Food Safety and Nutrition, Majadahonda, Madrid (Spain)
Email: antia.lestido@usc.es

Abstract
Polymeric coatings are complex formulations that can contain different components such as cross-linking agents, resins, lubricants, solvents, etc. To evaluate the safety of the coatings it is necessary to identify the potential migrants. In the last years, polyester-based coatings are being used as an alternative to epoxy res-ins due to the uncertainties about its potential adverse effects. In this work, several analytical techniques were used in order to characterize the type of coating on the in-side of the cans. Firstly, infrared spectra were acquired using an ATR-FTIR spectrometer. The identification was performed by comparation with polymer spectrum libraries. The coatings analysed were identified as polyesters. Confocal Raman microscopy provided a three-dimensional characterization of the samples. In order to investigate the potential migrants, the samples were extracted with an organic solvent and ana-lysed by MALDI-TOF MS in positive mode. Data published in the scientific literature were used to create a homemade database of possible monomer combinations and tentatively identify some of them used in manufacturing. This research was funded by the Ministerio de Ciencia, Innovación y Universidades, Fondo Europeo de Desarrollo Regional (FEDER), and Agencia Estatal de Investigación Ref. No.PGC2018-094518-B-I00 “MIGRACOATING” (MINECO/FEDER, UE).

Keywords: *polyester coating, FTIR-ATR, MALDI-TOF MS*

Proceedings ECS
2021
Brussels, Belgium, September 7-9, 2021

Abstract T-34

A PREDICTIVE MODEL FOR SLOT-DIE COATING OF NANOCELLULOSE FILMS

P.A.Fuaad [1]***, Agne Swerin*** [2,3] ***Fredrik Lundell*** [3]***and Martti Toivakka*** [2]

[1]Åbo Akademi University, Turku, Finland
[2]Karlstad University, Karlstad, Sweden
[3]KTH Royal Institute of Technology, Stockholm, Sweden

Email: fpanikav@abo.fi presenting/corresponding author

Abstract

One of the current challenges using nanocellulose as a coating material in a slot-die, compared to petroleumbased alternatives, is precise control of the coating-mass applied on the substrate[1]. Nanocellulose suspensions exhibit a wide range of rheological behaviour depending on its level of fibrillation, particle interaction and consistency. In particular, the shear-thinning rheology is governed by the evolution of the underlying microstructure and depends strongly on concentration [2]. We present results of pipe-rheometry experiments of nanocellulose suspensions by varying the consistency. Using that, we develop a predictive Volume of Fluid (VoF)[3] CFD model incorporating two key properties that pose many practical challenges: yield stress and wall-slip. Particle depletion at the wall leads to a non-uniform distribution in the flow and influence the flow pattern and the final coat-weight. Yield stress brings about stagnation regions in the flow inducing undesired effects such as defects and heterogeneous deposition. Also, process windows highlighting the critical coating speeds without air-entrainment at the moving contact-line is constructed.

Keywords: *nanocellulose coating, slot-die, rheology*

References

Kutty, F P A., Koppolu, R., Swerin, A., Lundell, F., and Toivakka, M (2020). Tappi Journal, 19(11), 575–582.
Koponen, A I., (2020). Cellulose 27 1–19.
Hirt, C W. and Nichols, B. D.. (1981). Journal of computational physics, 39(1), 201–225

INKJET PRINTING LINES ONTO THIN, MOVING POROUS MEDIA - SIMULATIONS

Gianmarco Venditti, Vignesh Murali and Anton A. Darhuber

Department of Applied Physics
Eindhoven University of Technology, The Nederlands

Corresponding author: a.a.darhuber@tue.nl

***Keywords**: Inkjet printing, Richards equation, porous media, evaporation, evaporative cooling*

Inkjet printing consists of the ejection and deposition of ink droplets on substrates that are moving underneath the printhead [1]. For printing on paper, water-based inks have been developed that are beneficial from an environmental standpoint. The printing of semi-infinite or long lines on moving paper substrates lead to a steady-state distribution of moisture and heat which are a suitable way to study the interplay between heat and mass-transfer. Lateral wicking and evaporative mass loss are the dominant mass transfer mechanisms, while evaporative cooling reduces the temperature of paper by up to 6K. Moreover, sorptive heating [1] needs to be considered, which can cause temperature increases above ambient on the order of 1K at the perimeter of the wet zone.
We developed a mathematical model coupling the Richards equation for moisture transport in unsaturated porous media with evaporative mass loss and heat transfer. The model is two-dimensional and only considers in-plane moisture transport, i.e. the short transient effects of moisture penetration in the thickness direction of the paper sheet are disregarded. We systematically varied the speed of motion of the printhead relative to the substrate (UIJ) and the frequency of droplet deposition (f) to compare with the experimental data. Fig. 1 shows a schematic of our numerical domain which represents the top-view of a paper sheet moving at speed UIJ. The blue circle (not to scale) is the stationary source region of the moisture content, where the inkjet droplets are deposited. Fig.2(a) shows a typical two-dimensional moisture content profile and Fig. 2(b) the corresponding thermal profile.

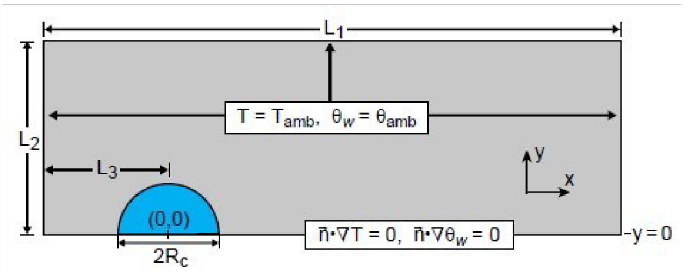

Fig.1: A sketch of the two-dimensional computational domain including the relevant boundary conditions.

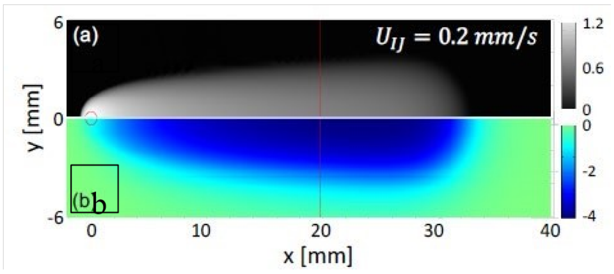

Fig.2: (a) Normalized moisture content for UIJ= 0.2 mm/s and t=150s after commencement of ink jetting. (b) The corresponding temperature profile (colorbar units K).

Abstract T-17

Our numerical model reproduces several key features of the experimental data. For example, the transverse widths of the moisture and temperature distributions, the maximum attained cooling amplitude and their scaling behavior as functions of U_{IJ} and f are well captured by our model.

References

[1] V. Murali, J. C. H. Zeegers, A. A. Darhuber, International Journal of Heat and Mass Transfer **147**, 118875 (2020).

FOOD CONTACT COATINGS: IDENTIFICATION BY FTIR AND ANALYSIS BY GC-MS

***P. Vázquez Loureiro*[1], *A. Lestido-Cardama*[1], *R. Sendón*[1], *J. Bustos*[2], *Mª.I. Santillana*[2], *P. Paseiro Losada*[1], *A. Rodriguez Bernaldo de Quirós*[1]**

[1]Department of Analytical Chemistry, Nutrition and Food Science, Faculty of Pharmacy, University of Santiago de Compostela
15782-Santiago de Compostela, Spain
[2]Food Center, Spanish Agency of Food Safety and Nutrition
E-28220 Majadahonda, Spain

Email: patriciavazquez.loureiro@usc.es

Abstract

Metal cans are internally coated with a polymeric coating to protect both, the food from the potential release from the material and the metal substrate from corrosion. The coating may contain different components including resins, cross-linking agents, additives and solvents. Fourier Transform Infrared (FTIR) analysis has shown to be a simple, fast and useful analytical tool for the identification of polymers. In this work, a FTIR spectrometer equipped with an ATR (attenuated total reflectance) accessory was used to identify two polymeric can coatings material samples. The identification was achieved based on the spectral comparison with KnowItAll® 17.4.135.B IR Spectral Libraries of Polymers & Related Compounds (Bio-Rad Laboratories, Inc.). The food contact surfaces of the samples analysed were identified as organosols and epoxy resins. In the second part of the work, the semi-volatile compounds present in the samples, were investigated. For that purpose, methanolic extracts were obtained and analysed by GC-MS (EI) in scan mode (35- 500 m/Z) using a Rxi-5SilMS (30 m x 0.25 mm, 0.25 μm) column as stationary phase and He as carrier gas. Several compounds were detected although no good library matches were observed in some cases.

Keywords: *epoxy resin, semivolatile compounds, FTIR*

Acknowledgements: This research was funded by the Ministerio de Ciencia, Innovación y Universidades, by Fondo Europeo de Desarrollo Regional (FEDER), and by Agencia Estatal de Investigación Ref. No. PGC2018-094518-B-I00 “MIGRACOATING” (MINECO/FEDER, UE). Authors are grateful to “Ministerio de Ciencia, Innovación y Universidades” for the Predoctoral fellowship (ref. PRE2019-088195) awarded to Patricia Vázquez Loureiro.

IDENTIFICATION OF NON-VOLATILE COMPOUNDS IN EPOXY RESINS AND ORGANOSOLS INTENDED FOR FOOD CONTACT

P. Vázquez Loureiro[1], ***A. Lestido-Cardama***[1], ***R. Sendón***[1], ***Mª.I. Santillana***[2], ***J. Bustos***[2], ***P. Paseiro Losada***[1], ***A. Rodriguez Bernaldo de Quirós***[1]

[1]Department of Analytical Chemistry, Nutrition and Food Science, Faculty of Pharmacy, University of Santiago de Compostela
15782-Santiago de Compostela, Spain
[2]Food Center, Spanish Agency of Food Safety and Nutrition
E-28220 Majadahonda, Spain

Email: patriciavazquez.loureiro@usc.es

Abstract

Polymeric coatings are applied in the inner surface of food metal cans acting as a barrier between food and the metal surface. During the polymerization process, side reactions can occur, and reaction products can be formed, which have the potential to migrate into the food and may constitute a risk for the consumer health. Epoxy or organosol resins are one of the most used for internal food and beverage can linings due to the excellent chemical resistance. In the present study high performance liquid chromatography with fluorescence detection (HPLC-FLD) and liquid chromatography coupled to tandem mass spectrometry (LC-MS/MS) with atmospheric pressure chemical ionisation (APCI) were used for the identification and quantification of compounds in epoxy resins and organosols can material samples. Previous to the chromatographic analysis, of 3 coated metal samples were extracted with acetonitrile. Some of the compounds identified in the samples included BADGE, BADGE.H2O and cyclo-di-BADGE.

Keywords: *coatings, LC-MS/MS, bisphenol analogues and BADGEs*

Acknowledgements: This research was funded by the Ministerio de Ciencia, Innovación y Universidades, by Fondo Europeo de Desarrollo Regional (FEDER), and by Agencia Estatal de Investigación Ref. No. PGC2018-094518-B-I00 "MIGRACOATING" (MINECO/FEDER, UE). Authors are grateful to "Ministerio de Ciencia, Innovación y Universidades" for the Predoctoral fellowship (ref. PRE2019-088195) awarded to Patricia Vázquez Loureiro.

Proceedings ECS 2021
Brussels, Belgium, September 7-9, 2021

Abstract T-47

CFD SIMULATION OF SLOT DIE COATING FOR LITHIUM-ION BATTERY ELECTRODES AS PART OF A SIMULATION PLATFORM OF THE PROCESS CHAIN

T. Heckmann[1,2], ***S. Spiegel***[1,2], ***A. Hoffmann***[1,2], ***P. Scharfer***[1,2], ***W. Schabel***[1,2]
[1]Thin Film Technology (TFT),
[2]Material Research Center for Energy Systems (MZE)
Karlsruhe Institute of Technology (KIT)
Karlsruhe, Germany
Email: thilo.heckmann@kit.edu

Abstract
The processing of electrodes for lithium-ion batteries (LIB) consists of multiple sequential steps that mutually affect each other. Hence, defects in an early processing step (e.g. coating) detrimentally affect succeeding processing steps. Common coating defects, limiting the minimum wet film thickness are air-entrainment and low-flow streaks. Schmitt et al. address these coating defects by generating a coating window based on physical models and geometry factors (Schmitt et al. 2013). Another coating defect is the formation of elevated bulges on the side edges of the wet film. Especially for thick electrodes, this edge configuration leads to a substrate deformation during calendaring and winding up the electrodes. In this study, a model to describe the formation of side edges during slot-die coating based on material properties and geometrical factors is developed. A three-dimensional CFD-tool simulates the stationary velocity profile in the slot die as well as in the gap between slot die and substrate. The Volume of Fluids method serves as basis for the simulation, enabling a consideration of two phases. The CFD-tool provides the basis to derive models by carrying out parameter studies for slot dies of different inner geometries at differing process parameters. Special focus lies on viscosity variation and changes within the slot die as well as on slip/no slip boundary conditions for the openFOAM simulation platform. Coating experiments with inline wet-film profile measurements will validate the model. This model contributes to an integrated simulation platform that considers the entire process chain of the battery-electrode production.

Keywords: *coating, lithium-ion-batteries, simulation*

Acknowledgements: This work contributes to the research performed at CELEST (Center for Electrochemical Energy Stor-age Ulm Karlsruhe) and Material Research Center for Energy Systems (MZE) and is funded by the Federal Ministry of Education and Research (BMBF) under Project ID 03XP0242C (Epic).

References:

Schmitt, Marcel; Baunach, Michael; Wengeler, Lukas; Peters, Katharina; Junges, Pascal; Scharfer, Philip; Schabel, Wilhelm (2013): Slot-die processing of lithium-ion battery electrodes—Coating window characterization. In: Chemical Engineering and Processing: Process Intensification 68, S. 32–37. DOI: 10.1016/j.cep.2012.10.011.

Proceedings ECS 2021
Brussels, Belgium, September 7-9, 2021

Abstract T-52

INVESTIGATION OF INK-JET PRINTED LACQUER SYSTEMS FOR COATING APPLICATIONS

I. Preda [1], S. Filliger [1], N. Carrie [1] and G. Gugler [1]

[1]iPrint Institute, University of Applied Sciences and Arts of Western Switzerland, Fribourg, Switzerland
Email: gilbert.gugler@hefr.ch

Abstract
This work presents a material screening study conducted while researching an 100% UV lacquer for an ink-jet coating application. In the first part of the study, spin-coating was used for creating a uniform coating of 7 µm over a metallic substrate. The uniformity and the defect-free characteristics of the coating were confirmed by FIB microscopy and by electrical tests, which were found to be a reliable tool for ensuring the preparation of defect-free coatings over metallic substrates. In the second part of the study, the manufacturing process was switched to ink-jet. The best jetting and UV curing parameters were found to ensure good wetting between consecutive coating layers while having sufficient curing. Although thicker coatings of about 20 µm/layer were produced using ink-jet, the defect-free characteristics were conserved up to 50 consecutive layers, confirming that thicker yet uniform coatings could be obtained by ink-jet. The new testing method was helpful during the material screening. Furthermore, we have shown that lacquer systems can be easily obtained by ink-jet printing and could be very useful for electrical engineering applications.

***Keywords**: 100% UV lacquer system, coating, dielectric breakdown strength, ink-jet, encapsulation.*

1. Introduction

Materials screening for coatings are very common and usually adhesion or humidity and temperature stability (85/85) tests are used to evaluate the quality and the compatibility of the coating with other materials such as metallic layers. When it comes to thicker, multilayer coatings or to multi-material systems, the previous tests can point towards the weaker point of the assembly but do not characterize the overall volume. As part of a material screening for a multilayer coating based on 100% UV lacquer for an ink-jet application, we have found that the quality of thicker layers could be sometimes hard to assess and that one possible solution comes from the use of dielectric breakdown tests.

2. Theory

Dielectric breakdown test consists of applying a high voltage over an insulating material sandwiched between two conductive layers. The obtained dielectric strength represents the maximum electric field that the insulator can withstand before undergoing irreversible degradation such as an electric short circuit between the electrodes (Figure 1). The maximum value of the voltage applied to the terminals is called the breakdown voltage and, given that the internal electric field is enhanced by defects, the higher the breakdown voltage, the lower the number of defects in the sample's volume.

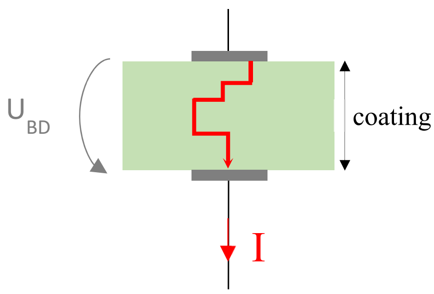

Figure 1. Schematics of a dielectric breakdown test

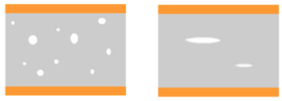

Figure 2. Possible defects found in the sample

Similar tests are usually used in order to assess the number of pin-holes in polymers films. But, unlike those tests, which are simply representing a pass/fail test, the measurement of dielectric strength allows for a more thorough volume characterisation of the material. Although it is impossible to know where the defects are located, the "qualitative" output is extremely useful during a material screening or while improving a coating process. Furthermore, given that the materials are evaluated under a high electric stress, the "quantitative" output can also point out towards the suitability of the coating material for applications in the energy sector, where electrical stresses with the same order of magnitude could occur.

Figure 3. Dielectric strength measuring setup

3. Experimental procedure and preliminary results

In the first part of this study, spin coating was used to create thin, uniform layers. For each investigated material, the coating speed was adjusted in order to obtain the desired thickness, knowing that the final uniform layers had to be 7 µm or less. Figure 4 presents the intermediate steps taken in order to determine the appropriate spin coating speed. The quality of the single layers was assessed by performing dielectric breakdown tests and part of the obtained results are presented in Figure 5.

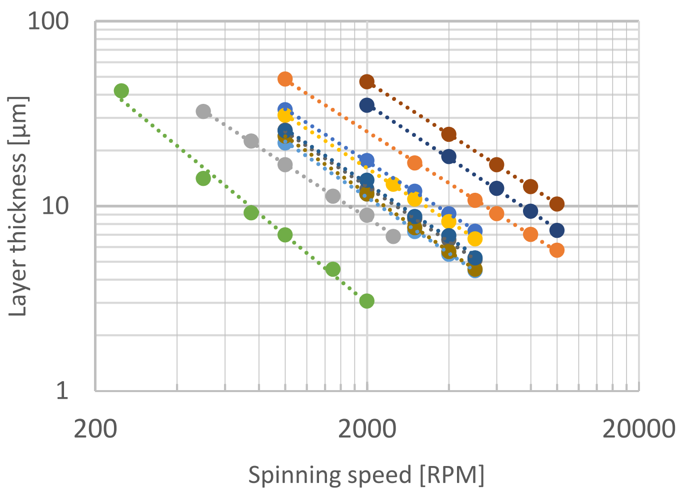

Figure 5. Layer thickness vs. spin-coating speed

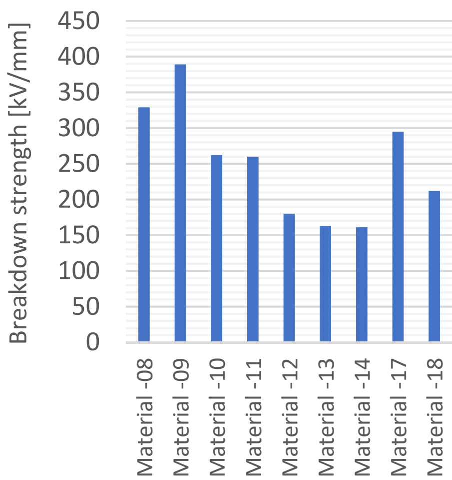

Figure 4. Dielectric breakdown strength for single-layer coatings

Once the best candidates were found – those with the higher dielectric strength being considered as being those having the lowest number of volume defects – spin coating was further used in order to create multi-layer coated samples. In between two insulating layers, a conductive layer was introduced in order to locally homogenise the electric field.

Additional dielectric tests were performed in order to confirm that the electrical properties are maintained and, before moving towards the ink-jet process, FIB Microscopy was used to further asses the homogeneity of the screen-printed coatings. Figure 6 shows one of the obtained images. Please note that the vertical line on the right is due to the alignment of the sample under the FIB beam.

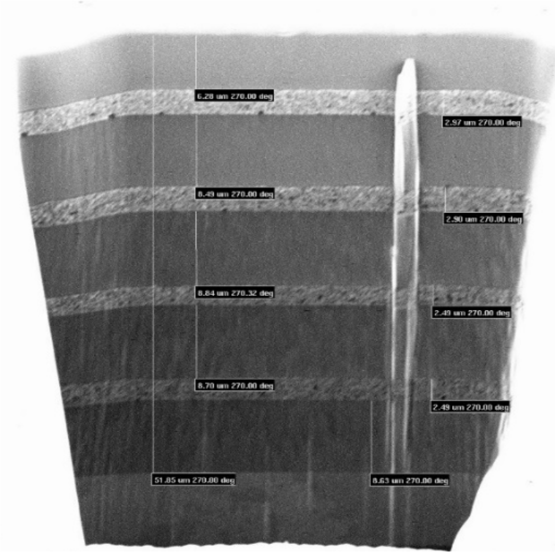

Figure 6. FIB microscopy presenting several spin-coated coating layers, "sandwiched" between spin-coated silver inter-layers

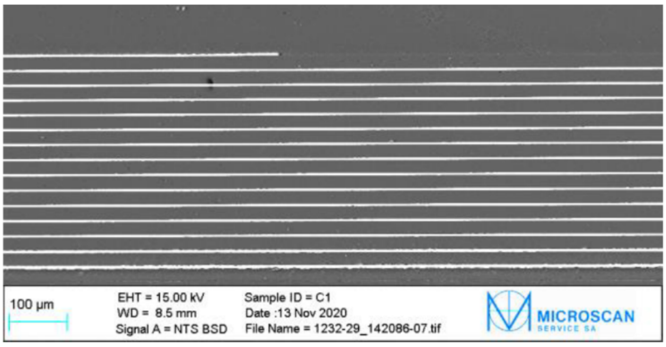

Figure 7. SEM microscopy presenting several ink-jet printed coating layers "sandwiched" between ink-jet printed silver inter-layers

4. Final results and discussion

Following our preliminary study using spin-coating, the goal objectives with respect to the coating layer's homogeneity were fixed, using both microscopy and electrical test results. We thus moved to the second part of the study which consisted of obtaining the same results by the use of the versatile ink-jet technology. First of all, thanks to drop watching technology, we were able to find the best recipe for printing uniform insulating layers sandwiched between metalized electrodes. After optimizing the UV curing process, we were able reproduce as closely as possible the samples manufactured at the beginning of the study. Yet, one drawback was quickly discovered: it was impossible to obtain the same thickness for and individual layer printed by ink-jet as it was previously the case for spin-coating. Actually, in order to obtain homogeneous layers, without dewetting, layers three times as thick had to be printed. This change in thickness has also slightly affected the overall quality of the samples from an electrical point of view. Nevertheless, the structural uniformity of the sample was maintained, as shown by the SEM microscopy image shown in Figure 7. The increase in the number of defects with respect to the thickness of the sample is a well-known phenomenon in electrical engineering and it was also confirmed by our results, as shown in Figure 8.

Hence, the ideal thickness for the ink-jet coated layer could be found as a compromise between a thin layer that is subject to dewetting and a thicker, uniform layer, having a minimum number of defects.

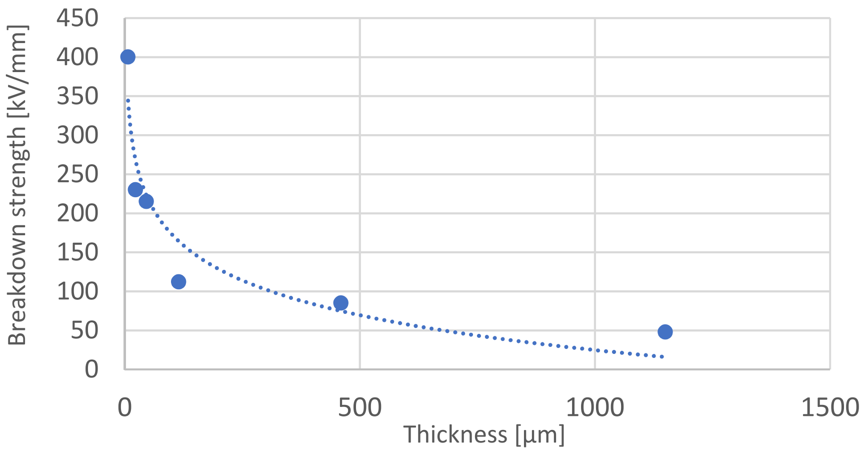

Figure 7. Breakdown strength values obtained for various thicknesses of the ink-jet printed layer

Furthermore, dielectric breakdown results have shown that the selected coating could be used as encapsulant for low and medium voltage applications, given that layers having a thickness of half a millimeter exhibit a breakdown strength of 100 kV/mm, thus opening the door for encapsulating power modules or for locally insulating energized nodes.

5. Conclusions

In conclusion, this work has allowed us to find the best 100% UV lacquer for an ink-jet coating application. The material study started with spin coating tests and moved to the final ink-jet technology. The use of dielectric breakdown tests was found to be a quick method to asses the quality of thicker ink-jet printed layers. Furthermore, we have shown that thicker, lacquer systems, can be easily obtained by multi-layer ink-jet printing.

Proceedings ECS 2021
Brussels, Belgium, September 7-9, 2021

Abstract T-86

PREDICTION OF THE DRIED SHAPE OF A POLYMER LAYER OBTAINED BY DRYING A THIN LIQUID FILM UNDER AN EVAPORATION MASK

***A. Faidherbe*[1], *L. Talini*[1] *and F. Lequeux*[2]**

[1] Laboratoire Surface du Verre et Interfaces, UMR 125, CNRS/Saint-Gobain
39 quai Lucien Lefranc, 93303 Aubervilliers, France
[2] Laboratoire Sciences et Ingénierie de la Matière Molle, UMR 7615, 1CNRS/UPMC/ESPCI ParisTech-PSL
10 rue Vauquelin 75005 Paris
Email: apolline.faidherbe@espci.fr

Keywords*: wet coating, evaporation, polymers*

Abstract

Liquid coating is a technique that consists in spreading a liquid film containing particles or polymers on a substrate and letting the solvent evaporate. It is of great interest for the glass industry as it may allow the functionalization of glass with such materials. However, when a thin film of complex fluid is dried on a substrate, thickness heterogeneities tend to appear. The propagation of a drying front from the edge to the center of the film is one of the phenomena that can lead to the formation of thickness heterogeneities, but its exact effect on the shape of the dried film remains unclear. Using an evaporation mask is a way to immobilize the drying front and simplify its study. We conduct experiments in which a thin film of polymer solution is dried below a cylindrical evaporation mask. A marked depression appears in the dried film under the mask. In parallel, we are developing a model based on the resolution of the thin film equation including evaporation effects. Accounting for viscosity variations of the polymer solution during drying and glass transition will shed light on thickness heterogeneities resulting from heterogeneous evaporation.

Abstract T-92

RECYCLING OF LITHIUM-ION BATTERY ELECTROLYTES – DESORPTION AND DRYING BEHAVIOUR TOWARDS A BETTER RECYCLING OF ORGANIC LIQUID ELECTROLYTE FROM ELECTRODE FILMS

L. Lödige[1,2]***, T. Heckmann***[1,2]***, J. Eser***[1,2]***, P. Scharfer***[1,2]***, W. Schabel***[1,2]

[1]Thin Film Technology (TFT), Karlsruhe Institute of Technology (KIT)
76131 Karlsruhe, Germany
[2]Material Research Center for Energy Systems (MZE), Karlsruhe Institute of Technology (KIT)
76131 Karlsruhe, Germany
Email: lukas.loedige@partner.kit.edu

Abstract
A high degree of sustainability of lithium-ion batteries (LIB) is achieved by establishing a circular economy, thus in improving the battery recycling process leading to an increase in resource efficiency. Therefore, an enhanced understanding of the process chain at the LIB end-of-life is required. According to the current state-of-the-art, Li-ion batteries with liquid electrolyte are mostly mechanically shredded. (Marshall et al., 2020) Subsequently, the highly volatile as well as the high boiling organic solvents released are removed by means of vacuum drying. In this context, especially the recovery of the low-volatile electrolyte components is a challenging task that requires further efforts. The prediction of the optimum drying time and the residual loading of the solvents in the cells are of major interest. From a safety point of view, the detection and quantification of these substances is crucial. (Harper et al., 2019)

The objective of this work is the simulative description of the drying process and its verification by experimental data. For this purpose, drying experiments will be conducted to provide data about phase equilibria and reveal information about the mass transfer kinetics. Furthermore, various spectroscopic measurement techniques will be employed to quantify the low volatile organic electrolyte components before and during drying. The aim of the simulative model is the calculation of critical process times depending on the boundary conditions of the drying process and the optimization of process parameters, hence a reduction in costs. Moreover, with the knowledge of residual loadings the safety of the overall recycling process is enhanced. In the end, the findings gained about the thermal processing and drying in the Li-ion battery electrolyte recycling can be used for the improvement of existing and the development of innovative industrial scale plants.

This work contributes to the research performed at CELEST (Center for Electrochemical Energy Storage | Ulm & Karlsruhe) and Material Research Center for Energy Systems (MZE). The authors would like to acknowledge financial support of the Federal ministry of Education and Research (BMBF) via the greenBatt cluster-project “LOWVOLMON” (Grant number: 03XP0354C).

Keywords*: drying, electrolyte recycling, monitoring, battery recycling*

References:
Marshall, J. et al. (2020). Disassembly of Li Ion Cells - Characterization and Safety Considerations of a Recycling Scheme. *Metals*, 10 (6), 773. DOI: 10.3390/met10060773.
Harper, G. et al. (2019). Recycling lithium-ion batteries from electric vehicles. *Nature*, 575 (7781), 75–86. DOI: 10.1038/s41586-019-1682-5.

PRINTING TECHNOLOGY

Proceedings ECS 2021
Brussels, Belgium, September 7-9, 2021

Abstract T-26

NUMERICAL SIMULATIONS AND IN SITU OPTICAL MICROSCOPY ANALYSIS OF CONTINUOUS BLADE COATING PROCESS FOR ORGANIC TRANSISTORS WITH SUPERIOR DEVICE UNIFORMITY.

***J.C. Lee*[1], *M. Lee*[2], *H.J. Lee*,[1] *K. Ahn*[3], *J. Nam*[2*], *S. Park*[1*]**

[1]Department of Materials Science and Engineering, Korea Advanced Institute of Science and Technology, Daejeon 34141, South Korea

[2]School of Chemical and Biological Engineering, Seoul National University, Seoul 08826, South Korea

[3]Department of Chemical Engineering, Sungkyunkwan University, Suwon 16419, South Korea

Email: stevepark@kaist.ac.kr and jaewooknam@snu.ac.kr

Abstract
Solution-based coating has many positive attributes such as high-throughput manufacturability and processability at ambient temperature and pressure, and large-area scalability However, strict tuning of thin-film properties duing solution-based coating is difficult due to the lack of precise control of flow behavior and thd the understanding of how it influences thin-film crystallization. In this work, a continuous-flow microfluidic-channel-based meniscus-guided coating (CoMiC) is introduced, which is a system that enables manipulation of flow patterns in the downstream region and analysis connecting flow pattern, crystallization, and thin-film properties. CoMiC can serve as a guideline for elucidating the relation between flow behavior, liquid-to-solid phase transition, and device performance, which has thus far been unknown.

Keywords: *blade coating, Organic semiconductor, Finite Element Method*

1. Introduction

The solution-based coating has many positive attributes such as high-throughput manufacturability,processability at ambient temperature and pressure, and large-area scalability. In this regard, solution-processed organic thin-film transistors (OTFTs) have been deemed as a highly promising technology. Contrary to vacuum deposition, the liquid-to-solid transition in solution-based coating is intricately dependent on the transport phenomena in the vicinity of the liquid-solid-boundary. Therefore, the precise control of thin-film properties necessitates careful tuning of flow behavior and the understanding of how it influences the crystallization process and thin-film properties. However, due to the complex interdependence of experimental parameters, independent control of flow behavior is challenging, rendering it difficult to elucidate the connection between flow behavior and thin-film properties. Herein, we introduce continuous flow microfluidic channel-based meniscus-guided coating (CoMiC), a system that enables precise control of flow behavior and comprehensive analysis connecting flow behavior, crystallization, and thin-film properties. In this study, the three types of microfluidic channel were tested: the flat microfluidic channel (FM), slanted groove microfluidic channel (SGM), and staggered herringbone microfluidic channel (SHM). Patterns inside the microchannels generate shape-induced pressure gradients, which can perturb laminar flow in the microchannel.

Abstract T-26

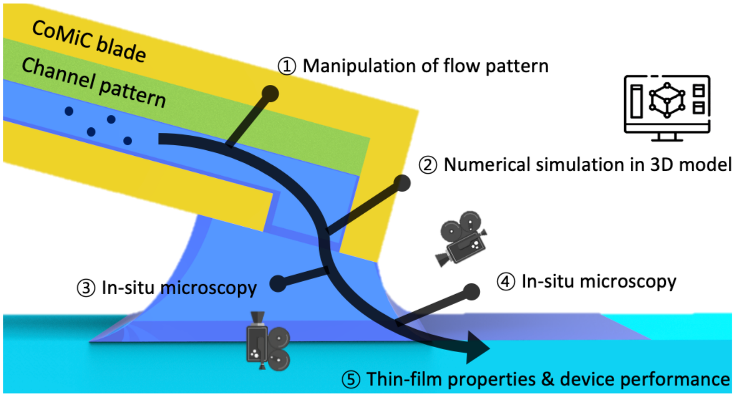

Figure 1. Schematic diagram of CoMiC-based comprehensive analytical system along the entire flow path connecting flow pattern, crystallization, and thin-film properties.

2. Mathematical formulation

Three-dimensional numerical simulations were conducted through numerical computation based on the Finite Element Method (FEM). The system of TIPS-pentacene solution with p-dopant was considered an isothermal flow an incompressible, Newtonian fluid with constant density, viscosity, and kinematic viscosity. The flow is governed by the Navier-Stokes equation and the mass transport is calculated by solving an advection-diffusion equation. The stabilized Galerkin Least-Squared (GLS) finite element method was used to solve the governing equations.

$$\nabla \cdot \boldsymbol{u} = 0,$$

$$\rho(\boldsymbol{u} \cdot \nabla \boldsymbol{u}) - \nabla \cdot \boldsymbol{\sigma} = \boldsymbol{0} \tag{1}$$

$$\boldsymbol{\sigma} = -p\boldsymbol{I} + \mu(\nabla \boldsymbol{u} + (\nabla \boldsymbol{u})^T)$$

$$\frac{\partial c}{\partial t} + \boldsymbol{u} \cdot \nabla c - D\nabla^2 c = 0 \tag{2}$$

3. Results and discussion

Figure 2a,b is side-view in situ images of the meniscus during coating for solution shearing and CoMiC (here, the microchannel did not have patterns), respectively. The liquid-air interface gradually changes since solution volume progressively depletes for solution shearing. On the oter hand, the shape of meniscus at the downstream is sustained by the continuous supply of solution during coating for CoMiC system Figure 2c,d is transfer characteristics of OTFTs made with solution shearing and CoMiC, respectively. For solution shearing, there is significant variation in transistor properties compared to that of CoMiC, because the volume of solution and the shape of meniscus are correlated to solvent evaporation rate.

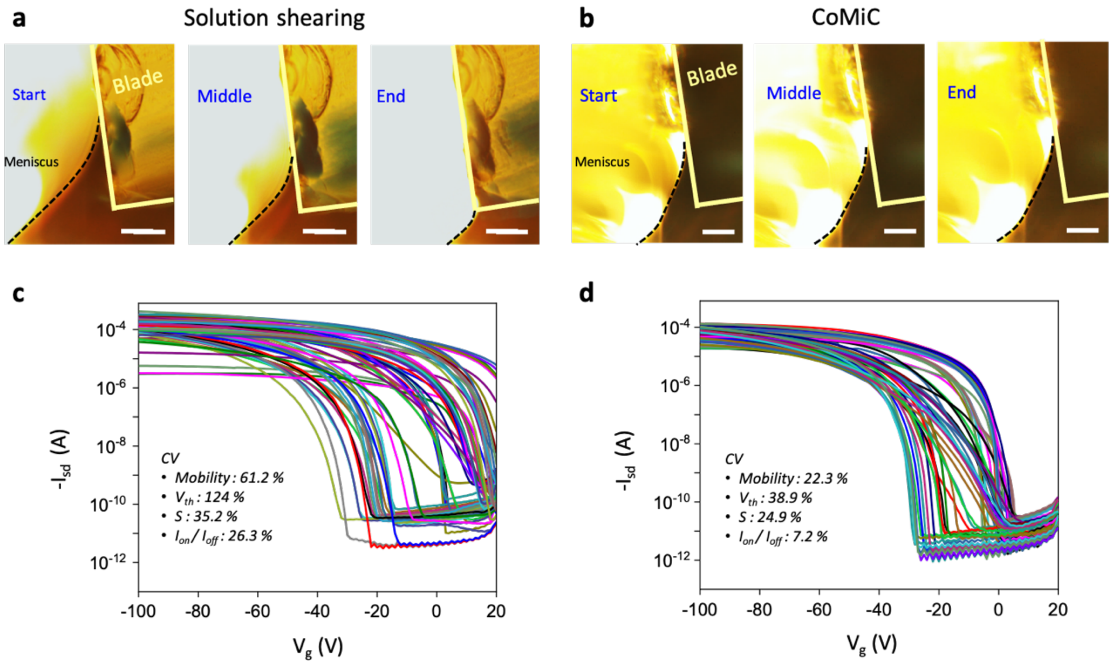

Figure 2. Side-view in situ image analysis of meniscus shape variation during the coating and the corresponding transfer characteristics of TIPS-pentacene thin-film transistors fabricated by conventional solution shearing (a,c) and CoMiC without patterns (b,d).

5. Conclusions

In summary, continuous-flow microfluidic channel based meniscus-guided coating (CoMiC) is introduced, which enabled the manipulation and systematic analysis of flow pattern and crystallization process. The flow pattern was determined to be maintained in the distribution region and affectd the crystallization process. We project that CoMiC will be critical for in-depth understanding of solution-based thin-film processing, through which the properties of OTFTs and other types of devices such as solar cells and displays can be further optimized.

References

Diao, Y., Shaw, L., Bao, Z., Mannsfeld, S.C.B., (2014). Morphology control strategies for solution-processed organic semiconductor thin films. *Energy & Environmental Science* 7, 2145-2159.

Gu, X., Shaw, L., Gu, K., Toney, M.F., Bao, Z., (2018) The meniscus-guided deposition of semiconducting polymers. *Nature communications* 9, 534.

Lee, J.C., Lee, M.H., Lee, H.J., Ahn, K.G., Nam, J.W., Park, S., (2020). Numerical simulations and in situ optical microscopy connecting flow pattern, crystallization, and thin-film properties for organic transistors with superior device-to-device uniformity. *Advanced Materials* 32, e2004864.

Proceedings ECS 2021
Brussels, Belgium, September 7-9, 2021

Abstract T-55

CHALLENGES OF FABRICATING CATALYST LAYERS FOR PEM FUEL CELLS USING FLATBED SCREEN PRINTING

***L. Ney*[1], R. Singh[1], J. Hog[1], N. Göttlicher[1], J. Wolken[1], R. Steffens[1], P. Schneider[1], S. Tepner[1], M. Klingele[1], R. Keding[1], F. Clement[1] and Ulf Groos[1]**

[1]Fraunhofer Institute for Solar Energy Systems, Freiburg, Germany

Email: linda.ney@ise.fraunhofer.de

Abstract

In this work, flatbed screen printing is evaluated for the production of catalyst layers of PEM fuel cells. Process parameters are varied to investigate their effect on resulting layer thickness and Pt-loading. The paste without water and optimal process parameters performed best under dry conditions. The main challenge of screen printing process development lies in the paste optimization to prevent evaporation effects over time and ensuring sufficient fuel cell performance.

Keywords: *catalyst layer, fuel cell, screen printing, catalyst ink, solvent evaporation*

1. Introduction

Today's fuel cell catalyst production research addresses the challenges of upscaling and optimizing various fabrication processes, in order to increase throughput rates while maintaining quality demands (Kampker et al., 2020; Ulsh et al., 2013). The catalyst paste can be applied directly onto the membrane (Wang et al., 2015) or indirectly by using the decal transfer method (Santangelo et al., 2019). The filament breakup underneath the screen has been studied in-depth by Potts et al. (Potts et al., 2020). This effect is not only dependent on the process parameters, but also on the surface energies of the paste, substrate, and screen. In this study, we apply flatbed screen printing by using a semi-automatic screen printer, which enables printing of sufficiently high layer thicknesses and the possibility of in-plane structuring of the catalyst layer, compared to e.g. slot die coating. In this work, printing process parameters as well as the surface tension of the paste will be examined and finally characterized by electrochemical in-situ testing.

2. Experimental procedure

At first, a carbon paste based on a suitable rheology for screen printing with Vulcan XC72R powder, a mixture of alcohols and ionomer dispersion (Aquivion D79-25BS), is developed. The water content of the ionomer dispersion has been evaporated prior to adding the carbon powder (Bonifácio et al., 2011), which resulted in a paste solid content of 18wt% with an ionomer-to-carbon ratio of 0.7 (Alink et al., 2020). All coatings are applied with a constant amount of platinum-free paste (7.499 g±0.025 g) while printing speed, screen mesh size and squeegee pressure are varied systematically. With the given paste volume, as many layers as possible are printed, in which four coatings are printed simultaneously with a screen aperture of 20 cm² each, as can be seen in Figure 1. The reference parameters that have been kept constant are 230/30 mesh (mesh count of 230 wires per inch and wire diameter of 30 µm), 100 mm/s printing velocity, 75 N squeegee force (approx. 750 kPa) and 2 mm snap-off distance. Each 9th print contains one silicon wafer as substrate. Due to their excellent cracking behaviour and electrical conductivity, SEM cross sections are taken at four different points per substrate, resulting in eight pictures per process variation. An image processing tool has been developed to extract corresponding height data for each vertical pixel column of each SEM image to calculate the average layer thickness and its deviation (Figure 1, right). At the end, functional catalyst pastes are designed and printed to verify the platinum-loading range at the anode and cathode side. Since the surface tension of the catalyst paste plays an important role in screen printing, the solvent composition is varied as well: alcohol-based solvents without water and paste with water content of 15.8wt%.

Finally, the produced catalyst layers are transferred onto the membrane by hot-pressing and tested electrochemically to verify the fabrication route and their reproducibility. For the in-situ performance characterization, UI-curves were measured under H_2/air conditions at 80° C. To differ between humidified inlet, and dry outlet conditions of a fuel cell stack, the UI curves were conducted at 100% and 40% relative gas humidity (Alink et al., 2020).

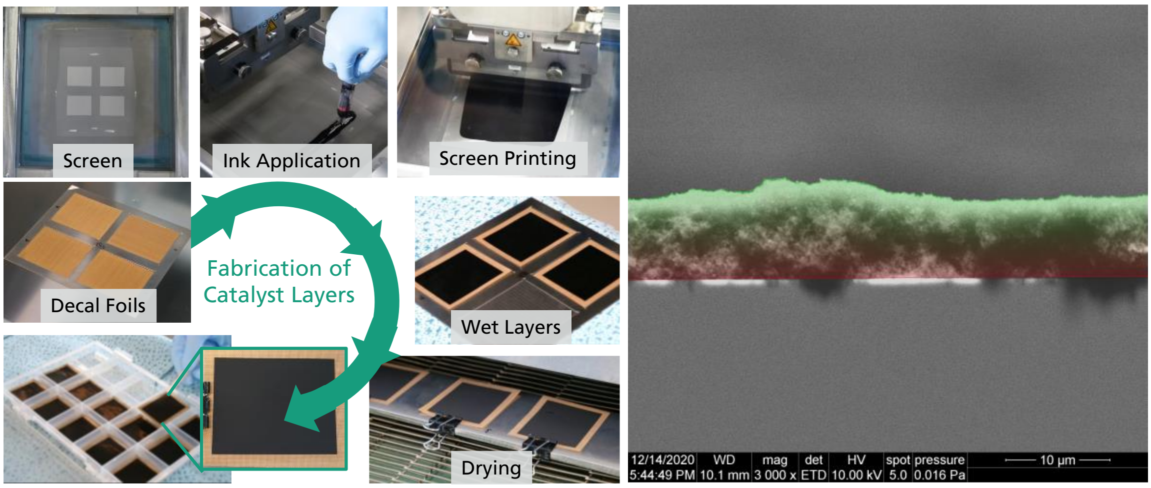

Figure 1. Left: Process route of fabricating catalyst layers by screen printing at Fraunhofer ISE; Right: SEM image of a catalyst layer on Silicon substrate: cross section with automatically highlighted layer thickness

3. Results and discussion

The specific layer weight of the catalyst layer increases by choosing coarser meshes, as can be seen in Figure 2. The highest number of prints has been reached with the finest mesh of 400/18, because it results in the lowest layer weight per print. Increasing the printing velocity, the layer thickness increases slightly, but more importantly results in a more homogeneous layer thickness as can be seen from the standard deviation. The applied squeegee force on the other hand has no significant effect for the chosen set of parameters. Therefore, adjusting the specific layer weight or Pt-loading, different meshes should be chosen while keeping a constant printing velocity of 300 mm/s and force of e.g. 80 N. These printing parameters have been applied in Figure 3 for separately developed catalyst pastes for the anode and cathode side. The anode paste has been printed with a 400/18 mesh to aim for a Pt-loading of 0.05mg/cm² and the cathode pastes with the 230/30 mesh. The cathode paste without water yields at higher Pt-loadings, which might be due to the reduction of the polar part of the surface tension. Since the PTFE substrate has almost no polar bonding part of its surface energy, the wetting behaviour of the water-free paste is increased.

Therefore, from a process optimization perspective, adjusting the polar and dispersive energy of the pastes through the choice of the solvent mixture, the filament breakup will be affected, which changes the deposited layer weight. We also observe that during all printing processes the layer weight increases, which might be due to solvent evaporation effects. Therefore, it is crucial for future experiments to select solvents with higher boiling points. This has to be done carefully because changing paste recipes will always affect the fuel cell performance whereas drying temperatures are limited to the glass transition temperature of the ionomer. As can be seen in Figure 3, the performance of the catalyst layers produced with and without water differs significantly, depending on the relative humidity during electrochemical testing. Therefore, changing the paste recipe for the purpose of process optimization must be carried out taking into consideration its effect on performance. A possible solution might be the implementation of a solvent rich atmosphere within the coating chamber. Hence, further experiments considering different solvents are currently being conducted and will follow within the scope of this study.

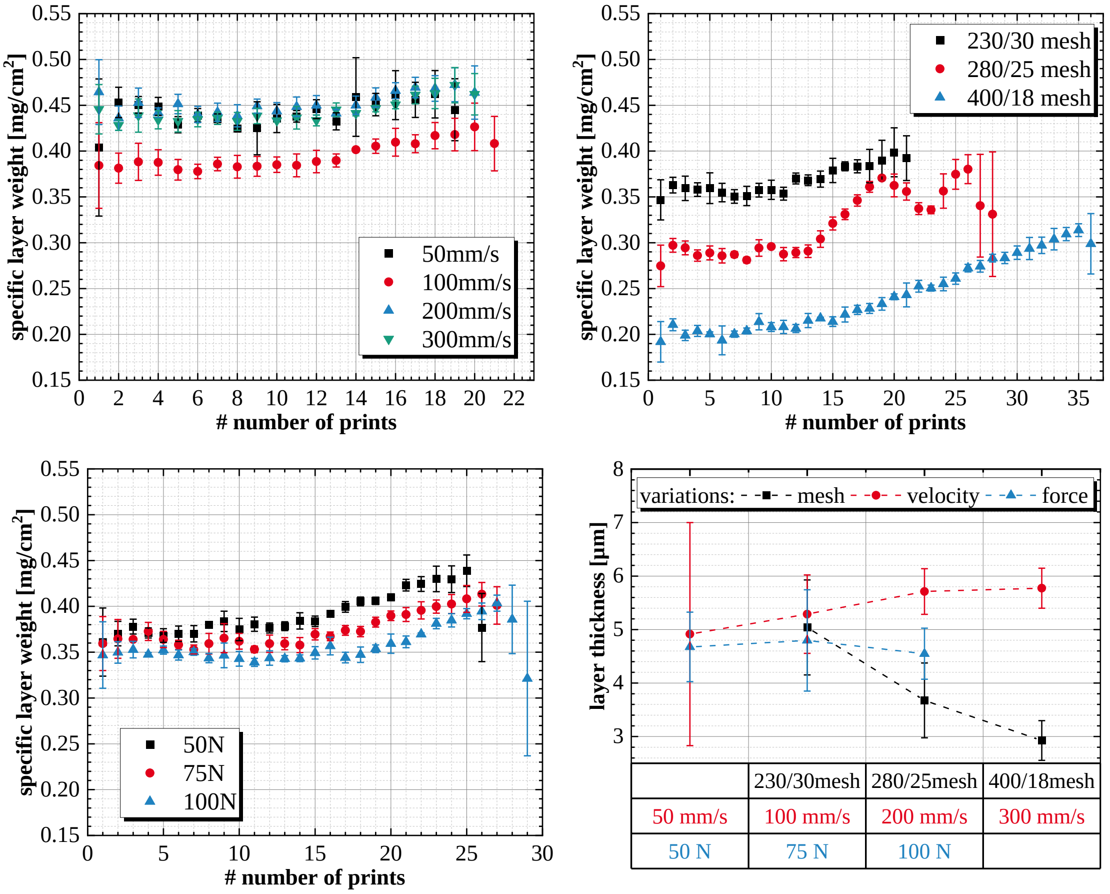

Figure 2. Top left: variation of printing squeegee velocity, top right: variation of meshes, bottom left: variation of printing squeegee force and their impact on the specific layer weight. In each printing step, four catalyst layers have been printed. Bottom right: Measured layer thickness of each variation by analysing SEM images.

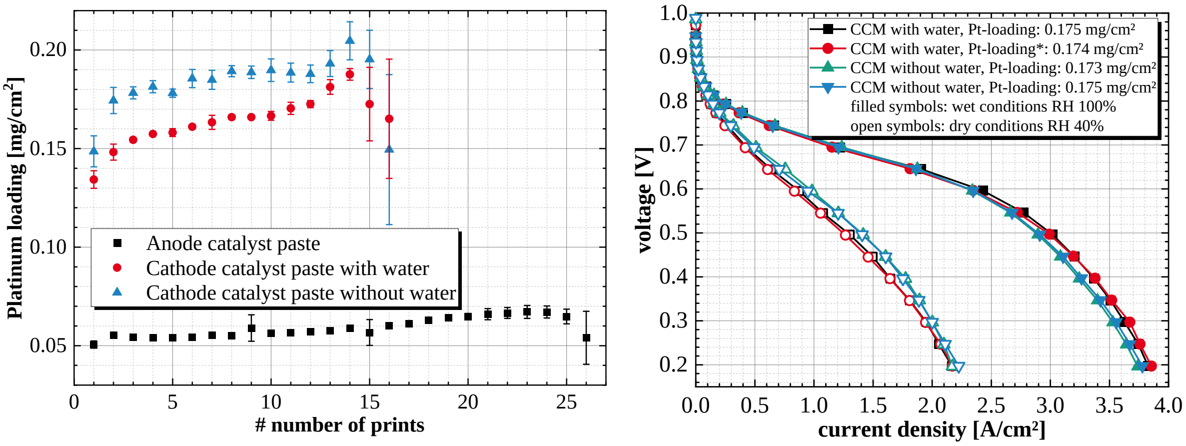

Figure 3. Left: Platinum loadings with anode and two catalyst pastes: with (15.8wt%) water and without water. Right: Polarization curve of four CCMs characterized in dry conditions (relative humidity (RH) 40%, open symbols) and wet conditions (RH 100 %, filled symbols). Every CCM has an anode loading of 0.055mg/cm², except the red indicated CCM with 0.1 mg/cm² at the anode.*

Abstract T-55

4. Conclusions

Screen printing process parameters like printing velocity, squeegee pressure and different meshes have been varied to evaluate their impact on the specific layer weight and thickness of catalyst layers for PEM fuel cells. It was shown and verified by SEM images that the adjustment of the Pt-loading should be done by changing the mesh, whereas the increase of the printing speed results in a more homogeneous coating thickness. Catalyst pastes without water content showed an increase in applied Pt-loading and performed best in dry conditions, compared to fabrication of catalyst layers with water. It has been shown that the fabrication of catalyst layers with constant process parameters is highly reproducible and exhibits very good overall performance. The main challenge for the screen printing technology is the dependence of process stability on the evaporation of the solvents during the printing process, which causes an increase in Platinum-loading over time. Further studies are currently being conducted to examine air-stable solvents and their effect on fuel cell performance to enable the industrial fabrication of catalyst layers by flatbed or rotary screen printing, flexographic or gravure printing.

5. Acknowledgements

The authors thank the Ministry of the Environment, Climate, Protection and the Energy Sector Baden- Württemberg for the financial support of the project HyFab-Baden-Württemberg, contract no. L7520113 and the Project Agency Karlsruhe, Baden-Württemberg Programs (PTKA-BWP) for the administration as well as both for the good cooperation.

References

Alink, R., Singh, R., Schneider, P., Christmann, K., Schall, J., Keding, R., & Zamel, N. (2020). Full Parametric Study of the Influence of Ionomer Content, Catalyst Loading and Catalyst Type on Oxygen and Ion Transport in PEM Fuel Cell Catalyst Layers. Molecules (Basel, Switzerland), 25(7). https://doi.org/10.3390/molecules25071523

Bonifácio, R. N., Paschoal, J. O. A., Linardi, M., & Cuenca, R. (2011). Catalyst layer optimization by surface tension control during ink formulation of membrane electrode assemblies in proton exchange membrane fuel cell. Journal of Power Sources, 196(10), 4680–4685. https://doi.org/10.1016/j.jpowsour.2011.01.010

Kampker, A., Ayvaz, P., Schön, C., Karstedt, J., Förstmann, R., & Welker, F. (2020). Challenges towards large-scale fuel cell production: Results of an expert assessment study. International Journal of Hydrogen Energy. Advance online publication. https://doi.org/10.1016/j.ijhydene.2020.07.180

Potts, S.-J., Phillips, C., Jewell, E., Clifford, B., Lau, Y. C., & Claypole, T. (2020). High-speed imaging the effect of snap-off distance and squeegee speed on the ink transfer mechanism of screen-printed carbon pastes. Journal of Coatings Technology and Research, 17(2), 447–459. https://doi.org/10.1007/s11998-019-00291-6

Santangelo, P., Cannio, M., & Romagnoli, M. (2019). Review of Catalyst-deposition Techniques for PEMFC Electrodes. TECNICA ITALIANA-Italian Journal of Engineering Science, 63(1), 65–72. https://doi.org/10.18280/ti-ijes.630109

Ulsh, M., Sopori, B., Aieta, N. V., & Bender, G. (2013). Challenges to High-Volume Production of Fuel Cell Materials: Quality Control. ECS Transactions, 50(2), 919–926. https://doi.org/10.1149/05002.0919ecst

Wang, W [Wentao], Chen, S., Li, J., & Wang, W [Wei] (2015). Fabrication of catalyst coated membrane with screen printing method in a proton exchange membrane fuel cell. International Journal of Hydrogen Energy, 40(13), 4649–4658. https://doi.org/10.1016/j.ijhydene.2015.02.027

Preceedings ECS

2021

Brussels, Belgium, September 7-9, 2021

Abstract T-24

FABRICATION OF GRADATED PATTERNED THIN FILMS USING SCALABLE COATING METHOD

***Tae-Joong Jeong*[1] *and Tequila A. L. Harris*[1]**

[1] *Woodruff School of Mechanical Engineering, Georgia Institute of Technology, Atlanta, GA, USA*

Corresponding author: tjeong7@gatech.edu

Abstract

Gradient structures in thin film have very high potential in various research areas having applications including enhancing flexible device encapsulation, fabrication of lab-on-a-chip and nanopaper printing. Prevalent coating methods for gradated thin film production, such as spin coating, inkjet printing and spray coating, although can achieve user's desired output, are not capable in terms of scalability, material selection variety and waste efficiency. However, slot die coating is a feasible method that can mitigate these problems. In this work, slot die coating on the roll-to-roll system is introduced to scale up the formation of gradient thin film structures, with precise control over the film structure, thickness, and width. To accomplish this, the internal mixing phenomenon and the flow dynamics within the coating bead are investigated. The quality of the gradient structures is analyzed using various mechanical testing techniques to evaluate the strength and gradient quality of the film. Using this method, the manufacturability of the thin film will improve as there are minimal restrictions on material selection and feature sizes to allow for mass production of gradient thin film.

Keywords: *slot die coating, gradient, microfluidics, mixing*

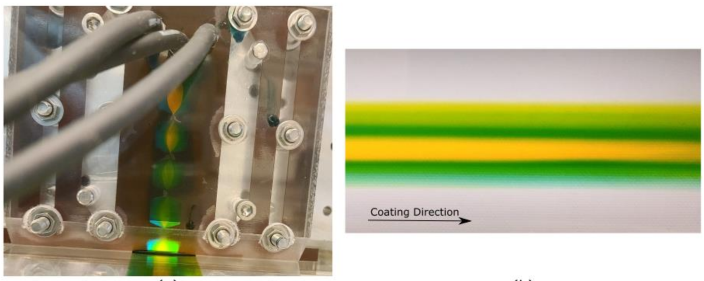

(a) (b)

Figure 1. Resultant coating of two different concentration of PVA at (a) internal phase and (b) external phase

T-44 LONG DISTANCE JETTING: DIGITAL PRINTING ON NON-PLANAR SHAPES

***O. Bürgy*[1], *N. Muller*[1], *N. Carrie*[1], *G. Gugler*[1], *Y. Domae*[1]**

[1]iPrint Institute, HEIA-FR, HES-SO University of Applied Sciences and Arts Western Switzerland
Fribourg CH-1700, Switzerland

Email: olivier.buergy@hefr.ch

Abstract

The inkjet printing technology plays a major role in the digital printing field. Having the possibility to digitally and selectively print or coat areas offers a great advantage. Usually inkjet was limited to flat substrates but nowadays with modern printheads and advanced waveform tuning, it is possible to extend the jetting distance and print on non-planar shapes. This paper will compare different printheads and the strategies used to increase the jetting distance.

***Keywords**: inkjet technology, long distance jetting, direct to shape, selective coating*

1.Introduction

Inkjet printing technologies have been consistently growing over the last years. Digital printing has been extensively used in the graphical printing field, but the number of applications is constantly increasing. Inkjet printheads can nowadays be used for digital coating applications where they shine thanks to their flexibility and their low ink wastage. However, such coating techniques were often limited to flat or slightly curved substrates due to the low jetting distance required by the printheads (3). Manufacturers have now greatly improved the design and manufacturing of printheads to deliver higher quality products achieving superior jet straightness, and with advanced waveform tuning, opening the door to higher distance jetting. In this context, three different printheads offering a native resolution of 600 DPI were evaluated in order to find the most suitable candidate for long distance jetting. The jetting straightness measured on printed samples was considered as criterion in order to compare different printheads.

2.Theory

One of the important aspect to reach a high-quality print is the drop placement on the substrate. A good placement will have an impact on the color reproduction for graphical printing or on the wetting behavior in coating applications. Firstly, the nozzle will influence the droplets trajectory. The shape (4) or the accuracy in the drilling or manufacturing of the nozzle may affect the jetting straightness of the droplets. A lot of progress has been accomplished in the manufacturing technologies using MEMS manufacturing techniques to etch accurate geometries in silicon. Moreover, as soon as the droplet exits the nozzle, external factors may change the trajectory of the droplet. Air molecules will have the most impact by slowing down droplets and given their small size, airflows will deviate the droplets (1-2). The challenge of the airflow on the droplet flight is a well-studied phenomenon and the airflow changes with the gradient of speed between the printhead and the substrate (the printing speed), ink discharge (productivity) or even the printhead design (row-to-row distance). The flow of ink jetted by the printhead creates eddies between the nozzle rows. Some strategies were implemented to mitigate this problem by trying to control the airflow, but a preferred workaround is to spend the least amount of time in the printing gap by having a fast and heavy droplet that will be less carried around by airflows because of its higher momentum.

3. Experimental procedure

The evaluation of each printhead was performed in two steps. The process started with a waveform optimization using dropwatching to have droplets with a high kinetic energy. Black UV inks were chosen considering the specified viscosity range of each printhead. All inks had a viscosity around 8-10 mPas at 45°C. A set of waveforms were selected for each printhead to be tested during printing tests. The droplets had a volume ranging from 25 up to 60 pl and a velocity between 7.5 and 10 m/s measured at 1 mm away from the nozzle plate. The following image shows the drop formation of a 6-pulses waveform with six individual sub-droplets that merge into a single droplet and increase the speed and the volume of the droplet.

Figure 1. Drop formation for a 6-pulses waveform resulting in a 30 pl droplet.

To evaluate the jetting straightness of each printhead, a set of images containing a grid was used while the printing quality was visually assess using a standard pattern. All prints were done on inkjet paper to remove all wetting behaviors that could impact the result. A printed grid of dots was used to measure the drop placement on the substrate using a digital microscope. The position of each dot on the substrate was computed and the data points were processed to fit a theoretical straight line pattern. The deviation of the dot from this line could be quantified. The steps are illustrated on the following figure.

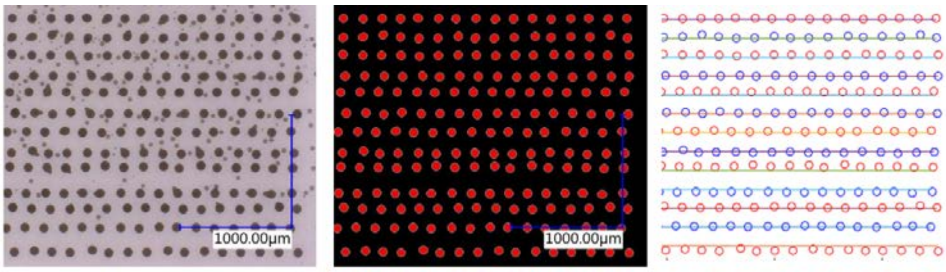

Figure 2. Scanned printed grid, drop position and fitting of each printed line

The deviation from the theoretical position follows a normal distribution law and it is therefore possible to fit a gaussian curve to the data points to compute the printed resolution that the printhead achieved at the given jetting distance. A criterium of two sigmas corresponding to half the nozzle pitch was used to fit the gaussian curve. Using this criterium for a 600 DPI printhead, 95.4% of the drop should land within a ±21µm error from the theoretical position.

4. Results and discussion

A set of three native 600 DPI printheads were tested and the drop placement was measured. Under these conditions, one printhead was still able to maintain a 600 DPI printing resolution up to an 8-mm jetting distance. All printheads showed an exponential decrease in the accuracy according to the distance.

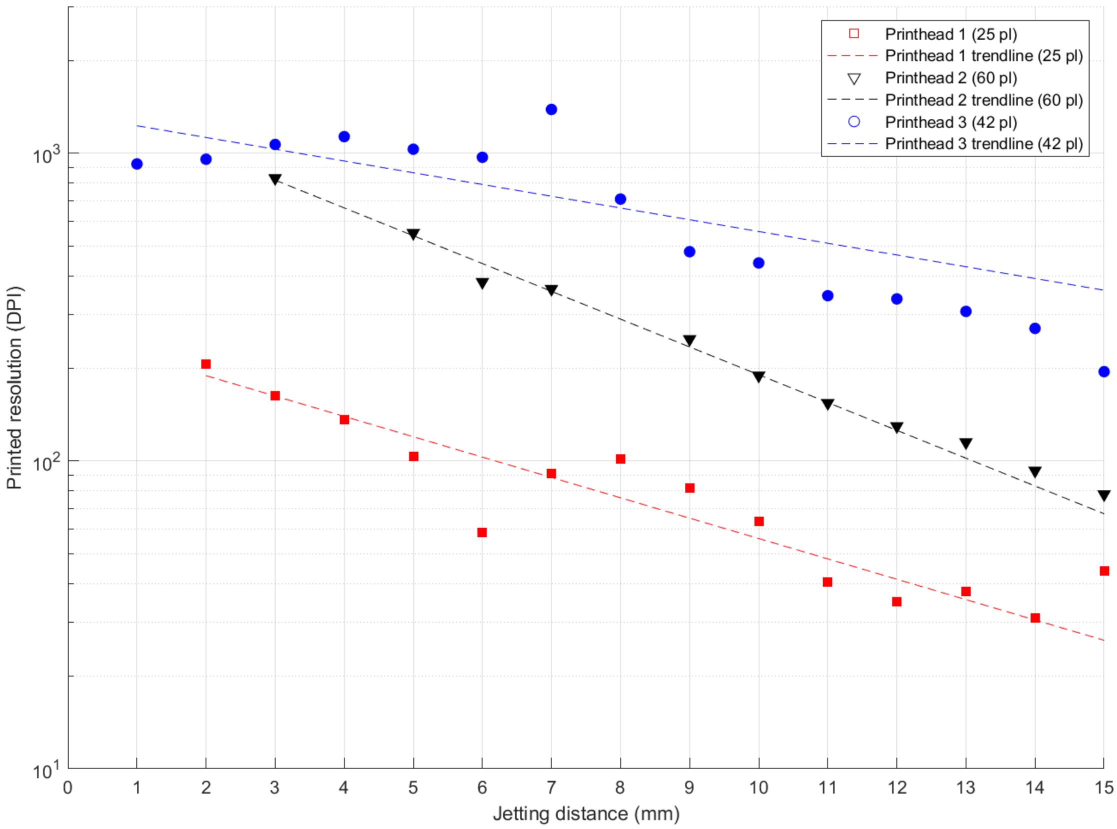

Figure 3. Printed resolution according to the jetting distance for three different printheads.

Nonetheless, these results show the potential to print using piezo inkjet printheads at greater distances than the industry standard of 1 to 2 mm. An increase in the printing gap opens the doors to non-planar substrate for decoration or functional printing.

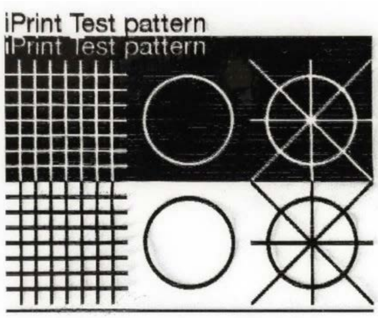

Figure 4. Pattern printed at 8 mm (the grid has 1 mm square)

The printed images show a decent quality perfectly suitable for selective coating applications or lower resolution graphical printing.

5.Conclusions

We have compared different inkjet printheads to measure the jetting straightness and the achievable printing resolution for a given jetting distance ranging from 1 up to 15 mm. One printhead was able to maintain a 600 DPI printing resolution up to 8 mm and over 300 DPI up to 12 mm. These results show the possibility to extend the range of applications toward curved shapes while still maintaining a decent printing quality.

Reference

1. Link, N., et al. (2009), *Chemical Engineering and Processing: Process Intensification*, Vol. 48, 84-91
2. Rodriguez-Rivero, C., et al. (2015), *NIP & Digital Fabrication Conference*, 1, 29-38
3. Thorp, D., et al. (2017), *Handbook of Industrial Inkjet Printing*, Vol. 1-2, 787-797
4. Trip, R., et al. (2018), *NIP & Digital Fabrication Conference*, 6, 215-220

Proceedings ECS 2021
Brussels, Belgium, September 7-9, 2021

Abstract T-12

T-12: PRINTING AND GENERATING STRUCTURAL COLORS BY MEANS OF INKJET TECHNOLOGY

***N. Muller*[1]*, P. Yazghur*[2]*, F. Scheffold*[2]*, G. Gugler*[1]**

[1]iPrint Institute, HEIA-FR, HES-SO University of Applied Sciences and Arts Western Switzerland Fribourg CH-1700, Switzerland

[2]Department of Physics, University of Fribourg
Fribourg CH-1700, Switzerland

Email: nicolas.muller@hefr.ch

Abstract

In the context of Industry 4.0, inkjet technology has the unrivaled advantage of being digital and versatile by its nature. The recent breakthrough in the understanding of structurally colored materials provides new design platforms for pigments in a variety of applications. An appealing approach is the design of photonic pigments for inkjet printing. However, inkjet technology imposes strict limitations with respect to pigment size. Here we show the deposition and the fabrication of photonic pigments by inkjet technology.

1. Introduction

Over the last decade, tremendous progress has been achieved towards the understanding of structural coloration both from crystalline and non-crystalline materials (4), (5). The latter are of particular importance since they provide non-iridescent stable coloration, which is similar in appearance to conventional dyes and thus often preferred. Having no chemical pigments, structural colors never age, stay ultra-resistant to bleaching and can be manufactured from low toxic materials, thus having much lower environment and human health impacts. The delivery or deposition of the materials remains however a major hurdle towards practical applications such as graphical printing. One way to overcome these problems is to confine first nanoparticles inside emulsion droplets to produce micrometer sized clusters of photonic crystals (3) – "photonic balls" (PB), and then use the obtained colored ink for practical applications (2) in the domain of inkjet printing.

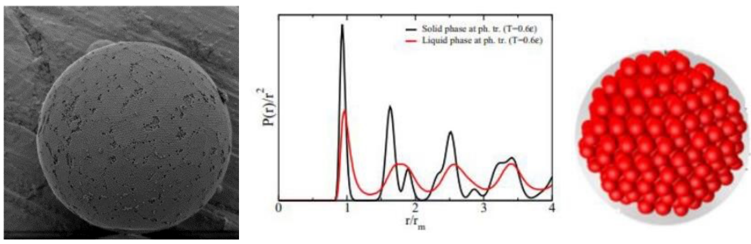

Fig. 1. Left: Experimentally fabricated Photonic Pigment, Right: Numerical Simulation of a particle filled droplets, black/ red line denote amorphous solid/liquid structure near close packing conditions

2. Theory

Ordinary pigments that are used for color formation in clothes, paintings, etc. usually start to fade and to bleach after a certain lifetime. In most pigments, molecules absorb incident white light over a certain spectral range and the reflected or transmitted light acquires the color of the light that is not absorbed. During this process the molecules slowly degrade or bleach and the color intensity diminishes. This is why other color forming systems are sought after. One way to achieve this is by using systems that generate color by interference, meaning that a physical system presents structural properties such that certain wavelengths constructively interfere. This range of wave vectors that are not allowed to penetrate inside the system and are reflected back, similar to a mirror, is called a photonic bandgap. The corresponding wavelengths, for a given angle of illumination, give rise to what is known as iridescent colors; colors that are very bright but highly angle dependent. Wavelengths outside the photonic bandgap mainly penetrate the structure without being altered. The central wavelength at which the bandgap is located and by this defining the color, depends mainly on three parameters: the size of the underlying crystalline lattice, the refractive index of the units that form the system and the incidence angle.

Recently it was shown that disordered, but highly correlated, systems can also produce color. Being intrinsically disordered, their photonic bandgap is completely isotropic, meaning that the resulting colors are not angular dependent. By carefully organizing spherical submicron-sized particles, for example made of polystyrene, it is possible to generate colors. Such structures are in the following referred to as photonic balls. The colors that such photonic balls produce depend mainly on the size and the refractive index of its subunit particles. Different colors can be achieved by carefully tuning the size of these sub-unit particles. The colors that arise from these photonic balls are isotropic, which is a major advantage compared to purely periodic systems.

Moreover, such systems are formed by sub-unit particles of around 200-300 nm, and to achieve color effects they need to be assembled in photonic balls of a size in the micrometer range or larger. This adds additional challenges when depositing them with standard inkjet technology. The nozzle of state of the art printheads range from 10-50 um, meaning that the acceptable pigment size is around 1-5 um. To cope with these challenges a customized printing platform is used together with an adequate printhead. The platform is able to handle these photonic ball loaded inks from a fluid supply point of view (recirculation to avoid sedimentation and agglomeration) as well as from a printhead point of view with the best possible performance.

3. Experimental procedure

Structural colors are easily obtained in colloidal suspensions of repulsive spheres as shown in the work on structural coloration ('photonic liquids') dating back to 2004 (1) or thin nanoparticle films. Droplets with low volume fraction of nanoparticles are first formed and the solvent is then removed from the interior of the droplets. In order to do so, the classic approach of removing solvent in a controlled manner by osmotic solvent-extraction drying was employed in this work. Decanol was chosen as the appropriate solvent. The as-formed photonic particles are then dispersed in pentanol and subsequently jetted with a state of the art industrial printhead (Ricoh Gen4, Seiko RC1536).

4. Results and discussion

First, thin films were deposited with a 50 um homogeneous film spreader in order to evaluate color formation. It was found that multiple scattering dominated, resulting in a white appearance. Incorporating small amounts of carbon black inside the photonic balls resulted in the suppression of multiple scattering and lead to the appearance of the desired photonic color.

Figure 2. Dried films of photonic balls.

In a second step, the as-formulated inks were printed by means of inkjet printing.

Figure 3. Photonic balls printed by means of inkjet technology. Left: Redish color. Right: Greenish color

In addition, we show an alternative route to fabricate photonic pigments of spherical and disk-like shapes. To this purpose, an industrial printhead is employed as a micrometer drop generator. The asformed drops are jetted on a decanol surface, which will extract, via osmotic pressures, the water from inside the droplets. Due to geometrical constraints disk-like particles are formed.

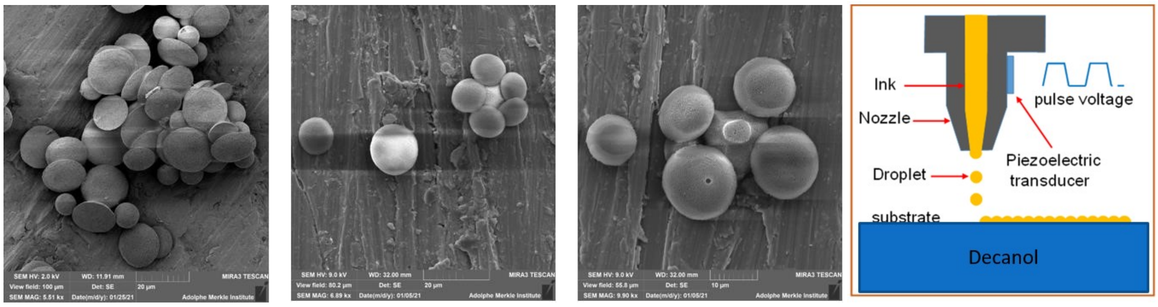

Figure 4. Photonic pigments of disk-like shape, fabricated by jetting a PS nanoparticle suspension on decanol.

Moreover, drops are jetted into air and drying was achieved in the gas phase, resulting in photonic pigments of spherical shape.

5. Conclusions

We have shown the reproducible deposition of um sized photonic pigments by means of inkjet technology. Color intensity was enhanced by incorporating carbon black into the photonic balls, thus supressing multiple scattering. Moreover, the photonic pigments, manufactured with this novel method, present a higher degree of monodispersity, form highly uniform color and can be readily scaled in diameter according to the desired field of application.

Reference

1.Rochas, L.F., et al. (2004), Phys. Rev. Lett, 93, 073903
2.Liu, G., et al (2017), Materials & Design, 114, 10-17
3.Park, J-G, et al. (2014), Ang. Chem. Intl. Ed, Vol. 53, 2899-2903
4.Vogel, N., et al. (2015), Proceedings of the National Academy of Sciences of the United States of America, 112 (35), 10845-10850
5.Zhao, Y., Xie, Z., Gu, H., Zhu, C., & Gu. (2012), Chemical Society Reviews, Vol. 41, 3297-3317

Proceedings ECS 2021
Brussels, Belgium, September 7-9, 2021

Abstract T-29

CLASSIFICATION OF PATTERN FORMATION PHENOMENA IN GRAVURE PRINTING USING DEEP LEARNING APPLIED TO HIGH SPEED VIDEOS

***P. Brumm**[1,2], N. Ciotta[1], H. M. Sauer[1,2], E. Dörsam[1,2]*

[1]Technical University of Darmstadt, Department of Mechanical Engineering, Institute of Printing Science and Technology
Magdalenenstr. 2, 64289 Darmstadt, Germany

[2]Collaborative Research Center (CRC) 1194, Interaction between Transport and Wetting Processes, Project C01
Alarich-Weiss-Str. 10, 64287 Darmstadt, Germany
Email: brumm@idd.tu-darmstadt.de

Abstract
Highly dynamic pattern formation phenomena like viscous fingering strongly influence the homogeneity of printed layers. We investigate fast liquid filament dynamics in gravure printing during fluid splitting using labeled high speed videos showing finger, dot and mixed patterns. We train neural networks on a given dataset and achieve high classification accuracies of more than 90 %. The trained models allow for future automated pattern classification in order to find cause-effect correlations between pattern class and complex flow dynamics during fluid transfer.

Keywords: *pattern formation, gravure printing, forced dynamic wetting, machine learning*

1. Introduction

Highly dynamic pattern formation phenomena like viscous fingering (Saffman & Taylor, 1958) and other liquid film instabilities strongly influence the homogeneity of printed layers (Brumm et al., 2019). Especially in functional printing, e. g. in printed electronics, large-area, homogeneous surfaces with constant thickness are required (Hernandez-Sosa et al., 2013). We investigate fast liquid filament dynamics in gravure printing during fluid splitting using 555 manually labeled, in-situ high speed videos from Schäfer (Schäfer et al., 2019, Schäfer, 2020a). Each video is labeled with one of the following three classes: finger pattern (345 videos), dot pattern (138) or mixed pattern (72).

Figure 1 shows an exemplary frame from a selected finger pattern video as well as examples for all three patterns as seen on the quadratic region of interest (ROI) in the center of the example frame. Whereas finger patterns mostly occur as a printing defect in functional printing, dot patterns are used in graphical printing in form of micrometer-sized raster dots for the generation of printed images. The mixed patterns inherit great potential for future applications such as printed electronics or security features but have not been very thoroughly investigated yet (Brumm et al., 2021).

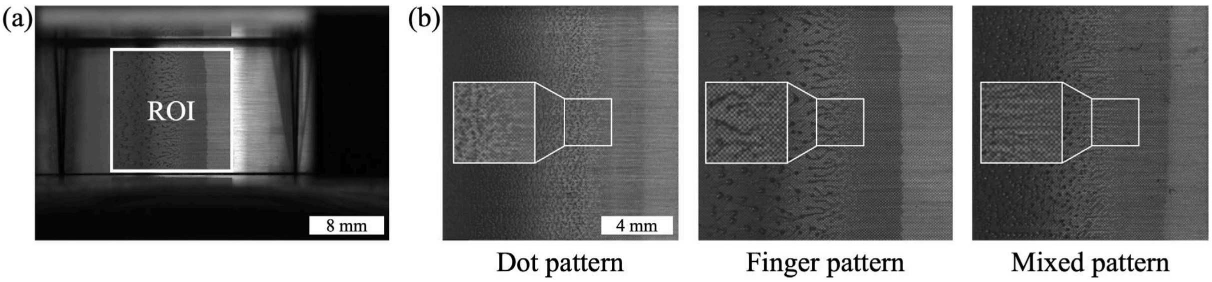

Figure 1. Examples for pattern formation phenomena in gravure printing based on the Schäfer dataset (Schäfer, 2020a, 2020b). (a) Exemplary frame with highlighted ROI (region of interest) and (b) examples for the pattern classes, cropped to the ROI.

Complex wetting processes whose exact flow dynamics are unknown are divided into phenomenological classes in order to identify a cause-effect correlation. For example, correlations between the raster engraving of the printing cylinder and the printed patterns or between the raster engraving and the dynamics of the meniscus during finger development are of interest.

Since manual labeling of the video data is a repeating, tiring and very time-consuming task, which is subject to biased human observers, we investigate the suitability of automated, supervised deep learning methods for pattern classification. Supervised learning algorithms need labeled data for training, but once trained, they can be used to classify an arbitrarily large amount of data without the need for further manual labeling. However, the trained model has the same bias as the underlying labeled data. This problem could only be avoided by using unsupervised learning approaches.

2. Experimental procedure

For automated pattern classification, we use the programming language Python together with the PyTorch-library to train neural networks of two different architectures: A recurrent neural network (RNN) architecture based on a pre-trained 'ResNet-18' model (He et al., 2016) and a three-dimensional convolutional neural network (3D-CNN) architecture based on a pre-trained 'ResNet 3D 18' model (Tran et al., 2018). Code snippets from Avendi (2020) are used as a basis for programming.

We use two thirds of the video dataset for training and the rest for validation. In a pre-processing step four frames per video (512 x 768 px @ 49.6 m/px) are extracted. Then the frames are cropped to 512 x 512 px and resized to 224 x 224 or 448 x 448 px before feeding them to the neural networks. The chosen neural network architectures take into account the temporal relationship between the extracted frames of one video. For the best performing model, additional variants with data augmentation, which increases the variety of the input data to prevent overfitting, and dataset balancing are implemented. Some models are trained only on dot and finger pattern videos (2-class-models) and the others are trained on videos of all three classes including the mixed pattern videos (3-class-models). 2,220 (1,932) frames are used for the training and validation of each 3-class-model (2-class-model). Class activation maps (CAMs) are used to investigate what parts of the input images the neural network pays attention to. In addition, for selected videos the probability for the presence of each pattern class is examined.

3. Results and discussion

After 20 training epochs, we achieve classification accuracies of more than 90 % on the validation dataset for all models, see Table 1. It can be observed that the 3D-CNN- is more suitable for this classification task than the RNN-architecture since it achieves higher validation accuracies and that the 2-class-models perform better than the 3-class-models. The latter could be explained by the fact that dot and finger patterns are more distinct from each other than dot and mixed patterns or finger and mixed patterns, see Figure 1. Therefore, the 3-class classification problem seems to be more challenging for the neural networks than the 2-class classification problem and thus achieves lower validation accuracies.

Investigation of class probabilities for selected videos supports the assumption that the mixed pattern class is the most challenging to recognize. For example, model #2, a 3-class-model, classifies a selected dot pattern video with 99.96 % probability as a dot pattern, 0.04 % as mixed pattern and 0.00 % as finger pattern whereas it classifies a selected mixed pattern video with only 76.75 % probability as a mixed pattern, 21.19 % as dot pattern and 2.06 % as finger pattern. In this case, the model is less confident when correctly classifying a mixed pattern than it is when correctly classifying a dot pattern.

Table 1. Validation accuracies of all deep learning models after 20 training epochs.

Model	Architecture	Resolution of input images in px x px	Type of model	Validation accuracy in %
#1	3D-CNN	224 x 224	2-class-model	100.0
#2	3D-CNN	224 x 224	3-class-model	99.5
#3	RNN	224 x 224	2-class-model	99.4
#4	RNN	224 x 224	3-class-model	94.6
#5	RNN	448 x 448	2-class-model	100.0
#6	RNN	448 x 448	3-class-model	95.7

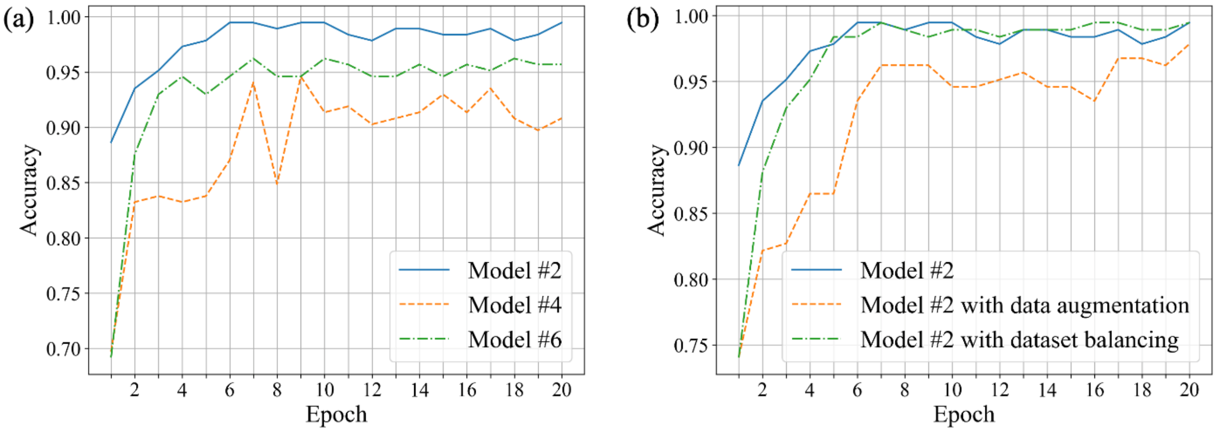

Figure 2. Validation accuracy of different models over 20 epochs. (a) Comparison of all 3-class-models and (b) influence of dataset balancing and data augmentation on the performance of model #2.

Figure 2a shows the validation accuracy plotted against the training epochs for the three 3-class-models. The best performing 3-class-model is model #2 with a maximum validation accuracy of 99.5 %. As observed in Figure 2b, additionally implementing dataset balancing does not change the validation accuracy (99.5 %), however, data augmentation slightly decreases the validation accuracy to 97.8 %. In future research, training of model #2 with data augmentation shall be extended to more than 20 epochs since the accuracy curve seems to have a rising trend from epochs 16 to 20.

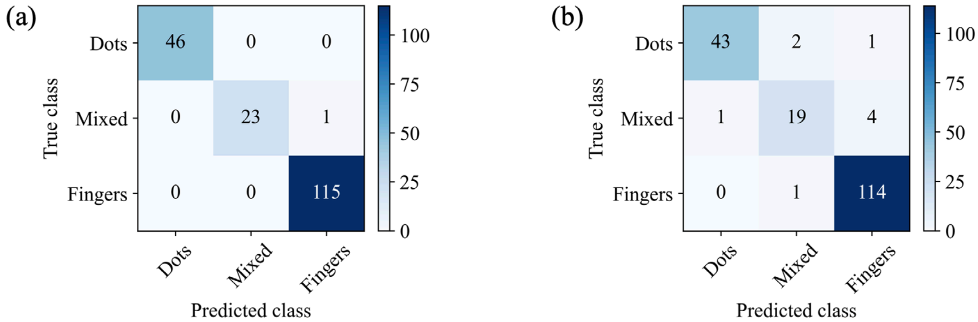

Figure 3. Confusion matrices of 3-class-models with the highest and lowest validation accuracy. (a) Model #2 and (b) model #4.

Confusion matrices for model #2 and #4 are shown in Figure 3. Both models never misclassify finger patterns as dot patterns and are most likely to misclassify the mixed pattern.

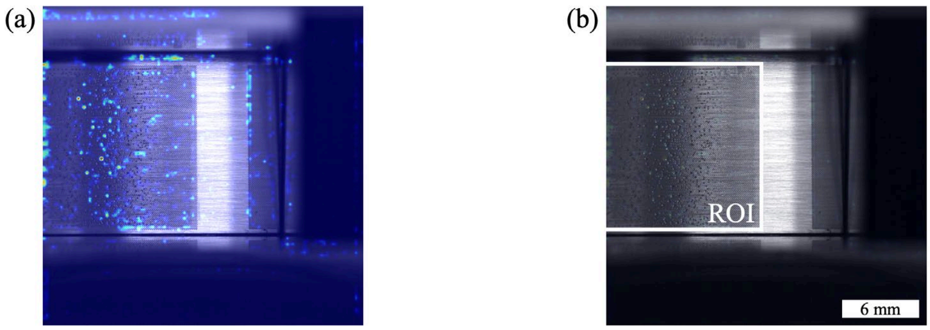

Figure 4. CAM (class activation map) for one frame of a dot pattern video. (a) Originally generated CAM and (b) adjusted CAM with more transparent heat map in order to better identify the dots in the ROI.

CAMs of selected frames applied to the first of four main-layers of model #2 are evaluated. The warmer the color of an area in the heat map, the more important this area was for the classification decision.

Figure 4 shows that the neural network pays attention to many areas within the ROI, but also to some outside the ROI. In future research it has to be validated in more detail if the neural networks focus on the ROI in later layers of the network, which would be the desired behavior.

4. Conclusions

The trained neural networks allow for automated classification of pattern formation phenomena of an arbitrarily large number of videos without further manual labeling and with high validation accuracies of more than 90 %, provided that the experimental high speed video setup does not change significantly from Schäfer's setup (Schäfer et al., 2019). In case of a significant change, the performance of the neural networks must be validated and, if necessary, the models have to be retrained with labeled high speed videos from the new experimental setup. Consideration can be given to training the models only on the stabilized ROI to obtain deep learning models more independent from the experimental conditions like the field of view. For future research, the influence of data augmentation for a training duration of more than 20 epochs should be evaluated. 'White box' approaches in the form of deterministic classification algorithms shall be developed for comparison with the 'black box' deep learning approach as investigated in this paper.

5. Acknowledgements

We kindly acknowledge the financial support by the Deutsche Forschungsgemeinschaft (DFG, German Research Foundation) – Project-ID 265191195 – SFB 1194 'Interaction between Transport and Wetting Processes', project C01.

References

Avendi, M. (2020). *PyTorch Computer Vision Cookbook: Over 70 recipes to master the art of computer vision with deep learning and PyTorch 1.x*. Packt.

Brumm, P., Sauer, H. M. & Dörsam, E. (2019). Scaling Behavior of Pattern Formation in the Flexographic Ink Splitting Process. *Colloids and Interfaces*, 3 (1), 37. https://doi.org/10.3390/colloids3010037

Brumm, P., Weber, T. E., Sauer, H. M. & Dörsam, E. (2021). Ink splitting in gravure printing: localization of the transition from dots to fingers. *Journal of Print and Media Technology Research*. Accepted for publication. He, K., Zhang, X., Ren, S. & Sun, J. (2016). Deep residual learning for image recognition. In *Proceedings of the IEEE conference on computer vision and pattern recognition* (pp. 770-778).

Hernandez-Sosa, G., Bornemann, N., Ringle, I., Agari, M., Dörsam, E., Mechau, N. & Lemmer, U. (2013). Rheological and Drying Considerations for Uniformly Gravure-Printed Layers: Towards Large-Area Flexible Organic Light-Emitting Diodes. *Advanced Functional Materials*, 23 (25), 3164–3171. https://doi.org/10.1002/adfm.201202862

Saffman, P. G. & Taylor, G. (1958). The Penetration of a Fluid into a Porous Medium or Hele-Shaw Cell Containing a More Viscous Liquid. *Proceedings of the Royal Society A: Mathematical, Physical and Engineering Sciences*, 245 (1242), 312–329. https://doi.org/10.1098/rspa.1958.0085

Schäfer, J., Roisman, I. V., Sauer, H. M. & Dörsam, E. (2019). Millisecond fluid pattern formation in the nip of a gravure printing machine. *Colloids and Surfaces A: Physicochemical and Engineering Aspects*, 575, 222–229. https://doi.org/10.1016/j.colsurfa.2019.04.085

Schäfer, J. (2020a). *In situ Untersuchung der hochdynamischen Grenzflächeninstabilität im Zylinderspalt*. TUprints. https://tuprints.ulb.tu-darmstadt.de/14204

Schäfer, J. (2020b). *Messdaten und Auswertungssoftware für die hochdynamische Grenzflächeninstabilität im Zylinderspalt*. [Software, Image, Other] https://doi.org/10.25534/tudatalib-191.2

Tran, D., Wang, H., Torresani, L., Ray, J., LeCun, Y. & Paluri, M. (2018). A closer look at spatiotemporal convolutions for action recognition. In *Proceedings of the IEEE conference on Computer Vision and Pattern Recognition* (pp. 6450-6459).

MATERIAL COATING

Proceedings ECS 2021
Brussels, Belgium, September 7-9, 2021

Abstract T-62

EXTRUSION AND DEPOSITION OF A MOLTEN POLYMER IN FUSED DEPOSITION MODELING

A. Gosset[1], ***D. Barreiro-Villaverde[2]***, ***J. C. Becerra-Permuy[1]***, ***M. Lema[2]***, ***A. Ares-Pernas[1]***, ***M. J. Abad López[1]***

[1]Techonological Research Center (CIT), University of A Coruña
Campus de Esteiro, 15403 Ferrol, Spain

[2]CITIC Research, University of A Coruña
Campus de Elviña, 15072 A Coruña, Spain

Email: anne.gosset@udc.es (corresponding author)

Abstract

In this work, the behaviour of a molten thermoplastic extruded from the nozzle of a Fused Deposition Modeling (FDM) printer head is analysed numerically and experimentally, focusing on high printing speeds. The extrusion and deposition of a single strand of Poly-Lactic Acid (PLA) is characterized before crystallization with a high-speed visualization technique. A two-phase CFD model is validated with this data in terms of strand height and meniscus shape. The dimensions of the printed layer are also in good agreement with the measurements of the solidified strands by microscopy.

Keywords: *3D printing, Fused Deposition Modeling, Thermoplastic, CFD simulation, flow visualization.*

1. Introduction

Fused Deposition Modeling (FDM) is an additive manufacturing technique that has gained great popularity due to the decreasing cost of desktop 3D printers and their availability to a large public. In this technique, a thermoplastic filament is melted in a liquefier and then extruded through a small diameter nozzle, which moves in a controlled manner to deposit layers on top of each other and form a 3D object (figure 1). The final quality of the pieces fabricated with FDM is strongly linked to the shape, size and surface finish of the strands deposited successively, which themselves depend on the printing parameters and extruded material properties (Turner et al., 2014). In presence of a newly designed material, with given functional properties and rheology, it is thus important to be able to determine the process window in which the extrusion and deposition will be optimum. For that purpose, we use in this work a simplified two-phase CFD model based on isothermal and viscous flow assumptions as in (Comminal et al., 2018) and (Serdeczny et al., 2018), to predict the behaviour of the molten polymer flow during the deposition of a single strand on a solid surface. On the other hand, an experimental characterization of the process is carried out on a desktop 3D printer with Poly-Lactic Acid (PLA), by means of high-speed visualization of the bead region between the substrate and the nozzle, where the molten polymer is still in liquid phase and where the behaviour of the meniscus determines the limits of the process in terms of printing speed (Gosset et al., 2020).

2. Numerical Methodology

The numerical simulations were carried out with the two-phase incompressible flow solver *interFoam* of the open-source finite volume libraries *OpenFOAM*. The tracking of the interface between the molten polymer and the air is based on the Volume of Fluid (VOF) method. The flow is considered isothermal in the computations; as we are mostly interested in the region right after extrusion, the variation of temperature, and thus of viscosity, is assumed to be small enough to have no influence in this inertialess flow regime. A shear-thinning viscous flow behaviour is assumed for the molten polymer, while viscoelastic effects are disregarded. The simulations reproduced the exact conditions of the experiments described in section 3, with the measured printing velocity and the estimated extrusion velocity. The computational domain includes the final part of the extrudor nozzle, which is 1.3 mm long, with 0.2 mm thick rims. The computational grid was built using the opensource libraries *cfMesh*. The base mesh shown in figure 2 features cubic cells of size 80 μm, refined to 20 μm in the region of the strand.

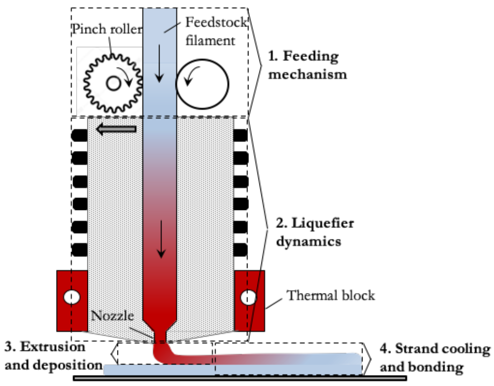

Figure 1. Sketch of a FDM 3D printer head

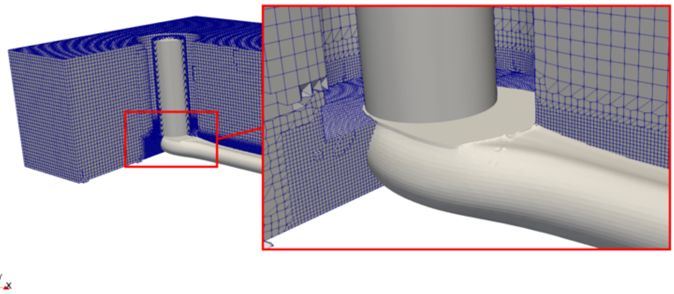

Figure 2. Details of the computational mesh and strand interface

3. Experimental characterization

The experiments were conducted on a desktop open-source MendelMax XL V6 3D printer. A simple perimeter was printed, for which the G-code is manually written. The high-speed visualizations were carried out during the printing of the first 278 mm long straight line. A Phantom camera was used, with a Canon macro-lens to capture the meniscus region with a spatial resolution of $9.4 \pm 2\%$ $\mu m/pxl$. A frame rate of 3600 FPS with an exposure time of 140 μs was deemed sufficient to capture accurately the motion of the printing head. The region was illuminated by an array of pulsed LEDs synchronized with the camera, whose light was diffused with translucent paper. The experiments were carried out with commercial PLA (Smartfil, ivory) at a temperature of 215 ± 1°C, while the substrate was maintained at 60 ± 1°C. The filament had a diameter $D_f = 1.75 \pm 0.05$ mm. Two values were considered for the nozzle to substrate separation h: 0.2 and 0.3 mm, corresponding to normalized separations $h/d = 0.5$ and 0.75, where d is the nozzle diameter. For each of them, three different print speeds were tested ($V = 15$, 22 and 30 mm/s), with the extrusion volumetric rate adjusted to reach a strand width of approximately 0.4

This means that the ratio of the printing speed V to the mean extrusion speed U was kept constant while varying V. This ratio V/U was equal to 2 for $h/d = 0.5$ and 1.3 for $h/d = 0.75$. The high-speed animations were processed with Matlab to extract the strand contours (figure 3), as well as the instantaneous velocity of the printing head. After the tests, the morphology of the solidified strands was analysed using an Emission Scanning Electron Microscope, with a magnification $\times$ 200. The samples were introduced in liquid nitrogen and cryogenically broken to avoid the plastic deformation on fracture surfaces and strand section.

4. Results and discussion

The longitudinal profiles of the strand are first confronted to the high-speed images, when the melt flow is still in liquid phase. An example is shown in figure 3, for the two sets of conditions. The shape of the meniscus is in general very well recovered within the spatial resolution of the images.

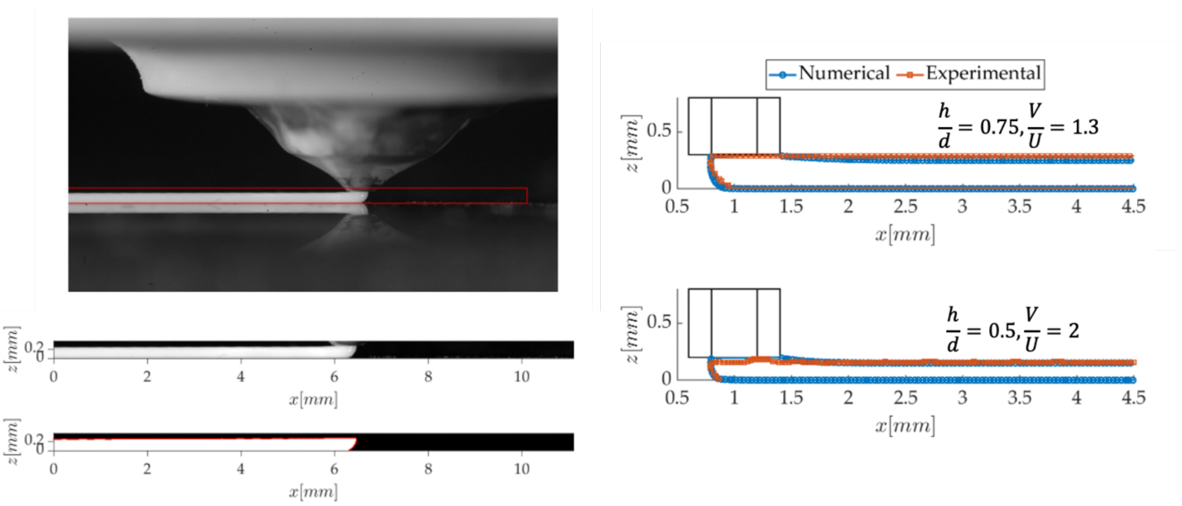

Figure 3. High-speed flow visualization and extraction of strand contours (left), comparison of numerical predictions and experimental results for $h/d = 0.75, V/U = 1.3$ and $h/d = 0.5, V/U = 2$ (right).

In spite of their interest to analyse the meniscus region, the high-speed animations do not provide information on the layer width. For that, the solidified strands were used, whose magnified cross section is shown in figure 4. The comparison of the strand shape is illustrated for the two values of h/d in the same figure, where the experimental shape results from the averaging of 3 to 5 sections. The agreement is in general very good, indicating that even when viscoelastic and thermal effects are disregarded, the CFD model used here is a reliable tool to predict the final shape of the printed filaments within the range of printing parameters under study. Finally, the effect of the printing to extrusion velocity ratio on the strand height (H) and width (w) is illustrated in figure 5. As expected, the deposited polymer road is wider at smaller V/U values, for a constant separation h/d: this is because the extruded volumetric flux is larger compared to the printing speed. It is also interesting to note that the layer height is smaller than h for $V/U = 2$, while it is equal to h for a ratio of 1. In the later case, one can observe how the contact between the nozzle rims and the strand sets the layer height, even if there is a slight depression in the center (also observed in Comminal et al., 2018, in similar conditions).

At the larger printing speed $V/U = 2$, the interaction between the deposited stream of melt and the nozzle is weaker (at least on the bead side), and therefore the strand is more "free" to set its height. Comminal et al. (2018) state that the common approximation that the layer height H equals the nozzle separation h is valid only when $h < d\sqrt{U/V}$. While it is clearly verified for $V/U = 1$, this relation does not hold for the highest ratio. However, the authors did not investigate such a high velocity ratio range. This finding might be of interest for further studies focusing on high printing speeds.

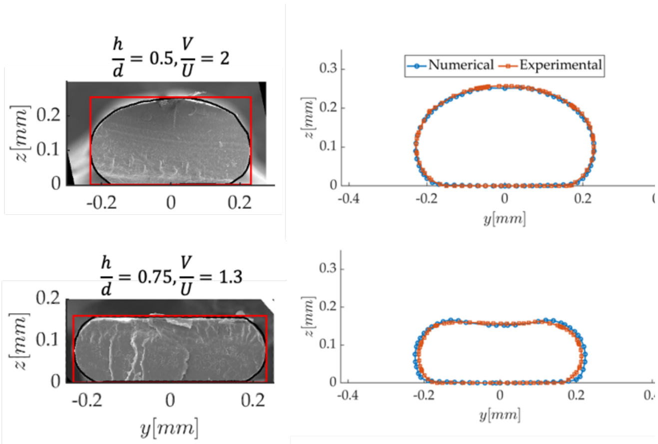

Figure 4. Magnified cross-section of the solidified strands (left) and comparison with numerical predictions (right).

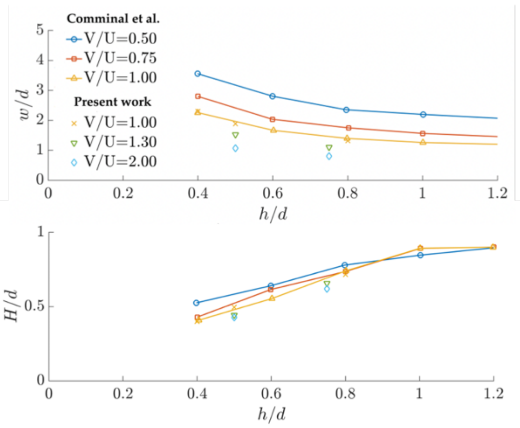

Figure 5. Strand width (top) and height (bottom) as a function of the printing parameters.

5.Conclusions

This paper presents an experimental and numerical study of the extrusion and deposition of a single strand of PLA by FDM. The predicted shape of the extruded flow in the meniscus region is well validated by high-speed visualization, and the strand dimensions predicted by CFD coincide in general very well with the ones of the solidified samples measured by SEM. This extends the conclusions of Serdeczny et al. (2018) to high printing speeds.

References

Comminal, R., Serdeczny, M. P., Pedersen, D. B., Spangenberg, J. (2018) Numerical modeling of the strand deposition flow in extrusion-based additive manufacturing. Add. Manuf., 20, 68-76.
Gosset, A., Barreiro-Villaverde, D., Becerra Permuy, J.C., Lema, M., Ares-Pernas, A., Abad López, M.J. (2020) Experimental and Numerical Investigation of the Extrusion and Deposition Process of a Poly(lactic Acid) Strand with Fused Deposition Modeling. Polymers, 12(12), 2885. https://doi.org/10.3390/polym12122885
Serdeczny, M. P., Comminal, R., Pedersen, D. B., Spangenberg, J. (2018) Experimental validation of a numerical model for the strand shape in material extrusion additive manufacturing. Add. Manuf., 24, 145-153.
Turner, B. N., Strong, R., Gold, S. A. (2014). A review of melt extrusion additive manufacturing processes: I. Process design and modeling. Rapid Protot. J., 20, 192-204.

Proceedings ECS 2021
Brussels, Belgium, September 7-9, 2021

Abstract T-56

ROLL-TO-ROLL COATING OF CHNF AND CNC BILAYER THIN FILM

Kwangjun Jung[1]*, *Yue Ji[2]*, *Tae-Joong Jeong[1]*, *J. Carson Meredith[2]*, *Tequila A. L. Harris[1]

[1] School of Mechnical Engineering, Georgia Institute of Technology, United States
[2]School of Chemical and Biomolecular Engineering, Georgia Institute of Technology, United States

Abstract
Cellulose and chitin are two of the most copious naturally produced biopolymers that have great potential in an application for sustainable barrier materials for various packaging. The objective of this work is to understand the limitations and establish a cost-efficient manufacturing process associated with fabricating barrier layer thin films composed of chitin nanofiber and cellulose nanocrystal using dual-layer slot die coating on a roll-to-roll system. It has been found that barrier properties are improved when forming this bilayer.

***Keywords**: Continuous Roll-to-Roll, dual layer slot die coating, biopolymers, barrier layer thin films, Drying*

1. Introduction

Two of the most abundant biopolymers produced in nature are Cellulose and chitin.[1,2] Cellulose and chitin nanomaterials are perfect to be fabricated into the barrier films because of high crystallinity, resulting in high modulus tensile strength.[3,4] This made them the promising candidate for renewable, biodegradable materials for applications such as primary packaging for food, electronics, and pharmaceutical/ medical products.[5.] This study explores the feasibility of lab-scale manufacturing cellulose nanocrystals (CNC) and chitin nanofibers (ChNF) using a continuous dual-layer coating process and discusses the challenges related to the process. In addition, the functionality related to the barrier properties of the film will be discussed relative to film thick and drying conditions. This work provides a gateway for fabricating biodegradable bilayer thin films using a scalable approach.

2. Theory

Slot die coating requires an understanding of the fluid properties for both the coating and drying process. For dual-layer slot die coating the flow and interfacial dynamics between two liquids must be understood during the liquid and/or solidification phases, to avoid defect formation. During the coating process, the surface tension of coating material on the bottom must be higher than the surface tension of the coating material on top to ensure the uniform spreading of the top layer across the bottom layer.[6]

Further, a balance between the viscosity of the upper and lower viscosity is necessary.

3. Experimental procedure

The contact angle and the surface tension of both coating materials were measured using the Sessile drop and Pendant drop methods on a goniometer at room temperature. The contact angle between the coating materials and cellulose acetate (CA) film was measured. The surface tension of each coating material was measured. Prior to coating, the surface of the CA substrate was UV-ozone treated. Duallayer slot die coating were formed with varying substrate speeds and flow rates for each coating material, by pumping the fluids onto a moving web. A schematic of the dual-layer slot die coating system on a roll-to-roll (R2R) is shown in Figure 1. Subsequently, the barrier film was dried and the oxygen transmission rates measured.

4. Result and discussion

The surface tension of ChNF was found to be higher than that of CNC. Therefore, CNC acted as the top coating of the ChNF/CNC bilayer coated on a CA substrate during the dual-layer coating process. To promote wetting, the surface of the CA substrate was surface treated for up to 5 mins. Then the optimal UV ozone treating condition was determined based on the scalability of the process and the upper working temperature of the CA substrate. Guided by partial coating windows of each fluid and the balance between the fluid properties and flow dynamics, dual-layer slot die coating process was established to successful fabricate ChNF/CNC barrier layer film. After establishing a sufficient drying time and temperature, the samples were characterized where it was found that the permeability was improved by greater than 10% for the dual-layer slot die coated barrier layers, compared to spray coated film.

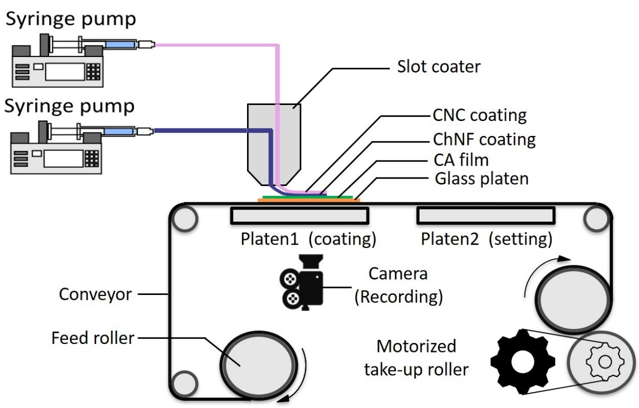

Figure 1. Schematic of dual layer slot die coating on a R2R setup

Abstract T-56

5. Conclusions

It has been shown that dual-layer slot die coating of cellulose and chitin-derived materials on a R2R system will lead to enhanced barrier film properties. This work allows for processing biodegradable thin film more rapidly with a scalable process.

References

(1)Klemm, D.; et al. Cellulose. In Biopolymers in 10 volumes (volume 6 Polysaccharides II: Polysaccharides from Eukaryotes); De Baets, S., Vandamme, E., Steinbüchel, A. T., Eds.; Wiley-VCH: Germany, 2004.
(2)Barikani, M.; Oliaei, E.; Seddiqi, H.; Honarkar, H. Preparation and application of chitin and its derivatives: a review. Iran. Polym. J. 2014, 23, 307−326.
(3)Belbekhouche, S.; Bras, J.; Siqueira, G.; Chappey, C.; Lebrun, L.; Khelifi, B.; Marais, S.; Dufresne, A. Water sorption behavior and gas barrier properties of cellulose whiskers and microfibrils films. Carbohydr. Polym. 2011, 83 (4), 1740−1748.
(4)Wu, J.; Zhang, K.; Girouard, N.; Meredith, J. C. Facile Route to Produce Chitin Nanofibers as Precursors for Flexible and Transparent Gas Barrier Materials. Biomacromolecules 2014, 15 (12), 4614−4620.
(5)Satam, Chinmay C.; Irvin,Cameron W.; Lang, Augustus W.; Jallorina, Jerel Cedric R.; Shofner, Meisha L.; Reynolds, John R.; Meredith, Carson J. "Spray-Coated Multilayer Cellulose Nanocrystal—Chitin Nanofiber Films for Barrier Applications." ACS Sustainable Chemistry & Engineering, vol. 6, no. 8, 2018, pp. 10637–10644., doi:10.1021/acssuschemeng.8b01536.
(6)Gutoff, EB, Cohen, ED, Coating and Drying Defects. Wiley, New York, 1995

Proceedings ECS 2021
Brussels, Belgium, September 7-9, 2021

Abstract T-77

DEVELOPMENT OF SOLID ELECTROLYTE CELL BY SPRAY COATING

M. Jacobs,[1], ***Evgeniya Khomyakova***[2] ***and V. Middelkoop***[1]

[1] Coating And Shaping Technologies, Flemish Institute for Technological Research

Boeretang 200, 2400 Mol, Belgium

[2] Ceramic Powder Technology AS, Cerpotech

Kvenildmyra 6, N-7072 Heimdal, Norway

Email: Marijke.jacobs@vito.be presenting/corresponding author

Abstract
Solid oxide electrolyte cells can be used as oxygen separator to generate a CO stream after the plasmolysis of CO2. Electrode layers of the cell are applied by spray coating on yttria-stabilized zirconia planar electrolytes. The coating parameters such as atomization pressure and coating speed were optimized to obtain uniform coatings and to control the thickness. The suspension formulation was adjusted to have an optimal adhesion and quality of the coating. The coating thickness, porosity and internal resistance were determined.

Keywords: *Spray coating, SOEC, electrodes*

1. Introduction

In recent years, more and more efforts have been made to shift to renewable energy to reduce CO_2 emissions and to combat global warming. Most known types of renewable energy are solar and wind energy, but they suffer from a non-constant supply of power. To overcome this limitation, the storage of energy is needed to match supply and demand of energy. Solid oxide cells (SOCs) are a very promising technology for temporary energy storage and offer a high energy efficiency (50-70 %) at high operating temperatures (600 to 900 °C). They can be used as solid oxide fuel cell (SOFC) to convert fuels such as natural gas or hydrogen with a high efficiency into electricity and heat. SOCs can also operate in reverse mode as solid oxide electrolysis cell (SOEC) to convert water steam into hydrogen using electricity.

As such, SOECs allow the use of surplus renewable electricity to produce hydrogen as storable fuel. In addition, these SOECs can also reduce CO_2 and steam into H_2 and CO directly, the so-called co-electrolysis process. The obtained syngas can serve as the basis for the production of other fuels in further steps (Bernadet, 2020). Another less known function of SOEC is the capability as electrochemical oxygen separator to separate oxygen from an oxygen containing gas mixture such as after plasma CO_2 dissociation. This function is an important step in the European KEROGREEN project which aims to develop sustainable aircraft kerosene based on water and air powered by renewable electricity. To create a CO stream for Fischer-Tropsch synthesis after the plasmolysis of CO_2 an oxygen separator based on a solid oxide electrolyte cell was chosen. Such a cell consists of a plasma electrode, a dense electrolyte and an oxygen electrode. All these layers are rather thin (<50 µm) except one to give mechanical robustness. Depending on which layer is thick, the solid oxide cell is called electrolyte or anode based for example.

In this work, the focus is on electrolyte based solid oxide cells. The electrolyte substrates need to be covered with thin porous electrode layers to have a complete cell. Several technologies exist to apply these thin electrode layers: i) chemical methods such as chemical vapor deposition and sol-gel; ii) physical methods as thermal spraying, laser deposition and physical vapor deposition; iii) ceramic powder processing methods (tape casting, screen printing, dip coating, spin coating and spray coating) (Kim, 2006). The ceramic powder processing methods are often selected as these methods are less expensive, more simple and industrially scalable compared to the chemical and physical methods to overcome the high manufacturing cost of SOCs (dos Santos-Gómez, 2018). Spray coating is selected as deposition technology since this technology allows a) a greater control of the thickness of the coated layers, b) the accommodation of larger substrates and c) the ability to obtain porous layers onto both planar and tubular electrolyte substrates.

2. Theory

A schematic of a solid oxide electrolyte cell which is used as oxygen separator is shown in Figure 1. In general high oxygen fluxes are needed and the cell should be stable. The electrolyte should have a low resistance and a high oxygen ion conductivity. Both electrodes must have both electronic and ionic conductivity. In case of the plasma electrode, the CO oxidation must be limited. As electrolyte yttria stabilized zirconia is most widely used due to its good ionic conductivity, low electronic conductivity and outstanding chemical stability. This layer should also be dense, while the electrodes must be porous to have a large surface exchange area.

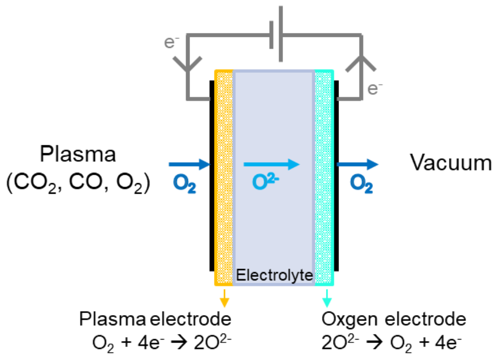

Figure 1. Schematic of an oxygen separator based on a solid oxide electrolyte cell.

3. Experimental procedure

The electrode layers are applied by spray coating on yttria-stabilized zirconia (YSZ) planar substrates of 250 µm thickness and 20 mm diameter, which serve as the electrolyte layer (Jacobs, 2015). For the electrodes the most promising La-based perovskite materials were selected based on their conductivity and ability to suppress the CO to CO_2 back reaction at the plasma side, and produced by Cerpotech (Middelkoop, 2014). As these perovskites tend to react with the zirconia at temperatures >1000 °C, a dense interlayer is needed to prevent reactions between the electrolyte end the electrodes. For this interlayer, $Ce_{0.8}Gd_{0.2}O_2$ (GDC) was chosen as it is most often used in literature. The coating parameters such as atomization pressure and coating speed were optimized to obtain uniform coatings and to control the thickness. The suspension formulation was adjusted to improve the adhesion and the quality of the coating. Profilometry and microscopy were used to determine the coating thickness and porosity. Furthermore, electrochemical impedance spectroscopy were carried out.

4. Results and discussion

Several YSZ discs were first coated with a dense interlayer to prevent reactions between electrolyte end electrodes. Then, an oxygen and plasma electrode layer were applied, followed by thermal treatment up to 1100 °C for 2h. The coatings show a good adhesion to the YSZ discs and look rather uniform. Both electrode layers are porous and are about 10 µm thick. SEM images of the cross section of the produced electrode layers are given in Figure 2. Both interlayers are dense and only of a few µm thickness. Based on the EDS mappings, there seems to be no interactions between the different layers.

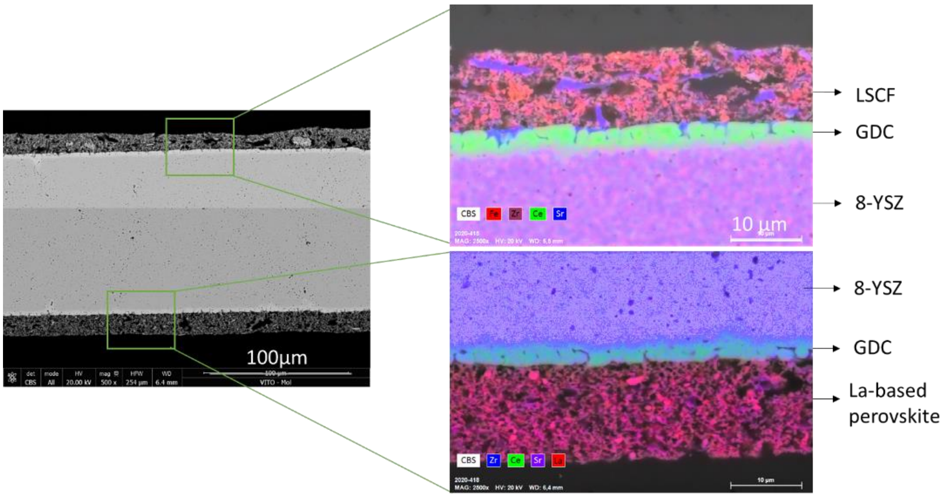

Figure 2. SEM/EDS images of the cross section produced SOEC by spray coating with LSCF as oxygen electrode, GDC as interlayer, 8-YSZ as electrolyte and a La-based perovskite as plasma electrode.

Besides the microstructural characterization, the internal resistance of the developed cells was measured by electrical impedance spectroscopy at different temperatures. The total impedance determined at 800°C in dry air was reduced to 10 Ohm by using the extra interlayer to prevent interactions compared to the impedance of the cell without interlayers. This indicates that the interlayer was successfully applied.

5. Conclusions

For the removal of oxygen from a plasma atmosphere, an oxygen separator based on a solid oxide electrolyte cell (SOEC) was selected. For the deposition of the electrode layers of the SOEC spray coating was used as it allows a good control over the coating thickness. Uniform, thin porous electrode layers and a dense interlayer were successfully achieved by i) optimization of the coating parameters such as atomisation pressure and coating speed and by ii) optimization of the suspension properties, namely the formulation, particle size and the suspension viscosity. The electrochemical performance of the SOEC was determined by impedance spectroscopy. Cells with an interlayer exhibited a lower resistance and thus improved performance compared with cells without interlayers.

References

Bernadet, L. et al (2020). High-performing electrolyte-supported symmetrical solid oxide electrolysis cells operating under steam electrolysis and co-electrolysis modes. *International Journal of Hydrogen Energy,* in press. dos Santos-Gómez, L. et al (2018). Durability and performance of CGO barriers and LSCF cathode deposited by spray-pyrolysis. *Journal of the European Ceramic Society*, 38, 3518–3526.
Jacobs, M. et al (2015). Surface activation of asymmetric $CaTi_{1-x}Fe_xO_{3-\delta}$ tubular membranes for oxygen separation. *Journal of Membrane Science*, 477, 58-64.
Kim, W.-H. et al (2006). Intermediate temperature solid oxide fuel cell using (La,Sr)(Co,Fe)O3-based cathodes. *Solid State Ionics*, 177, 3211–3216.
Middelkoop, V. et al (2014). Development and characterisation of dense lanthanum-based perovskite oxygen-separation capillary membranes for high-temperature applications. *Journal of Membrane Science,* 468, 250-258.

Acknowledgement

The KEROGREEN project receives funding from the European Union's Horizon 2020 Research and Innovation Programme under Grant Agreement 763909.

Proceedings ECS 2021
Brussels, Belgium, September 7-9, 2021

Abstract T-23

ANALYSIS ON COATING DIE MANIFOLD FLOWS OF VISCOPLASTIC MATERIALS

***H. Jung*[1], *J. Nam*[2]**

[1,2]Department of Chemical and Biological Engineering, Seoul National University
Seoul 08826, South Korea
Email: jaewooknam@snu.ac.kr

Abstract
Slot coating is one of the most preferred processing methods to manufacture lithium-ion secondary battery electrodes. Battery slurries may exhibit Newtonian behavior or shear-thinning behavior depending on the specification of the final products. In particular, there are many battery slurries that exhibit yield stress, which behave like a solid below that stress. If such an unyielded area occurs inside the slot die manifold, it may affect the flow uniformity at the feed slot exit. In this study, we used the Electrical Network Method (ENM) with an optimization scheme to find a minimum of flow rates deviations with a constraint of minimum unyielded regions. The viscoplastic fluid was modeled by the Papanastasiou's viscosity function. The results were validated through numerical computation based on Finite Element Method (FEM). The FEM results also predict nonlinear phenomena such as recirculating flows due to the inertia, which cannot be explained with ENM.

Keywords: *Slot coating, Die manifold, Yield stress, Electrical Network Method, Finite Element Method*

1. Introduction
Slot coating is a preferred industrial processing method to manufacture thin and uniform films since it is possible to control the film thickness precisely by flow rate and production speed. In the slot coating method, a coating die manifold, which consists of a large cavity and a narrow channel, plays a significant role in the uniformity of final film products because it is the first region where coating solutions are fed and distributed in the width direction. The existing coating die manifolds focus on maintaining a high degree of flow rates uniformity of Generalized Newtonian Fluids.

However, many materials such as slurries, pastes, or concentrated suspensions are used as a coating solution, which they often exhibit yield behavior: they can only flow above a certain level of stress. Therefore, they can continue to accumulate in the unyielded region inside the coating die manifold and damage the flow rates uniformity. To prevent this, the relationship between the unyielded region and the flow rates uniformity should be clearly identified, and the die manifold should be designed in consideration of this.

Generally, there are two numerical methods for the flow analysis of coating die manifold: One is Computational Fluid Dynamics (CFD) method, which is rigorous and has strength in detailed analysis. However, it requires high computational costs for sensitivity analysis or finding an optimal die design. Alternatively, Electrical Network Method (ENM), which is based on the fluidics - electronics analogy, is rather simple but more useful for the above analysis. Here, we used both methods to analyze the viscoplastic flows inside the die manifold.

2. Theory
In this study, we considered an incompressible, isothermal, Bingham fluid flow with constant density inside the die manifold. The Papanastasiou's model is used to model viscoplastic fluid.

$$\eta(\dot{\gamma}) = \eta_N + \frac{\tau_y(1 - \exp(-n|\dot{\gamma}|))}{|\dot{\gamma}|} \tag{1}$$

Electrical Network Method (ENM)
In ENM, die cavity and feed slot are divided into finite number of control volumes, assuming cylindrical and rectangular channels, respectively. Flow through the control volumes is assumed to be 1-dimensional Hagen-Poiseuille flow, which has the simplifying relationship as

$$Q = \frac{\Delta p}{R_H} \tag{2}$$

where the hydraulic resistance R_H is defined as

$$R_H = \frac{8\eta L}{\pi R^4}\ (Circular\ channel), \qquad R_H = \frac{12\eta L}{WH^3}(Rectangular\ channel). \tag{3}$$

Based on the physical similarities between fluidics and electronics, the fluidic networks can be analyzed with block matrix calculation of Ohm's law & Kirchhoff's law.

$$\begin{bmatrix} \underset{(m\times m)}{\mathbf{C}^{-1}} & \underset{(m\times n)}{\mathbf{A}} \\ \underset{(n\times m)}{\mathbf{A}^T} & \underset{(n\times n)}{\mathbf{0}} \end{bmatrix} \begin{bmatrix} \underset{(m\times 1)}{w} \\ \underset{(n\times 1)}{u} \end{bmatrix} = \begin{bmatrix} \underset{(m\times 1)}{b} \\ \underset{(n\times 1)}{f} \end{bmatrix}$$

$\mathbf{C}$: Conductance matrix
$\mathbf{A}$: Incidence matrix
w : edge currents
u : node voltage
b, f : sources

Figure 1. Block matrix related to the fluidic networks

3. Results and discussion

Effect of yield stress on flow rates uniformity
As seen in Figure 2, the greater the yield stress, the worse the flow rates uniformity in the width direction. It is because unyielded region inside the die manifold prevents the flow from being evenly distributed.

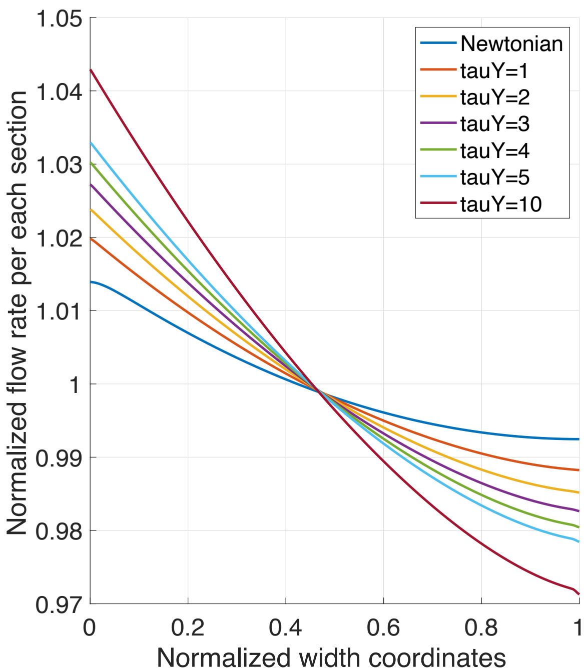

Figure 2. Flow rates per unit width at the feed slot exit with varying yield stress.

Figure 3 is a CFD result showing how the unyielded region is formed inside the manifold. At the low yield stress level, the unyielded region exists only at the both ends of the cavity. However, in the case of a fluid with high yield stress, it can be confirmed that it is also generated inside. To be precise, the trend depends on the size of Reynolds number and Bingham number.

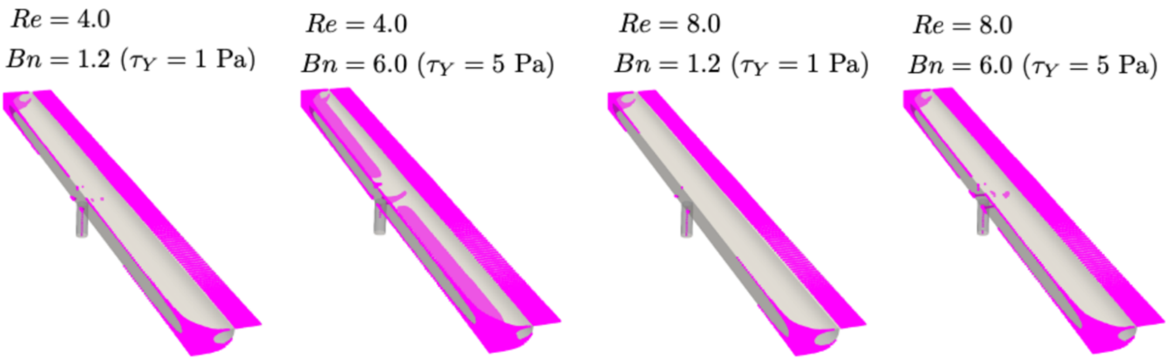

Figure 3. CFD result showing the unyielded area inside the die manifold.

4. Conclusions

Papanastasiou's viscosity model is widely used to describe ideal Bingham fluid. With this model, we used two numerical methods, ENM and CFD, for the viscoplastic flow inside the coating die manifold. ENM results show the flow rates uniformity at the feed slot exit gets worse with increasing yield stress. Moreover, detailed information of velocity fields or the location of unyielded area are also shown in the CFD results. Based on these results, we can propose an optimal die manifold design when using the viscoplastic material as a coating solution.

References

Sartor, L. (1990), *Ph.D.Thesis* (University of Minnesota)
Papanastasiou, TC. (1987), *Journal of Rheology* **31**, 385-404
Yilmaz, O., Kirkkopru, K. (2020), *Fibers and Polymers* **21**, 204-215

Proceedings ECS 2021
Brussels, Belgium, September 7-9, 2021

Abstract T-32

SIMPLE METHODS FOR OBTAINING FLOW REVERSAL CONDITIONS IN COUETTE-POISEUILLE FLOWS

***H. Kwak*[1], J. Nam[1]**

[1]School of Chemical and Biological Engineering, Seoul National University
1 Gwanak-ro, Gwanak-gu, Seoul 08826
Email: jaewooknam@snu.ac.kr

Abstract
In this study, exact and approximate methods for computing the critical conditions at which flow reversal occurs in the Couette–Poiseuille flows are presented. The fluid considered in the study is generalized Newtonian fluid which does not exhibit yield stress. The approximate method predicted the critical conditions under most operating parameter range with the exception of the cases where the flow curve in log–log scale exhibited high nonlinearity.

Keywords: *Couette–Poiseuille flows; Flow reversal; Approximation methods; Generalized Newtonian fluids*

1. Introduction
When certain operating conditions are met, vortices can form within the coating bead flow of slot die coating process. Once formed, they can cause numerous problems such as particle aggregation and destruction of widthwise flow uniformity, all of which severely interfere with the process operation and degrade the quality of final coated product. Thus it is important to figure out the range of operating conditions that lead to the formation of vortices in advance and avoid operating within that range.

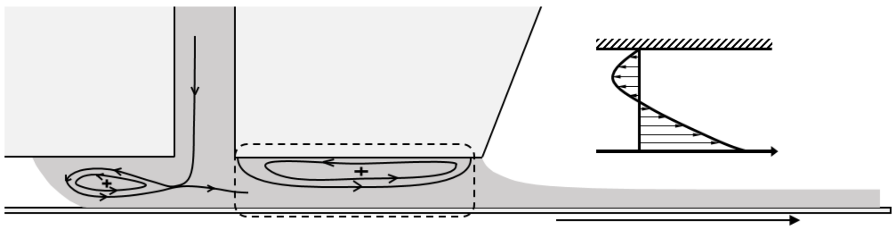

Figure 1. System under consideration

2. Methods
One simple method for determining the critical operating condition is to assume the coating bead flow under the die lip as a simple one-dimensional (1-D) Couette–Poiseuille (C–P) flow and find the flow reversal condition instead, which strongly hints the existence of vortex in the actual flow. In this study, we propose a semi-analytical method for determining the flow reversal condition in the C–P flow of generalized Newtonian fluids (GNFs), as well as a fully-analytical approximate method for determining same condition with a reasonable accuracy.

The *semi-analytical method* is derived using Weissenberg–Rabinowitsch equation (Kim, 2018; Makosko, 1994), which is used extensively in the field of capillary rheometry. It does not require one to obtain the velocity profile, saving the computational load and time required to solve the non-linear differential equation. The only numerical procedure involved is the numerical integration and a simple root-finding algorithm, whose convergence is guaranteed owing to the properties of the C–P flow.

We also propose a method which approximates the viscosity to follow power-law locally around an apparent shear rate. With this *local power-law approximation* (LPLA) method, it is possible to derive a fully analytical expression of the flow reversal condition for different types of GNFs.

3. Results and discussion

The methods are applied to the flows of Carreau–Yasuda (C-Y) and Bingham–Carreau–Yasuda (B–C–Y) fluids. The critical flow rate and pressure gradient conditions predicted by the LPLA method agreed well with the exact values computed by the semi-analytical method. The relative errors of the estimated values were mostly within the acceptable range (< 10%), excluding the cases where the log–log flow curve showed high nonlinearity.

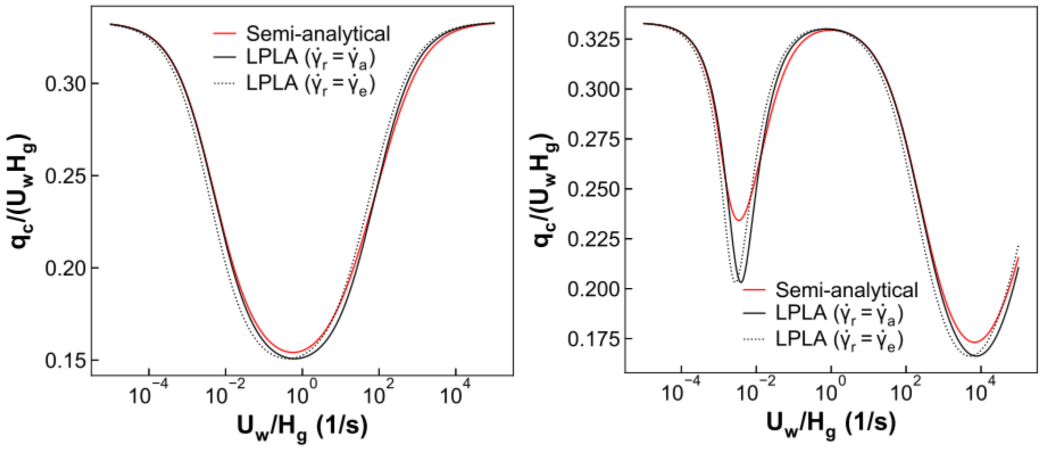

Figure 2. Dimensionless critical flow rates computed for C–Y and B–C–Y fluids using two methods presented in this work

References

Kim, S. K. (2018). Flow-rate based method for velocity of fully developed laminar flow in tubes. *Journal of Rheology*, 62(6), 1397–1407.

Makosko, C. W. (1994). *Rheology: Principles, Measurements, and Applications*. Wiley-VCH.

INFLUENCE OF MOISTURE AND TEMPERATURE ON THE MECHANICAL PROPERTIES OF COATED FIBER-BASED SUBSTRATES AND ITS APPLICATION TO INDUSTRIAL COATING PROCESSES

T. Nienke[1], D. Eggerath[2]

[1]Department of Paper and Packaging Technology, University of Applied Sciences, Munich, Germany

Email: tobias.nienke@hm.edu

Abstract
The influence of temperature and moisture on the mechanical properties of coated fiber-based substrates is investigated. The moisture content in dependence of the relative humidity and temperature is shown as sorption isothermes. The hygroexpansion is measured and much more pronounced in cross direction, a minor influence of the coating is noticed. The influence on the mechanical properties is most pronounced for relative humidity > 60-70%.

Keywords: *coating, fiber, moisture, process*

1. Introduction

Fiber-based substrates are used for various roll-to-roll production processes. They are extremely popular for high volume tapes and consumer or industrial packaging material. For a majority of the coated products water based coating fluids are used. High stiffness, low cost and renewable resources are convincing selling points for fiber-based materials. However, the fiber's anisotropic properties challenge the control of the converting process. Along the web path wet coating fluid is applied onto the web, drying reduces the moisture content, re-moisturizing devices can be used to add additional moisture to the dried web before rewinding.This results in several dimensional changes of the individual fiber during dwell times of a view seconds at machine speed of 1000 m/min. Converted materials are stored in large rolls. In this work the influence of moisture and temperature on the mechanical properties of coated and uncoated fiber-based substrates is investigated.

2. Theory

Paper webs consist of individual fibers, due to the paper making process, mostly oriented in machine direction. Since paper is highly porous it is very sensitive to changes in the surrounding environment. The absolute moisture content is defined in DIN EN ISO 638 as:

$$w_{H_2O} = \frac{m_0 - m_1}{m_0} \times 100 \tag{1}$$

Where m_0 is the mass of the sample and m_1 the mass of the sample after drying till constant mass is reached. The fibers react to moisture intake by dimensional changes, mostly in cross direction (CD) and less pronounced in machine direction (MD) (Blechschmidt, 2013). Different theories exist to explain the mechanism of moisture intake: Surface adsorption theory: The large internal faces of fiber-based material contain polar groups, which are mostly hydroxyl groups. They are distributed in a monomolecular fashion at the initial uptake of water and polymolecular at higher relative humidity. Even though this theory was used in the past to develop models to describe the isotherms (Brunauer-Emmett-Teller, Guggenheim-Andersen-de Boer) it does not explain the rapid increase in moisture content at high relative vapor pressures. (Venkatesvaran, 1970). Capillary condensation theory: For higher relative humidity the capillary condensation theory is used to describe the moisture content. The Kelvin equation is used to calculate the amount of filled pores. The moisture content depends on the radius of the capillary. Capillary condensation is not significant below a water activity of 0.8. (Venkatesvaran, 1970).

Knudsen Diffusion: If the pore dimensions are less than the mean free path of the water vapour molecules, the chance of adsorption increases due to the higher chance of collisions with the surround pore walls. Free diffusion: Free diffusion is possible in the voids of the fibrous network. The moisture content of fibrous samples at different relative humidity is shown in sorption isothermes. The sorption isothermes show a sigmoid-shaped curve. Coatings usually contribute relatively little to the total moisture content, but can influence the dimensional change and mechanical characteristics of the material. In general, the moisture content for the sorption and desorption processes do not coincide. This observation is called hysteresis. Different theories to explain this phenomenon are found in the literature including the Domain theory, the theory of hydroxyl groups and the swelling theory (Kaarlo, 2008). Parker (Parker et. al, 2006) has summarized available data for sorption isotherms of different fiber-based material. The influence of coatings has not been subject of the study. The processing during the paper making process (e. g. bleaching, beating) also influences the moisture content (Parker et. al, 2006)

3. Experimental procedure

3.1 Material

Different coated fiber-based materials were analysed. Wood free, unbleached paper with a grammage of 50 gsm, a 1.6 gsm base coating, a metal coating of approx. 20 nm and an topcoating with 1.6 gsm is compared to similar material with a paper grammage of 70 gsm. Both are also compared to their raw paper without coating. Additionally, a 70 gsm unbleached kraft paper with a 20 gsm LDPE coating is analysed and compared to a bleached kraft paper with the same grammage and coating.

3.2 Methodology

Moisture content / sorption isothermes

Samples of 100 cm^2 are conditioned in a climate chamber at different levels of relative humidity and temperature. The absolute moisture content is determined gravimetrically using the oven-drying method.

Hygroexpansion

The Hygroexpansion is determined by installing a stripe of the material in a device with two clamps. One of the clamps is movable and connected to a micrometer indicator. The hygroexpansion can be measured by exposing the loaded device to different humidity conditions in a climate chamber.

Tensile test

Tensile tests according to DIN EN ISO 1924-3:2007 are performed using a 2.5 kN tensile tester and samples with a width of 15 mm conditioned at different relative humidity levels. Different characteristic values can be derived from the data recorded by the tensile tester:

Breaking force index:

$$\sigma_T^W = \frac{1000\ \bar{F}_T}{b\ w} \quad (2)$$

Tensile energy absorption (TEA):

$$W_T^b = \frac{1000\ \bar{U}_T}{b\ l} \quad (3)$$

Tensile energy absorption index (TEAI):

$$W_T^W = \frac{1000 W_T^b}{w} \quad (4)$$

Tensile stiffness index

$$E^W \frac{E^b}{w} \quad (5)$$

where

$$E^b = \frac{\bar{S}_{max} l}{b} \quad (6)$$

and

$$S_{max} = \left(\frac{\Delta F}{\Delta \delta}\right)_{max} \quad (7)$$

4. Results and discussion

4.1 Moisture Content

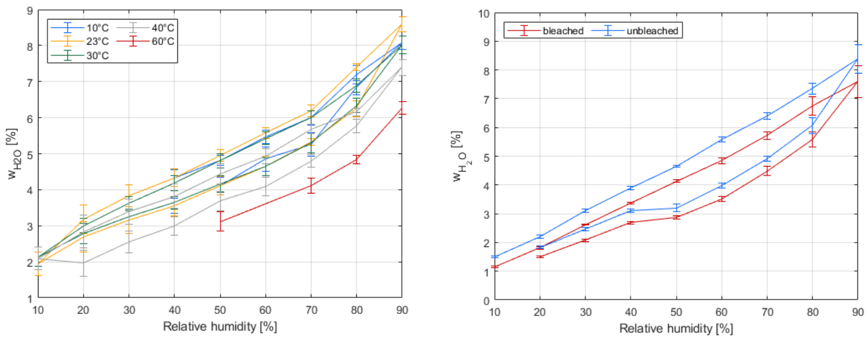

Figure 1. Sorption Isothermes of 50 gsm metallized paper (a) and kraft paper (b)

Figure 1 a shows the moisture content at different relative humidity and temperatures between 10°C and 60°C. The known hysteresis effect can be observed. The absolute moisture of the material increases with the same slope between 10 and 70 % r.h. For higher relative humidity the moisture increases more rapidly, which can be explained by the capillary condensation described earlier. Temperatures between 10 and 30°C do not result in significant differences in absolute moisture, except for high relative humidity. At 40°C a significant difference in moisture content is observed. The equilibrium moisture content is about 10 % lower. It decreases even more when the temperature is raised to 60°C. The moisture content of the unbleached kraft paper with LDPE coating is higher than the unbleached equivalent. Figure 1b shows this for 23°C. Wahba and Nashed (Whaba and Nashed, 1957) have seen a difference between 20°C and 30°C, but no difference between 30° C and 40°C.

4.2 Hygroexpansion

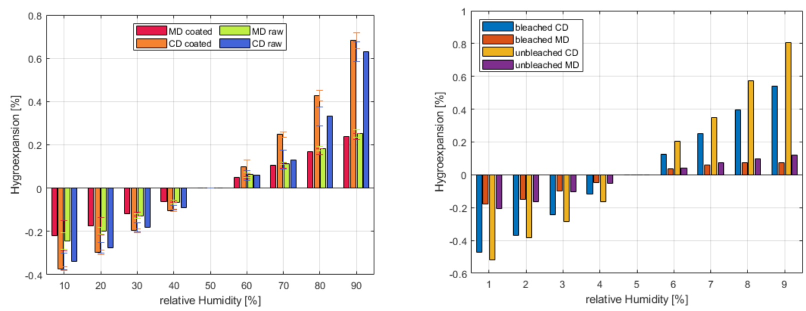

Figure 2. Hygroexpansion of metallized paper (a) and kraft paper (b)

Figure 2a shows the hygroexpansion of the metalized paper and its raw material. The dimensions of the material decrease with decreasing relative humidity. The dimensional change is much more pronounced in cross-direction. The material dimensions change about the same from 10 to 50 % as they do from 50 to 90 % r.h. for the machine direction. It is about 50 % larger in the Cross direction for the highest r.h. compared to the lowest. The coated material shows less dimensional change in MD and more in CD compared to the raw material.

Figure 2b shows the hygroexpansion of the kraft paper. A significantly higher expansion in CD is observed. The unbleached fiber shows less expansion. Bleaching decreases the moisture content and results in less fiber swelling (Parker, 2006)

4.3 Tensile tests

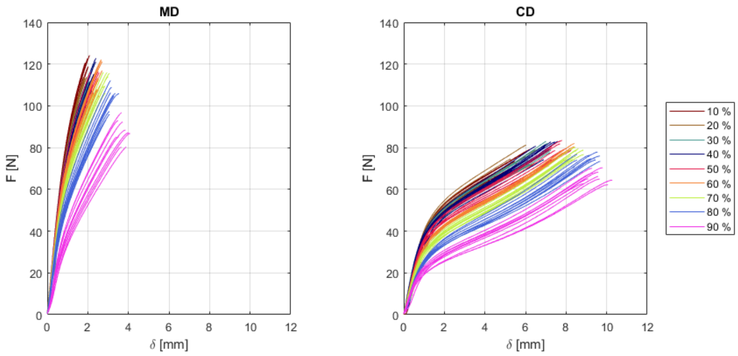

Figure 3 – Tensile Test results of bleached kraft paper

In general samples tested in machine direction show higher breaking forces and less elongation, as shown in Figure 3. The tensile energy absorption index of the coated kraft papers increases with increasing moisture content. The metallized paper and their raw material show less dependency on the moisture for the tensile energy absorption. The breaking force index decreases for relative humidity >70%. It is slightly larger for unbleached kraft paper in machine direction compared to bleached kraft paper. The tensile stiffness index decreases for relative humidty > 60% in both directions. The tensile stiffness of the metallized paper in cross direction is higher compared to its raw material.

5. Conclusions

The influence of temperature and moisture on the mechanical properties of coated fiber-based substrates has been investigated. The influence on the mechanical properties is most pronounced for relative humidity > 60-70%. Roll-to-roll processes should avoid moisture content in this dimension to eliminate the risk of web breaks. In the next step, those laboratory measurements at steady-state conditions should be transferred to industrial trials to investigate transient effects during moisture changes during production.

References

Blechschmidt, J et al. (2013) Taschenbuch der Papiertechnik. München: Fachbuchverlag Leipzig im Carl Hanser Verlag.

Deutsches Institut für Normung e.V. (2007) DIN ISO 1924-3:2007 - Paper and board - Determination of tensile properties - Part 3: Constant rate of elongation method (100 mm/min)

Deutsches Institut für Normung e.V. (2009) DIN EN ISO 638:2009 - Paper, board and pulps – Determination of dry matter content – Oven-drying method.

Kaarlo et. al. (2008) *Papermaking Science and Technology*, Paper Physics, Helsinki, FPEA

Parker, M. E.; Bronlund, J. E.; Mawson, A. J. (2006) Moisture sorption isotherms for paper and paperboard in food chain conditions. *Packaging Technology and Science* 19(4):193–209.

Seaborg, Stamm (1931). Sorption of water vapor by paper-making material. I. Effect of beating. *Ind. Eng. Chem.*; 23: 1271-1275.

Venkateswaran, A. (1970) Sorption of aqueous and nonaqueous media by wood and cellulose. *Chemical Reviews*, 70(6):619–637.

Wahba, M.; Nashed, S. (1957). Moisture Relations of Cellulose. Sorption Hysteresis and the effect of temperature. *Journal Of The Textile Institute.* 48(1)

THE FLUID MECHANICS OF TENSIONED WEB ROLL COATING

***H. Benkreira*[1], *Y.Shibata*[1,2] *and K. Ito*[2]**

[1] Chemical & Process Engineering Division, School of Engineering
R&KT Centre in Advanced Materials Engineering
University of Bradford, BD7 1DP, United Kingdom, UK
[2]Films R&D Centre, Toyobo Co. Ltd., Otsu, Japan
Email: H.Benkreira@Bradford.ac.uk

Abstract
Although widely used, tensioned web-roll coating has received only scant research attention. We have developed a new semi-empirical model that reproduces accurately data collected on an industrial pilot line over a range of operating conditions. We also mapped the coating window and found evidence of hydrodynamic assistance above Ca=0.4 enabling stable operation up to speed ratio ≈ 0.8. We attribute this to the confinement of the coating bead.

Keywords*: tension web roll coating, hydrodynamic assistance*

1. Introduction

Tensioned web roll coating is a simple coating method in which the web is driven under tension in "reverse kiss coating" mode as shown in Fig. 1. Such elasto-hydrodynamic flow situation limits the amount of liquid that is metered, allowing for nearly 100% film transfer from the applicator roller to the moving web with wet films achieved typically 10 µm thick. Although widely used, this coating flow has been little investigated with only two papers presenting analyses. One is by Gaskell et al. (1998) who solved the problem for very low $Ca = \mu v_A/\sigma < 0.01$ using a lubrication analysis with the web regarded as a flexible membrane of constant tension T to arrive at a solution that, for speed ratio $S = v_W/v_A \leq 1$ and wrap angle β gives the applicator to web film transfer ratio, TR_G as:

$$TR_G = \frac{v_W h_W}{v_A h_A} = 1 - \frac{6}{5}\frac{r_A}{h_A} Ca(1-S)^2 \left(\frac{\sigma}{T\beta}\right) \qquad (1)$$

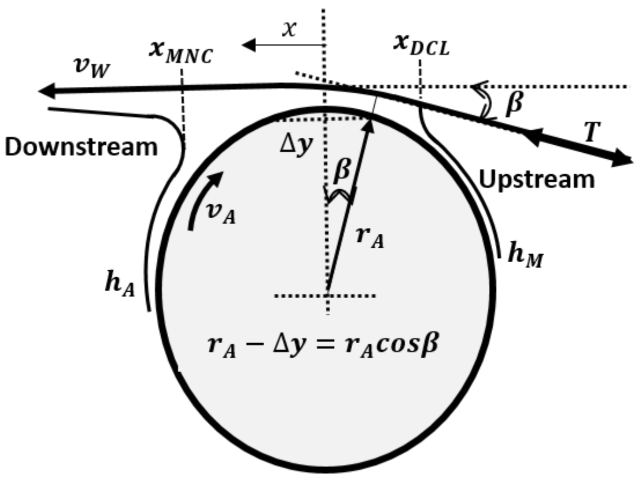

Fig. 1*: Tensioned Web Roll Coating*

Gaskell et al. (1998) did not provide experimental data to support this prediction nor did they consider the stability of the flow. The second study is that of Carvalho (2003) who analysed the metering section of this flow with the transfer section completely flooded, i.e. no transfer film was considered. Carvalho (2003) used a full free boundary analysis and this limited the scope of his results, given only for $Ca = 0.1$ and tension number $\tau = \mu v_A/T = 10^{-6}$, the aim of the analysis being to assess the effect of S and on the stability of the metered film h_M.

The predictions are presented in Figs. 2 and 3. They show that for $\beta < 1^0$, h_M follows first an approximately linear decrease with increasing S then an upturn above a critical S. Such a variation is also observed with reverse roll coating (Coyle et al., 1990) with the upturn point signalling the onset of cascade instabilities resulting from the penetration of the dynamic wetting line past the minimum coating gap. Fig. 2 shows that for $\beta > 1^0$, no upturn in h_M is observed, rather, turning points in the solution path. Carvalho (2003) suggests that these turning points depicts the onset of another form of instabilities, "rivulets". Carvalho (2003) did not provide experimental data (illustrative photographs were given).

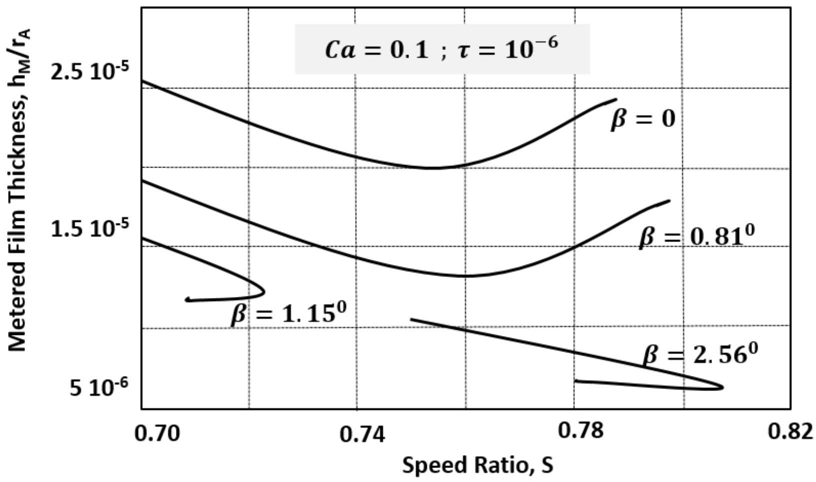

Fig. 2: Carvalho' s (2003) predictions of h_M/r_A for various wrap angle β.

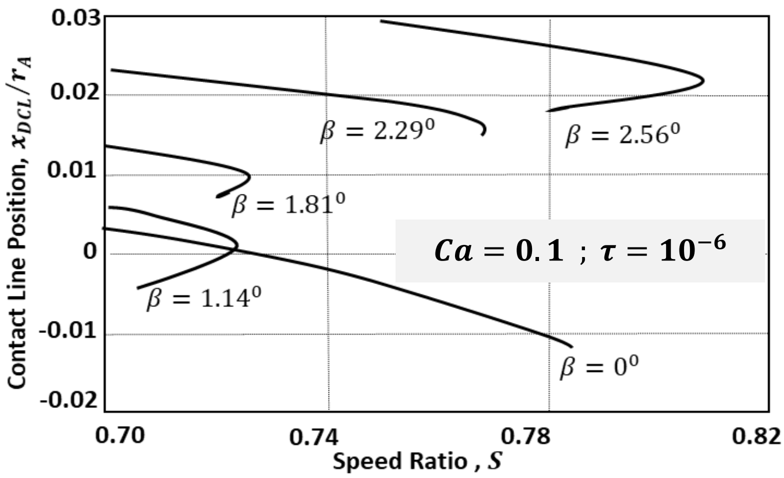

Fig. 3: Carvalho' s (2003) predictions of $\boldsymbol{x_{DCL}/r_A}$ for various wrap angle β. [Scale shows penetration into and past the nip mid-position when $\boldsymbol{x_{DCL}/r_A}$ turns negative.]

2. Theory

Following from Carvalho (2003) predictions in Figs. 2, we observe fortuitously that the metered film thickness h_M varies with speed ratio approximately linearly up to the turning points as:

$$\frac{h_M}{r_A} = a(1 - S) \text{ ; constants } a \text{ depending on } Ca, \tau \text{ and } \beta \qquad (2)$$

Applying a mass balance around the bead we deduce the applicator to web film transfer ratio, TR_C as:

$$TR_C = \frac{v_W h_W}{v_A h_A} = 1 - \frac{r_A}{h_A} a(1 - S) \qquad (3)$$

Rather than using the tension number τ as defined by Carvalho (2003), we introduce a modified number that reflects the relative magnitude of the hydrodynamic viscous force acting at the bead $\mu(v_A - v_M)$ and lifting the web to the counter elastic pressure force resulting from the applied tension $Tsin\beta \cong T\beta$:

$$N_{vw} = \mu(v_A - v_M)/T\beta \equiv \mu Ca(1-S)(\sigma/T\beta) \quad (4)$$

We observe then that Gaskell et al. (1998) Eq. (1) can be expressed as:

$$TR_G = 1 - \frac{6}{5}\frac{r_A}{h_A} N_{vw} (1-S) \quad (5)$$

It follows thus that the constant a in CarvalhoEq. (3) must also be a function of N_{vw} so we have:

$$TR_C = 1 - \frac{r_A}{h_A} f(N_{vw}) (1-S) \quad (6)$$

We see then the similarity in the results in Eqs (5) and (6) from this two very different approaches. We are unable to establish $f(N_{vw})$ as Carvalho (2003) predictions were carried out for only one value of $Ca = 0.1$ and $\tau = 10^{-6}$. The more general form, Eq. (6) constitutes our semi-empirical model.

3. Experimental procedure

A reverse roll tensioned web coating pilot line at Toyobo Films R&D Centre in Otsu, Japan was used in this research (Fig. 4). The web was a 50 µm transparent PET film. The coating liquid was fed to a die onto the applicator roller. The gap between the applicator and metering rollers was adjusted so that a 10 µm stable wet film h_A was achieved on the applicator roller side leading to the web. The web film thickness h_w was measured using a light interference gauge. The metered film thickness was not measured directly but calculated from measured h_W and mass balance ($v_A h_A = v_A h_M + v_W h_W$). Visualisations of the coating bead between applicator roller/tensioned web were achieved by focusing a microscope through the running transparent film. These visualisations enabled us to locate the upstream and downstream menisci and the dynamic wetting line and observe air entrainment. Surface instabilities on the coated web were detected by the naked eye. Table 1 gives the range of operating conditions tested.

***Table 1**: Range of operating conditions tested.*

Applicator Roll Speed, v_A (m/s)	**Speed Ratio, v_W/v_A**	**Web Tension, T (N/m)**	**Wrap Angle, β (°)**	**Viscosity μ $(mPa.s)$**	**Surface Tension, σ (mN/m)**
0.5, 1.0, 1.5	0.71, 0.77, 0.83, 0.91, 1.0, 1.11, 1.25	800, 1200, 1600, 2000, 2400	0.57, 1.72, 2.86, 4.00, 5.14	3, 44, 105	25.5, 26.2, 34.5

4. Results and discussion

Fig. 4 provides a comparison of the measured transfer ratio TR with model Eq. (6). Within experimental errors and over the entire range of conditions tested, the correlation reduces simply to:

$$TR = 1 - 1.10(1-S) \quad (7)$$

Fig. 5 displays the measured coating window. It shows that with increasing Ca, the critical speed ratio S^b increases until it hits S^{ae}at $Ca = 0.40$, signalling that the bead has now stabilised against rivulets but instead breaks due to dynamic wetting failure but at web speeds higher than those in dip coating at the same viscosity suggesting hydrodynamic assistance due to bead confinement. It is interesting to note that our measured values of $S^b = 0.71 - 0.83$ are similar to those identified by Carvalho's (2003) as turning points signalling the breaking of the metering film from a 2D to a 3D structure. As Carvalho (2003) simulations were limited to one condition of Ca and τ, it would be interesting to perform simulations over a range of Ca to see if results similar to those in Fig. 6 are found.

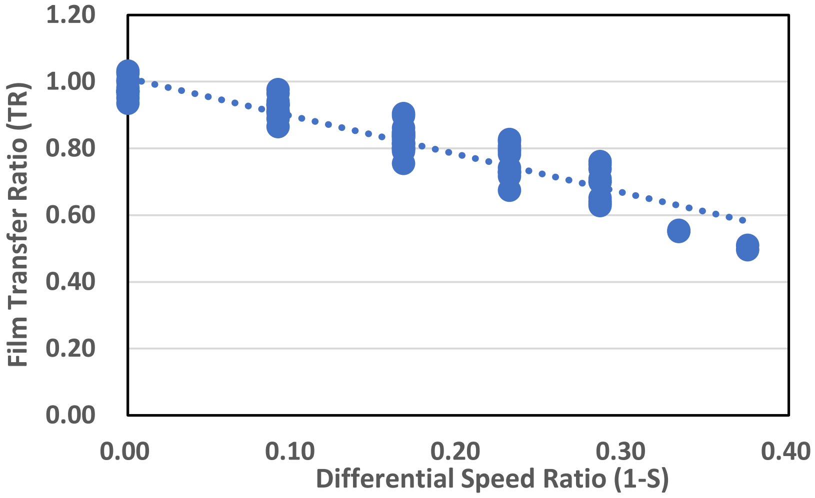

Fig. 4: Comparison of all data with semi-empirical Eq. (6).

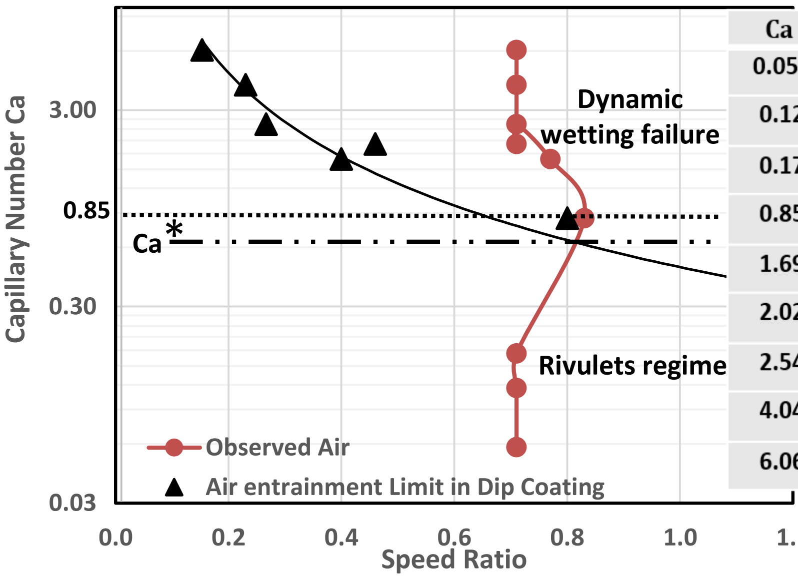

Ca	τ	S^b
0.058	1.25E-06	0.71
0.12	2.50E-06	0.71
0.17	3.75E-06	0.71
0.85	1.83E-05	0.83
1.69	3.67E-05	0.77
2.02	4.38E-05	0.71
2.54	5.50E-05	0.71
4.04	8.75E-05	0.71
6.06	1.31E-04	0.71

Fig. 6: Air entrainment regimes in web tensioned roll coating ($\beta = 1.72^0, T = 1200\ N/m$).

5. Conclusions

This experimental study has provided useful information to guide the design and operation of tensioned web roll coating. We have shown that the film transfer ratio follows a simple linear correlation. With regard to flow stability we identified two regimes of air entrainment: rivulets and dynamic wetting failure assisted hydro-dynamically by the bead being confined. We also observed that Carvalho (2003) *turning points* are very close to the limits of air entrainment instabilities measured in our study.

References

Carvalho, M. (2003). Elastohydrodynamic of tensioned web roll coating process. Int. J. Numer. Meth. in Fluids 41, 561-576.

Coyle, D.J., Macosko, C.W., Scriven, L.E. (1990). The fluid dynamics of reverse roll coating. AIChE. J. 36 (2)**,** 61-174.

Gaskell, P.H., Rees, S.R., Savage, M.D., Storey, S.P. (1998). A mathematical model of roll to web kiss coating. Trans IChemE. 76(A), 29-37.

Proceedings ECS 2021
Brussels, Belgium, September 7-9, 2021

Abstract T-33

DYNAMICS OF COATING FLOW ON ROTATING ELLIPTICAL CYLINDERS

***J. D. Reilly*[1], *A. W. Wray*[1], *S. K. Wilson*[1]**

[1]Department of Mathematics and Statistics, University of Strathclyde,
Livingstone Tower, 26 Richmond Street, Glasgow, G1 1XH
Email: james.d.reilly@strath.ac.uk

Abstract
Coating the exterior of an object with a fluid layer is a fundamental problem in fluid mechanics and is relevant to many industrial processes, such as the production of photographic film and aluminium foil. While the coating of a circular cylinder has been well studied since the pioneering work of Moffatt (1977) and Pukhnachev (1977), there has been almost no work on non-circular cylinders, which is surprising given that the substrates in many applications (e.g. the coating of orthopaedic implants (Zhang et al., 2014)) are not perfectly circular. Even a slight eccentricity can cause a radical difference in the behaviour compared to the perfectly circular case (Li et al., 2017).

Two-dimensional flow on the surface of a rotating elliptical cylinder was first studied by Hunt (2008) and more recently by Li et al. (2017), both of whom used Direct Numerical Simulations (DNS). In the present work we will use Lubrication Theory to derive and analyse a reduced model for thin-film flow on a rotating elliptical cylinder. This model retains the essential physics inherent in the full problem, but is much less computationally expensive than DNS and is also more analytically tractable. A parametric study of the cylinder rotation rate reveals four characteristic behaviours of the fluid: an oscillating hanging bulge (see Fig. 1), a bulge formed by gravity and centrifugation which travels around the cylinder, bulges formed at the cylinder tips by centrifugation which travel around the cylinder (see Fig. 2), and bulges formed and held at the tips by centrifugation.

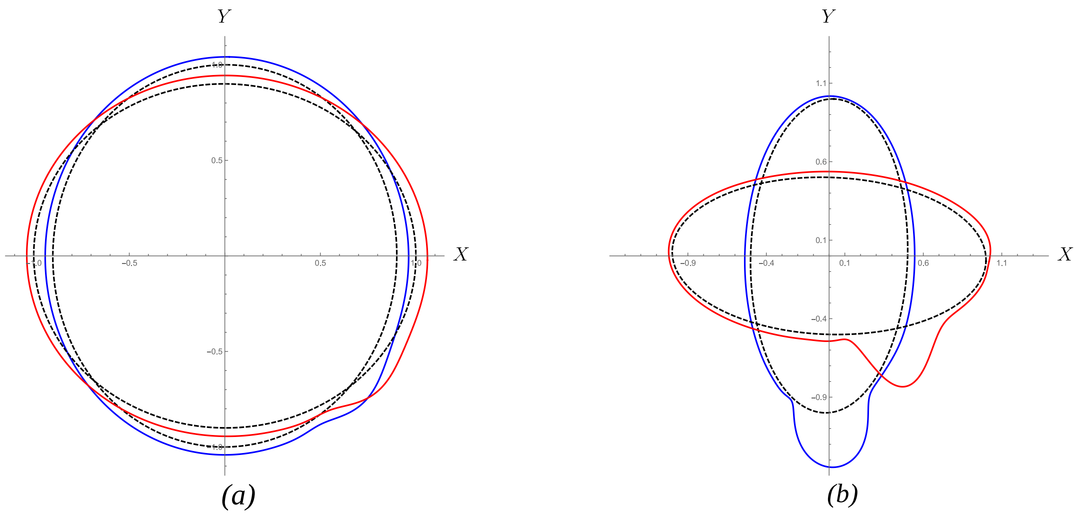

Figure 1. The interface in the laboratory frame when the semi-minor axis b is instantaneously parallel to the direction of gravity (red) and when the cylinder has rotated π/2 radians (blue) for (a) b=0.9 and (b) b=0.5.

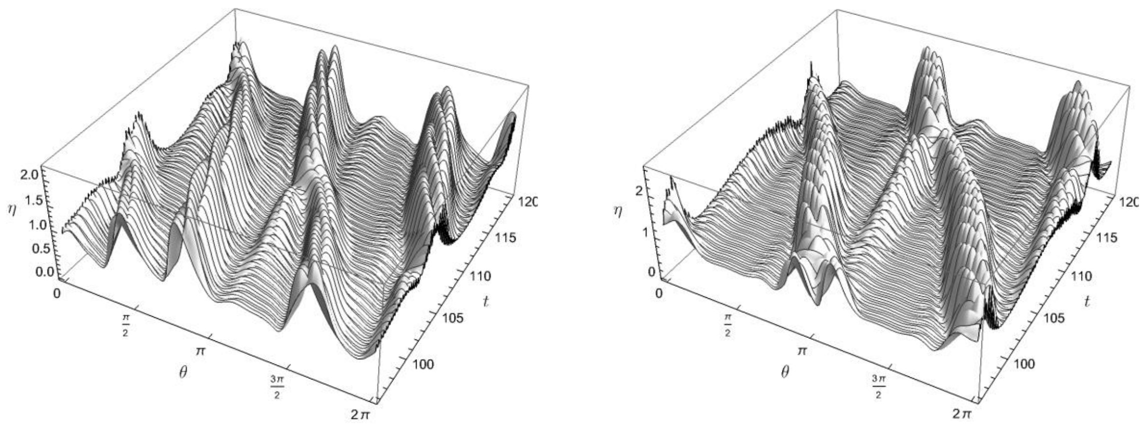

(a) *(b)*

Figure 2. Space-time plot for the interface in the rotating frame for (a) W=0.86 and (b) W=0.9 where W is the dimensionless rotation rate.

Keywords*: coating, ellipse, thin film*

References

Hunt, R. (2008). Numerical solution of the free-surface viscous flow on a horizontal rotating elliptical cylinder. *Numerical Methods for Partial Differential Equations*, 24 (4), 1094-1114.

Li, W., Carvalho, M. S., and Kumar, S. (2017). Viscous free-surface flows on rotating elliptical cylinders. *Physical Review Fluids*, 2 (9), 094005.

Moffatt, H. K. (1977). Behaviour of a viscous film on the outer surface of a rotating cylinder. *Journal de Mécanique*, 16 (5), 651-673.

Pukhnachev, V. V. (1977). Motion of a liquid film on the surface of a rotating cylinder in a gravitational field. *Journal of Applied Mechanics and Technical Physics*, 18 (3), 344-351.

Zhang, B. G., Myers, D. E., Wallace, G. G., Brandt, M., and Choong, P. F. (2014). Bioactive coatings for orthopaedic implants—recent trends in development of implant coatings. *International Journal of Molecular Sciences*, 15 (7), 11878-11921.

Proceedings ECS 2021
Brussels, Belgium, September 7-9, 2021

Abstract T-73

SCALE-UP BETWEEN R&D AND PILOT COATING PROCESSES

Harald Doell[1] ***and Beat Mathis***[2]
[1] TSE Troller AG, Murgenthal, Switzerland
[2] Werner Mathis AG, Niederhasli, Switzerland
Email: harald.doell@tse-coating.ch presenting/corresponding author

Abstract
For some applications such as battery electrodes, fuel cells and others it is important to coat well defined patches on both sides of a substrate with high accuracy in cross-web (CD) and machine direction (MD). In a first scale-up process still in a S2S- setup the repeatability of the coated patches on both sides and a comparable drying process to a later R2R- setup are crucial. By a combination of a high precision S2S- coater and an industrial dryer with adjustable drying performance the interval between pure S2S- coating and a later R2R-production can be bridged.

Keywords: *slot die coating, development thin films, battery and fuel cell electrodes*

1. Introduction

Premetered coating in the slot format is an attractive method to apply single or multilayer structures of functional layers to continuously running substrates.

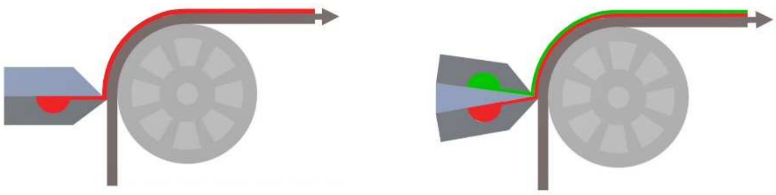

The main advantages of premetered coating methods are the following:

- Average coat weight or film thickness is not affected by formulation
- Reactive liquids (multi- component) systems can be coated
- Multiple layers coated simultaneously
- Excellent uniformity of coated film in both, cross-web and machine direction
- The coating process can be scaled up from R&D over pilot to full production scale.

Quite often, the very first steps in development of new products in the field of flexible electronics or battery electrodes are performed with spin coaters or manually driven drawdown bars. This mainly helps to compare the technical performance of different formulations, but drying typically is not near to a later production setting and since this process is not scalable it is used for a star only. In a next step, small-scale sheet-to-sheet (S2S) coaters using the slot coating process in preparation for a later roll-to-roll (R2R) process are in operation in order to examine the application technology as well. On such units, typically the dryer is also not comparable with a later production machine.

2.Well-proven Sheet-to-Sheet-Coaters

The specific S2S- coater using high or ultra-high precision slot dies is many times proven and tested for several demanding applications, such as flexible electronics and thin optical films with dry thicknesses in the sub-micron range and as well for rather thick layers for Lithium Ion Battery (LIB) applications. In all these applications, the layers are applied to one side of the substrate, and subsequently dried with various methods. One option for drying could be a suction hood for drying, which is extracting the solvent vapour off the coated substrate very uniformly. These are drying the coated layer gently by a combination of a warm movable plate and a uniform suction flow. The picture below refers to such a unit, which is additionally placed in an enclosure with either laminar airflow or a suction port.

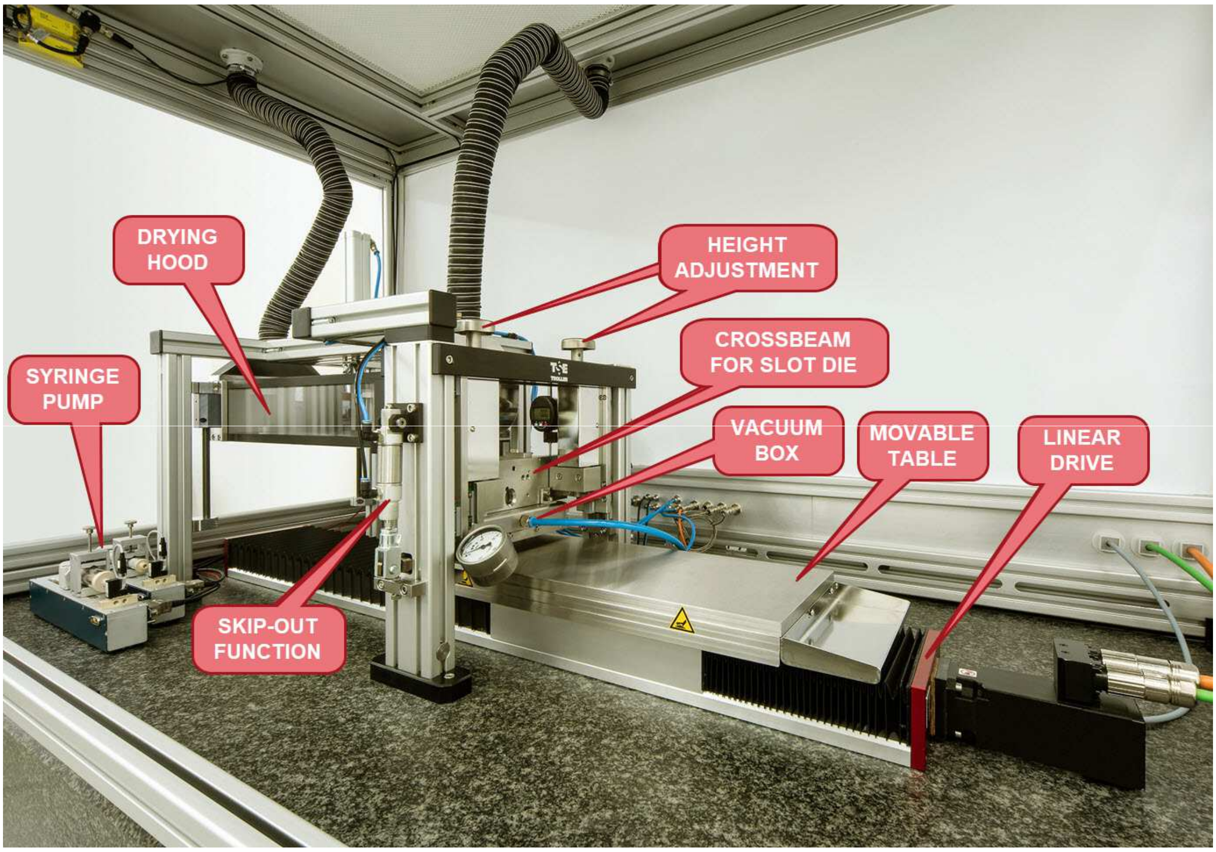

Figure 1. TSE- TableCoater with single layer slot die, dryer and enclosure

Another possibility for drying could be blowing warm air onto the substrate or using an Infrared (IR) Dryer, depending on the application and the kind of solvents. Such drying methods are often used for a first screening of the formulations and their functionality, but especially for process development in relation with a later up-scale process a drying unit similar to R2R- facility shall be used.

In the field of flexible electronic and optical layers typically a single sided application is performed. In LIB- and Fuel-Cell- applications the electrodes and membranes need to be coated on both sides with high accuracy in terms of size and position of the coated patches. The requirement to place the same layer with a maximal deviation in the sub- millimetre range requires a very precise positioning of the substrate to be coated, both in cross-web direction (CD) and a perfect actuation and stop of the coating flow in machine direction (MD).

3. Combination of S2S- Coater with industrial dryer

Especially for sensitive substrates and coating with high grammage, the method described in the following is beneficial for the scale-up process.

In order to maintain both, the repeatability and accuracy of the double-sided coating as well as planar thick coatings without any influence to the substrate to be coated the foil or film is fixed in a kind of stentering frame. The substrate will be fixed in the frame in order to keep it in a fixed position, without overstretching it. The frame can be used for holding the substrate either on two or all four edges and can be pulled in MD only, or in MD and CD. By this, the width of the substrate can be variable and selected to the actual requirements. For sensitive substrates like membranes, it is recommended to pull it to all four sides, but other settings can be tested and depend of the substrate properties.

This stentering frame can be precisely positioned and fixed to the movable table of the S2S- coater for the coating process for the first side. The substrate will be placed such it is laying flat on the movable table without any wrinkles. During the coating process it is very important to maintain the accurate coating gap for achieving a constant coating result. After the first side coating the stentering frame is lifted pneumatically off the table and can subsequently be transferred manually to the guide rails of the dryer. The conveyor system then moves the frame with the coated substrate into and through the dryer at various speeds and dryer settings. The dryer can be equipped with different drying nozzles, depending on the substrates and the coatings. This shall be harmonized ideally between the final user of the system and the dryer supplier.

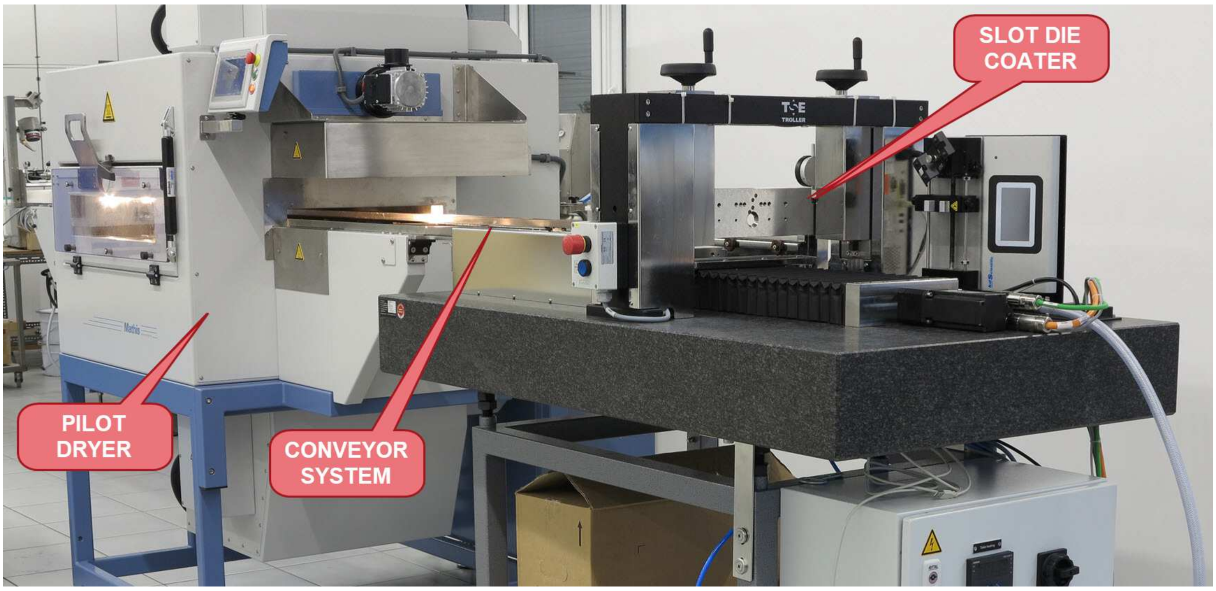

Figure 2. TSE- TableCoater with single layer slot die and Mathis KTF- dryer

After the drying of the substrate the stentering frame then will be turned manually upside-down und placed on the S2S- coater again and moved pneumatically to the working position. Pins precisely secure the position of the frame after turning to the opposite side. The second side finally will be coated similarly to the first side, then, the movement to the dryer and subsequent drying process will be initiated.

4. Summary and Outlook

By combination of the high precision S2S- coater with an industrial pilot dryer the following can be achieved:

1. Both-side coating with high accuracy both in CD and MD
2. Repeatable positioning of sensitive substrates and coated patches
3. Simulation of later R2R- process by using scalable industrial methods like a flotation dryer

Outlook:

1. For higher capacity the handling of the stentering frame could be automated to a higher degree
2. Optimization of material flow in S2S- coater
3. Fully automated machine with continuous handling of multiple stentering frames.

Proceedings ECS 2021
Brussels, Belgium, September 7-9, 2021

Abstract T-37

DEVELOPMENT OF A SELF-STRATIFYING COIL COATING

***S.Sarma*[1], N. Stevens[1], P. Barker[2], C. Mills[1]**

[1]Tata Steel Europe R&D
9, Voyager building, Coventry, CV4 7EZ

[2]Tata Steel Colors
Shotton works, Deeside, Flintshire, CH5 2NH

Email: Sreedhara.Sarma@tatasteeleurope.com

Abstract
Pre-finished steel products are consistently produced through coil coating process, creating high quality products. This established method requires the coating layers to be applied at separate coating stations. Multilayer coatings may be consistently applied at high speed by using advanced pre-metered coating methods. However, it requires wet on wet application of the coating layers, which leads to many potential issues. To understand this, here the level of stratification or incompatibility of the coating system is determined using the Hansen Solubility Parameters (HSP).

Keywords*: Coil coating, Stratifying, Curtain coating*

1. Introduction

Pre-finished steel products are consistently produced through a multi-layer roll-to-roll application known as coil coating, creating high quality products with guarantees of up to 40 years long. This established method, however, requires the coating layers to be applied at separate coating stations and steps. Each layer contributes its own function to the system including corrosion protection, adhesion improvement and aesthetics. This results in a long cumbersome process with many steps and associated higher carbon footprint. Alternative coating deposition methods have therefore been explored, mainly to improve efficiency and cost effectiveness but also increasingly to improve the sustainability of processes.

Multilayer coatings may be applied at high speed whilst still producing a consistent coating, by using a pre-metered coating method like a slide coater (Hens, 1997). As all coating layers can be applied in one process step, considerable benefits can be achieved namely a shorter production line with a significant reduction in energy costs and other environmental requirements. A single application method requires a wet on wet application of the coating layers, which leads to a number of potential issues. Mixing of layers within coating systems could result in a negative impact on the properties of the end product, affecting any guarantees. By ensuring coating layers have the ability to stratify from one another, a high quality product has the potential to be produced. This requires a degree of incompatibility between coating layers so that they naturally separate. Prior literature (Verkholantsev 1996), has shown that a stratified system can be produced when two different incompatible resins are mixed with two solvents with preference for one resin. Methods have been explored to predict the degree to which coating layers may stratify when completely mixed through the use of Hansen Solubility Parameters (HSP) and surface tension and interfacial energy calculations (Beaugendre, 2017b).

2. Theory

Effective coating systems are composed of multiple layers with each layer contributing its own function. A promising area of interest within the coating industry is the use of self-stratifying coatings to allow all layers to be applied onto the surface in one deposition step. By the process of stratification, each layer will form separate distinct layers. Several patents for example, within the automotive (Berkau, 2007; Baghdachi, 2011) and powder coating (Murase, 1977) industry, detail the use of self-stratifying coatings.

If systems become too incompatible, unwanted impacts including adhesion issues may occur due to the coating layers completely separating. Therefore, as shown in Figure 1, a very slight compatibility between the coating layers creates a gradient effect within the coating system which can be beneficial (Beaugendre, 2017a).

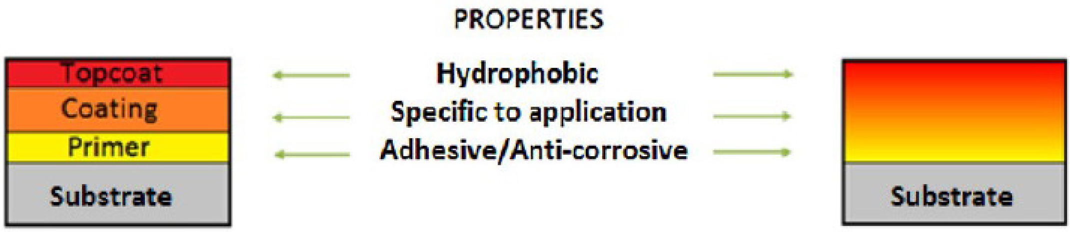

Figure 1: Self-stratifying coating gradient (Beaugendre 2017a)

Many methods have been identified and tested to predict the degree of stratification for a system. These can include the UNIFAC model, surface energy calculations, phase state diagrams and HSP (Beaugendre, 2017a, 2017b). HSP consists of three solubility parameters connected with separate bonding interactions; dispersive, polar and hydrogen bonding. The total solubility parameter (δ) is a product of each individual solubility parameter squared as shown in equation (1), where δ_d, δ_p, δ_h makes up the dispersion, polar and hydrogen bonding contributions to the solubility parameter.

$$\delta^2=\delta_d^2+\delta_p^2+\delta_h^2 \quad (1)$$

By calculating the compatibility between two components, it is possible to predict the chance of stratification. The more incompatible a system, the greater the chance of stratification. Methods to alter the HSP of a component within a system can help to promote incompatibility and so stratification. The addition of solvents, present within a sphere of one component will alter the overall solutions solubility parameter. This idea has been used to show options for the replacement of solvents with for example, alternatives which are greener and less hazardous but have the same effects on compatibility. (Sánchez-Camargo, 2019).

3. Experimental procedure

Three coatings obtained from Tata Steel, identified as P1, P2 and P3 were tested. Each coating (0.5 g) was dissolved in selected solvents (1 mL) and were shaken for 20 minutes at 800 rpm. Solubility rankings were given between 1 and 6 according to table 1. These rankings were inputted into HSPiP software to create a solubility sphere for each paint and to calculate the δD, δP, δH parameters.

Table 1: Solubility ranking evaluation standard

Solubility Rank	Precipitate	Turbidity
1	None	None
2	None	Weak
3	None	Strong
4	Trace	Strong
5	Moderate	Weak
6	Complete	None

4. Results and discussion

Table 2 displays solubility rankings for P1, P2 and P3 for some of the standard solvents used for all three coatings.

Table 2: Solubility rankings using standard solvents for each coating (Part of whole matrix)

	Solubility Score		
Solvent	P1	P2	P3
Acetonitrile	1	1	1
1-Bromonaphthalene	2	3	5
n-Butyl Acetate	1	1	1
Γ-Butyrolactone	1	1	5
Cyclohexanone	1	2	1
Decamethylcyclopentasiloxane	6	6	6

Through incorporating these solubility rankings into the HSPiP software solubility sphere diagrams were produced for each coating. A single and double sphere algorithm was tested. The HSP distance indicates the distance between the two centre points on the spheres, the higher the value the further the distance and so the greater the incompatibility. This value can be used to determine the Relative Energy Difference (RED) which represents the distance relative to another sphere. RED values need to be above 1 to be incompatible with one another. Values under 1 in Table 3 are highlighted as they indicate compatibility between the coatings. The HSP and RED values show a degree of compatibility exists between at least one of the spheres of each of the coatings.

Abstract T-37

Table 3: RED values

RED	P1 (1)	P1 (2)	P2 (1)	P2 (2)	P3 (1)	P3 (2)
P1 (1)	-	-	0.26	2.09	1.16	0.42
P1 (2)	-	-	1.60	0.64	0.98	1.81
P2 (1)	0.40	2.48	-	-	1.94	0.73
P2 (2)	1.78	0.55	-	-	1.22	2.11
P3 (1)	0.99	0.83	1.08	1.22	-	-
P3 (2)	0.41	1.81	0.47	2.44	-	-

Finally, to confirm predicted compatibilities between the three coatings, each coating was placed on top of each other in a test tube and left for various time periods.

5. Conclusions

Here the likelihood of industrial coil coating systems mixing is investigated to determine the potential for a single multi-layer application method which requires the coatings to be applied wet on wet. In order to determine the level of stratification or incompatibility of the coating system, the HSP of each layer was measured. This has then allowed the identification of potential methods to influence the degree of mixing between layers.

References

Baghdachi. J, Hernandez. H. R. P, Templeman. C. G (2011), Self-Stratifying Automotive Topcoat Compositions and Processes, (US Patent No. 7,863,375 B2)
Beaugendre. A, Degoutin. S, Bellayer. S, Pierlot. C, Duquesne. S, Casetta. M, Jimenez. M (2017), Self-Stratifying Coatings: A Review, *Progress in Organic Coatings, 110*, 210 – 241.
Beaugendre. A, Degoutin. S, Bellayer. S, Pierlot. C, Duquesne. S, Casetta. M, Jimenez. M (2017), Self-Stratifying Epoxy/Silicone Coatings, *Progress in Organic Coatings, 103*, 101 – 110.
Berkau. R, Gailberger. M, Gruber. T, Holdik. K, Meichsner. G, Mezger. F (2007). Coating Composition for Forming Self-Layering or Self-Coating Lacquer Systems (US Patent No. 7,186,772 B2)
Hens. J, Van Abbenyen. W (1997), Chapter 11b Slide Coating, S. F. Kistler, P. M. Schweizer, *Liquid Film Coating* (427 – 462), London, Chapman and Hall.
Murase. H (1977), Powder Coating Method for Forming Multilayer Coatings (GB Patent No. 1,570,540)
Sánchez-Camargo. A, Bueno. M, Parada-Alfonso. F, Cifuentes. A, Ibáñez. E (2019), Hansen Solubility Parameters for Selection of Green Extraction Solvents, *Trends in Analytical Chemistry, 118*, 227 – 237.
Verkholantsev. V, Flavian. M (1996), Polymer Structure and Properties of Heterophase and Self-Stratifying Coatings, *Progress in Organic Coatings, 29*, 239 – 246.

Proceedings ECS 2021
Brussels, Belgium, September 7-9, 2021

Abstract T-40

DETERMINATION OF OPERATING LIMITS OF SLOT COATING PROCESS: EFFECTS OF SHEAR THINNING AND YIELD STRESS ON SLOT COATING WINDOW

***Myungjae Lee**, Jaewook Nam*

School of Chemical and Biological Engineering, Seoul National University
1, Gwanak-ro, Gwanak-gu, Seoul, Republic of Korea
Email: jaewooknam@snu.ac.kr

Abstract
Nowadays, coating solutions contain nano/micro-sized particles or polymers for the functionalities. These kinds of solutions usually show yield stress and shear-thinning behavior. Therefore, we focused on the effect of these rheological properties on the slot coating operating limits. In this study, we visualized slot coating flows experimentally using Carbopol solution as a model Herschel-Bulkley fluid. We also developed a simple model to predict the coating window.

***Keywords**: Herschel-Bulkley model, shear-thinning, slot coating, viscocapillary model, yield stress*

1. Introduction
Shear-thinning and yield stress are two important rheological properties in industrially relevant coating liquids, such as suspensions and slurries, and the Herschel-Bulkley constitutive equation can represent them reasonably. In this study, we use aqueous Carbopol polymer solutions as a model Herschel-Bulkley fluid to visualize the slot coating flow.

2. Theory
We develop the simple model of Herschel-Bulkley fluid based on the 1-D viscocapillary model.

3. Experimental procedure
The visualization is performed using a custom-made apparatus that mimics all essential features of industrial-grade slot coaters to detect the location and shape of gas/liquid interfaces and contact lines.

4. Results and discussion
To understand this system, we should know which dimensionless numbers are governing this system. From the rheological/process parameters, we can get four dimensionless numbers. For low-concentration Carbopol solutions, which show a weak yield stress behavior, the experimental results and simple model data support that dimensionless number values for the onset of slot coating operating limits are reasonably overlapped. This implies that the dimensionless vacuum is dependent on only Rgt (gap-to-thickness ratio). The system is not sensitive to the change of Bingham number and the capillary number.

On the other hand, a simple model analysis implies that the yield stress effect is tremendous when the target thickness becomes thin. With thin wet thickness conditions, the pressure drop occurring through the channel is augmented by the effect of yield stress. This results in the upper shift of the coating window.

References
Lee, J., & Nam, J. (2016). A simple model for viscoplastic thin film formation for coating flows. Journal of Non-Newtonian Fluid Mechanics, 229, 16-26.
Tsuda, T. (2011). Coating flows of power-law non-Newtonian fluids in slot coating. Nihon Reoroji Gakkaishi, 38(4_5), 223-230.
Weinstein, S. J., & Ruschak, K. J. (2004). Coating flows. Annu. Rev. Fluid Mech., 36, 29-53.

Proceedings ECS 2021
Brussels, Belgium, September 7-9, 2021

Abstract T-54

STUDY OF EDGE FORMATION DURING SLOT DIE COATING OF LI-ION BATTERY ELECTRODES

S. Spiegel[1,2]***, T. Heckmann***[1,2]***, A. Altvater***[1,2]***, R. Diehm***[1,2]***, P. Scharfer***[1,2]***, W. Schabel***[1,2]

[1] Thin Film Technology (TFT)

[2] Material Research Center for Energy Systems (MZE)
Karlsruhe Institute of Technology (KIT), Karlsruhe, Germany
Email: sandro.spiegel@kit.edu

Abstract
In today's production of battery cells, the slot die coating process in large roll-to-roll systems is state of the art. In addition to the known limiting coating defects, such as air entrainment and low-flow limit, there is a formation of superelevations at the edges of the coating in the coating step. These super-elevations can cause damage in subsequent process steps, resulting in production reject. During calendaring and winding up the electrodes, edge elevations can lead to an inhomogeneous force distribution in cross-web direction of the coating, which causes waves and cracks at the edges of the electrode and the current collector. Edge elevations can be reduced by optimizing the flow profile at the outlet of the slot die. By changing the internal geometry or adjusting process parameters such as the gap between the slot die and the current collector, the flow profile can be adapted. Schmitt et al. have already published studies on the influence of the gap and the coating speed on the edge formation. The adaptation of the internal geometry is an important step to optimize the coating quality for battery electrodes, in order reduce production reject. To be able to eliminate edge elevations, it is important to develop an understanding of the edge formation. Therefore, in this work, the influence of the internal geometry of the slot die, material properties and process parameters on the edge formation was investigated experimentally. The authors would like to acknowledge financial support of the Federal ministry of Education and Research (BMBF) via the ProZell cluster-project “HiStructures” (Grant number: 03XP0243C).

Keywords*: slot die coating, edge formation, coatings for batteries*

Proceedings ECS 2021
Brussels, Belgium, September 7-9, 2021

Abstract T-16

FAST TRANSIENT SIMULATION OF THERMAL SPRAY COATING ON 3D OBJECTS USING LBM-BASED LEVEL SET EQUATION SOLVER

***T. Van Hoof*[1]**

[1]Computational Multi-Physics Software Development Team, Cenaero ASBL
Rue des Frères Wright 29, 6041 Gosselies, Belgium
Email: thibaut.vanhoof@cenaero.be presenting/corresponding

Abstract
An innovative numerical method is proposed to predict the growth of the layer during the thermal spray coating of a 3D objects. The complex spray trajectory and the resulting shadowing effects that may strongly affect the final footprint are considered. The method is based on the level set approach to capture the evolution of the deposited layer interface. The specificity of the proposed method is to use the Lattice Boltzmann Method (LBM) instead of standard elements-based approaches to solve the level set equation. The resulting numerical method shows promising capabilities for industrial applications especially in terms of ease of use, since LBM do not request a preliminary mesh, and high computational efficiency leading to fast simulation of realistic cases.

Keywords*: thermal spray coating, transient simulation, 3D object, process optimization*

1. Introduction
With the appearance of new technologies like 3D printing and shape optimization methods, the industry develops components with increasing geometrical complexity. The coating of such 3D objects is challenging since the control of the final coating layer requests the tailoring of the coating process parameters (involving complex source and/or object trajectories) to deal with 3D specific effects like the variation of the local deposition angle or the shadowing which have a strong impact on the final footprint. Currently, the identification of the coating process parameters for a new 3D component still relies on expensive trial and error procedures. In a previous publication (Van Hoof et al., 2019), an innovative numerical method is proposed to simulate the thermal spray coating (Tucker, 2013) (Fauchais et al., 2014) of 3D components in order to predict the shape of the resulting coating layer. The proposed method is based on level set approach to track the time evolution of the footprint during the coating process. The properties of the thermal spray source are modeled using analytical distributions with parameters fitted to reproduce experimental data. The proposed simulation method has been successfully assessed through a real aeronautic test case. The main limitation of the method proposed in (Van Hoof et al., 2019) is the computational costs: several hours are needed for a single coating simulation on a standard computer. Moreover, a volume mesh surrounding the object must be provided in order to solve the level set equation with the provided standard finite element method. The objective of the present work is to alleviate these limitations to provide a numerical tool able to efficiently assist the identification of coating process parameters for 3D object. The idea is to solve the level set equation using the 'Lattice Boltzmann Method' (LBM) to reduce the computational costs and avoid the need of a support mesh for the level set computations.

2. Theory
LBM is a fluid flow simulation method based on the discretization of the Boltzmann equation in time, physical and velocity spaces (Krüger et al., 2017). The fluid is described by a set of discrete-velocity distribution functions (or "populations") f_i representing densities of particles evolving according to a set of discrete velocities $\bar{c_i}$. The populations are defined and evolves on a regular grid according to the lattice Boltzmann equation:

$$f_i(\bar{x} + \bar{c_i}\Delta t, t + \Delta t) = f_i(\bar{x}, t) + \Omega(\bar{x}, t) \qquad (1)$$

Where Ω is the collision operator that involves most of the physics to be captured (fluid flow, thermal flow,etc.). It is generally approximate by a linear relaxation of the populations toward an equilibrium ${f_i}^{eq}$ as proposed by Bhatnagar-Gross-Krook (BGK):

$$\Omega(\bar{x},t) = -\frac{f_i(\bar{x},t) - {f_i}^{eq}(\bar{x},t)}{\tau}\Delta t \tag{2}$$

τ is a relaxation time related to diffusion. The time, space and velocity discretizations are performed in a coherent manner such that, at each time iteration, each population f_i travels exactly from one grid nodes $\bar{x}$ to the one pointed by the discrete velocity at $\bar{x} + \bar{c_i}\Delta t$. It results in a very simple and efficient algorithm. Each time iteration is a succession of a local "collision" operation, followed by a "streaming" step where the post-collided populations are displaced on the grid. LBM is used to simulate many different physical phenomena including multi-phase flows, heat exchanges, etc... However, the simulation of purely hyperbolic problems, like the level set equation, is still challenging due to the intrinsically diffusive nature of LBM. In the present work, new equilibrium populations are proposed to efficiently approximate the level set equation:

$$f_0^{eq}(\bar{x},t) = \sum_i f_i(\bar{x},t);\ f_{i>0}^{eq}(\bar{x},t) = \frac{f_0^{eq}}{c_s^2}\bar{c_i}.\bar{u} \tag{3}$$

The proposed LBM based level set solver has been implemented in the using the Palabos framework (Latt et al., 2021) and equipped with all the numerical tools allowing to simulate 3D coating processes. The overall numerical methodology is very similar to the one described in (Van Hoof et al., 2019).

3. Results and discussion

Fig. 1 shows the Cenaero butterfly coated on a sphere. The color map represents the thickness of the footprint. A mask with the butterfly shape (a 2D mesh) is placed in between the coating source and the target sphere. A ray-tracing method account for the shadowing effect leading to the butterfly shaped footprint.

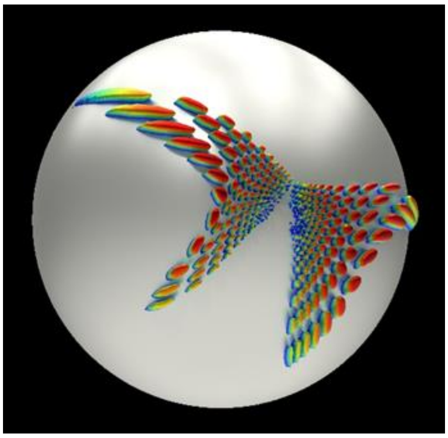

Figure 1. Coating of a sphere using a mask representing the Cenaero butterfly. The colormap allows to better observe the footprint thickness distribution.

Fig. 2 represents three different stages during the coating process of a gear in fast rotation (200RPM). The coating source is aligned with the gear radius. The observed asymmetry of the footprint is due to the relative velocity between the source and the fast-rotating gear surface.

The asymmetry is observed experimentally but is hard to advice and control. That example illustrates the promising capabilities of the numerical method to assist the development of complex 3D coating.

Figure 2. Coating of a fast-rotating gear with a source pointing toward to the gear centre. Snapshots of the footprint at three different times are presented

Finally, the accuracy and computational efficiency of the LBM based method is assessed through the comparison with the finite element tool (FE) for the real aeronautic test case as described in (Van Hoof et al., 2019). Fig. 3 shows the footprint obtained with the LBM solver which is very similar to the footprint obtained with FE in (Van Hoof et al., 2019). The observed maximal thickness differences are of the order of the percent. On the other hand, the definition of the numerical problem is far easier since the LBM based method simply request the surface mesh of the object and the computational grid for the level set is automatically build around the object with a uniform space resolution defined as a free input parameter of the simulation. Furthermore, the LBM based approach is one order of magnitude faster than the FE approach: the LBM based simulation runs in 10 minutes while the FE simulation requests 200 minutes using similar time and space resolutions and the same laptop computer.

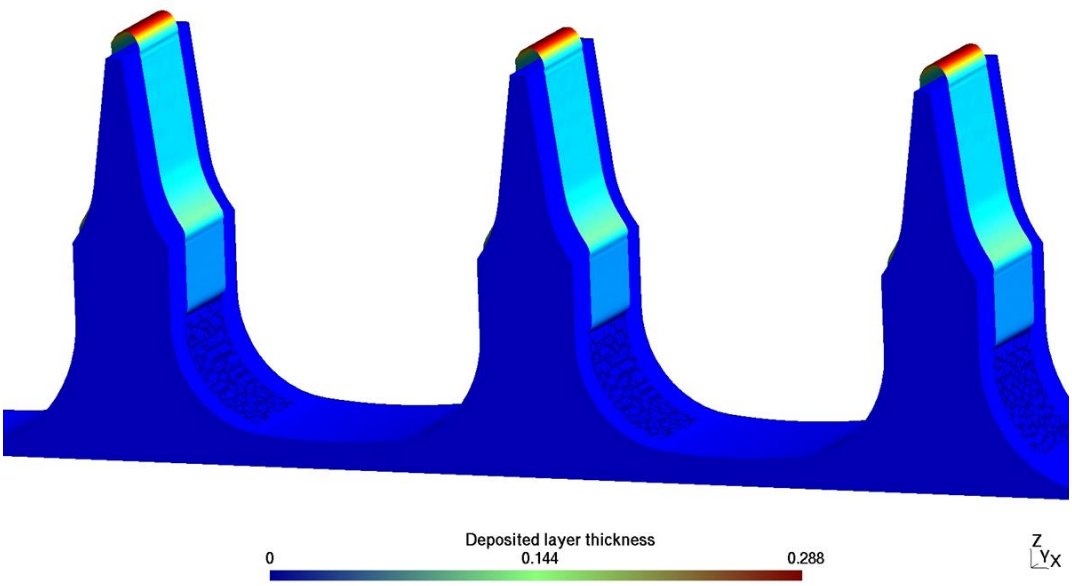

Figure 3. Aeronautic test case as described in (Van Hoof and al., 2019) performed using the new LBM based method. The resulting footprint is very similar to the one obtained with standard FE method in (Van Hoof and al., 2019).

5.Conclusion

A numerical method to simulate the growth of the footprint during the thermal spray coating on 3D objects has been proposed. The method is based on an innovative combination of level set and LBM methods to provide a fast and easy to use numerical solution able to face the challenges of realistic industrial applications. The method has been successfully assessed on three different test cases, including a real aeronautic test case already presented in (Van Hoof et al., 2019). In future works, the proposed approach can be improved to account for more complex physics in volved in coating processes (e.g. thermal exchanges) taking advantage of the LBM capabilities. It can also be assessed/extended to other manufacturing technologies (e.g. other coating processes, additive manufacturing).

References

Fauchais, P., Heberlein, J.V.R., & Boulos, M. (2014). *Thermal Spray Fundamentals from Powder to Part*, Springer, US.
Krüger, T, Kusumaatmaja, H, Kuzmin, A, Shardt, O, Silva, G., Viggen, EM (2017). *The Lattice Boltzmann Method Principles and Practice*, Springer International Publishing, Switzerland
Latt, J. et al. (2021), Palabos: Parallel Lattice Boltzmann Solver, *Computers & Mathematics with Applications*, 81, 334-350
Tucker, R.C., (2013). *ASM Handbook Volume 5A Thermal Spray Technology*, ASM International, New York
Van Hoof, T., Fradet, G., Pichot, F., Selezneff, S., & Poletz, N. (2019). Simulation of Thermal Spray coating on 3D Objects: Numerical Scheme and Aeronautic Test Case, *Journal of Thermal Spray Technology*, 28, 1867-1880.

Proceedings ECS
2021
Brussels, Belgium, September 7-9, 2021

Abstract T-31

GRAPHENE AS A DIFFUSION BARRIER FOR DIRECT METHANOL FUEL CELLS (DMFC)

Philipp Quarz[1,2]***, Víctor Gracia***[1,2]***, Angela Kruth***[3]***, Jens Wartmann***[4]***, Philip Scharfer***[1,2] ***and Wilhelm Schabel***[1,2]

[1]Thin Film Technology (TFT), Karlsruhe Institute of Technology (KIT), 76131 Karlsruhe, Germany
[2]Material Research Center for Energy Systems (MZE), Karlsruhe Institute of Technology (KIT), 76131 Karlsruhe, Germany

[3]Leibniz Institute for Plasma Science and Technology (INP), 17489 Greifswald, Germany
[4]The hydrogen and fuel cell center ZBT GmbH, 47057 Duisburg, Germany

Email: Philipp.quarz@kit.edu presenting/corresponding author

Abstract

Fuel cells are a key technology in the transition to renewable energy carriers. For example, (excess) capacities from renewable energies can be stored chemically as fuel (e.g. hydrogen or methanol) and converted to heat or electric energy at any given time. This flexibility makes fuel cells predestined for power-heat systems in self-sufficient building applications and in the transport sector.

A current challenge of direct methanol fuel cells (DMFC) is an undesirable methanol crossflow through the membrane electrode assembly (MEA). Market maturity of DMFC necessitates overcoming this challenge, a further cost reduction and an increase in efficiency along with large scale processabil-ity. Efficiently coated membranes meet these requirements and graphene qualifies as an excellent pro-ton conductor as well as an effective barrier against undesired crossover species. In combination with its outstanding mechanical stability, it represents an ideal membrane component that ensures a signifi-cant increase in performance and long-term stability of proton-conducting membranes.

Subject of this study is to improve the stability of a graphene suspension by adding polymer as well as producing homogeneous thin films in the range of a few micrometers. For this purpose, the stabilized suspension is characterized and the mass transfer during drying is simulated, which considers the dif-fusion of the graphene as well as the polymer. The drying conditions influence the morphology of the dry film. Experiments conducted with confocal micro-Raman spectroscopy validate the simulated dry-ing behavior. In addition, exploring the processing of promising nanoparticle systems is a focal point of this study.

The authors would like to acknowledge financial support of the Federal Ministry for Economic Affaires and Energy (BMWi) via Institut für Energie- und Umwelttechnik e. V. (IUTA) and the Ger-man Federation of Industrial Research Associations (AiF) in the "Graphenblocker"-project (Grant number: 20738 BG).

Keywords: *graphene, direct methanol fuel cell (DMFC)*

Proceedings ECS 2021
Brussels, Belgium, September 7-9, 2021

Abstract T-51

IMPROVING REDUCED ORDER SPATIAL MODELS FOR MICROPARTICLE COMPOSITE THIN FILM PROCESS-STRUCTURE LINKAGES

***Peter R. Griffiths*[1], *Tequila A.L. Harris*[1]**

[1] George W. Woodruff School of Mechanical Engineering, Georgia Institute of Technology, Atlanta, GA Email: pgriffiths3@gatech.edu presenting/corresponding author

Abstract
Material Informatics (MI) has been demonstrated to create predictive Process-Structure (PS) linkages for a variety of material systems and processes. However, each material system and its associated morphological features provides a challenge for which the MI workflow must be adapted to. Microparticle Composite Thin Films (MPCTFs) can present a difficulty due to their lack of separation of length scales between the morphological features and the thickness. The Material Knowledge System (MKS) has been proposed as a system adaptable to MPCTFs. Appropriate reduced order microstructure spatial models of the material in question are the key link which makes using MKS possible for robust PS linkages.

The objective of this work is to identify improvements in reduced order microstructure spatial models for MPCTFs and demonstrate their ability to capture short, mid, and long-range spatial microstructure features in films with particle concentrations gradients. Improved models were applied to a previously proposed workflow to create PS linkages for simulated microstructures created from slot-die coating simulation results. The impact to changes in the training data size and the reduced order microstructure spatial models on their ability to capture microstructure spatial features and PS linkage accuracy was evaluated.

***Keywords**: Material Informatics, Machine Learning, Process-Structure Linkages, Microparticle Composites*

Proceedings ECS
2021
Brussels, Belgium, September 7-9, 2021

Abstract T-30

VACUUM LIMIT FOR THE THIN-FILM SLOT COATING USING THE VISCOCAPILLARY MODEL AND CRITICAL RADIUS OF CURVATURE OF COATING BEAD

***J. Yoon*[1], *J. Nam*[1,*]**

[1]Department of Chemical and Biological Engineering, Seoul National University, Seoul 08826, South Korea
[*]Email: jaewooknam@snu.ac.kr

Abstract
Slot coating is one of the optimal processes for uniform thin-film production, i.e., the coated wet thickness on the moving web is smaller than half of the coating gap. Based on the standard viscocapillary model by Higgins and Scriven (1980), we related the maximum stable web speed limit of the thin-film slot coating without vacuum and the critical radius of curvature of the meniscus near the contact line. Finally, we derived a table for the vacuum limits of various Newtonian coating liquids.

Keywords*: thin-film slot coating, viscocapillary model, the critical radius of curvature, coating bead, vacuum limit*

1. Introduction

Slot coating is the representative process for the film product with uniform thickness varying from 10 to over 100 μm (Ding et al., 2016). In the whole unit in the slot coating process, the fundamental unit is the coating station, where the coating liquid is applied on the moving web. The uniformity of the thickness is possible under the coating station with stable operating conditions, e.g., coating gap, web speed, flow rate per unit width of the web. The stable operating condition keeps the stable coating bead, i.e., the coating liquid bridge between slot die and moving web with upstream and downstream menisci. Otherwise, various coating defects may occur. Especially when the upstream meniscus breaks out due to extremely high web speed, the uncoated area is obtained, i.e., bead break-up.

The coating gap is an order of 100 μm, which leads slot coating to be classified as thin and thick-film slot coating. The thin-film slot coating means the coated wet thickness is smaller than half of the coating gap, i.e., web speed is relatively high compared to the low flow rate per unit width for a given coating gap. Regarding the destabilizing effect on the coating bead in a thin-film slot coating, the viscous stress by moving web is much higher than in a thick-film slot coating. Therefore, one should stabilize a coating bead with a vacuum chamber at upstream of the coating station when the viscous stress exceeds the threshold by increasing the web speed. The previous studies, deformed from the standard viscocapillary model by Higgins and Scriven (1980), have tried to predict stable operating conditions for various slot coating systems. However, any previous work did not suggest the threshold above which a vacuum should be applied for the high web speed. Furthermore, researches on the wetting phenomenon of the slot coating without vacuum, which is crucial for the vacuum limit, are relatively scarce.

Interestingly, most previous researches have focused on the apparent dynamic contact angle (DCA) regarding the wetting phenomenon of the coating process. Ahn et al. (2018) firstly considered slot coating without vacuum and measured both DCA and the static contact angle (SCA) between static slot die and coating bead. However, according to Ahn et al. (2018), the SCA was not constant with respect to increasing web speed, and the DCA cannot be measured with a fixed other control variable, SCA. However, the radius of upstream meniscus curvature is accurately measurable instead of contact angles, at least in the slot coating station. Therefore, instead of an approach with apparent DCA or SCA, we investigated the vacuum limit by observing the critical radius of curvature at the maximum stable web speed in the thin-film slot coating. Finally, we could obtain a simple equation and a table of the vacuum limit for each Newtonian coating liquid.

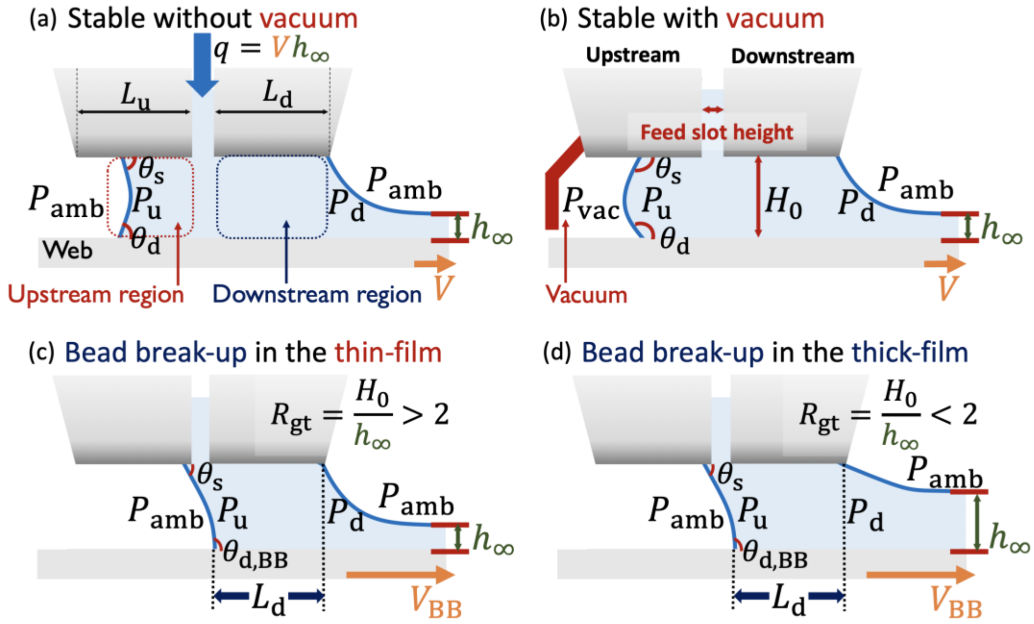

Figure 1. The coating bead for the thin and thick-film production

2. Theory

We derived the vacuum limit above which the thin-film slot coating requires a vacuum. We figured out that the vacuum limit is the web speed at the onset of bead break-up when R_{gt} ($=H_0/h_\infty$), the gap to wet thickness ratio, is two by using the Hoffman-Voinov-Tanner's law (Voinov, 1982) and the standard viscocapillary model. For a given R_{gt}, the standard viscocapillary model predicts the onset of bead break-up when $N_{\mathrm{Ca,BB}}$ ($= \mu V_{\mathrm{BB}}/\sigma$) satisfies

$$0 = ax^3 + bx^2 - c, \tag{1}$$

where $x = N_{\mathrm{Ca,BB}}{}^{\frac{1}{3}}$, and the coefficients are as follows:

$$a = \frac{6L_{\mathrm{d}}}{H_0}\left(1 - \frac{2}{R_{\mathrm{gt}}}\right),$$
$$b = 1.34 \cdot R_{\mathrm{gt}},$$
$$c = \cos\theta_{\mathrm{s}} + \cos\theta_{\mathrm{d,BB}} > 0.$$

Here, the subscript BB indicates the critical value at the onset of bead break-up (BB). On the other hand, we figured out that the governing equation, Eq. 1, has the maximum value for the root, x, when R_{gt} is two, i.e., $a = 0$. Provided $a = 0$, one can simply solve the $0 = bx^2 - c$ to obtain the maximum $N_{\mathrm{Ca,BB}}$ and V_{BB}. Here, Rushack (1976) and Scriven (1960) defined the DCA as shown in Fig 2(a), but we focused on the reason for why DCA is defined as in Fig 2(b). Therefore, the critical radius of curvature at the onset of bead break-up, i.e., r_{BB}, is obtained as below,

$$\frac{H_0}{r_{\mathrm{BB}}} = \cos\theta_{\mathrm{s}} + \cos\theta_{\mathrm{d,BB}}\,. \tag{2}$$

As a result, the maximum V_{BB}, V^{ub}, is given as follow:

$$V^{\mathrm{ub}} = \frac{\sigma}{\mu}\left(\frac{H_0/r^*_{\mathrm{BB}}}{2.68}\right)^{3/2}, \tag{3}$$

where the superscript * indicates the critical value when R_{gt} is two.

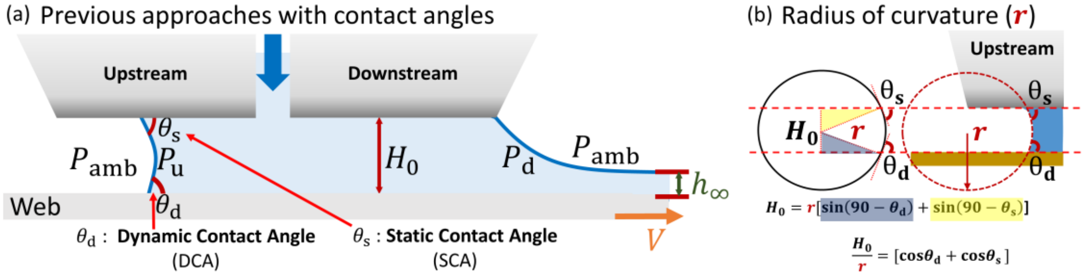

Figure 2. The radius of curvature of the upstream meniscus

3. Experimental procedure

Here, our research goal is to verify Eq. 3 by measuring both r^*_{BB} and V^{ub} (=V^*_{BB}), i.e., the web speed at the onset of bead break-up when R_{gt} is two. Furthermore, if we can obtain the representative value of r^*_{BB} for various coating gaps in the range of 100 - 200 µm, we can provide the representative V^{ub} for the typical range of the coating gap.

Figure 3 shows the lab-scale R2R (roll to roll) slot coater used by Hong and Nam (2017) and two visualization systems used to verify Eq. 3. For a fixed gap, one can increase the web speed and the flow rate per unit width (q) simultaneously to keep R_{gt} is two, i.e., $R_{gt} = H_0/h_\infty = VH_0/Vh_\infty = VH_0/q = 2$. The front-view is used to detect the bead break-up, as shown in Fig. 3(a). One can find V^{ub} by observing the transition of the location of upstream meniscus from the stable to the bead break-up. The side-view is used to detect r^*_{BB} as shown in Fig. 3(b). Our in-house program can measure H_0/r^*_{BB} by the number of pixels in 60 images for each second. Therefore, we can average H_0/r^*_{BB} for a few seconds of videos.

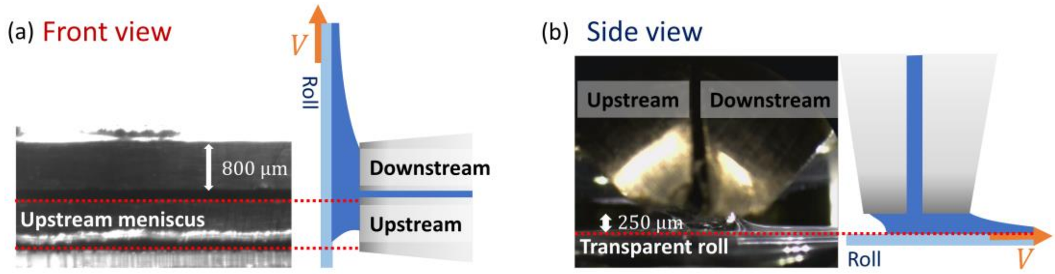

Figure 3. R2R slot coater with two visualization systems

4. Results and discussion

Because of damage on the transparent roll, we only conducted one experiment with a 95 wt% GW (Glycerine/Water) solution at $H_0 = 200$ µm. We changed with the new roll and planned to measure both $V^{ub}$and r^*_{BB} for 70 wt% and 95 wt% GW solutions at two coating gaps:100 µm and 200 µm.
By using assumed H_0/r^*_{BB}, one can get Table 2, which denotes V^{ub}, i.e., a criterion for the investment on the vacuum chamber. After the experiments on July 2021, we plan to obtain the average value of r^*_{BB} of each coating liquids for the two coating gaps: 100 and 200 µm. Therefore, we look forward to provide a more accurate V^{ub} than Table 2.

Table 2. The vacuum limit for Newtonian coating liquids in the thin-film slot coating with a typical coating gap of 100 to 200 µm.

Model fluid (GW: Glycerine/Water)	Viscosity* [cP]	Surface tension* [mN/m]	Assumed $r_{BB,avg}$**	Vacuum limit [m/min]
70 wt% GW	22.5	67.9	0.3	7
80 wt% GW	60.1	67.3	0.3	3
90 wt% GW	219	66.6	0.3	0.7

*Data from Takamura et al. (Takamura et al., 2012)
**To be measured by experiments on July 2021.

5. Conclusions

In this study, after the experiments planned for July 2021, we expect to obtain an accurate vacuum limit for the thin-film slot coating of each Newtonian coating liquid. We utilized the analytic approach based on the standard viscocapillary model and the radius of upstream meniscus showed Eq. 3. This approach avoids measurements for apparent DCA and SCA in the confined channel of the slot coating system. By using the side-view system, we would average r_{BB}^{*} for numbers of images, i.e., r_{BB}^{*} could be measured accurately. Provided Eq. 3 is verified, the standard viscocapillary model ensures that one can measure V^{ub} solely for various Newtonian coating liquids without any information for r_{BB}^{*} or DCA in industrial fields. Therefore, the experimental procedures above would be a standard to investigate the vacuum limit.

References

Ahn, W.G., Lee, S.H., Nam, J., Kim, S.J., Lee, K.Y., Jung, H.W., (2018). Effect of upstream meniscus shape on dynamic wetting and operating limits of Newtonian coating liquids in slot coating bead flows. *Journal of Coatings Technology and Research* 15, 1067–1076.

Ding, X., Liu, J., Harris, T.A., (2016). A review of the operating limits in slot die coating processes. *AIChE Journal* 62, 2508–2524.

Higgins, B.G., Scriven, L.E., (1980). Capillary pressure and viscous pressure drop set bounds on coating bead operability. *Chemical Engineering Science* 35, 673–682.

Hong, H., Nam, J., (2017). Automatic detection of contact lines in slot coating flows. *AIChE Journal* 63, 2440–2450

Mues, W., Hens, J., Boiy, L., (1989). Observation of a dynamic wetting process using laser-doppler velocimetry. *AIChE journal* 35, 1521–1526.

Ruschak, K.J., (1976). Limiting flow in a pre-metered coating device. *Chemical Engineering Science* 31, 1057–1060

Scriven, L., (1960). Dynamics of a fluid interface equation of motion for Newtonian surface fluids. *Chemical Engineering Science* 12, 98–108.

Takamura, K., Fischer, H., Morrow, N.R., (2012). Physical properties of aqueous glycerol solutions. *Journal of Petroleum Science and Engineering* 98, 50–60.

Vandre, E., Carvalho, M.S., Kumar, S., (2012). Delaying the onset of dynamic wetting failure through meniscus confinement. *Journal of fluid mechanics* 707, 496.J.